TUM School of Engineering and Design
Technical University of Munich

Advancing the Understanding of the Fatigue Behaviour of AISI 316L Manufactured via Powder Bed Fusion of Metals Using a Laser Beam (PBF-LB/M)

Johannes Diller

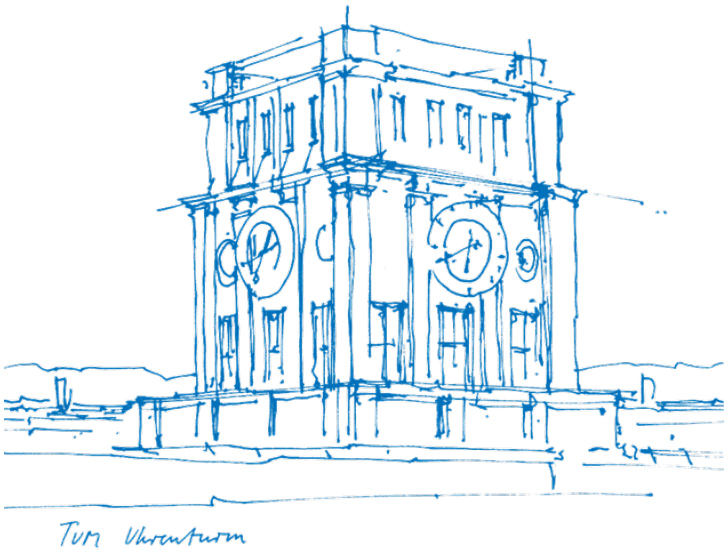

Advancing the Understanding of the Fatigue Behaviour of AISI 316L Manufactured via Powder Bed Fusion of Metals Using a Laser Beam (PBF-LB/M)

Johannes Diller

TUM School of Engineering and Design
Technische Universität München

Advancing the Understanding of the Fatigue Behaviour of AISI 316L Manufactured via Powder Bed Fusion of Metals Using a Laser Beam (PBF-LB/M)

Johannes Diller

Vollständiger Abdruck der von der TUM School of Engineering and Design der Technischen Universität München zur Erlangung des akademischen Grades eines

Doktors der Ingenieurwissenschaften (Dr.-Ing.)

genehmigten Dissertation.

Vorsitz: Prof. Dr. Kathrin Dörfler

Prüfende der Dissertation:
1. Prof. Dr.-Ing. Martin Mensinger
2. Prof. Dr.-Ing. Frank Krafft
3. Prof. Dr.-Ing. habil Marcus Rutner

Die Dissertation wurde am 15.04.2024 bei der Technischen Universität München eingereicht und durch die TUM School of Engineering and Design am 11.07.2024 angenommen.

1 Preface

This dissertation marks a significant chapter in my journey as a research associate at the Chair of Metal Structures at the Technical University of Munich. At the outset, my deepest gratitude goes to Prof. Dr.-Ing. Dipl. Wirt.-Ing. (NDS) Martin Mensinger, full professor of the Chair of Metal Structures. Your willingness to give me the chance to do a doctorate at your chair has been a cornerstone of my academic development. Your approach to helping young researchers by giving them the freedom to explore their scientific interests while simultaneously teaching us a mixture of scientific and practical knowledge has been invaluable.
I extend my sincere thanks to Prof. Dr.-Ing. Marcus Rutner and Prof. Dr.-Ing. Frank Krafft for their roles as co-advisor, and to Prof. Dr. Sc. techn. Kathrin Dörfler for her role in chairing the doctoral examination.
A special note of appreciation is reserved for Prof. Dr.-Ing. Frank Krafft. Our discussions throughout my time at the chair have been very helpful. The access to your laboratory at the Munich University of Applied Sciences has been very beneficial in my research. Your openness and eagerness to educate others and share your knowledge have influenced me professionally and encouraged me to transfer these qualities in my interactions.
I am equally thankful to my research group on fatigue and lightweight structures, led by Dr.-Ing. Christina Radlbeck. Your guidance extended beyond the daily tasks of academia, providing support in numerous personal challenges as well. I am particularly grateful to Dorina Siebert and Jakob Blankenhagen for their friendship, discussions, and support. Our collaborative efforts in brainstorming and generating new ideas have been a cornerstone of my academic and personal growth.
I extend my heartfelt regards to all my colleagues at the Chair of Metal Structures. The insightful discussions we have had were enriching to my work. Outside of our daily work routine, the various activities we engaged in played a crucial role in maintaining the balance necessary to complete my doctorate.
I also want to extend my sincere appreciation to everyone involved in the collaborative research centre DFG TRR 277. Your contributions gave me valuable insights into new and fascinating research areas, greatly expanding my horizons beyond my specific research topic. A special note of gratitude is directed towards Prof. Dr.-Ing. Michael F. Zaeh and David Wenzler from the Chair of Machine Tools and Manufacturing Technology of the Technical University of Munich for their collaboration during the research project. The opportunity to work together has been highly appreciated. I learned a lot from you, as your standards in challenging tasks is outstanding.
Furthermore, I am grateful to Prof. Dr. Jan Torgersen for granting me access to your laboratory during the final phase of my time at the Chair of Metal Structures. Your openness and innovative spirit have been a source of inspiration. I extend my best wishes to you and your continued success at the Institute of Material Science.
A special and profound thank you is dedicated to my family: Ulrich, Ulrike, Valea and Linda. While your contribution to this work may not have been direct, the foundation you have provided me with has been indispensable. The values, support, and encouragement you gave in me have been critical in reaching this milestone. I owe a great deal of my success to you and for that, my gratitude knows no bounds.
I want to extend my heartfelt gratitude to my wife, Anna, for her unwavering support from the very start of my master's thesis journey. Through countless challenges, you stood by my side, offering the support and freedom I needed to chase my dreams. Thank you.

2 List of Abbreviations

Name	Unit	Description
a	mm	Crack length
AI	-	Artificial intelligence
A_5	%	Elongation at fracture
AB	-	As built
ANN	-	Annealing
AD	-	Artificial defects
AX	-	Axial
C	-	Cylindrical
CT	-	Compact tension specimen
CNC	-	Computer numerical control
DB	-	Dogbone specimen
D_l	mm^2/s	Diffusion coefficient
d_{hkl}	μm	Interplanar spacing of a crystal
d_k	μm	Average grain size
E	J/mm^3	Volumetric energy density
F	-	Flat
FCC	-	Face centered cubic
FCP	-	Fatigue crack propagation
G	K/mm	Thermal gradient
h	μm	Hatch distance
HG	-	Hourglass specimen
K	-	Material constant for Hall-Petch relationship
K_t	-	Stress concentration factor
K_I	MPa$\sqrt{mm}$	Stress intensity factor at loading mode I
M	-	Machined
M-AX	-	Multiaxial load
N	-	Number of cycles
n	-	Order of reflection for XRD
NT	-	No heat treatment
P	W	Laser power
PBF-LB/M	-	Powder bed fusion of metals using a laser
R	-	Stress ratio
$R_{p0.2}$	MPa	Yield strength
R_m	MPa	Ultimate tensile strength
ST	-	Surface treatment
t	μm	Layer thickness
TWIP	-	Twinning induced plasticity
XRD	-	X-ray diffraction
XY	-	Horizontal building direction
Z	-	Vertical building direction
$\Delta\sigma$	MPa	Stress range
γ_{SFE}	mJ/m^2	stacking fault energy

Name	Unit	Description
ΔT	$^{\circ}C$	Temperature difference
σ_y	MPa	Yield strength
σ_0	MPa	Maximum shear stress of a single crystalorder to generate dislocation movement
σ_I	MPa	Macroscopic residual stresses
σ_{II}	MPa	Microscopic residual stresses
σ_{II}	MPa	Sub-microscopic residual stresses
σ_θ	MPA	Tangenial normal stress
λ	μm	Wavelength
v	mm/s	Scanning velocity
ρ	$^{\circ}$	root radius

Contents

3 Introduction

3.1 Additive manufacturing

In December of 1996, Dr. Wilhelm Meiners and Dr. Konrad Wissenbach jointly submitted their invention titled "Selective Laser Sintering at Melting Temperature" (EP0946325B1) to both the German and European patent offices. This groundbreaking innovation was officially granted a patent in October 1999. This invention laid the foundation for the method of powder bed fusion of metals using a laser. The ASTM 52900 standard [1] defines this process as the PBF-LB/M process. The material used in this process can be put at the end of the name, e.g. PBF-LB/M/316L or PBF-LB/M/AlSi10Mg. This and several other additive manufacturing processes garnered so much attention that even former US President Obama said in 2013, "...3D printing that has the potential to revolutionise the way we make almost everything." [2]. Today, the machines are not only equipped with multiple lasers (up to 16), but they are also equipped with highly modern monitoring systems to improve the build quality and ensure reproducible part quality [3]. The complexity of reproducible parts continues to advance annually, with the capability of manufacturing parts without the need for support structures [4]. Moreover, the build volumes of PBF-LB/M machines steadily expand year by year. In fact, these machines now have build volumes of up to 1200 mm x 600 mm x 1500 mm (x, y, z) [5]. This increased build volume is particularly appealing to the construction industry, where the production of larger parts is more common compared to the aerospace or automotive sectors, where the process is already used for serial production. In the construction industry, a primary application of this process lies in the manufacturing of connection nodes within space frames. These are characterised by complex geometries and substantial load-bearing requirements. Indeed, special applications like steel hysteretic dampers with complex geometries can benefit from the capabilities of the PBF-LB/M process. It allows for the production of complex and customised components, making it suitable for a range of specialised and non-standard applications where traditional manufacturing methods may not be as effective or efficient.

3.2 Challenges, objectives and approach

Despite the numerous advantages highlighted in Chapter 3.1, there remain unresolved challenges, and in certain instances, these issues are inherently unsolvable due to the unique characteristics of the manufacturing process. The components, manufactured for the application areas mentioned earlier within the construction industry are invariably subjected to fatigue loading. The PBF-LB/M process introduces defects in different scales that have not been observed in any other manufacturing process. These defects include surface topology issues, porosity at a different scale compared to casting, anisotropy, and the cooling rate, among others. They highly affect the fatigue properties. In order to guarantee the safe application of additively manufactured components in the construction sector, a thorough examination of the fatigue properties of the material is imperative.

Enhancing the fatigue properties of PBF-LB/M/316L has been the focal point of numerous research initiatives and development endeavours. Nevertheless, numerous areas remain unexplored, as this thesis diverges from optimising laser parameters and instead focuses on using optimised laser parameters while comprehensively characterising the resultant mechanical properties of the material.

In this context, the objective is to assess how surface and internal defects, as well as the unique microstructure, affect the static mechanical properties and the fatigue properties of PBF-LB/M/316L. This exploratory research approach is supported by investigations to gain a deeper understanding of the structural behaviour across the spectrum from low-cycle fatigue to high-cycle fatigue. This thesis aims to showcase the potential use of additively manufactured components with complex geometries within the construction industry.

To achieve the stated objectives, it is imperative to initially examine the influencing factors in isolation. These factors include the impact of grain size on mechanical properties, the cyclic plastic material behaviour, the effects of surface topology and internal defects on fatigue behaviour, and the ability to predict the fatigue performance. Furthermore, post-processing methods, such as hot isostatic pressing and vibratory grinding, are investigated in relation to their influence on fatigue behaviour. Following this, conventional post-processing methods are researched in combination with a focus on their effects on fatigue behaviour.

3.3 Structure of the thesis

This thesis is divided into six chapters. After the introduction in chapter 1, chapter 2 provides the necessary fundamentals regarding the PBF-LB/M process, the mechanical behaviour of the used material, and the statistical methods applied to evaluate the fatigue behaviour. In chapter 3, the state of the art is introduced, explaining the formation of the microstructure, the porosity and the surface topology during the PBF-LB/M process. Chapter 4 outlines the research approach adopted in this thesis, encompassing the establishment of scientific objectives and the fine-tuning of the methodology employed. Chapter 5 represents the publication-based section of this dissertation, summarising a concise overview of the key research findings of the author. The dissertation concludes in Chapter 6, summarising the key results and outlining potential future research.

4 Fundamentals

In this chapter, the necessary basics for understanding this dissertation are introduced. Since this thesis focuses on the investigation of the PBF-LB/M process using 316L, in chapter 4.6 the principle of the process is described. Chapter 4.1 and 4.2 explain the materials engineering aspects of the stainless steel alloy 1.4404 (316L). Chapter 4.3 provides a comprehensive introduction to the fundamental principles of residual stresses. Chapter 4.4 describes the geometrical as well as the material influences of the alloy on the fatigue behaviour. In Chapter 4.5, selected methods of artificial intelligence are presented.

4.1 AISI 316L - 1.4404

The chromium-nickel stainless steel alloy 1.4404/AISI 316L (hereinafter referred to as 316L) is one of the most widely used corrosion-resistant stainless steel alloys. The alloy is used in plant engineering and tank construction, the automotive industry, the construction industry, the chemical industry, the food industry, aviation, mechanical engineering and pharmaceuticals [6]. The mechanical properties of 316L are shown in Table 4.3. Depending on the manufacturing process, the mechanical properties, especially the yield strength, may vary greatly. The reason for that is thoroughly explained in chapter 4.2.2.

4.1.1 Crystal structure

In this chapter, the structures are briefly discussed, followed by a more detailed description of γ-austenite. The metallic elements predominantly crystallise in three types of lattices: body-centred cubic (bcc), face-centred cubic (fcc), and hexagonal close-packed (hcp), each approximately in equal proportions. Many properties, particularly the mechanical ones, are associated with the crystal structure. [7] 316L is a fully austenitic stainless steel according to [8]. 316L has a fully austenitic structure (γ-austenite) due to the alloy composition. γ-austenite consists of a face-centred cubic (fcc) crystal lattice. [6, 9] This means that there is an atom at every corner and in every face of the cubic elementary cell. A hard-sphere unit cell representation, as well as a reduced-sphere unit cell, are shown in Figure 4.1. The critical resolved shear stress for slip to occur is

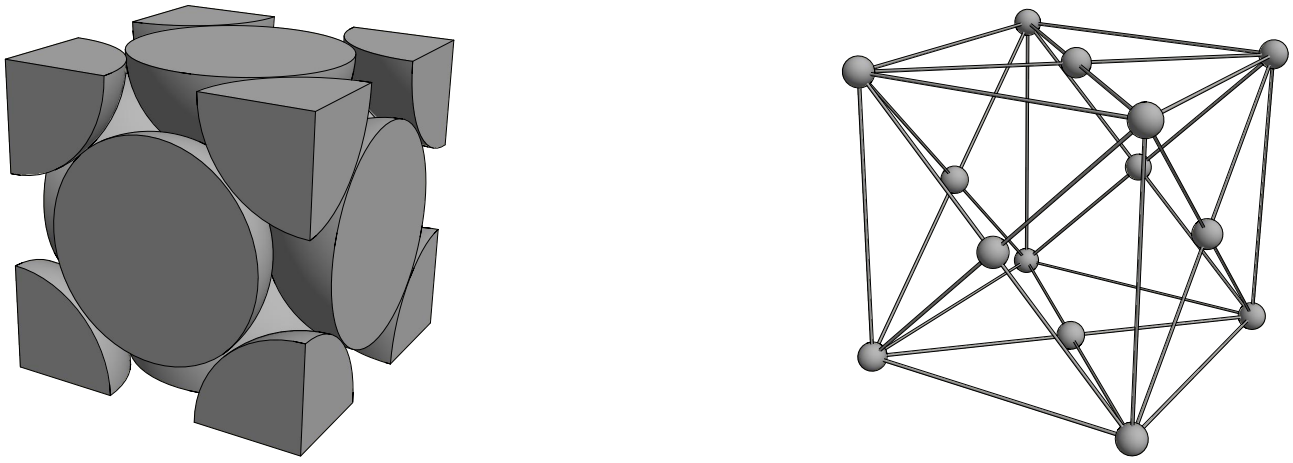

(a) *A hard-sphere unit cell representation* **(b)** *A reduced-sphere unit cell*

Figure 4.1: *Face-centered cubic crystal structure; adapted from [9]*

relatively low in fcc metals due to the closely packed nature of the (111)-planes and the availability of multiple slip systems. This means that FCC metals can begin to deform plastically under lower stresses compared to metals with fewer slip systems. Most metals with a face-centred cubic structure are known for their high ductility, and their reduction in strength decreases with increasing temperature [10]. The main slip plane of fcc-structures is the (111)-plane and consists of four slip planes and has up to 12 slip systems [9]. The atomic packing factor for fcc structures is about 0.74, which is the highest packing efficiency among the simple crystal structures. This means that in an fcc structure, 74 % of the volume is occupied by atoms, indicating a very efficient use of space.

4.1.2 Alloying elements

316L is a high-alloyed, low-carbon steel. 316L is known for its excellent weldability and exceptional resistance to corrosion. The low Carbon content eliminates or minimises the Carbon precipitation during welding. In stainless steels with higher carbon levels, Titanium is added to enhance intergranular corrosion resistance by forming titanium carbide, which prevents carbon from binding with chromium, a process that leads to intergranular corrosion. In the case of 316L, Titanium is not required as an additive to form a carbon bond. The formation of Titanium carbides is thus prevented, which increases processability. [6] The chemical composition according to [11] is shown in Table 4.1.

Table 4.1: *Chemical composition of 316L in wt.-% according to [11]*

Cr	Ni	Mo	Mn	Si	C	N	P	S
16.5 – 18.5	10.0 – 13.0	2.0 – 3.0	2.0	1.0	0.03	0.1	0.045	0.015

As illustrated in Figure 4.2 and in accordance with the Schaeffler-diagram [12], the composition of 316L primarily comprises austenite, with the ferrite content being influenced by the amount of nickel and chromium present. In the specific scenario depicted in Figure 4.2, the steel contains 17.85% chromium, 12% nickel, and 2.23% molybdenum.

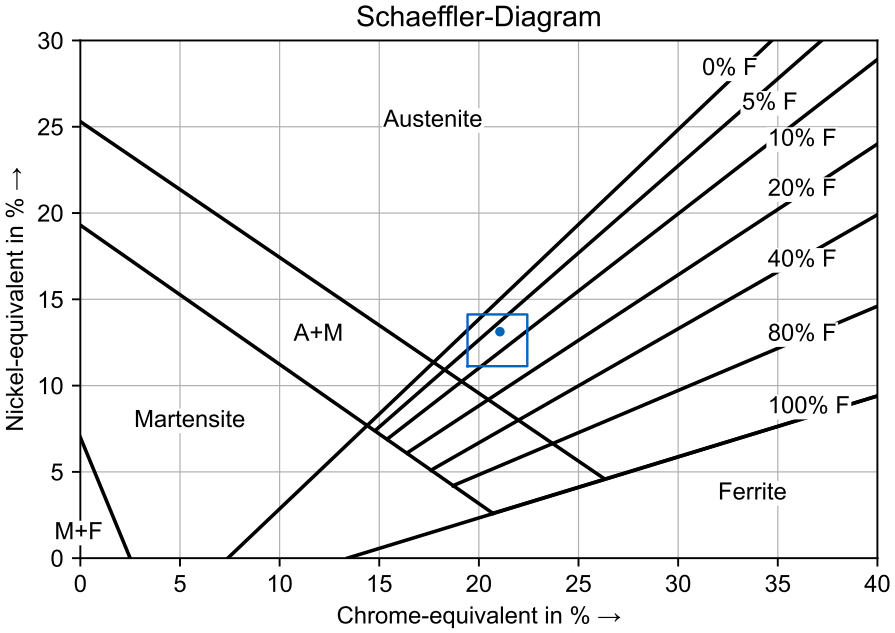

Figure 4.2: *Schaeffler-diagram, the blue dot marks 17.85 % Cr, 12 % Ni and 2.23 % Mo. The blue frame marks the range of 316L, listed in Table 4.1; adapted from [12]*

Each alloying element in 316L has a distinct influence on its mechanical properties. Table 4.2 provides an overview of the primary alloying elements and their effects on the mechanical properties and the microstructure. It is worth noting that Chromium, Nickel, and Molybdenum can be adjusted within certain limits. Consequently, 316L can exhibit variations in its austenite and ferrite content, along with potential fluctuations in austenite stability. Reducing the austenite stability may lead to a α'-martensite phase transformation during plastic deformation. [6, 9]

Table 4.2: *Influence of the main alloying elements on the microstructure and the mechanical technological properties; adapted from [6].*

Alloying element	Microstructure	Mechanical properties
Chromium	Ferrite creator	Main alloying element of stainless steels Passivation of steel from 12% minimum content
Nickel	Austenite creator	Second most important alloying element Can expand austenite range to below room temperature Improves corrosion resistance
Molybdenum	Ferrite creator	Increases corrosion resistance in reducing media Increases high-temperature strength
Manganese	Austenite creator	No influence on corrosion resistance Impairs α'-martensite formation
Silicon	Ferrite creator	Increased scaling resistance Improved corrosion resistance under certain stresses
Carbon	Austenite creator	Most essential alloying element of steel Strong extension of austenite range Very low content in stainless steels for corrosion reasons
Nitrogen	Austenite creator	Increase in austenite stability and yield strength No reduction in toughness

4.1.3 Mechanical properties

Static mechanical properties

The static mechanical characteristics of 316L may exhibit considerable variation based on the specific manufacturing approach employed. For instance, when 316L is hot-rolled, it typically demonstrates a yield strength between 190 MPa and 240 MPa [13]. In contrast, wrought 316L has the potential to reach a higher yield stress of 310 MPa. Conversely, 316L produced through PBF-LB/M can achieve a yield strength of up to 575 MPa, depending upon the orientation during the fabrication process, see Table 4.3. This significant disparity in strength attributes can be largely attributed to grain refinement, which is further explained in detail in Chapter 4.2.2, but will not be further presented in this section.

Fatigue Properties

Figure 4.3 illustrates a collection of S-N curves for 316L in various manufacturing conditions. It is evident from these curves that the fatigue properties of conventionally manufactured 316L, including hot-rolled and wrought variants, can exhibit considerable variations depending on the applied manufacturing process. Notably, wrought 316L typically displays superior fatigue resistance in comparison to hot-rolled 316L. This difference in fatigue performance can be attributed to the grain size, as elaborated upon in Chapter 4.2.2. Further insights into this phenomenon are also provided in Chapter 5.4.

Table 4.3: *Mechanical properties of 316L for different manufacturing methods at ambient temperature. The angles are the building directions perpendicular to the build plate.*

Manufacturing process	$R_{p0.2}$ MPa	R_m MPa	A_5 %	Source
Hot-rolled	220	520 – 670	45	[6]
Wrought	310	620	30	[6]
PBF-LB/M 0°	450 – 470	575	50 – 55	[14]
PBF-LB/M 90°	575	690	26 – 29	[14]

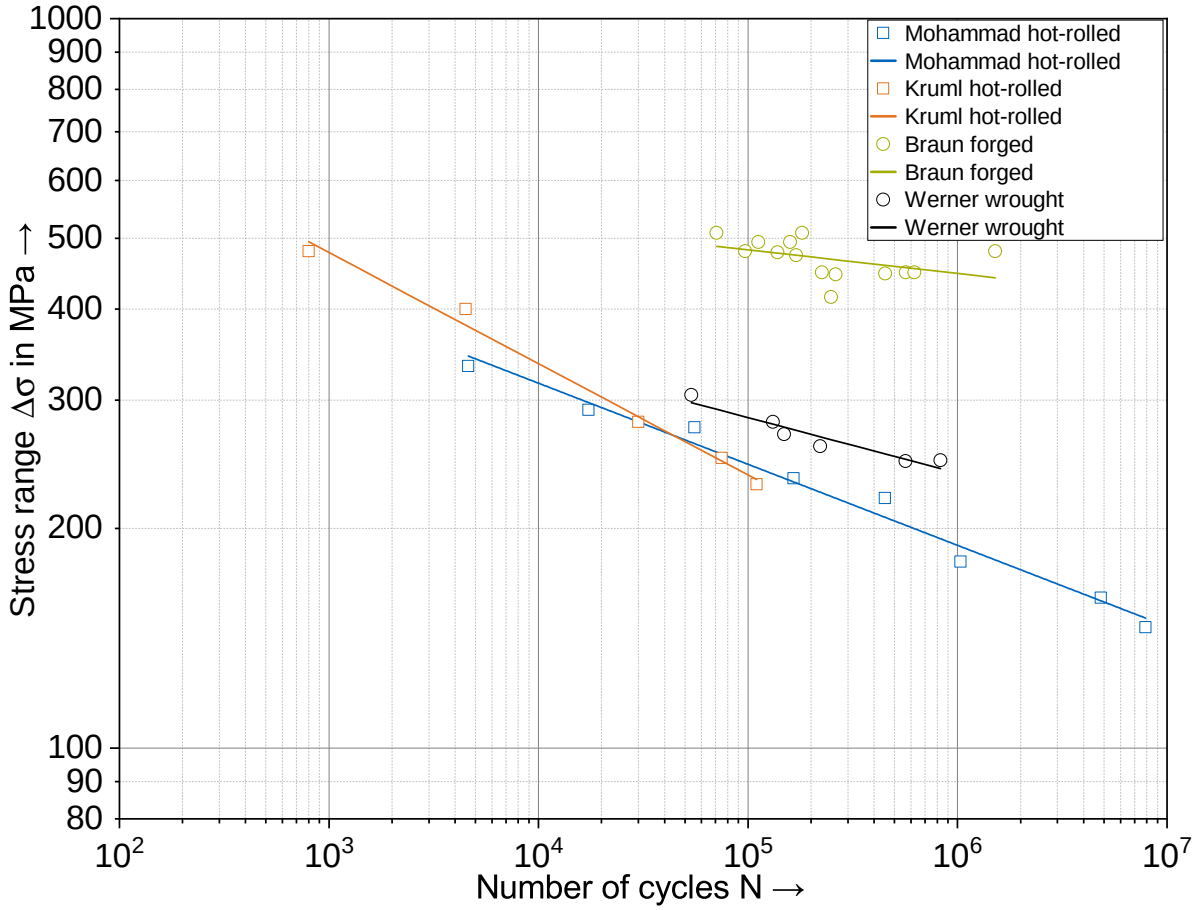

Figure 4.3: *S-N curves from literature of conventionally manufactured 316L from [15–18]*

4.2 Plastic deformation mechanisms

This chapter serves as an introduction to the foundational principles of plastic deformation mechanisms and the associated defects. Chapter 4.2.1 provides an elucidation of lattice defects relevant to the material in consideration. In Chapter 4.2.2 the mechanisms of the strengthening mechanisms occurring during plastic deformation are explained.

4.2.1 Lattice defects

Lattice defects can be divided into three types of defects which are point defects, linear defects and interfacial defects. In this chapter, only the lattice defects which occur at 316L are presented. For completeness, Table 4.4

gives an overview of all possible lattice defects. The crystal defects are divided into three categories according to their dimensionality. The lattice defects marked in red are described in more detail. The remaining elements are less significant in this work and have not been elaborated further.

Table 4.4: *Overview of lattice defects in metals according to [9]; The lattice defects marked in red are described in more detail.*

Dimension	Defect	Type
0	Point defect	Vacancies, interstitial atoms, substitutional atoms
1	Linear defect	Dislocations
2	Interfacial defect	Grain boundaries, twin boundaries, stacking fault, phase boundaries

Dislocation

A dislocation is, as shown in Table 4.4 and Figure 4.4, a linear or one-dimensional defect. It can be subdivided into an edge dislocation, a screw dislocation and a mixed dislocation. An edge dislocation can be described as an additional plane of atoms (half plane) in between two planes. This is also called the dislocation line. This dislocation line results in a localised lattice distortion. The planes next to the dislocation line are pushed together, and the planes below the dislocation line are pushed apart. The screw dislocation can be described as shear stress, which again results in a distortion of the lattice. Figure 4.4 shows a schematical description of a dislocation.

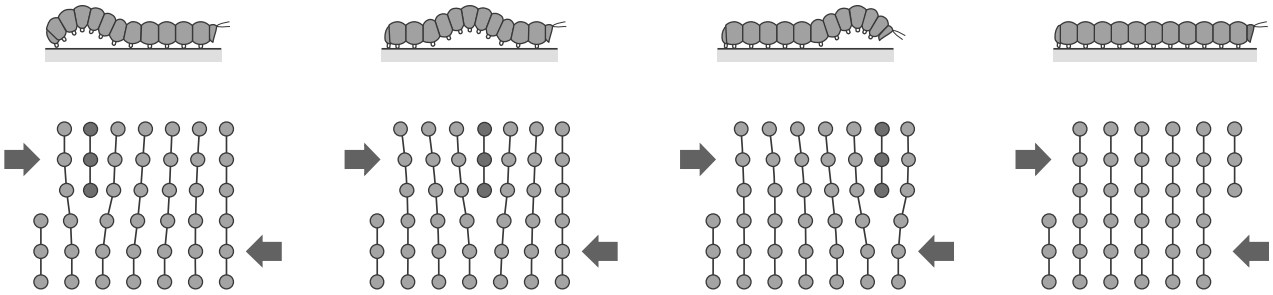

Figure 4.4: *Schematical description of a dislocation, extracted from [9]*

Grain boundary

A grain boundary is separating two small grains or crystals with different crystallographic orientations within a polycrystalline material. The boundary region is as small as several atom distances. The atomic mismatch in a transition from the crystalline orientation of one grain to another creates an increase of the critical resolved shear stress to overcome this boundary. The grain boundary usually consists of edge dislocations.[7, 9] Grain boundaries can be distinguished into high-angle and low-angle grain boundaries. A low-angle grain boundary is present if the mismatch between two adjacent grains is low. If the mismatch is large, the term high-angle grain boundary is used. Figure 4.5 shows a schematical description of low- and high-angle grain boundaries.

Twin boundary

A twin boundary is a type of interface that separates two regions of a crystal with identical atomic structures but different orientations. This means that the atomic arrangement on one side of the twin boundary is a mirror image of the arrangement on the other side, but the arrangement is not the same (see Figure 4.6). Twin boundaries occur when a crystal undergoes a deformation or growth process that results in a change in the crystal orientation. [9] A description of twinning-induced plasticity is discussed in chapter 4.2.2.

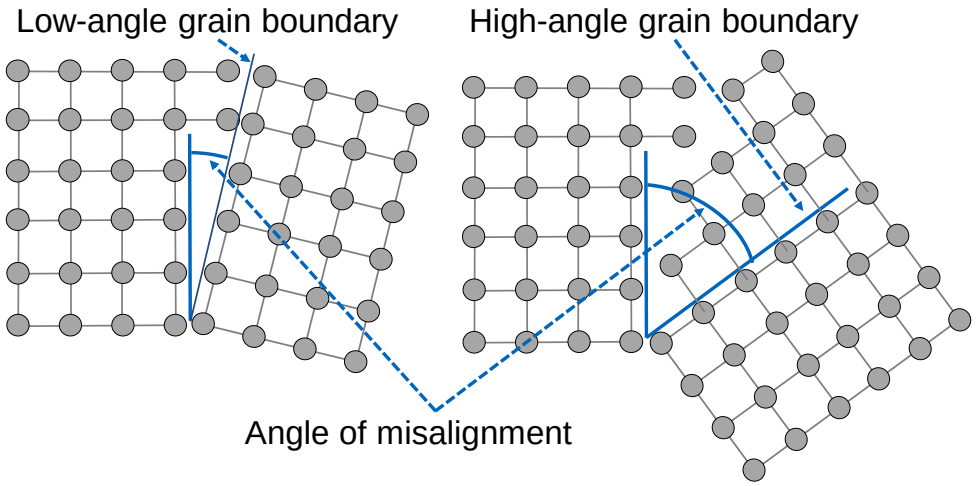

Figure 4.5: *Schematical description of low- and high-angle grain boundaries; adapted from [9]*

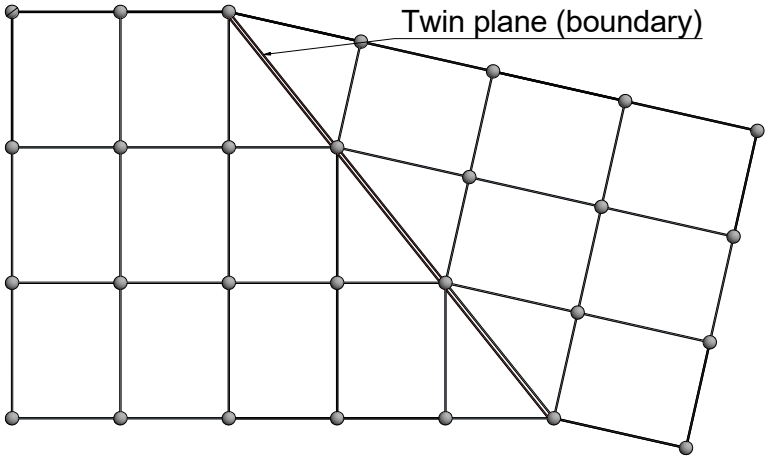

Figure 4.6: *Illustration of a twin plane or boundary along with the neighbouring atom positions adapted from [9]*

Stacking fault

All considerations on this subject should refer to the face-centred cubic lattice corresponding to the atomic arrangement of austenitic steels. This atomic arrangement has its preferred slip planes in the (111)-planes since they represent the most densely packed planes. When the distribution of atoms on these planes is closely examined, it becomes apparent that consecutively aligned unit cells are observed. These unit cells repeat themselves in a specific sequence. This sequence is known as an ABC sequence. If this sequence has been disrupted by any means and becomes, for instance, ABABCABC, it is referred to as a stacking fault. Stacking faults can be divided into intrinsic and extrinsic stacking faults. Figure 4.7 depicts an intrinsic stacking fault where one plane is missing due to the accumulation of lattice vacancies. On the other hand, an extrinsic stacking fault would be formed due to an interstitial agglomeration. [9]

These disruptions possess a particular stacking-fault energy. The width of a stacking fault results from the equilibrium between the repulsive force between two partial dislocations on one side and the attractive force caused by the surface tension of the stacking fault on the other. Consequently, the equilibrium width is partly influenced by the stacking-fault energy. The stacking-fault energy (SFE) is a material property at a very fine scale, denoted as γ_{SFE}, and is measured in units of energy per area. [7, 9]

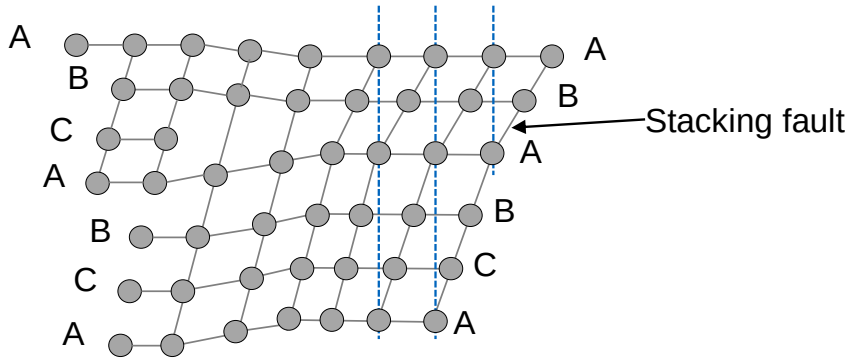

Figure 4.7: *Illustration of a stacking fault in a crystal lattice; adapted from [7]*

4.2.2 Strengthening mechanisms

Grain boundary strengthening and grain refinement

The deformation of crystallites within polycrystalline structures is constrained, as the overall structure must undergo deformation as a whole, preventing individual grains from disintegrating. Thus, each grain must participate in the deformation, and each grain must coordinate its deformation with its neighbouring grains to ensure the cohesion of the crystals along their grain boundaries. This boundary condition has decisive consequences for the deformation and strength of the polycrystalline structure. A polycrystalline structure consists of differently orientated grains. If an external tensile force is applied, the grains with favourably oriented slip systems start to deform. The grains with less favourable orientations have not yet reached the critical resolved shear stress. The deformation of one grain now leads to a distortion which is not shared by the surrounding grains. This deformation needs to be suppressed elastically. This usually leads to high stress, reaching the critical resolved shear stress at the surrounding grains. Only when all grains of a polycrystalline structure deform plastically, the yield stress is reached. [7]
With more grain boundaries to overcome, a higher external tensile load needs to be applied. Hence, the grain size affects the yield stress. This relationship is called the Hall-Petch relationship. The grain boundaries act as barriers due to two reasons. The first reason is the difference in the orientation from one grain to another. If a dislocation from one grain passes to another grain with a different angle to the first one, the dislocation needs to change its direction of motion. With increasing misorientation of the grain, the change of direction of the dislocation becomes more difficult. The second reason is the atomic disorder within a grain boundary. The atomic disorder leads to a discontinuity of slip planes from one grain to another. Ultimately, a fine-grained material consists of a larger grain boundary area in comparison to coarse grain materials. [19, 20]

Figure 4.8 shows a schematic illustration of the Hall-Petch relationship at the grain boundary of two grains. As soon as the critical resolved shear stress of the single crystals has been overcome, a buildup of the atoms already displaced in a grain is following. The slip planes in the neighbouring grain have a different orientation and are usually not parallel to each other. The dislocations at the grain boundary exert a back stress on subsequent dislocations, and the yield strength is thus increased. The Hall-Petch-relationship can be explained with the following equation:

$$\sigma_y = \sigma_0 + \frac{K}{\sqrt{d_k}} \tag{4.1}$$

In this equation σ_y is the yield stress in MPa, σ_0 is the maximum shear stress of a single crystal in order to generate dislocation movement, K is a material constant and d_k is the average grain size in μm.

Twinning induced plasticity

Twinning-induced plasticity (TWIP) is a deformation mechanism that occurs, amongst others, in 316L. It particularly occurs in materials that have a low stacking fault energy (SFE) such as austenitic stainless steels. TWIP involves the formation of twins, which are explained in chapter 4.2.1. This process leads to an increase

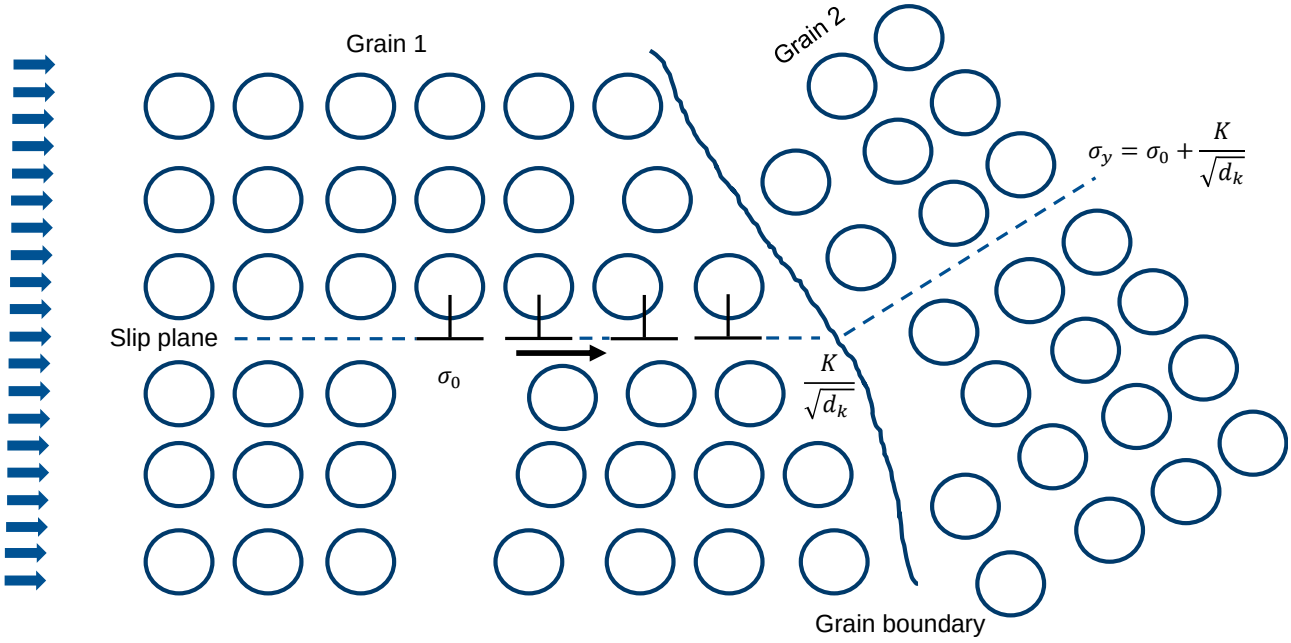

Figure 4.8: *Schematic representation of dislocation impediment at grain boundaries of two grains; adapted from [21]*

in the number of defects within the material, which in turn enhances its ability to deform plastically under stress.

During TWIP, the material undergoes plastic deformation through the generation of new twin boundaries. These twin boundaries allow for the material to accommodate deformation by forming new regions with different crystallographic orientations that can slide relative to each other. The new twin boundaries formed during TWIP can either nucleate at grain boundaries, or at pre-existing twin boundaries. [7, 9]

The presence of twins in the material causes the deformation to occur by a process known as mechanical twinning, which is different from slip deformation, which is the primary mode of deformation in most metals. In slip deformation, atoms move along crystal planes by dislocation motion, whereas in mechanical twinning, atoms are displaced across twin boundaries. This mechanism leads to an increased ability of the material to deform and hence improve its strength and ductility. [7, 9]

4.3 Residual stresses

Residual stresses are internal stresses within a component that exist without the application of external forces. Therefore, within a component, there must be regions with tensile residual stresses in equilibrium with those containing compressive residual stresses [22]. Depending on the distribution of the residual stresses and the external loading, residual stresses can be beneficial but also disadvantageous. This chapter provides the necessary information about the types of residual stresses in 4.3.1, followed by the applied measurement technique in chapter 4.3.2 and subsequently the effect of surface treatment on the residual stresses in chapter 4.3.3.

4.3.1 Types of residual stresses

Residual stresses can be categorised into three distinct groups based on the scale of observation. Figure 4.9 provides a visual representation of these three types of residual stresses. These categories include macroscopic stresses (σ_I), microscopic stresses (σ_{II}), and sub-micro stresses (σ_{III}). Macroscopic stresses (σ_I) extend over a considerable length and eventually reach an equilibrium state where they are balanced. Microscopic stresses (σ_{II}) are distributed and balanced within the confines of a single grain, spanning the length of that grain. Sub-micro stresses (σ_{III}) operate at the atomic scale, compensating for stress variations within a single grain. [9, 23]

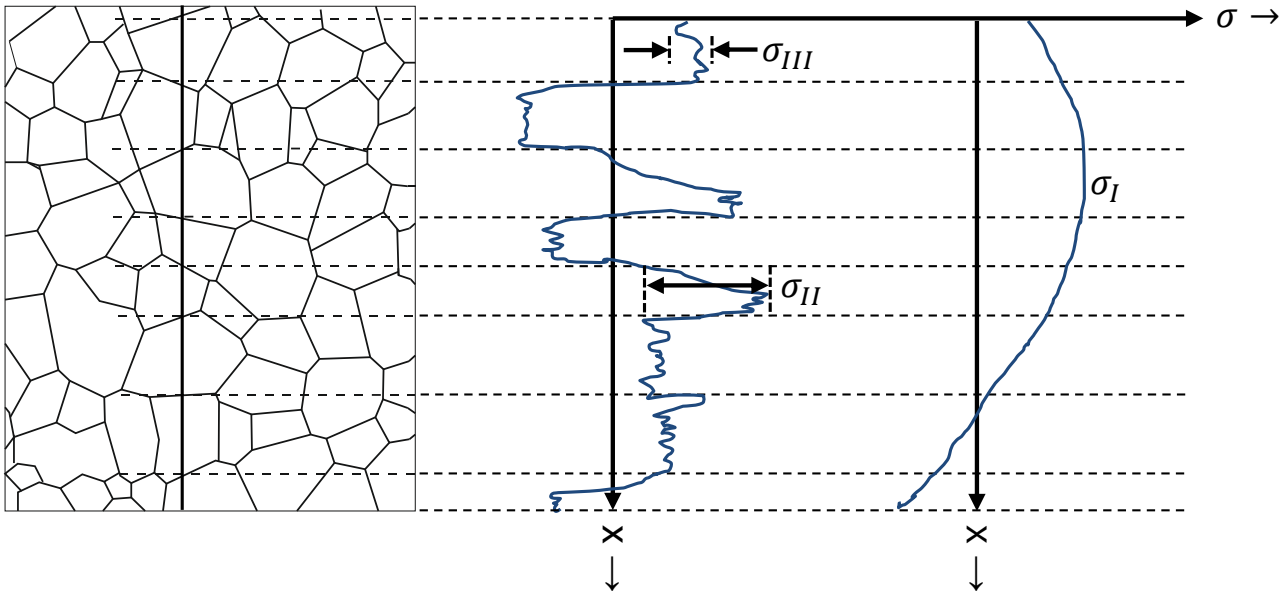

Figure 4.9: *Three types of residual stresses (σ_I, σ_{II} and σ_{III}) categorised according to different length scales; adapted from [23]*

4.3.2 Measurement of residual stresses

Various techniques exist for the measurement of residual stresses, but in this thesis, the focus is laid solely on X-ray diffraction. X-ray diffraction (XRD) is a non-destructive measurement method for identifying single crystal structures within a mixture of crystal structures. It offers detailed insights into the internal lattice of crystalline materials, including parameters like cell dimensions, bond lengths, and bond angles. An X-ray diffractometer comprises three primary components: an X-ray source, a sample holder, and an X-ray detector. [24]

The process begins with the heating of a filament in a cathode ray tube, generating X-rays. These X-rays are then accelerated toward a target by increasing the voltage. After impacting the target material, X-ray photons interact with the atomic structure of the electrons, causing some of the incident beam photons to scatter away

and be captured by the X-ray detector. Figure 4.10 illustrates the fundamental principles of X-ray diffraction, featuring the X-ray source, the X-ray detector (counter), and the goniometer. Typically, the goniometer is a 3- or 4-axis device, representing the four angles (2Θ, χ, ϕ, and Ω). 2Θ is the angle between the incoming and diffracted X-ray beams, which is important for determining the spacing between crystal planes. χ describes the rotation of the sample around an axis perpendicular to the X-ray beam, allowing for sample orientation adjustments. ϕ is the rotation of the sample around its own axis, useful for accessing different crystal planes during analysis. Ω refers to the rotation around an axis parallel to the X-ray beam, which is critical for setting the direction of the incident beam relative to the sample. [24]

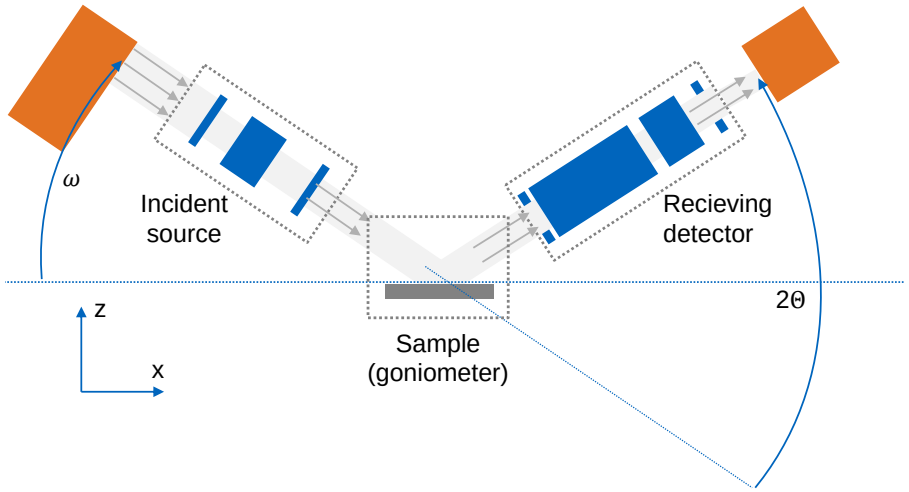

Figure 4.10: *Basic principle of X-ray diffraction; adapted from [25]*

When diffracted waves from multiple atoms interfere with each other, the resulting intensity distribution is significantly modulated by the interaction between X-rays and the electrons of the material. Assuming periodic arrangement of atoms, as in crystalline structures, the diffracted waves yield certain interference peaks that exhibit the same symmetry as the atom distribution. These peaks are directly associated with atomic distances (d) within a crystal structure. Figure 4.11 demonstrates the Bragg's law reflection principle, which mathematically explains the relationship between incident X-ray wavelengths, the angle of incidence, and the spacing between atomic lattice planes. Bragg's law is expressed as follows [24]:

$$n \cdot \lambda = 2 \cdot d_{hkl} \cdot sin\Theta \tag{4.2}$$

Where λ is the wavelength, emitted by the X-ray source, n is the order of reflection, d_{hkl} is the interplanar spacing of the crystal and Θ is the angle of incidence. [24]

Diffracted X-rays exhibit peaks when the difference in the distances between paths ABC and A'B'C' corresponds to an integer multiple of the wavelength (λ). The goniometer is used to scan the specimen at various angles. Subsequently, a plot depicting peaks is generated, providing a visualisation of distinct crystallographic planes. After measuring the crystallographic planes using X-ray diffraction, deviations from the expected distances between these planes can be measured. These deviations indicate lattice distortion, providing information about the presence and magnitude of residual stresses within the material. The lattice distortions are indirectly incorporated into the calculation of residual stresses through the measurement of the lattice spacing (d-spacing) using X-ray diffraction. The lattice spacing is related to the strain (ε) through the formula:

$$\epsilon = \frac{\Delta d}{d} \tag{4.3}$$

Where Δd is the change in lattice spacing, and d is the original lattice spacing. Once the strain is determined from the lattice distortions, it can be substituted into Hooke's law ($\sigma = \frac{E \cdot \varepsilon}{1-\nu}$) to calculate the corresponding residual stresses (σ) within the material.[9, 26]

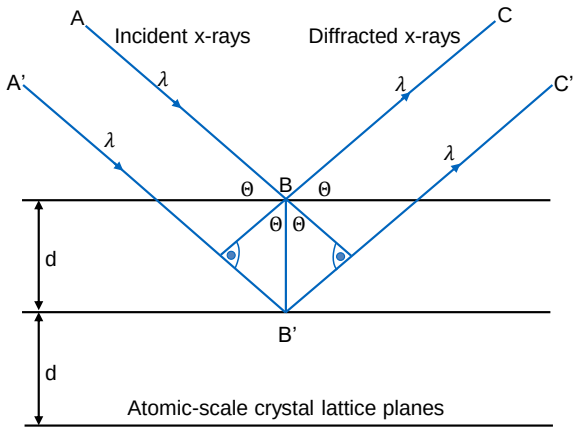

Figure 4.11: *Constructive interference in a crystalline solid: Two beams with identical wavelength and phase encounter the solid, scattering off distinct atoms within it. The lower beam travels an additional path of* $2d\sin\Theta$*. Constructive interference arises when this path matches an integer multiple of the radiation wavelength.; adapted from [24]*

4.3.3 Effect of surface treatment on the surface residual stresses

Surface quality enhancement often involves various surface treatments, such as manual polishing, machining. For complex geometries, methods like vibratory grinding and electrochemical polishing are used. Depending on the specific process applied, surface compression residual stresses are induced [27–29]. These residual stresses can potentially enhance fatigue resistance. However, if these processes are not executed correctly, the opposite effect may occur [29].

Figure 4.12 provides an example of how shot peening can introduce a metallurgical notch into the surface. This metallurgical notch arises due to a sudden change in residual stresses, thereby increasing the likelihood of early fatigue crack initiation [30].

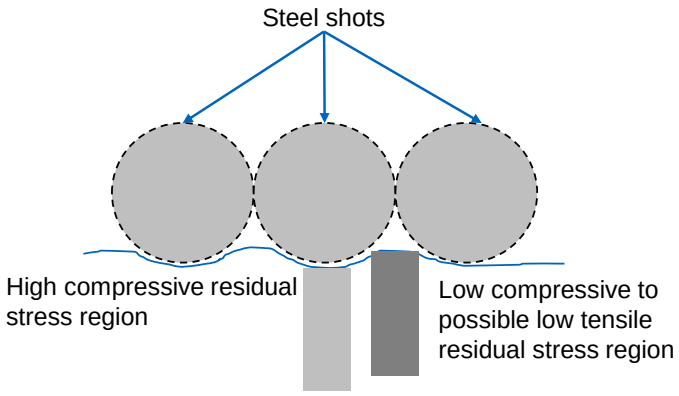

Figure 4.12: *Residual stress distribution in subsurface due to shot peening; adapted from [24]*

The high-velocity impact of steel shot onto the material induces plastic deformation, resulting in the generation of compressive residual stresses on the surface. In regions adjacent to the impact zone, the material experiences deformation as well, albeit with reduced compression force. As mentioned earlier in this chapter, residual stresses are balanced locally within a given region. Consequently, this process can lead to various residual stress states, varying from low compressive to low tensile residual stresses. [24, 28]

4.4 Fatigue and fracture mechanics

Fatigue is the progressive and localised structural damage that occurs when a material is subjected to cyclic loading. Over time, these repeated stress cycles can initiate and propagate cracks, eventually leading to failure at stress levels lower than the yield strength of the material. The phenomenon is influenced by various factors, including the magnitude and frequency of the loads, material properties, environmental conditions and defects of the material. Figure 4.13 presents the potential defects or imperfections within the microstructure, as well as the inclusive scope of the discipline of metallurgy. Furthermore, a clear distinction between geometrically related defects and those intrinsically associated with the microstructural composition can be made. These geometric defects are universal and not contingent upon specific materials, observable across diverse metal types. [31]

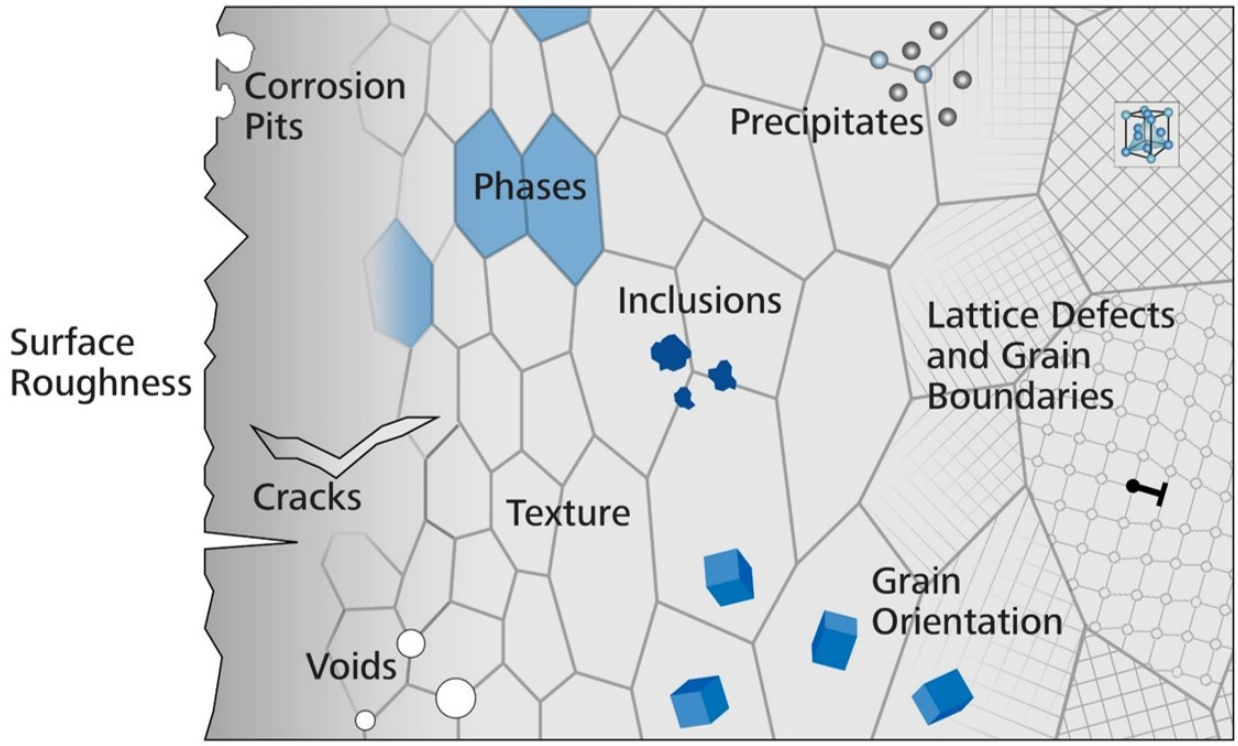

Figure 4.13: *Overview of defects in metals showing microstructural as well as geometrical defects; extracted from [32]*

4.4.1 Nominal Stress

Typically, stress S-N curves are generated through force-controlled fatigue testing at various amplitudes. These curves represent the endurance limit of the material, illustrating the highest number of cycles it can withstand at specific stress amplitudes before failure. In fatigue analysis, nominal stress is a basic stress measure to approximate the load conditions a material or structure faces throughout its service life. Assuming the material is defect-free and subjected to a uniaxial stress condition, the nominal stress represents the current stress state of the material. However, stress concentrations can arise when dealing with complex geometries and/or the presence of defects within the material. This localised increase in stress can significantly affect the response to fatigue of the material, deviating from the simplified scenario described by nominal stress. [31]

4.4.2 Stress concentration

The phenomenon known as 'stress concentration' occurs when the stress at the edge of a hole or a notch root surpasses the remote stress, resulting in a higher stress value. This elevated stress level often leads

to the initiation of fatigue cracks at these stress concentration sites. Once a crack is initiated, the stress concentration at the crack tip becomes a crucial consideration with regard to fatigue and part failure. [33] Therefore the stress concentration factor K_t is used in linear elastic fracture mechanics. Equation 4.4 describes the formula for the stress concentration. K_t is the stress concentration factor, σ_0 is the nominal stress and σ_θ is the tangential normal stress. [31, 33]

$$\sigma_\theta = K_t \cdot \sigma_x \tag{4.4}$$

In Figure 4.14 (a), a circular hole is depicted in a finite plate subjected to a uniaxial external tensile stress, σ_0, in the A-direction. At points A and C, the tangential normal stress, σ_θ is three times the uniaxial remote stress. Figure 4.14 (b) illustrates a wide plate with an elliptical hole subjected to uniaxial tension in the y-direction, where the stress concentration factor is determined as [34]:

$$K_t = 1 + \frac{(2a)}{b} \tag{4.5}$$

In the context of equation 4.5, the factor a represents the half-width of the ellipse, and b represents the half-height of the ellipse. The ellipse refers to the shape of the stress distribution around the circular hole under the given uniaxial remote tensile stress. [34]

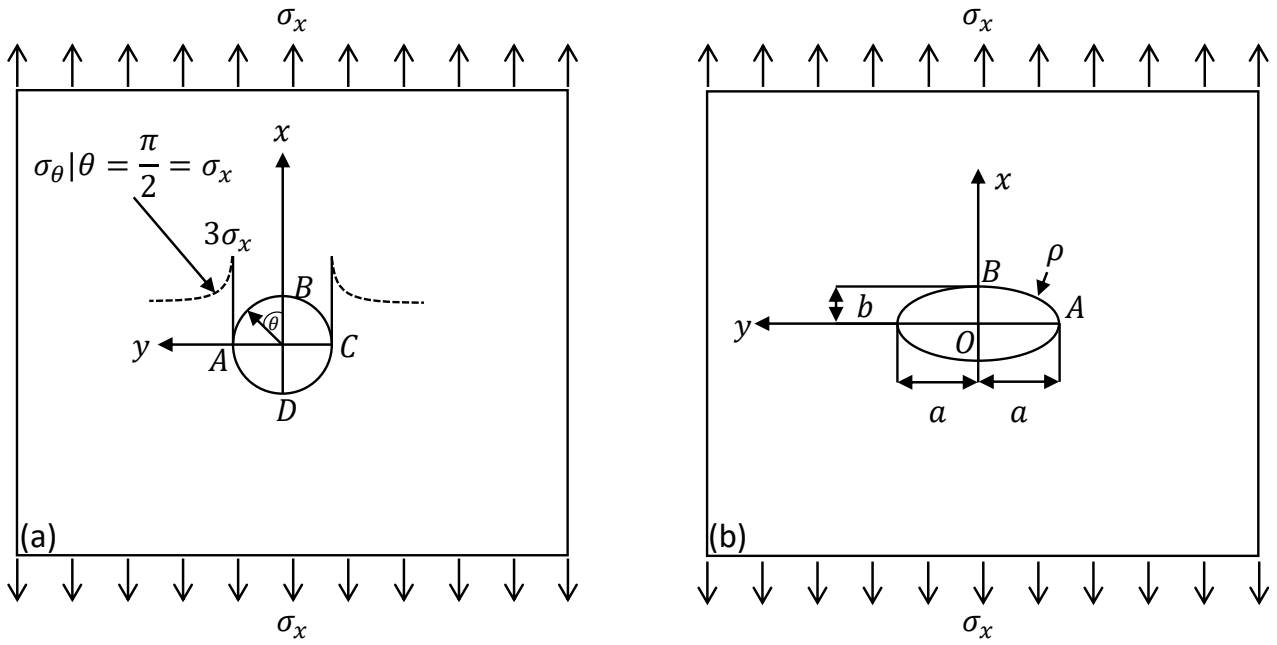

Figure 4.14: *Schematic representation of stress concentrations of circular (a) and elliptic (b) holes in a plate; adapted from [33]*

4.4.3 Stress intensity

The application of stress concentration factors to cracks is limited due to the sharp tip of the crack with a root radius ρ close to zero. When using Equation 4.4 to calculate the theoretical stress concentration factor, it would always result in an infinite value, regardless of the crack length. This theoretically infinite stress would suggest an immediate fracture, which does not align with the observed behaviour. In reality, a plastic zone forms around the crack tip due to the high deformations. This plastic zone causes the crack tip to have an opened, nonzero radius. As a result, the stress is reduced to a finite value. The concept of the plastic zone is illustrated in Figure 4.15, demonstrating how the stress concentration at the crack tip is mitigated by the formation of this plastic zone, preventing the immediate fracture that would be expected from an infinite stress concentration factor. [33, 35, 36] To describe this effect, Murakami et al. introduced the stress intensity factor

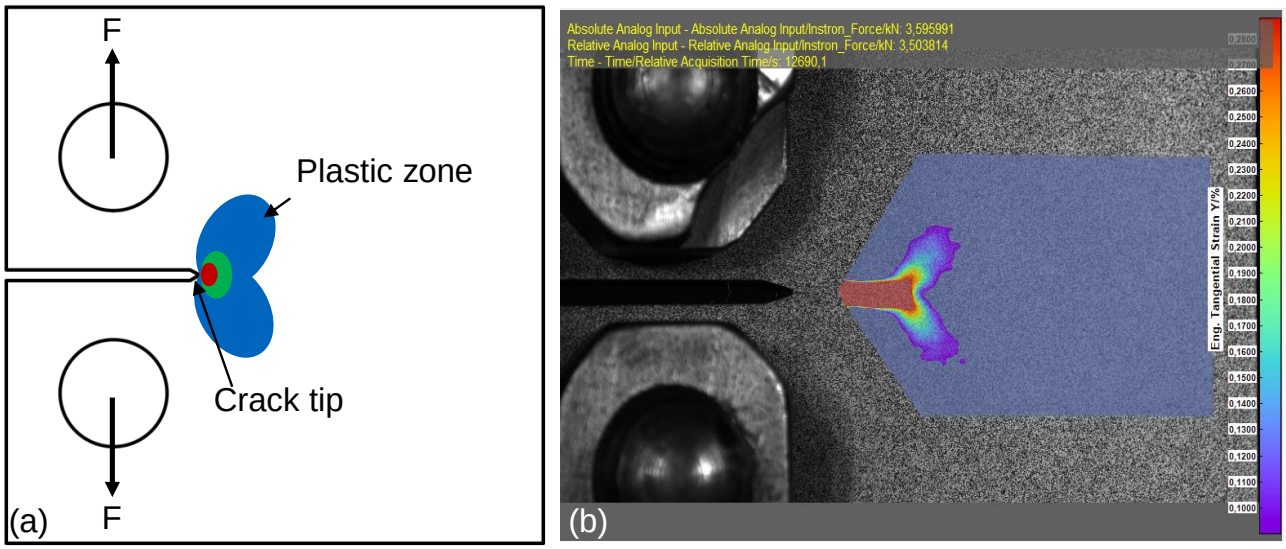

Figure 4.15: *Schematic representation (a) of a plastic zone near a crack tip and a strain field measurement (b) of a CT specimen using digital image correlation. The engineering tangential strain in the y-direction is shown.*

[33]. The resulting formula for a stress intensity factor in the linear elastic fracture mechanics is expressed as follows:

$$K_I = Y \cdot \sigma \cdot \sqrt{\pi \cdot a} \tag{4.6}$$

The stress intensity factor at mode I (opening) is denoted as K_I. It is determined by a dimensionless function Y, which depends on the geometry of the defect. Additionally, σ represents the nominal applied stress, and a represents the crack length [33].

4.4.4 Geometrical defects

Geometrical defects have a significant impact on fatigue resistance, as shown in the study by Murakami (2019) [33]. The severity of these geometrical defects can vary greatly depending on factors such as size, location, morphology, and other characteristics. Geometrical defects can be categorised into two main types: internal defects and surface defects. The concept of stress intensity, which was elaborated further in Chapter 4.4.3, plays a fundamental role in understanding geometrical defects.

Internal defects

To calculate the stress intensity of complex geometries of defects analytically, the $\sqrt{\text{area}}$-method was introduced by Murakami et al. [33]. This method involves creating an ellipse around a defect and calculating the area enclosed by the ellipse. A schematic description is shown in Figure 4.16.

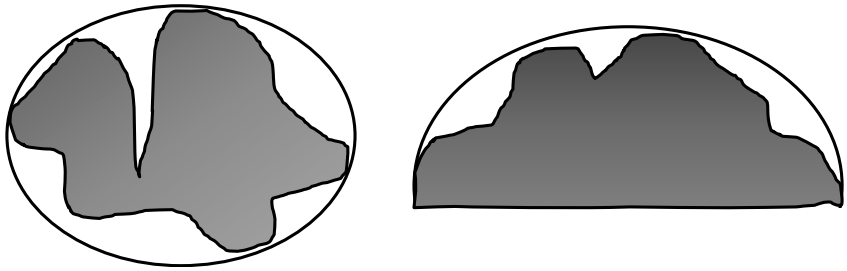

Figure 4.16: *Irregularly shaped crack, and estimation method for effective area; adapted from [33]*

The stress intensity factor of internal elliptical cracks is described by the following equation [33]:

$$K_I = 0.5 \cdot \sigma \cdot \sqrt{\pi \cdot \sqrt{area}} \tag{4.7}$$

$$\frac{a}{h} \geq 0.8 \tag{4.8}$$

Where a represents the radius of the defect, and h is the distance from the center of the defect to the surface. Figure 4.17 shows a schematic description of the radius of the defect and the distance from the defect to the surface.

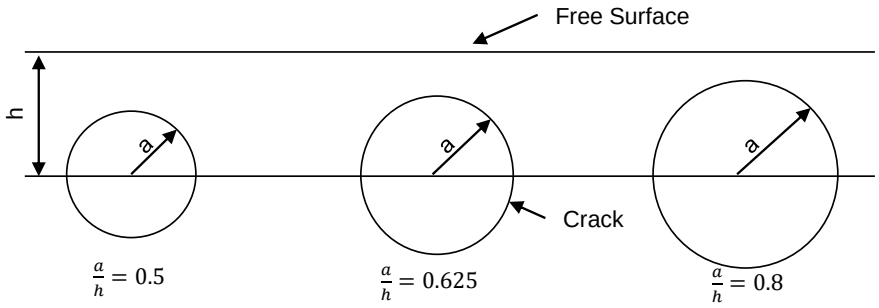

Figure 4.17: *Stress intensity factors for a circular crack close to a free surface; adapted from [33]*

When dealing with very shallow or very deep surface cracks with a length or depth greater than ten times their width, the estimation of $\sqrt{area}$ is calculated as follows:

$$\sqrt{area} = \sqrt{10} \cdot a \tag{4.9}$$

The stress intensity factor is primarily applicable within the linear elastic range of materials. However, this concept can also be extended to materials experiencing small-scale yielding at a crack tip. [33]

Surface defects

The equation for the calculation of stress intensities of surface defects is based on equation 4.7. However, for wider surface cracks, the following equation is used:

$$\sqrt{\text{area}_R} \approx \begin{cases} 2.97 \cdot \frac{a}{2b} - 3.51 \cdot \left(\frac{a}{2b}\right)^2 - 39.74 \cdot \left(\frac{a}{2b}\right)^3 & \text{for } \frac{a}{2b} < 0.195 \\ 0.38 & \text{for } \frac{a}{2b} > 0.195 \end{cases} \tag{4.10}$$

In this scenario, the variable $2b$ represents the distance between one peak and the next peak on the surface, while a denotes the depth of the surface defect. [35, 37]

4.4.5 Microstructural defects

This chapter describes the relevant microstructural defect types for 316L and the PBF-LB/M process. Other microstructural defect types that are not relevant to this research are intentionally omitted from the discussion. Microstructural defects related to the examined 316L material have been discussed in Chapter 4.2.1. This chapter offers insights into how these defects influence the fatigue behaviour.
If the plastic zone greatly exceeds the size of the individual grain and the distance between inclusions, no significant effects compared to those observed in uniformly deformed specimens should be expected. However, when the size of the plastic zone is of a similar order of magnitude or smaller than that of the grains, novel effects are expected [38]

Grain size

The Hall-Petch relationship describes the relationship between the grain size and the yield strength as described in chapter 4.2.2 and establishes the base for this chapter [19, 20]. Numerous studies have consistently demonstrated that a smaller grain size contributes to an increased fatigue resistance in comparison to materials with larger grains [39–43]. The key factor contributing to the enhancement of fatigue behaviour is the delay or retardation of fatigue crack initiation. The grain size also affects the cyclic strain hardening behaviour [44].

Stacking fault energy

To characterise the formation of stacking faults, the stacking fault energy (SFE) γ is used. Without considering this energy, the dislocations would theoretically move further apart from each other to reach an energy minimum. However, as the separation distance between partial dislocations increases, the stacking fault energy also increases proportionally. Consequently, an equilibrium state is eventually reached. This equilibrium is governed by the stacking fault energy, which effectively exerts a counteracting force against dislocation splitting. Stacking fault energy, therefore, may serve to restrict excessive separation between the two partial dislocations. Measuring the dislocation splitting distance using transmission electron microscopy offers a practical method for quantifying this parameter. A high SFE means that it takes a relatively large amount of energy to create stacking faults, making it energetically unfavourable. Conversely, a low SFE means that stacking faults can be easily formed. The presence of stacking faults and their interaction with dislocations can facilitate the initiation of fatigue cracks. These cracks can start at locations where stacking faults have formed and subsequently propagate through the material. Materials with high SFE values are less prone to the formation and accumulation of stacking faults during cyclic loading. As a result, the initiation and propagation of fatigue cracks are inhibited. This leads to improved fatigue resistance, as the material is better able to withstand cyclic loading without premature crack initiation and propagation. [45, 46]

4.5 Artifical intelligence

Artificial Intelligence (AI) represents a field dedicated to creating intelligent systems and machines capable of executing tasks that traditionally would need human intelligence. This encompasses a wide range of applications and approaches, including Machine Learning and Deep Learning. Machine Learning is a subset of AI that focuses on the development of algorithms capable of learning from data. These algorithms have the ability to recognise patterns within data and make decisions based on their observations. While machine learning systems can operate autonomously, they may require human intervention when confronted with incorrect decisions or unexpected situations. Deep Learning, on the other hand, is a specialised branch of artificial intelligence that uses artificial neural networks. These networks are designed to model complex patterns and relationships within data, enabling them to make highly accurate predictions and conclusions. Deep learning systems can often function independently, making them particularly well-suited for tasks where human intervention is limited or impractical. This technology has shown success in various fields, including computer vision, natural language processing, and speech recognition. [47] This chapter only deals with machine learning algorithms. Figure 4.18 shows the basic procedure from the data generation to the final model.

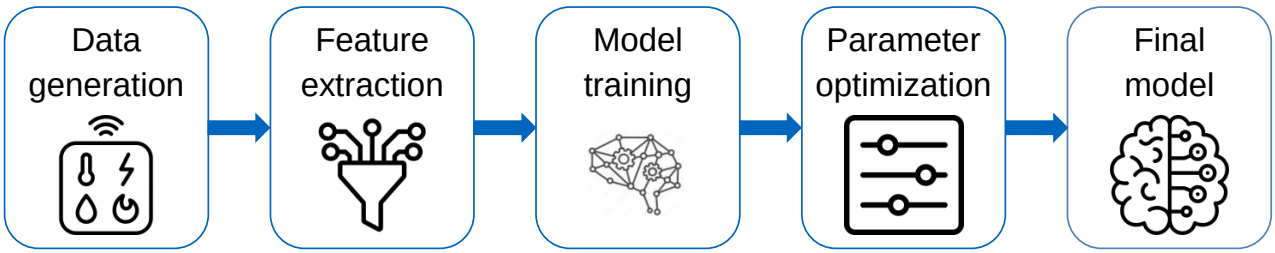

Figure 4.18: *Procedure of a machine learning task from data generation to the final model*

The process of data generation and analysis plays a pivotal role in extracting valuable insights from complex data sets. It is imperative to use a structured approach to ensure the integrity and reliability of findings. This process involves a series of important steps aimed at transforming raw data into actionable knowledge.

Data quality assurance stands as a foundational element in data analysis. It encompasses three key dimensions. Firstly, data accuracy is fundamental, demanding that all collected information must be free from errors or inaccuracies. Secondly, consistency is essential to maintain similarity across various data sources or time frames, thus eliminating contradictions or variations that may impede interpretation. Lastly, the relevance of data ensures that the information collected aligns directly with the research objectives, consequently excluding irrelevant or extraneous data that may introduce noise into the analysis. Prior to analysis, data generation (preprocessing) is higly important. This step is divided in several steps. Data cleaning addresses issues such as wrong or missing values, outliers, and anomalies within the data set, ensuring that data integrity and accuracy remain intact. At the same time, formatting and converting data are done to make sure data looks consistent and to change data types if needed, making analysis easier. Moreover, normalization or standardization is done to adjust data to a similar scale, making it easier to compare different features or variables. To ensure that datasets accurately represent the real-world scenarios being studied, specific factors need to be taken into account. Data diversity necessitates incorporating a wide range of data sources and types to accurately capture the complexity and variability inherent in the subject matter. Reducing bias in data is imperative, requiring active rectification of biases within data collection and sampling processes to restrain skewed or unfair representations that can lead to incorrect conclusions. Ultimately, data sets need to accurately reflect real-world situations or environments to maintain the relevance and applicability of subsequent analysis. For machine learning applications, dividing data into training, validation, and testing sets is done. The training data set forms the foundation for instructing machine learning models, enabling them to differentiate patterns and relationships within the data. The validation data set provides a distinct space for fine-tuning model parameters and avoiding overfitting, ensuring an unbiased evaluation of model performance. Finally, the test data set acts as the ultimate benchmark for unbiased model evaluation, testing its capacity to generalize to new, unseen data. In data analysis, feature engineering emerges as a crucial component. This process involves selecting key features or variables that have a substantial impact on the analysis while discarding those considered irrelevant to improve model efficiency. Feature transformation is another facet, which involves modifying features to meet the assumptions of chosen analysis techniques, such as ensuring normality or linearity. Moreover, the creation of new features from existing ones can capture additional information or relationships within the data, thus enhancing the modelling process. [26, 47–50]

4.5.1 Machine learning

Figure 4.19 illustrates the three main categories of machine learning. They are subdivided into supervised learning, unsupervised learning and reinforcement learning. In supervised learning, algorithms are trained on labelled data sets, where each input is paired with a corresponding target or output. The goal is to learn a mapping from inputs to outputs, making it suitable for tasks like classification (assigning categories) and regression (predicting continuous values). Unsupervised learning deals with unlabelled data, aiming to uncover hidden patterns or structures within the data. Clustering and dimensionality reduction are typical tasks. Reinforcement learning focuses on learning optimal sequences of actions to maximise cumulative rewards in an environment. Agents interact with their surroundings, receive feedback in the form of rewards or penalties, and adapt their strategies accordingly. [50] In the following, classification and regression methods are explained further.

Supervised learning – Classification

The primary objective of supervised learning is to predict the value of the label t for an input x, which is not present in the training data set. Therefore, the insights gained from the examined data set D are applied to new inputs to predict their associated responses. The process involves utilising a set of N data points, denoted as $D = \{(x_n, t_n)\}_{n=1}^{N}$, where x_n corresponds to a covariate, also referred to as an explanatory variable or feature, and t_n represents the corresponding response or label. [49] In simpler terms, classification algo-

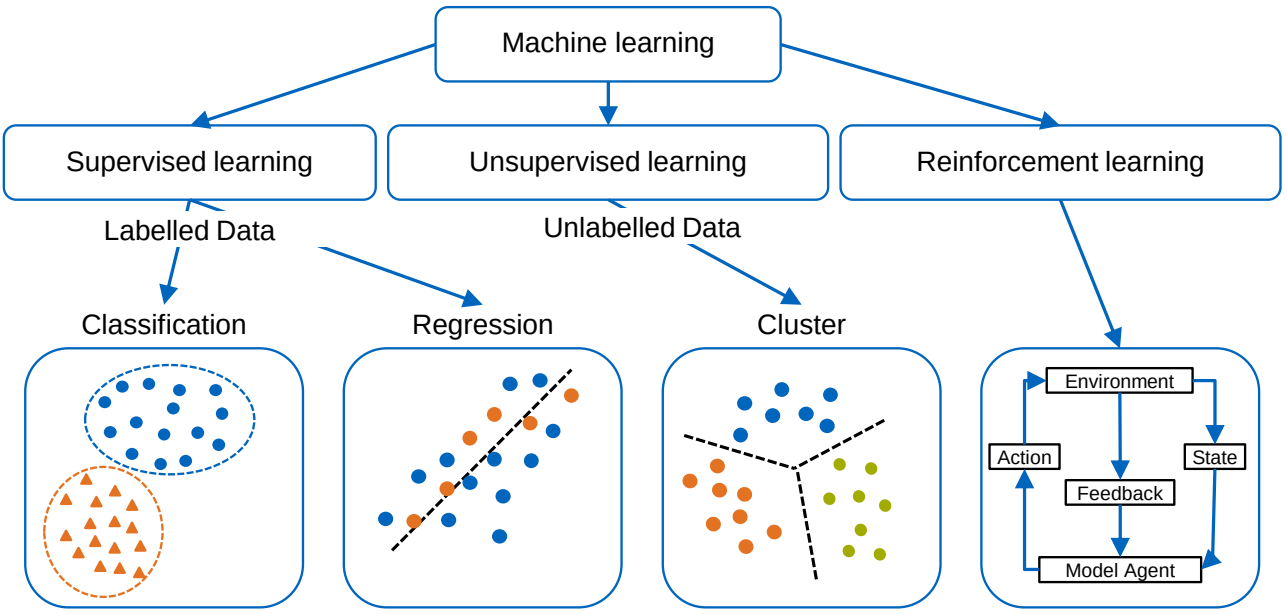

Figure 4.19: *Illustration depicting key facets of machine learning. The primary categories include supervised learning with classification and regression, unsupervised learning with clustering, and reinforcement learning for enhanced model performance. In the visual representation, training data is represented by coloured dots and triangles, while orange stars indicate new data that can be predicted using the trained model; adapted from [48]*

rithms are employed when we need to categorise data into distinct classes, such as identifying the presence of lack of fusion pores or gas pores. Initially, these algorithms are trained using labelled data. But once they are trained, they can autonomously classify new data into the predefined classes without requiring ongoing human intervention.

Supervised learning – Regression

In contrast to classification algorithms, the response variable t in regression problems is continuous. Regression is applied when fitting a function to measurement data or predicting temperature based on meteorological measurements. Learning a predictor is accomplished by identifying a predictive distribution $P(t|x)$ from a set of parameterised distributions given the training data $D = \{(x_n, t_n)\}_{n=1}^{N}$. [47, 49] As an illustration, regression algorithms can be applied to predict a specific outcome or value based on input data that influences the desired outcome. For example, when considering the stress amplitude applied to a material, it directly affects the number of cycles it can endure before failing. In such cases, regression analysis can be used to predict the exact number of cycles a material can withstand under different stress amplitudes.

4.5.2 Complexity and cross-validation

Finding the best model for the desired application requires exploring multiple types of models and optimising their complexity parameters. Depending on the specific model, there are various parameters that contribute to the complexity of the model. The relationship between the level of model complexity and its overall quality is best illustrated by the bias-variance tradeoff. When a model is overly simplistic, it fails to accurately approximate the underlying data, resulting in a high bias. Conversely, an excessively complex model can adapt to even the most intricate data patterns, including noise within the training data set, leading to increased variance. However, this adaptability comes at a cost. When such a complex model is applied to a different data set for testing, it can yield significantly different results, introducing a considerable variance. This phenomenon, known as overfitting, implies that the model has become overly tailored to the hypersensitivity of the training data, potentially sacrificing its ability to generalise to new, unseen data. In essence, it is important to recognise that a high level of complexity in a model does not necessarily translate to a superior model. Achieving

the right balance between bias and variance is essential for building a model that generalises effectively to real-world scenarios. [26, 50]

4.6 Powder-based fusion of metals using a laser (PBF-LB/M)

The PBF-LB/M process now looks back on a history of more than 20 years [51]. Since the first prototype development in 1999 by Meiners et al. [51], the technology has evolved greatly. The benefit of the PBF-LB/M process is the possibility to manufacture complex parts, independent of the number of parts. This chapter elucidates the steps from the CAD-file to the finished part.

4.6.1 Pre-processing

In the process of designing the geometries for additive manufacturing, traditional CAD programs (computer-aided design) are commonly employed, and the STL format stands out as a widely adopted choice. While the precise meaning of the acronym "STL" lacks universal standardisation, it is often interpreted as Surface Tesselation Language, StereoLithography, or Standard Triangulation Language. Originally developed for stereolithography, the STL format has evolved to become the cornerstone of additive manufacturing. It describes object surfaces by representing them as interconnected triangles defined by their nodes. This representation offers an approximation of curved surfaces rather than precise curves. The level of geometric accuracy during the manufacturing process can be enhanced by increasing the number of triangles used. However, this accuracy is consistently connected to the capabilities of the hardware employed. Moreover, deliberate refinements can be achieved through the application of the Finite Element Method (FEM). Moreover, shape- and topology-optimisation methods, e.g. vertex morphing [52]. FEM allows for the reduction of non-load-bearing sections within the geometry. This reduction not only conserves weight and material but also results in cost savings. Such tailored adjustments align the component with its intended application, enhancing its suitability and performance. [53]

Subsequently, the component is oriented within the build chamber. Optimal alignment with the recoater, aiming for a minimal initial surface area, prevents recoater skipping, which can lead to uneven powder bed distribution. Additionally, reducing the area melted by the laser per layer helps to reduce distortion caused by residual stresses. The angle with respect to the build platform depends on the machine type, powder, and laser parameter set. If the angle is too acute, the component may sink into the powder bed. Therefore, support structures are added. These structures bear the weight of the component but should be as minimal as possible. However, their attachment to the surface of the component requires manual removal during the post-processing stage, which affects surface quality. Moreover, the additional melting of powder due to support structures extends build time and increases costs. Support structures often require different laser parameters than the main component, with the goal of constructing them quickly and with reduced density for easier removal. For lightweight structures with hollow structures, internal lattice structures can be used for support. These structures replace solid material, improving the mechanical stability while reducing weight.

4.6.2 Principle of the PBF-LB/M process

This chapter explains the principle of the PBF-LB/M-process. Figure 4.20 describes the PBF-LB/M process schematically. At this point it should be mentioned that each manufacturer of the machines has a slightly different structure. However, the basic PBF-LB/M process remains the same and is explained below. A build chamber, filled with inert gas, consists of a build platform, a powder supply, an overflow and a recoater. The recoater applies a thin layer of metal powder to the build platform. The coating thickness varies between 20 and 100 μm [51]. A laser beam is deflected by a galvano-based scanner mirror and directed onto a metal powder bed. [54]

A F-θ lens is located closely behind the galvano-based scanner mirror and fulfils two tasks. Firstly, the laser beam is focused by the F-θ lens to the correct focal point. Secondly, the focal point is always kept in the working plane perpendicular to the optical axis of the lens. Once a powder layer is added to the build platform, the laser-beam melts the areas which need to be solidified. Areas which do not need to be solidified

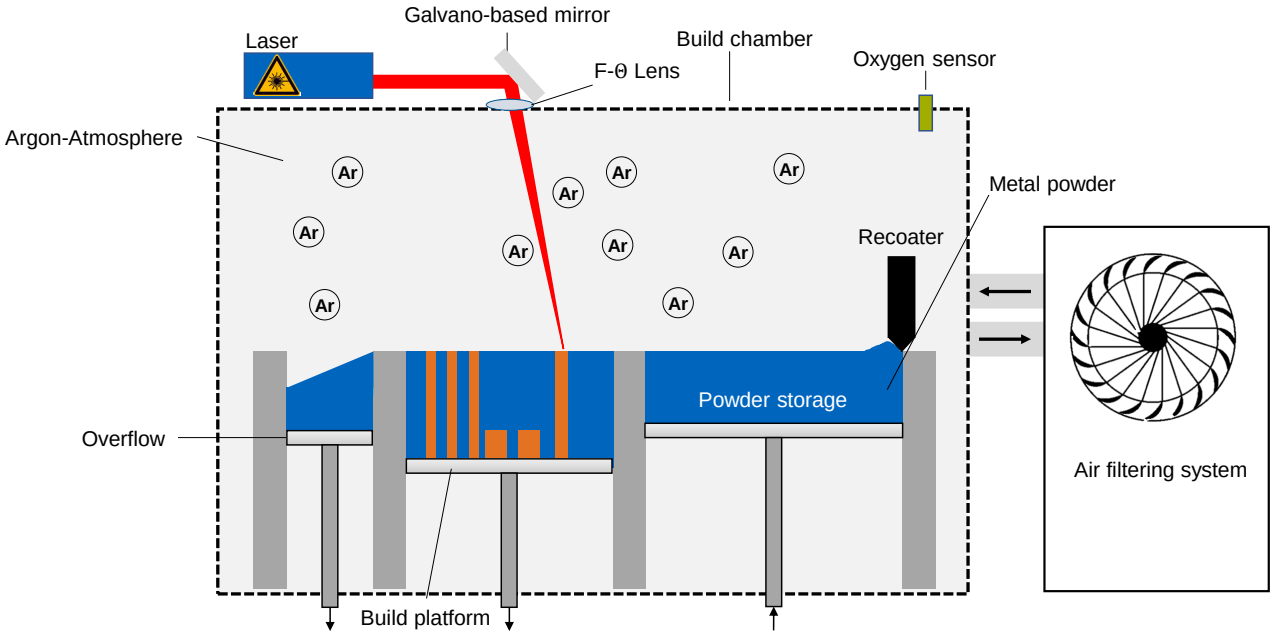

Figure 4.20: *Schematic illustration of the PBF-LB/M process, adapted from [55]*

at this height are not melted by the laser beam. After the melting process a new layer is added and the process is repeated until the part is finished. [54]

4.6.3 Process parameters

Each metallic alloy requires different laser parameters due to its different thermal properties. The relevant thermal properties include melting temperature, thermal conductivity, specific heat capacity, coefficient of expansion and crystal structure. The most important factors influencing the PBF-LB/M process are the laser power P in W, the scanning velocity v in mm/s, the track spacing h (hatch) in mm and the layer thickness t in μm. These parameters can be related by the energy density E in J/mm^3. The equation of the energy density E is as follows [54]:

$$E = \frac{P}{v \cdot h \cdot t} \tag{4.11}$$

The effect of the laser parameters on the mechanical properties is explained in Chapter 5.1.

4.6.4 Post-processing

Following the manufacturing process, several essential steps are required to prepare the part for use. Depending on the material and specific requirements, heat treatment may be employed, either to alleviate residual stresses or to achieve the desired mechanical properties. Subsequently, the parts are cut off from the build plate using a band saw or electric discharge machining. After that, the support structures are removed. In many instances, surface treatment becomes necessary, serving multiple purposes. It facilitates the joining of PBF-LB/M manufactured parts with other components, such as weld preparation and bolted connections. Additionally, it aids in reducing surface roughness, the significance of which is elucidated in Chapter 5.3. [54]

5 State of the Art

In this chapter, the state of the art is presented concerning the formation of the microstructure and the initiation of both internal and surface defects. Subsequently, an in-depth analysis of the fatigue behaviour of PBF-LB/M/316L is provided. Finally, a conclusion about the current state of the art is drawn, and a need for further investigation is identified to address the gaps in the understanding of the fatigue behaviour of PBF-LB/M/316L.

5.1 Formation of the microstructure and the resulting mechanical properties

The microstructure of PBF-LB/M manufactured 316L varies significantly from conventionally manufactured 316L (which involves processes like hot-rolling and forging). The distinctive microstructure resulting from the PBF-LB/M process is formed due to the establishment of very high thermal gradients, reaching up to 10^6 K/cm, and an exceptionally high solidification rate of the melt pools [56]. The material is composed of grains ranging in size from 20 – 30 μm. These grains, in turn, are composed of finer sub grains that are organised into colonies. Figure 5.1 displays micrographs of PBF-LB/M/316L and hot-rolled 316L.

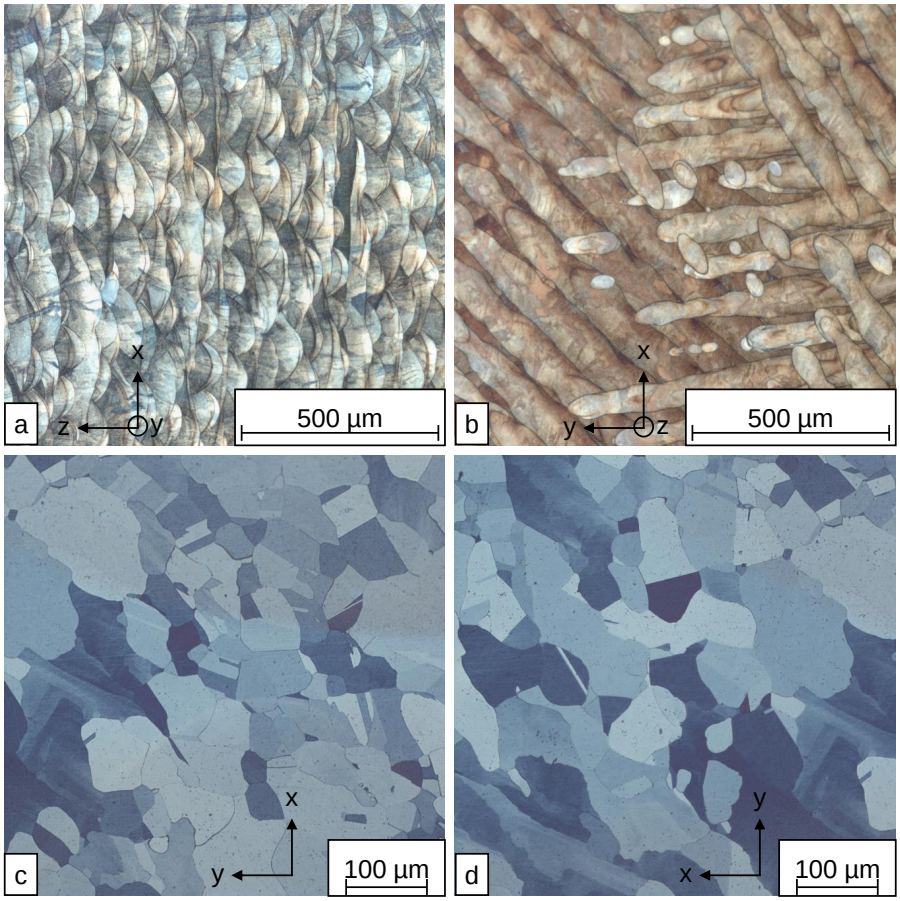

Figure 5.1: *Overview of microstructure of PBF-LB/M/316L in a and b. a represents a longitudinal view, whereas b represents a cross-sectional view. c and d show the microstructure of hot-rolled 316L from the longitudinal view c and the cross-sectional view d. The z-axis marks the building direction.*

Images a and b show the weld pools from different viewing directions, revealing distinct variations in the microstructure depending on the viewing direction. These disparities stem from the manufacturing process, as the metal powder essentially comprises numerous micro-welds. In contrast, the hot-rolled 316L exhibits a uniform microstructure across different viewing directions. In hot-rolled 316L, the grains are notably larger, with diameters extending up to 200 μm. The dimensions of both the grains and subgrains in PBF-LB/M/316L are illustrated in Figure 5.2. These subgrains can be characterised as columnar, needle-like structures, having a width ranging from 200 − 300 nm and a length of 2 − 3 μm.

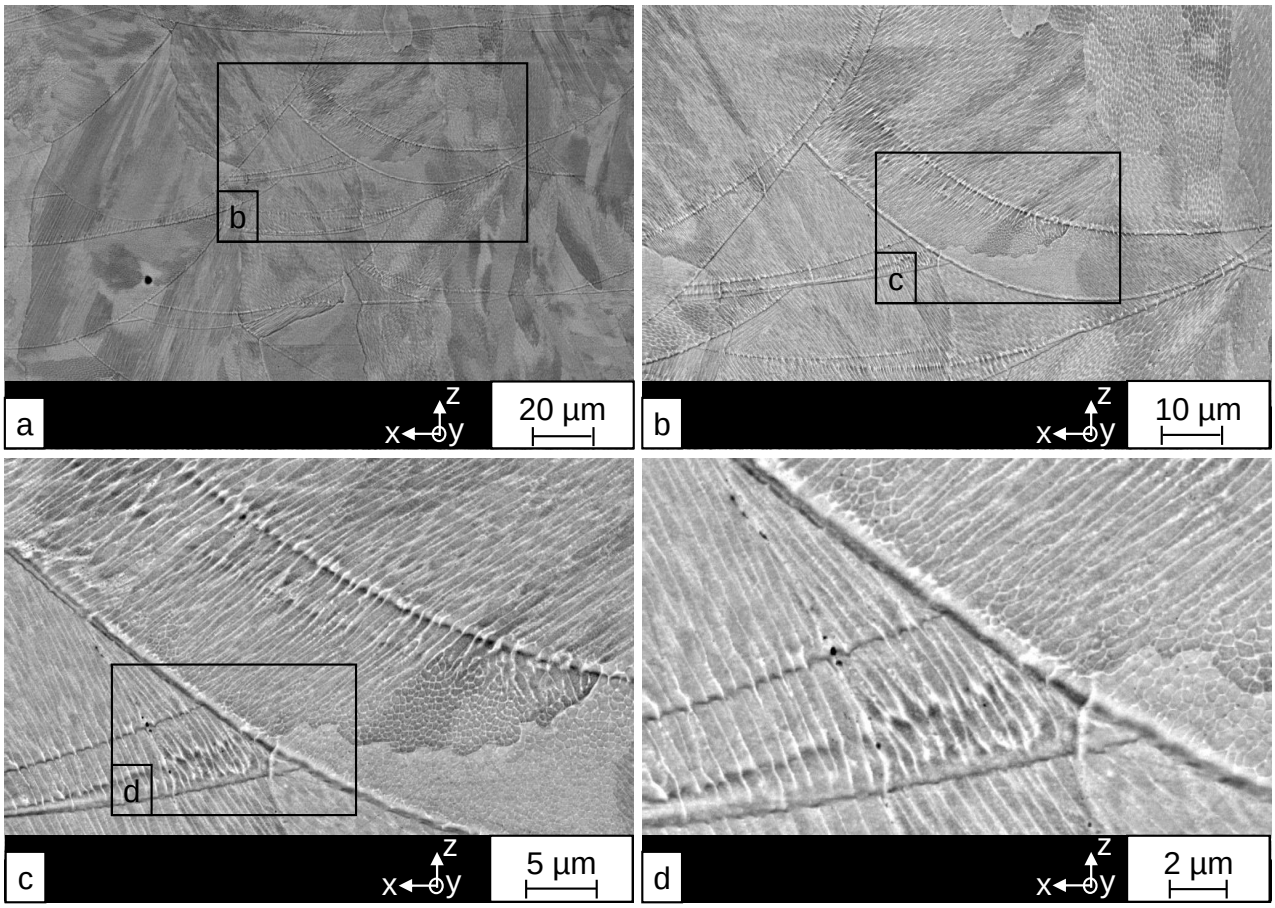

Figure 5.2: *SEM-images with high magnification of PBF-LB/M/316L. The magnification increases from a to d. a presents an overview, in b the boundaries of different overlapping weld pools are visible and in c and d the sub grains are visible. The black boxes indicate magnifications in the next images.*

As mentioned at the beginning of this chapter, the microstructure of PBF-LB/M/316L material after production consists of columnar grains, which can also be considered as colonies of cells, each with sometimes varying orientations. These colonies continue to grow across the layers and melt pool boundaries. [57] This raises the question of why these subgrains form during the manufacturing process. To understand this phenomenon, it is essential to investigate the boundary between the liquid and the emerging solid phase in the melt pool after the laser has moved on. In conventional manufacturing, a plane solidification process would typically occur. However, this process becomes unstable when the following equation is satisfied, leading to a cellular or dendritic solidification: [57]:

$$\frac{G}{R} < \frac{\Delta T}{D_l} \tag{5.1}$$

Where G is the thermal gradient in K/mm, R is the solidification rate in mm/s, ΔT is the temperature difference between the liquid phase and the solid phase in K and D_l is the diffusion coefficient in mm^2/s. When the solidification rate is very high, a transition occurs from a planar solidification to a cellular or dendritic solidification. This phenomenon is associated with the theory of undercooling, where the boundary layer

between the liquid and solid phase becomes unstable because the liquefied material is undercooled, meaning that the solidified front is warmer than the liquid phase due to the release of latent heat of solidification (thermal undercooling or supercooling). The resulting negative temperature gradient (heat flowing from the solid to the liquid phase) destabilises a flat interface, causing dendrites to randomly grow into the liquid phase, thereby accelerating crystallisation. [58] This phenomenon is shown in Figure 5.3. In the case of PBF-LB/M/316L, the presence of a high temperature gradient and a high cooling rate leads to the formation of a cellular structure, as depicted in Figure 5.2d. Hooper et al. [59] measured the cooling rate of the melt pools using a high-speed thermography setup. Cooling rates of up to 40 $K/\mu s$ were measured.

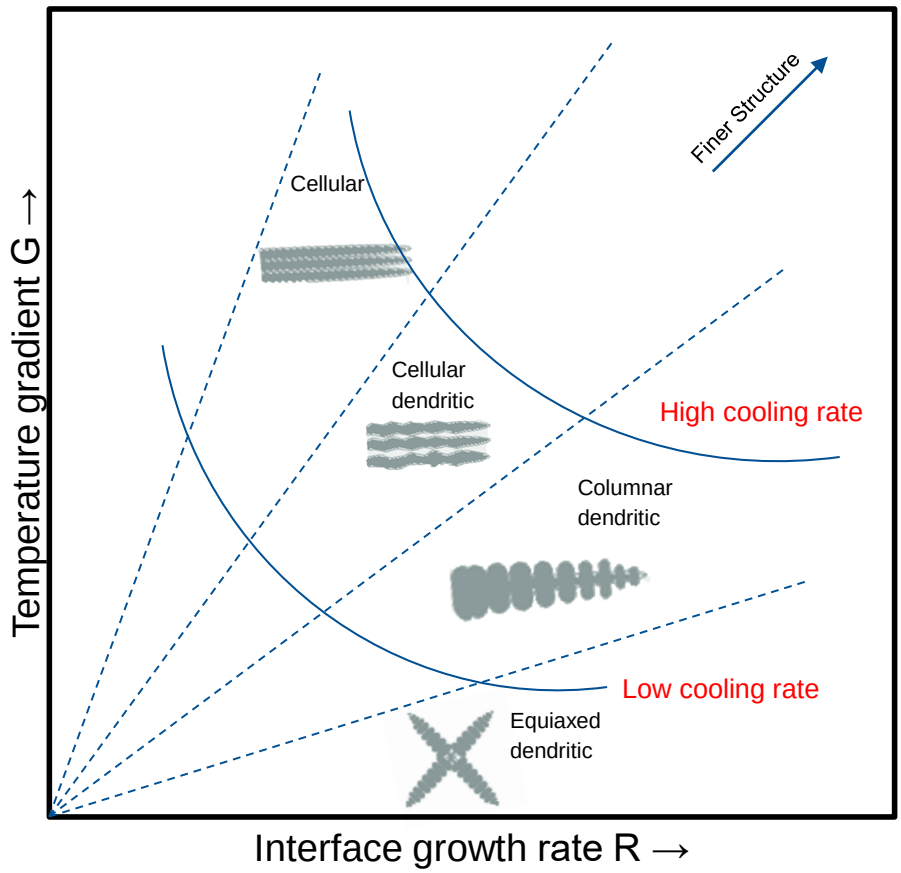

Figure 5.3: *Effect of temperature gradient and growth rate of various solidification types; adapted from [58]*

As discussed in Chapter 5.1, the microstructure is composed of exceptionally fine needle-like columnar subgrains. Furthermore, in Chapter 4.2.2 is was explained, that the presence of fine grains or grain refinement leads to an increase in yield strength while maintaining ductility. This phenomenon holds true for PBF-LB/M/316L. The static mechanical properties, as illustrated in Table 4.3, demonstrate a substantial difference in yield strength in comparison to hot-rolled 316L. Specifically, the yield strength of PBF-LB/M/316L surpasses hot-rolled 316L by more than double. Nonetheless, it is worth noting that Yakout et al. [60] demonstrated that the mechanical properties are significantly influenced by the energy density and laser parameters in general. They categorised laser parameters into five zones, each with distinct characteristics: Unstable melting, vaporisation, stable melting, balling, lack of fusion, and finally insufficient melting, as detailed in their study [60].

Interim conclusion

Numerous studies have been carried out to explore the mechanical characteristics of PBF-LB/M/316L (Charmi et al. [61], DebRoy et al. [62]). The formation of fine grains has also been elucidated in various research endeavours (Hooper et al. [59], Godec et al. [63]). Extensive investigations have been conducted regarding

how mechanical properties vary with the building direction (Van Nuland et al. [64]). Nevertheless, there remains an unexplored aspect: the impact of cooling rate on macroscopic-scale mechanical properties. The question persists regarding how mechanical properties are influenced by different cooling rates, such as those associated with varying areas connected to the build platform.

5.2 Formation of pores

The formation of pores can be attributed to various phenomena. Initially, it is necessary to classify pores into different categories. Pores can be divided into three primary classes: gas pores, lack of fusion pores, and keyhole pores. Indeed, there are other potential types of pores; however, they are not relevant to this particular study.

Gas pores

Gas pores are one of the common types of defects of the PBF-LB/M process. They result from the entrapment of gas, often from the atmosphere or residual gases within the metal powder. When the intense laser energy interacts with the powder, it can rapidly vaporise any trapped gas, creating cavities or pores within the solidifying material. These pores can be detrimental to the mechanical properties of the final part, as they weaken its structure and reduce density. [65, 66] Gas pores are easily recognisable by their high sphericity.

Lack of fusion pores

Lack-of-fusion pores occur when adjacent powder particles do not fully fuse together during the PBF-LB/M process. This can happen due to inadequate energy input from the laser or improper scanning speed. As a result, there are unbound regions or "incomplete welds" within the part, leading to the formation of pores. These pores can significantly reduce the integrity of the part, as they represent areas of reduced material continuity and strength. [66, 67]

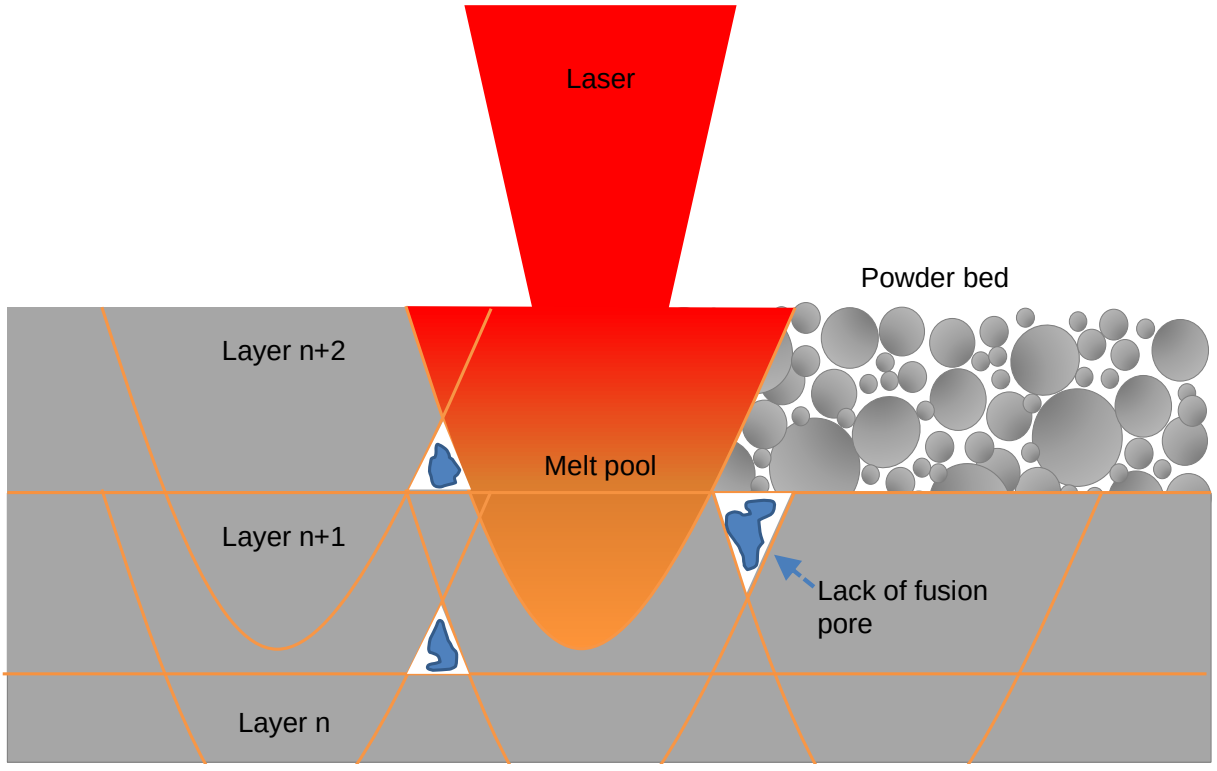

Figure 5.4: *Schematic illustration of the lack of fusion pore formation during the PBF-LB/M-process; adapted from [67]*

Keyhole pores

Keyhole pores are irregularly shaped voids that form when the laser partially penetrates the powder bed but does not completely melt the material beneath it. This can occur when the laser power is too high or the scanning speed is too fast, preventing proper material fusion. Keyhole pores can be particularly problematic, as they create regions of reduced material density and integrity within the part. [65] Figure 5.5 explains, how the formation of lack of fusion pores develops during the manufacturing process. A very deep cavity (dark red colouring in Figure 5.5) may trap gas in a pore below the surface of the component.

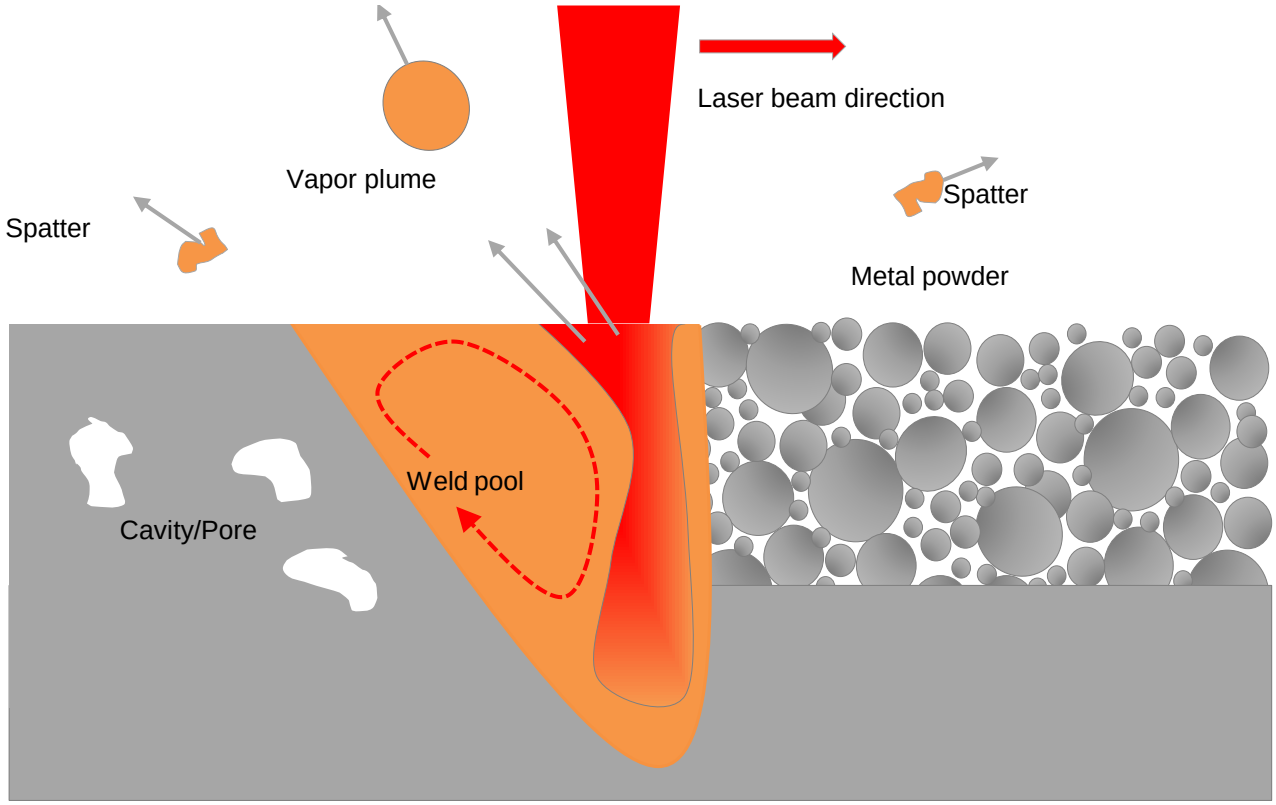

Figure 5.5: *Schematic illustration of the keyhole pore formation during the PBF-LB/M process; adapted from [65]*

Interim conclusion

Pore formation can be attributed to various underlying phenomena, as previously discussed. The geometric characteristics of these pores exert a significant influence on the mechanical properties of PBF-LB/M/316L. Several studies have investigated the impact of porosity [68–70]. Moreover, these studies have also explored the impact of pore type on the fatigue behaviour. However, several questions remain regarding additional geometric properties of pores. These include, but are not limited to, orientation, distance from the surface, Feret diameter, volume, and surface area.

5.3 Formation of surface topology

The parts are manufactured in a powder bed. A laser melts specific areas that need to be joined together. At the same time, nearby metal powder particles start to turn into liquid and stick to the melted surfaces partially. This process creates small valleys and peaks in the final structure. According to a study by Kleszczynski et al. [71], this problem becomes worse when the parts have overhanging surfaces. This is shown in Figure 5.6. It was hypothesised that the variations could be attributed to the interplay between the geometric configuration of the angle of incidence and various surface orientations.

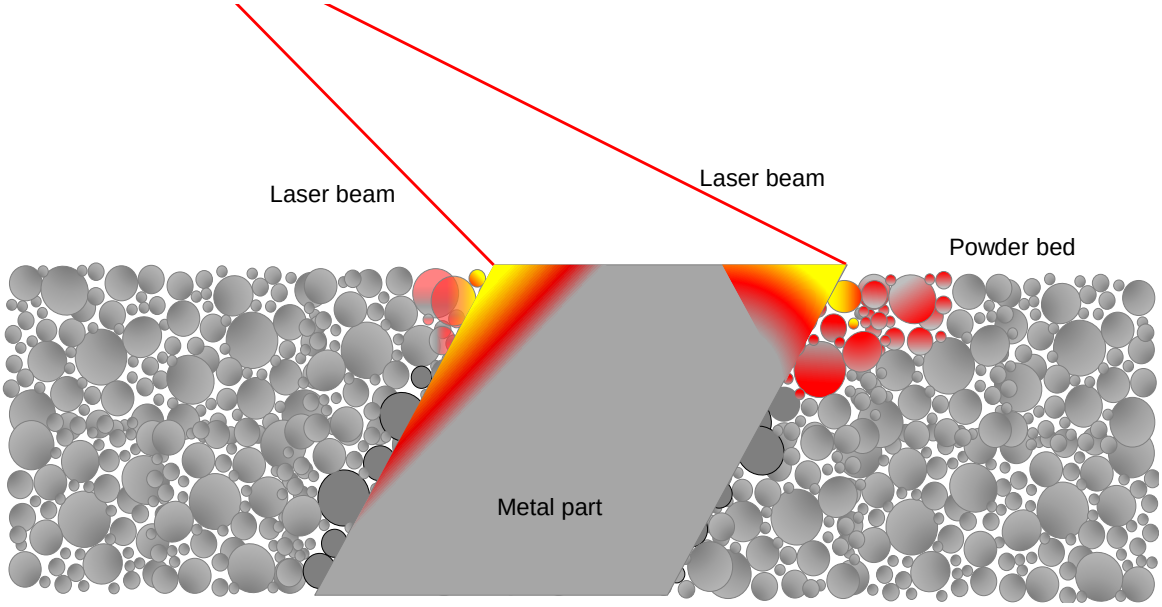

Figure 5.6: *Schematic illustration of the formation of surface roughness consisting of partially melted metal particles; adapted from [71]*

Figure 5.7 shows partially melted particles which adhere to the surface of a PBF-LB/M/316L manufactured part.

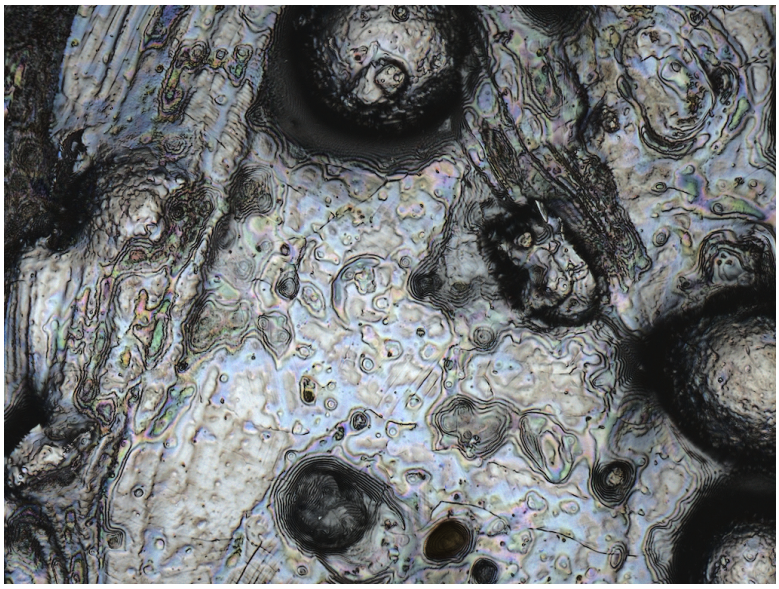

Figure 5.7: *Partially melted metal particles adhering to the solidified part. The image was taken using a Keyence VKX-1000 laser confocal mircoscope.*

Interim conclusion

The PBF-LB/M process creates a unique surface topology with a very high surface roughness. A high surface roughness may reduce the fatigue resistance of metal parts. There are however several questions which need to be addressed. The main influencing surface parameter concerning fatigue resistance has not been found yet. Additionally, the scattering of the fatigue life of PBF-LB/M/316L components increases with a high surface roughness. It has not been investigated, if the surface roughness parameters of PBF-LB/M/316L can be used to predict the fatigue life more accurately.

5.4 Fatigue behaviour

In Chapter 4.1.3, the fatigue properties of conventionally manufactured 316L are discussed. This chapter provides an overview of the current state of the art regarding the fatigue behaviour of PBF-LB/M/316L. It is divided into two sections: low-cycle fatigue and high-cycle fatigue. Initially, the existing research findings are presented, followed by an outline of the areas that remain unexplored in this field in form of an interim conclusion. In chapter 5.5 the final conclusion and need for action is presented.

5.4.1 Low-cycle fatigue behaviour

The low-cycle fatigue behaviour of PBF-LB/M/316L with a strain-based approach has been a relatively under-explored area, with only a limited number of studies available in the literature [69, 72–77]. Table 5.1 provides a compilation of publications that focus on low-cycle fatigue (LCF) testing utilising a strain-based approach. This table has been derived from the work of Avanzini in [78], supplemented with additional studies as appropriate.

Table 5.1: *List of publications concerning low-cycle fatigue using a strain-based approach, extracted from [78]; AB: as built , AX: axial, C: cylindrical specimen, DB: dogbone specimen, HG: hourglass specimen, HIP: hot isostatic pressing, M: machined, N: no heat treatment, TU: tubular, P: polished, XY: horizontal build direction, Z: vertical build orientation*

Ref.	Build orientation	Surface finish	Heat treatment	Specimen	Test type	R
[72]	Z	AB/M	N	C TU	AX	-1
[73]	-	M/P	N	C HG	AX	-1
[74]	-	-	N	C DB	AX	-1
[75]	Z	AB	P/HIP	C DB	AX	0.1
[76]	-	AB	SR	C DB	AX	-1
[69]	XY/Z/45	M	N	C DB	AX	-1
[77]	XY/Z/45	AB/M	N	C DB	AX	-1

Yu et al. [72] conducted a study on the buckling behaviour and the low-cycle fatigue behaviour of thin-walled tubular specimens. They examined specimens with various wall thicknesses in different states, including the as-built state, polished state, and machined state. Strain amplitudes of up to 2 % were applied. In their analysis of strain-life fatigue results, it was observed that the difference in lifetime between the as-built and machined surfaces became more pronounced at lower applied strain ranges. This difference can be attributed to the increasing sensitivity to stress concentrations as the strain level decreases. The results of the PBF-LB/M/316L were compared to wrought 316L. The hierarchy with regard to the fatigue life can be established as follows: Wrought cold worked > PBF-LB/M > Wrought solution annealed.

Beard et al. [73] investigated the low-cycle fatigue performance of PBF-LB/M/316L and compared it to wrought 316L. The low-cycle fatigue behaviour of both wrought and vertically PBF-LB/M/316L materials was evaluated, and the findings indicated that the vertically manufactured material exhibited fatigue performance comparable to its wrought counterpart.

Pelegatti et al. [74] conducted low-cycle fatigue testing, investigating strain amplitudes of up to 1.2%. However, their study did not primarily emphasise the examination of microstructural changes resulting from plastic deformation. Instead, their primary focus was on the development of a plasticity model. The results underscore that the combination of the Owen approach [79], along with the one-side tolerance interval method, yields the most conservative strain-life curves.

Kluczyński et al. [75] investigated the impact of heat treatment on the low-cycle fatigue characteristics of PBF-LB/M/316L. Strain amplitudes of up to 0.5% with a strain ratio of 0.1 were applied. Three distinct laser parameters were investigated. According to the research conducted by Yakout et al. [60], two of these laser parameter sets were located within the balling and lack of fusion region, whereas the remaining set was

positioned at the threshold between stable melting and vaporization. The results indicate that PBF-LB/M/316L, without undergoing any heat treatment, experienced a reduction in strength across the entire load cycle range. In contrast, conventionally manufactured material (as well as additively manufactured material following heat treatment) exhibited a noticeable stabilisation in strength within a certain range of cycles.

Liang et al. [76] performed low-cycle fatigue testing on PBF-LB/M/316L with strain rates of up to 0.75 % with a strain ratio of -1. The chosen laser parameters were set at the boundary to stable melting and vaporisation according to [60]. However, a random island scanning strategy was chosen, which significantly changes the orientation and , therefore, also the mechanical properties [80]. The main focus of this paper is the microstructural investigation of the material after low-cycle fatigue loading and high-cycle fatigue loading. The study yielded two significant findings. Firstly, under low-cycle fatigue loading conditions, the samples exhibited noticeable plastic deformation, primarily in the form of slip. Conversely, high-cycle fatigue loading did not result in visible plastic deformation, suggesting different sources of fatigue crack initiation between the two loading regimes. Secondly, process-driven defects, particularly lack of fusion defects in the material under investigation, played a substantial role in the high-cycle fatigue regime while having a negligible impact in the low-cycle fatigue regime. Additionally, the removal of surface roughness had a remarkable positive effect on the fatigue limit of this material. Interestingly, preserving the original as-built surface roughness had a detrimental effect on high-cycle fatigue performance while having no adverse impact on low-cycle fatigue performance in the case of PBF-LB/M/316L.

Interim conclusion

Only a few studies have been conducted to explore the low-cycle fatigue behaviour of PBF-LB/M/316L. Several questions in this domain remain unanswered. For instance, in the study by Liang et al. [76], the microstructure, including the application of EBSD, was examined. However, the investigation did not investigate the microstructural factors contributing to the softening or hardening behaviour of the material. Furthermore, the formation of twinning near the fracture surface was not explored, and there was no direct microstructural examination of how the cyclic plastic material behaviour varies at different strain levels. Furthermore, in the study conducted by Kluczyński [75], the impact of different laser parameters was investigated, but it was not explored in relation to the influence of porosity on the low-cycle fatigue life. Additionally, the study did not compare higher strain amplitudes with lower strain amplitudes. The investigation of higher strain rates holds particular significance, especially concerning the application of the PBF-LB/M process for steel hysteretic dampers, where high strain amplitudes are applied due to earthquakes. Many of the previously mentioned studies have compared PBF-LB/M/316L material to wrought or cold-worked 316L. From a practical point of view, the PBF-LB/M process is economically viable, primarily when manufacturing highly complex geometries. In such cases, CNC machining may be its main competitor. However, it is essential to note that CNC machining is a subtractive process that requires large steel blocks. 316L in the form of large blocks is typically available in the hot-rolled state, which possesses distinct mechanical properties compared to wrought 316L. As a result, comparing the cyclic plastic material behaviour between PBF-LB/M/316L and hot-rolled 316L remains an unexplored area of study.

5.4.2 High-cycle fatigue behaviour

The high-cycle fatigue behaviour of PBF-LB/M/316L with a stress-based approach has been the subject of extensive research in the scientific community since 2013. Avanzini provided a comprehensive summary of all relevant publications spanning from 2013 to 2023 [78]. Table 1 from this publication is presented in Table 5.2.

Table 5.2: *List of publications on high-cycle fatigue using a stress-based approach, extracted from [78]; AB: as built , ANN: annealing, AD: artificial defects, AX: axial, C: cylindrical specimen, CT: compact tension specimen, DB: dogbone specimen, F: flat, FCP: fat. crack propagation, HG: hourglass specimen, M: machined, M-AX: multi-axial load N: no heat treatment, ST: surface treatment, XY: horizontal build direction, Z: vert. build orientation*

Ref.	Build orientation	Surface finish	Heat treatment	Specimen	Test type	R
[81]	Z	AB/M	N	C HG	AX	0.1
[82]	Z	AB/M	N/SR/HIP	C HG	AX	-1
[83]	XY/Z	AB	SR/HIP	C HG	AX	-1
[84]	Z	AB/M/ST	N	C DB	AX	-1
[85]	XY	M	N	F DB	AX	0.1
[86]	XY	M	N/ANN	F DB	AX	0.1
[87]	XY	M	N/ANN	F DB	AX	0.1
[88]	XY/Z	M	N	C DB	AX	-1
[89]	XY/Z/45	M	N	C DB	AX	-1
[90]	Z	AB/M	N/SR	C HG	AX	-1
[91]	Z	AB	ANN	C HG/DB	AX/RB	-1
[68]	Z	AB	N	C DB	AX	0.1
[92]	XY/Z	AB/M/ST	N/SR	C HG	AX	0.1
[93]	XY/Z	M	N/ANN/HIP	F DB	AX	0.1/0.7/-1
[94]	XY/Z	M	SR	C DB	AX	-1
[95]	Z	M	ANN, HIP	C HG	AX	-1
[96]	Z	AB/M	N	C DB	AX	0.1
[97]	Z	M	SR	C HG	RB	-1
[98]	XY/Z	AB/M/ST	N	C DB	AX	0.1
[15]	Z	AB/M	SR	C HG	AX	0/-1
[99]	XY	N/D	N	F DB	AX	0.1
[100]	XY	M	N	C HG	AX	-1
[101]	Z	M	ANN	C HG	AX	-1
[102]	XY	M	SR	C DB	M-AX	N/A
[103]	XY	M	N/D	C DB	M-AX	N/A
[18]	Z	M	ANN	C DB	AX	-1
[104]	Z	M	ANN	C DB	AX	-1
[105]	Z	AB	SR	F DB	AX	0.1
[106]	Z	M/ST	SR	C HG	RevB	-1
[107]	XY	AB/ST	SR	F -	RevB	-1
[108]	XY/Z	-	SR	F CT	FCP	0.1
[109]	Z	M	N	C DB	AX/STP	0.1
[110]	-	M	N	C HG	AX/STP	0.1
[111]	Z	M	SR	C DB	AX/STP/AD	0.1
[70]	Z/45	-	SR/ANN	F CT	FCP	0.1
[112]	Z	M	N/HIP	F DB	AX	0
[113]	Z	M	N	C DB/HG	AX	0.1
[114]	Z	M	N	C HG	AX/AD	0.1

A total of 38 publications are included in this review. Based on the literature research of Avanzini [78], the following conclusions can be drawn: The fatigue resistance of PBF-LB/M/316L material demonstrates an enhancement with reduced grain size when compared to conventionally manufactured 316L. Notably, the build orientation plays a significant role, with horizontally produced specimens exhibiting superior fatigue resistance compared to vertically fabricated counterparts. Additionally, the application of stress-relieving heat treatment proves to be effective in increasing fatigue resistance, particularly when the specimens are left unmachined prior to undergoing such treatment. Moreover, there is potential for further improving fatigue response through surface treatments; however, it is essential to acknowledge the limited availability of relevant data, indicating the necessity for more comprehensive investigations. In contrast, the influence of annealing heat treatment and subsequent machining or polishing of the surface on fatigue resistance remains inconclusive due to substantial data scattering, necessitating additional research efforts for clarity. Furthermore, it is worth noting that the impact of porosity on the fatigue behaviour of PBF-LB/M/316L is relatively less severe when compared to the influence of surface roughness. Lastly, it is essential to mention that the number of studies that have measured residual stresses in this context is limited, underscoring the potential benefit of further investigations in this area.

Interim conclusion

Numerous studies have been conducted to explore the high-cycle fatigue behaviour of PBF-LB/M/316L, and the diversity showcased in these studies highlight the significance of the subject matter. Avanzini conducted a comprehensive literature review in 2022, as documented in [78], which provides a succinct synthesis of the principal discoveries stemming from these studies. Nevertheless, it is pertinent to acknowledge that several critical inquiries remain unanswered.

First and foremost, within the context of the 38 studies outlined in Table 5.2, it is noteworthy that 26 of these studies involved machining the material to its final dimensions. In contrast, only 13 out of the 38 studies examined the as-built state of the material without any post-processing treatments. Additionally, a mere four studies investigated surface treatment techniques. The necessity of machining specimens is twofold: it facilitates the comparison of mechanical properties, particularly fatigue-related aspects, with those of alternative manufacturing processes, and it establishes a benchmark due to the ease of reproducibility for machined surfaces. However, it is worth mentioning that achieving a machined surface is unfeasible using the PBF-LB/M process, as elucidated in Chapter 5.3. If the final geometry can be attained through machining, the utilisation of the PBF-LB/M process becomes redundant, and CNC machining is a more economical alternative. Consequently, there is a need to investigate different surface treatment processes, such as vibratory grinding, which has been sparingly explored and primarily addressed by Uhlmann et al. [84] in 2017. However, employing vibratory grinding to improve surface quality, and thus, fatigue resistance, raises a crucial question regarding the effect of resulting residual stresses on fatigue resistance. The combination of hot isostatic pressing with surface treatment methods is still a relatively unexplored area that warrants comprehensive investigation.

Lastly, it is pertinent to mention that internal defects have been found to be less detrimental in terms of fatigue resistance than surface topology. Nevertheless, the current state of research has yet to address a quantitative assessment of the severity of surface and internal defects as a basis for comparison.

5.5 Conclusion and need for action

Based on the fundamentals provided in Chapter 2, Chapter 3 describes the state of the art in the field of the PBF-LB/M process and the fatigue behaviour. Chapter 5.4 provides a comprehensive overview of the fatigue behaviour in the low-cycle fatigue range and the high-cycle fatigue range. A large part of these works deals with the high-cycle fatigue behaviour, while the low-cycle fatigue behaviour is less researched. Nonetheless, there remain certain aspects that require further elucidation:

- The influence of the cooling rate on the macroscopic scale on the static mechanical properties needs to be clarified.
- Investigation of the microstructural changes occurring during cyclic plastic deformation, particularly in terms of softening or hardening, has not yet been conducted.
- It is imperative to conduct a comparative study between PBF-LB/M/316L and hot-rolled 316L, focusing on microstructural alterations during cyclic plastic deformation.
- The investigation of the cyclic plastic material behaviour at higher strain amplitudes needs to be investigated.
- An inquiry into the criticality of defects, whether they are internal or surface-related, in relation to their effect on fatigue resistance is essential.
- The impact of vibratory grinding on the fatigue resistance of PBF-LB/M/316L requires further investigation.
- An assessment of how the combination of post-treatment methods, such as HIP and vibratory grinding, influences fatigue resistance is required. Especially, the influence of the resulting residual stresses needs to be considered in this study.
- The fatigue life prediction of PBF-LB/M/316L parts with internal and surface defects stemming from the manufacturing process should be investigated.
- To apply PBF-LB/M/316L safely in the future, the high-cycle fatigue behaviour should be compared to conventionally manufactured 316L.

Finally, when considering the adoption of the PBF-LB/M approach within the construction sector, it raises the question of which essential steps are required to integrate this method into the construction design workflow. In the following chapter, the open issues in the state of research and technology will be addressed, and the need for action will be derived within the context of the primary objectives of this work.

6 Research Approach

As mentioned before, this thesis is a publication-based dissertation. Therefore, in this chapter, the scientific objectives of this thesis are presented, along with the research approach that led to the publications discussed in Chapter 7. The state of the art supplies the fundamental information for formulating the scientific objectives, which are outlined in Chapter 6.1. From these overarching objectives, sub-objectives are derived. These sub-objectives form the basis for the methodical approach presented in Chapter 6.2. Lastly, the integration of the six publications, which compose the research foundation of this work, is presented.

6.1 Scientific objectives

The objective of this thesis is to expand the understanding of the overall fatigue characteristics of PBF-LB/M/316L. This encompasses not only the fatigue performance of PBF-LB/M/316L itself but also its comparison with conventional manufacturing processes such as hot-rolling. This comparison is essential due to the distinct microstructural scale and the presence of unique geometric defects, which may result in varying fatigue behaviour. Consequently, the feasibility and integration of the PBF-LB/M process into the construction design process must be examined. The main requirements of the construction industry are as follows:

- In the construction industry, prototyping is rarely conducted as each component is unique. Therefore, it is crucial to ensure the reproducibility of mechanical properties. Especially different scales should be investigated.
- A high fatigue resistance is essential, as most of the components are subjected to random dynamic loading over many decades with low maintenance.
- Usually, relatively small quantities of a component are manufactured, necessitating flexible production systems.

Six sub-objectives (SO) that characterise the prerequisites for this thesis can be derived and are listed below.

SO1: Influence of grain size on the mechanical properties of PBF-LB/M/316L

The origin of the unique, fine microstructure of PBF-LB/M/316L needs to be examined, and the resulting static mechanical properties should be characterised. The scattering of the mechanical properties needs to be evaluated.

SO2: Low-cycle fatigue behaviour and comparison to hot-rolled 316L

The low-cycle fatigue behaviour of PBF-LB/M/316L must be characterised concerning microstructural changes. High strain amplitudes should be employed, as they are required for applications in the construction industry, such as steel hysteretic dampers. Furthermore, the impact of various laser parameters needs to be explored. Finally a comparison of the hardening or softening behaviour between PBF-LB/M/316L and hot-rolled 316L should be investigated. The difference in cyclic plastic behaviour between these manufacturing processes should encompass scientific and engineering factors that influence the microstructure-strength relationships of materials and document the resulting alterations in mechanical behaviour.

SO3: High-cycle fatigue behaviour and comparison with hot-rolled 316L

The high-cycle fatigue performance of PBF-LB/M/316L with high density should be studied as a benchmark. The connection between microstructural and geometrical defects and fatigue resistance must be investigated. The overall high-cycle fatigue performance should be compared to conventional manufacturing methods like hot-rolling, cold-forming, and forging. A hierarchy of the factors influencing fatigue resistance should be established.

SO4: Influence of surface treatment and hot isostatic pressing on the fatigue properties

To enhance the fatigue performance of PBF-LB/M/316L, practical post-treatment methods like vibratory grinding and hot isostatic pressing should be applied. The fatigue performance should be compared to other surface treatment techniques and the as-built state. The consequences of these post-treatment methods, including surface residual stresses and changes in surface topology, must be investigated and linked to the fatigue performance.

SO5: Prediction of fatigue life with surface defects and internal defects

The existing geometrical defects in the material reduce fatigue resistance and increase variability. Due to this high variability, using S-N curves may not be safely applicable. Therefore, a foundation must be established to predict the number of cycles until failure. Various measurement techniques for geometric defects (both internal and surface defects) should be examined and assessed. Consequently, a prediction method must be developed to enhance the accuracy of fatigue performance predictions for PBF-LB/M/316L.

SO6: Implementation of the PBF-LB/M process into the construction design and manufacturing route

Lastly, a practical approach is imperative for integrating the PBF-LB/M process into the construction design and manufacturing workflow. Since the PBF-LB/M process is most relevant when highly complex geometries are required, shape optimisation procedures must be employed. Consequently, initial designs of the geometry, followed by optimisation iterations, should be incorporated into the daily routine of a structural engineer. Additionally, the manufacturing process must be integrated into the construction process. Finally, a qualification method for incorporating new materials into the entire process needs to be developed.

6.2 Methodology and integration of the publications

This section provides the classification of publications stemming from the research activities, with a focus on their thematic alignment relative to the research objectives delineated in Chapter 6.1. The categorization and incorporation of these publications within the methodology are summarised in Figure 6.1, while a more detailed exposition of the primary research findings is explained upon in Chapter 7.

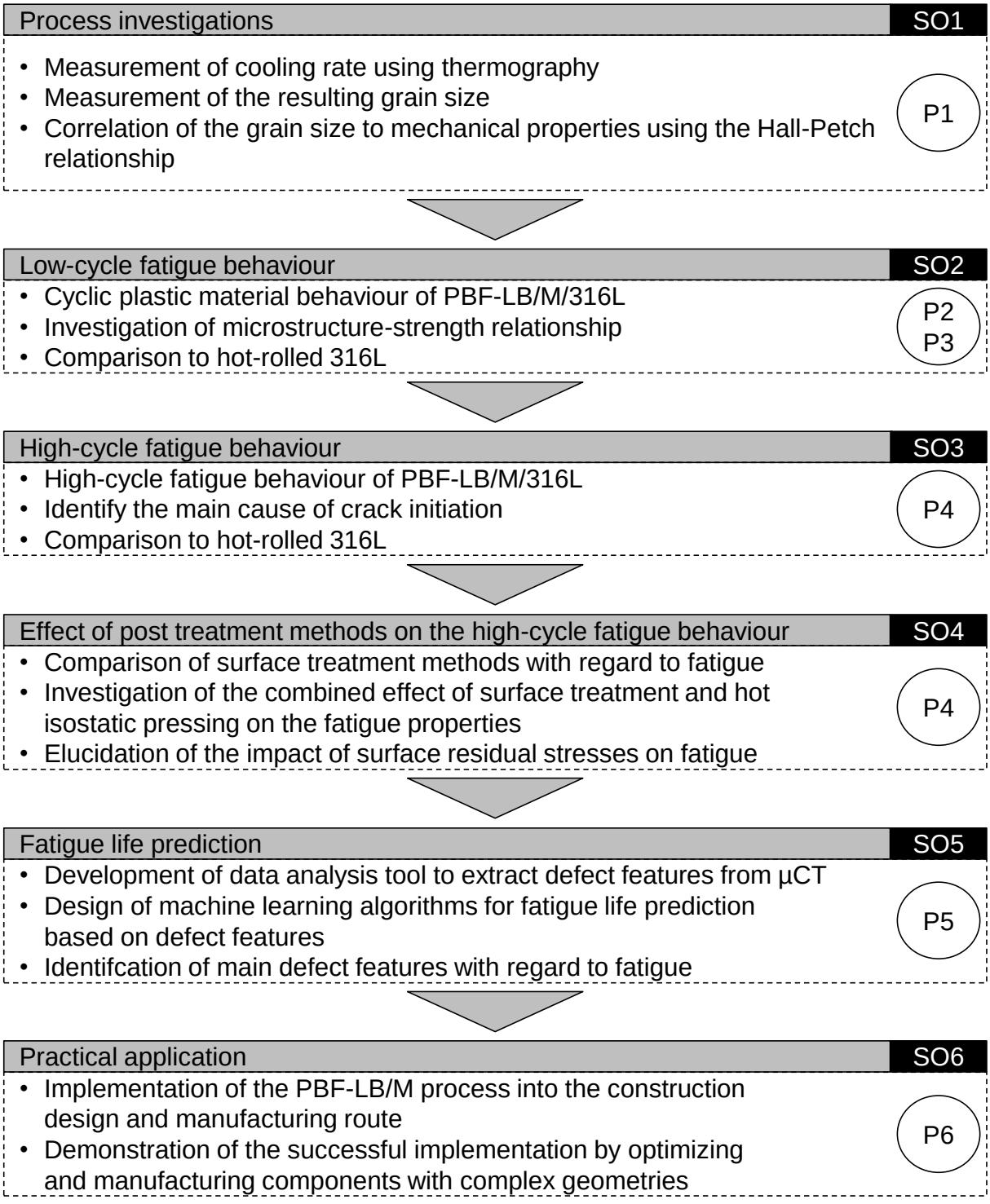

Figure 6.1: *Flow diagram of the methodical approach of the sub-objectives (SO), defined in Chapter 6.1 and the thematic placement of the publications (P) P1 to P6.*

Measurement of the cooling rate and correlation to mechanical properties

Initial process investigations are imperative for the PBF-LB/M process. These investigations aim to elucidate the origins of the formation of the distinct, fine-grained microstructure and ascertain the sensitivity of the process to variations in mechanical properties. To achieve these objectives, a thermographic setup is employed to quantify the cooling rate on a macroscopic scale. To explore the effect of cooling rate variations, it is necessary to produce tensile specimens of varying sizes. Subsequently, the resulting microstructure must be assessed by conducting local grain size measurements and employing the Hall-Petch relationship to establish correlations between grain size and mechanical properties. Finally, tensile tests should be conducted to validate the Hall-Petch relationship. This study is represented by publication P1.

Low-cycle fatigue behaviour of PBF-LB/M/316L and comparison to hot-rolled 316L

Following an investigation of the correlation between the manufacturing process and the resulting static mechanical properties attributed to the microstructure, an examination of fatigue behaviour becomes imperative. This fatigue behaviour analysis necessitates a subdivision into low-cycle fatigue and high-cycle fatigue regimes. To gain insights into the cyclic plastic material behaviour of PBF-LB/M/316L, it is imperative to conduct strain-controlled fatigue tests employing varying strain amplitudes. Furthermore, for practical applications such as earthquake steel hysteretic dampers, it is essential to subject the material to high strain amplitudes with a notably low number of cycles (ranging from 30 to 40 cycles) until failure occurs. Understanding the relationship between microstructure and strength is paramount in this context. Consequently, it is necessary to identify and classify the principal factors contributing to the cyclic plastic material behaviour. The phenomena of hardening or softening must be recognised and correlated with the underlying microstructure, a task that involves the utilisation of micrographs and Electron Backscatter Diffraction (EBSD) measurements on both undeformed and deformed materials after the application of varying strain amplitudes. These comprehensive investigations are investigated in publication P2. To contextualise the cyclic plastic material behaviour of PBF-LB/M/316L in comparison to conventional manufacturing processes, particularly hot-rolling, a comparative study is necessary. This involves directly comparing the results obtained from strain-controlled fatigue tests with those from hot-rolled 316L, employing identical strain amplitudes. The resultant hardening or softening behaviour is subsequently correlated with the microstructural characteristics. This comparative analysis is elaborated in publication P3. Both publications address the sub-objective SO2.

High-cycle fatigue behaviour of PBF-LB/M/316L and comparison to hot-rolled 316L

After the successful investigation of low-cycle fatigue behaviour, the study now shifts its focus to the exploration of high-cycle fatigue behaviour. To achieve this, an appropriate laser parameter set characterised by exceptionally high density and uniformly distributed melt pools must be selected for the fabrication of fatigue specimens. Subsequently, high-cycle fatigue tests employing a staircase approach encompassing multiple stress ranges must be conducted. This investigation serves as a benchmark, facilitating a comparative analysis between the as-built state of PBF-LB/M/316L material and conventional manufacturing techniques applied to 316L, including hot-rolling, casting, and forging. To elucidate the factors contributing to the varying fatigue properties of PBF-LB/M/316L in comparison to conventional methods, such as hot-rolling, it is imperative to undertake a comprehensive microstructure-strength comparison. This investigation aims to reveal the underlying reasons behind the superior or inferior fatigue properties displayed by PBF-LB/M/316L. The findings of this investigation pertaining to SO3 are detailed in publication P4.

Influence of surface treatment and hot isostatic pressing on the fatigue properties of PBF-LB/M/316L

To enhance the fatigue resistance of PBF-LB/M/316L, various post-processing methods can be employed, including vibratory grinding, surface polishing, and hot isostatic pressing. The impact of combining surface treatment with hot isostatic pressing on fatigue resistance has not been investigated yet. Hence, it is essential to establish S-N curves for different post-treatment techniques and compare their effects. The surface topography and roughness must be quantified before and after testing using laser confocal microscopy. Furthermore,

it is imperative to investigate changes in surface topography during fatigue testing to assess whether any alterations occur. Such changes may be attributed to induced surface residual stresses during the treatment process. Therefore, X-ray diffraction (XRD) should be applied. Additionally, Electron Backscatter Diffraction (EBSD) measurements should be conducted to examine variations in kernel-averaged misorientation (KAM) on the surface before and after fatigue testing. High KAM values indicate the potential for grain boundary sliding, which can result in surface intrusions and extrusions. These features can subsequently reduce fatigue resistance by initiating cracks prematurely. Additionally, scanning electron microscopy (SEM) measurements are essential to pinpoint the location of crack initiation. In conclusion, it is imperative to provide a recommendation for an optimal post-processing route aimed at enhancing fatigue resistance. This sob-objective SO4 is covered in publication P4.

Prediction of the fatigue life with surface defects and internal defects of PBF-LB/M/316L material

As mentioned in Chapter 5.5, internal and surface defects inevitably occur during the manufacturing process and may only be reduced in the case of internal defects. Therefore, the scattering may also be higher in comparison to conventionally manufactured 316L. With these occurring defects, every manufactured component has its unique fatigue life. Consequently, it becomes necessary to predict fatigue life based on the individual geometrical defects. To achieve this, μCT measurements and surface topology measurements on PBF-LB/M/316L fatigue specimens need to be conducted to identify internal and surface defects and extract the necessary defect features. Subsequently, fatigue testing should be carried out to investigate the number of cycles until failure. Machine learning algorithms need to be developed using the defect features as input parameters and the number of cycles until failure as the desired value to predict. Finally, the primary influencing defect features must be classified. This sub-objective, denoted as P5, is covered in publication P5.

Implementation of the PBF-LB/M process into the construction design and manufacturing route

Since the application of the PBF-LB/M process in the construction industry remains uncharted territory, it is imperative to undertake a practical study to establish the design and manufacturing approach, comparing it to the conventional methods employed in the construction sector. To accomplish this, a demonstrative structure must be identified where the application of the PBF-LB/M process is justified. An initial geometric design should be formulated, followed by a comprehensive shape optimisation process. The optimisation goals should revolve around achieving an optimal force distribution while simultaneously reducing the overall mass of the structure. In selecting a suitable material, cost-effectiveness and ease of handling and manufacturing must be taken into account. Furthermore, the mechanical properties of the chosen material must align with the requirements of the broader structural framework. Microstructural examinations are crucial to guaranteeing the achievement of high density and uniform weld pools within the PBF-LB/M process. Additionally, mechanical testing, including tensile and fatigue testing, should be conducted on standardised specimens, as well as on the final, shape-optimised geometry. This thorough testing route is vital to ensure the safe and reliable application of components within the construction industry. Ultimately, developing a processing route for the design and manufacturing of shape-optimised PBF-LB/M parts is important. Furthermore, integrating this processing route into the construction design process must be executed effectively.

7 Research Findings

7.1 Publication 1: Einfluss der Abkühlrate auf die mechanischen Eigenschaften von additiv gefertigten Zugproben aus 316L

Summary

In publication P1 "Effect of cooling rate on the mechanical properties of 316L tensile specimen, manufactured by Laser Powder Bed Fusion" [14], various sample geometries were manufactured, and their corresponding cooling rates were measured using in-situ thermography. Firstly, the influencing parameters of the PBF-LB/M process on the mechanical properties are presented and discussed. After that, the experimental plan is presented. This included the manufacturing of tensile specimens with varying sizes and the presentation of the different analysis techniques. The thermography setup is explained to measure the cooling rate. Subsequently, tensile tests and metallurgical investigations were performed. Depending on the geometry, different cooling rates were observed, which finally led to different tensile strength results.

Conclusion and main findings

With this study, it was possible to establish a correlation between the macroscopic cooling rates and the tensile mechanical properties of PBF-LB/M/316L. The following conclusions could be drawn:

- The cooling rate of the PBF-LB/M components depends on the geometry and the laser parameters.
- Faster scanning speed increases cooling rate, impacting resulting strength.
- The yield strength varies up to 29 MPa between the smallest and largest sample geometries.
- PBF-LB/M/316L exhibits a yield strength 2.5 times higher than conventionally manufactured counterparts.
- The grain size measurements and Hall-Petch relationship indicate differences in yield strength due to varying fine grain structures.
- The component geometry significantly influences the mechanical properties.
- Smaller sample dimensions result in lower yield strength due to cooling effects.
- In thicker sections, the yield strength is higher.
- The elongation at fracture remains relatively stable across geometries.

Contribution of the authors

Johannes Diller, the author of this thesis, developed the idea for measuring the cooling rate of PBF-LB/M parts during the manufacturing. He planned the experiments and was responsible for the evaluation of the measurement data. Ulrich Auer assisted within his master's thesis project in the execution of the experiments. The manuscript was written by Johannes Diller and edited by Christina Radlbeck, Frank Krafft and Martin Mensinger. All authors discussed and commented on the findings. Johannes Diller presented the results in a talk at the Münchner Stahlbautage in Munich, Germany in 2019. He won the prize for "Bester Nachwusvortrag" with this talk. All authors have reviewed and agreed to the content of the published version of the manuscript.

7.2 Publication 2: Cyclic plastic material behaviour of 316L manufactured by laser powder bed fusion (PBF-LB/M)

Summary

In publication P2 "Cyclic plastic material behavior of 316L manufactured by laser powder bed fusion (PBF-LB/M)" [115] the cyclic plastic material behaviour at high strain amplitudes of up to 3.0 % for AISI-316L, manufactured by PBF-LB/M, was investigated. Two different sets of laser parameters were applied. One was set outside the stable melting zone, and the other was set inside the stable melting zone as defined in [60]. The investigation involved metallographic analyses and static and strain-controlled fatigue tests with a strain ratio of
R = -1. The cyclic plastic material behaviour was predominantly characterised by softening, which reduced with increasing strain amplitude due to mechanical twinning. Indeed, twin-induced strain hardening was observed for strain amplitudes >2.5 %. A correlation was found between the twin-induced strain hardening behaviour and the resulting maximum stress curve per endured cycle. The laser parameters influenced the generated stress level during cyclic plastic loading. Furthermore, it was demonstrated that porosity significantly impacted fatigue life, particularly in the low-cycle fatigue range. Ultimately, the strain-life curve was determined and approximated using the Manson-Coffin fatigue parameters.

Conclusion and main findings

With this study it was possible to define the microstructure-strength relationship in the low to very low-cycle fatigue range of PBF-LB/M/316L. The following conclusions could be drawn:

- A higher porosity leads to a lower number of cycles until failure due to stress concentrations of the pores, resulting in an early failure of the specimens.
- A primary softening behaviour after the third cycle is observed at every strain amplitude.
- Most of the softening of the specimens loaded with a strain amplitude of 0.5 % - 2.0 % always occurs in the first quarter of the total cycle range.
- From a strain amplitude of 2.0 % and above, the primary softening rate decreases, as most of the softening can take up to 82 % of the whole lifetime.
- From a strain amplitude of 2.0 % and above, a secondary hardening behaviour is partly observed regardless of the laser parameters.
- The secondary hardening behaviour can be traced back to strain-induced mechanical twinning.
- It is assumed that the twinning-induced hardening, resulting from a higher strain, leads to a slower softening rate of the material.
- It is assumed that the dislocation density is higher for energy density E1 (low energy density) in comparison to energy density E2 (high energy density), resulting in higher generated stresses.
- The latter has to be confirmed with in-situ X-ray measurements during strain-controlled fatigue testing with an electron synchrotron particle accelerator.

Contribution of the authors

Johannes Diller planned, coordinated and executed the experiments. Lukas Rier supported the experiments within the framework of his master's thesis. Johannes Diller, Lukas Rier and Dorina Siebert analysed the experimental data and discussed the findings. The manuscript was written by Johannes Diller and edited by Dorina Siebert. Christina Radlbeck, Martin Mensinger and Frank Krafft commented on the results. All authors have reviewed and agreed to the content of the published version of the manuscript.

7.3 Publication 3: PBF-LB/M/316L vs. hot-rolled 316L — comparison of cyclic plastic behaviour

Summary

In publication P3 "PBF-LB/M/316L vs. hot-rolled 316L – comparison of cyclic plastic material behaviour" [116] the cyclic plastic material behaviour of PBF-LB/M/316L from publication P2 was compared to hot-rolled 316L. Powder-Bed Fusion of AISI 316L (1.4404) using a laser (PBF-LB/M) is known for its very high cooling rate of up to 40 K/µs [59]. This high cooling rate results in a fine needle-like microstructure. In comparison, hot-rolled, annealed AISI 316L consists of coarser grain structures. The quasi-static tensile properties, therefore, differ significantly. This may result in a completely different cyclic plastic material behaviour due to the grain boundary strengthening during the PBF-LB/M manufacturing process. This study compared the cyclic plastic material behaviour of PBF-LB/M/316L with that of hot-rolled, annealed AISI 316L. Strain-controlled fatigue testing of both PBF-LB/M and hot-rolled, annealed AISI 316L was conducted. The strain amplitudes varied from 0.5 % to 3.0 % in steps of 0.5 %. A microstructural investigation of selected specimens was conducted before and after testing. It consisted of surface etching, electron backscatter diffraction (EBSD), as well as spark spectrometry. The orientation, phase transformation, twinning formation, as well as the general microstructure, were compared. It was found that the PBF-LB/M manufactured specimens mainly showed a softening behaviour. Only from an applied strain amplitude of 2.5 %, a secondary hardening phenomenon was observed. In contrast, the hot-rolled and annealed specimens mainly showed a continuous hardening behaviour.

Conclusion and main findings

Through this study, it has been demonstrated that the cyclic plastic material behaviour of PBF-LB/M/316L exhibits a significant contrast to hot-rolled 316L. Specifically, PBF-LB/M/316L primarily undergoes softening during cyclic plastic deformation, whereas hot-rolled 316L experiences hardening accompanied by a phase transformation from austenite to martensite. The key findings are summarised as follows:

- The PBF-LB/M manufactured AISI 316L reveals higher initial maximum stresses, followed by a softening behaviour.
- The hot-rolled AISI 316L has lower initial maximum stresses, followed by a hardening behaviour.
- The PBF-LB/M manufactured AISI 316L has a higher fatigue life in comparison to hot-rolled AISI 316L.
- During cyclic plastic deformation of the PBF-LB/M manufactured AISI 316L, no to little martensite transformation occurs due to the small crystallite size.
- The martensite transformation during cyclic plastic deformation of the hot-rolled AISI 316L occurs due to the large grain size.
- The lower Ni-content of the hot-rolled AISI 316L leads to a higher transformation affinity from austenite to martensite.
- The hardening behavior of the hot-rolled AISI 316L can therefore be reasoned with both martensite transformation and strain-induced twinning.

Contribution of the authors

Johannes Diller planned and executed the experiments, conducted data analysis, and engaged in discussions regarding the findings. The manuscript was authored by Johannes Diller and underwent editing by Dorina Siebert, Christina Radlbeck, and Martin Mensinger. Johannes Diller presented the findings at the 23rd European Conference on Fracture in Funchal, Madeira Island, Portugal, in July 2022. All authors have reviewed and agreed to the content of the published version of the manuscript.

7.4 Publication 4: Combined effect of surface treatment on the fatigue properties of AISI 316L, manufactured by powder bed fusion of metals using a laser (PBF-LB/M)

Summary

Publication P4 "Combined effect of surface treatment on the fatigue properties of AISI 316L, manufactured by powder bed fusion of metals using a laser (PBF-LB/M)" [117] deals with the combined influence of surface treatment and heat treatment of 316L manufactured by powder bed fusion of metals using a laser (PBF-LB/M/316L) on the fatigue behaviour. Two surface treatment methods (manual polishing, vibratory grinding) were investigated. Fatigue testing of six different surface and heat treatment parameter setups was conducted. Metallurgical investigations such as etching patterns, density measurements, surface roughness measurements, fracture surface analysis with a scanning electron microscope (SEM), X-ray diffraction (XRD) and electron backscatter diffraction (EBSD) were performed. The mechanical properties were examined by tensile tests and fatigue tests. The influence of grain size on fatigue life was found to be the primary factor, followed by the surface roughness and subsequently the residual stresses on the surface ultimately contributing to the overall effect.

Conclusion and main findings

With this study, it was possible to define a hierarchy of the impact on the high-cycle fatigue resistance of PBF-LB/M/316L. The following conclusions could be drawn:

- The hierarchy of the impact on fatigue resistance may be established as follows: Grain size holds the greatest magnitude of influence, followed by surface roughness, and subsequently residual surface stresses.
- A small grain size increases the fatigue resistance.
- Locally opened pores and insufficient material removal due to vibratory grinding may reduce the fatigue resistance.
- Manual polishing closes pores near the surface and increases the compressive residual stresses, resulting in a higher fatigue resistance.
- Residual stresses on the surface may have a small influence on the fatigue resistance if opened pores near the surface are present.
- Surface topology of hot isostatically pressed and vibratory ground specimens changes rapidly after a few cycles in contrast to as-built PBF-LB/M/316L with the same surface treatment. To correlate surface roughness with fatigue, it is recommended to consider roughness after a few hundred cycles, accounting for evolving surface conditions and ensuring accurate representation for fatigue performance.
- The line roughness parameters, specifically Ra and Rz, do not exhibit a strong correlation between roughness and fatigue resistance. On the other hand, the surface roughness parameter Sz demonstrates a more favorable correlation in this regard. In addition to surface roughness parameters, other factors such as grain size, grain boundary sliding, twinning affinity, and residual stresses present on the surface exert a significant influence on fatigue resistance.

Contribution of the authors

Johannes Diller planned, coordinated and executed the experiments. Jakob Blankenhagen supported the experiments within the framework of his master's thesis. Johannes Diller and Jakob Blankenhagen analysed the experimental data and discussed the findings. The manuscript was written by Johannes Diller and edited by Dorina Siebert and Jakob Blankenhagen. Christina Radlbeck and Martin Mensinger commented on the results. All authors have reviewed and agreed to the content of the published version of the manuscript.

7.5 Publication 5: An integrated approach for detecting and classifying pores and surface topology in PBF-LB/M-manufactured 316L using µCT and machine learning algorithms for fatigue assessment

Summary

The objective of this publication P5 is to achieve an automated detection and analysis of critical internal and surface defects in metal components manufactured by powder bed fusion of metals using a laser (PBF-LB/M). The primary aim is to assess their impact on the fatigue behaviour of these components. To accomplish this, a combination of methods, including image processing of micro-computed tomography scans (μCT), fatigue testing, and machine learning, was applied. A systematic workflow was established to contribute to the non-destructive assessment of component quality and mechanical properties. Additionally, this study illustrates the application of machine learning to address a classification problem, specifically, the categorisation of pores into gas pores and lack of fusion pores. Although internal defects exhibited a reduced impact on fatigue behaviour compared to surface defects, it was noted that surface defects exert a more prominent influence on fatigue behaviour. Consequently, a machine learning algorithm was developed to predict the fatigue life using surface defect features as input parameters.

Conclusion and main findings

- Polished fatigue specimens have a higher fatigue resistance in comparison to as-built fatigue specimens.
- The primary cause of fatigue crack initiation in polished fatigue specimens is attributed to internal defects. Conversely, crack initiation consistently occurs on the surface in as-built fatigue specimens.
- The scattering of the number of cycles for polished fatigue specimens is notably greater in comparison to as-built fatigue specimens.
- The limited correlation observed in the polished specimens concerning fatigue resistance can be rationalised in accordance with the findings by Sanaei et al. [118]. Their research demonstrated that the surface roughness effect is detrimental and primary on the fatigue performance even in the presence of relatively large internal defects and for various microstructures.
- Additionally, they revealed that the fatigue limit increases as surface roughness decreases, irrespective of the microstructure. Nevertheless, some degree of variability was noted, which might be attributed to the secondary influences of internal defects and microstructure. The findings of this study align with and affirm the aforementioned observations.
- A workflow for extracting surface and internal features was successfully established.
- A pore classification machine learning algorithm was successfully developed with an accuracy of 92.4 %. This algorithm serves as a base for future investigations regarding a combined effect of surface defects and internal defects.
- A fatigue life prediction machine learning algorithm has been effectively developed, achieving a Root Mean Square Error (RMSE) of 29,139 cycles. This was achieved by incorporating newly introduced parameters, specifically the depth of the depression from the zero line (a) and the spacing between the zero-crossings as the notch width ($2b$). To improve the robustness of the machine learning algorithm, more variety of surface topology and data is necessary.

Contribution of the authors

Johannes Diller planned, coordinated and executed the experiments. Ludwig Siebert and Michael Winkler supported the experiments within the framework of their master's thesis. Johannes Diller, Ludwig Siebert and Michael Winkler analysed the experimental data and discussed the findings. The manuscript was written

by Johannes Diller and edited by Dorina Siebert, Jakob Blankenhagen, and David Wenzler. Christina Radlbeck and Martin Mensinger commented on the results. All authors have reviewed and agreed to the content of the published version of the manuscript.

7.6 Publication 6: Additive Manufacturing in Construction — Implementing Powder-Bed Fusion of Metals Using a Laser (PBF-LB/M) and Shape Optimisation in the Construction Design Process

Summary

In publication P6 "Additive Manufacturing in Construction — Implementing Powder-Bed Fusion of Metals Using a Laser (PBF-LB/M) and Shape Optimisation in the Construction Design Process" [119] the implementation of the PBF-LB/M process into the construction design and building process was investigated. To this purpose, a tensegrity tower was designed, planned, and built. The nodes between the compression rods and the tension cables were manufactured by PBF-LB/M/AlSi10Mg. Four different nodes were designed and shape optimised by vertex-morphing. In order to qualify the tensegrity nodes according to German regulations, mechanical as well as microstructural evaluations were conducted. Tensile tests of a manufactured tensegrity node in a fully hinged setup were carried out. Additionally, fatigue testing was conducted. The tensegrity nodes were heat-treated (T6) and subsequently vibratory ground to reduce the surface roughness. The results indicate that it is feasible to integrate the PBF-LB/M process into the design and construction process. The tower is now a permanent and tangible exhibit in the Deutsches Museum in Munich.

Conclusion and main findings

- The PBF-LB/M process was successfully integrated into the construction design process.
- A design and manufacturing route was proposed to safely implement the PBF-LB/M process into the construction design and manufacturing process.
- Shape optimization can be used to optimize the force flow in the part and reduce mass for faster production.
- A qualification method for PBF-LB/M machines for the construction sector is necessary, which is comparable to qualification methods of welding processes.
- Design restrictions should be implemented into the shape optimization process to reduce the danger of internal defects occurring.

Contribution of the authors

The conceptualization of the study was carried out by Johannes Diller and Dorina Siebert. Methodology development was led by Johannes Diller. Visualization of the data and findings was executed by Johannes Diller. Validation was performed jointly by Johannes Diller and Jakob Blankenhagen. The investigation was primarily carried out by Johannes Diller. The original draft preparation of the manuscript was the work of Johannes Diller. The review and editing of the manuscript were performed by Dorina Siebert, Christina Radlbeck, Florian Oberhaidinger, Drilon Gubetini and Martin Mensinger. All authors have reviewed and agreed to the content of the published version of the manuscript. Johannes Diller presented the results in a talk at the International Aluminium Conference (INALCO) in Québec City, Canada in October 2023.

7.7 Discussion of the results

This section provides a concise discussion of the results that led to publications P1 through P6, emphasising their significant contributions to the field in comparison with the most relevant works in the current state of the art. Figure 7.1 shows a classification of the publications P1 to P6 arranged to the respective fields of research. These research fields are: *process related mechanical properties (**Process**), post treatment related mechanical properties **(Post treatment)** and practical applications of the PBF-LB/M process in the construction sector **(Practical application)**.* The process related research includes the investigation of mechanical properties which are a result of the manufacturing process. Post treatment related research focuses on examining the mechanical characteristics arising from post-treatment methods. The effect of post treatment methods on the surface residual stresses and therefore on the fatigue behaviour is also included in this research field. The research field of practical application includes the development of design and manufacturing routes to implement PBF-LB/M into the construction sector. Those research fields are subdivided into the mechanical properties, consisting of low-cycle fatigue (LCF), static mechanical properties, and high-cycle fatigue (HCF) and into the prediction of the fatigue life.

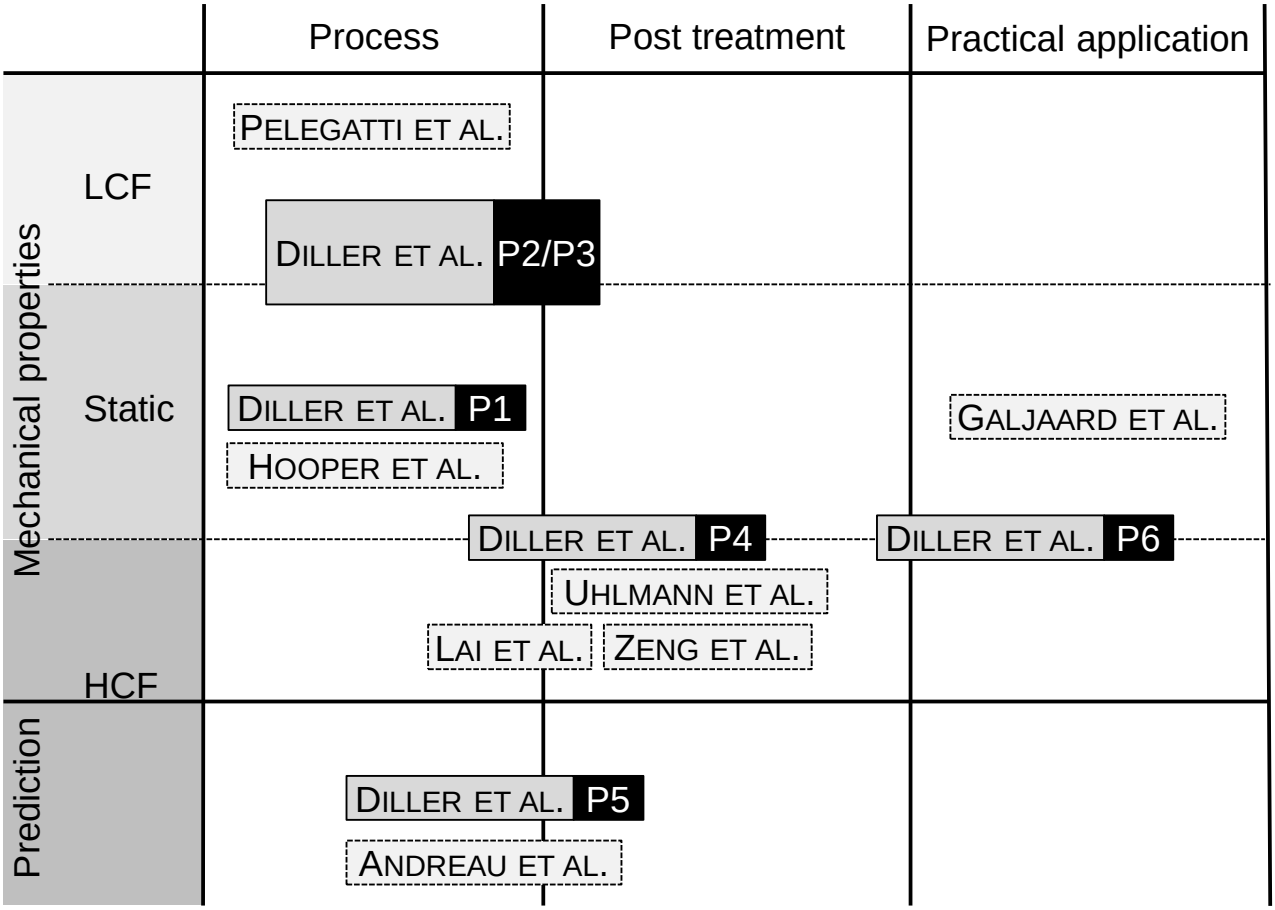

Figure 7.1: *Classification of the publications P1 to P6, arranged according to their respective field of research/innovation considering the closest publications from the previous state of the art (see Chapter 5.5)*

Publication P1 of this dissertation can mainly be asserted to the research field of the process related mechanical properties. Chapter 5.1 revealed that existing research in the state of the art did not adequately cover the impact of cooling rate on mechanical properties. In the works of Hooper et al. [59] and Godec et al. [63] the cooling rate was measured on a microscopic scale and the formation of the microstructure was explained thoroughly. However the correlation to the mechanical properties was not conducted. In P1 it was experimentally proven, that the cooling rate correlates to the yield strength and to the ultimate tensile strength. Therefore, P1 fulfils the scientific sub-objective SO1 as outlined in Chapter 6.1.

Publication P2 and P3 contributed to a more profound understanding of the cyclic plastic material behaviour of PBF-LB/M/316L and the differences in comparison to hot-rolled 316L. The publication P2 of this dissertation provided results that experimentally and analytically explain the microstructure-strength behaviour of PBF-LB/M/316L during cyclic plastic deformation. Until that point in time, only a few publications were available regarding the low-cycle fatigue behaviour of PBF-LB/M/316L (see Table 5.1. They mainly focused on the building direction [69, 77] and the development of plastic material models [74]. In P2, not only the effect of different laser parameters on the cyclic plastic material behaviour was investigated. Additionally, a higher strain amplitude was investigated and a thorough microstructure-strength evaluation was conducted. The analysis of two laser parameter sets also resulted in the investigation of the porosity on the low-cycle fatigue behaviour of PBF-LB/M/316L, which has not been done before. In publication P3, a comparison of the different hardening and softening behaviour of PBF-LB/M/316L and hot-rolled 316L was conducted. The microstructural analysis in P3, focusing on phase transformations and twinning behaviour, surpasses existing knowledge in the field. As such, it satisfies the criteria set forth in the sub-objective SO2, detailed in Chapter 6.1.

In Publication P4, investigations were conducted on the high-cycle fatigue behaviour of PBF-LB/M/316L. As shown in Table 5.2, the high-cycle fatigue behaviour has been studied elaborately. However, multiple questions have not been addressed. As the surface roughness of PBF-LB/M/316L is very high, adequate surface treatment methods for complex geometries need to be applied. Here, vibratory grinding is a useful surface treatment process to decrease the surface roughness at every area of a component with a highly complex geometry. The effect of the introduced surface residual stresses of vibratory grinding has however not been investigated. Additionally, a comparison of as-built surfaces, polished surfaces and vibratory ground surfaces including heat treatment (HIP) has not been investigated. Uhlmann et al. [84] conducted fatigue tests of vibratory ground PBF-LB/M/316L, but did not investigate the resulting microstructure and the surface residual stress. Zeng et al. [112] investigated the influence of hot isostatic pressing on the fatigue behaviour of PBF-LB/M/316L without any surface treatment. Lai et al. [101] conducted residual stress measurements of PBF-LB/M/316L specimens and correlated them to the fatigue behaviour but did not apply any post treatment. Publication P4 closed the gap between the aforementioned publications and the effects were investigated in combination. Therefore, sub-objective S04 was achieved.

In Publication P5, research was undertaken to identify the primary cause of crack initiation under fatigue loading, classify internal defects, and predict the fatigue life. It is worth noting that there is a low amount of studies focusing on the fatigue life prediction of PBF-LB/M/316L using machine learning algorithms. The majority of studies in this domain have primarily investigated Ti6Al4V, as indicated by Li et al. [120]. Predicting the fatigue life of individual specimens through a machine learning approach has not been previously carried out for PBF-LB/M/316L. The development of a machine learning algorithm for distinguishing between lack of fusion pores and gas pores introduces a novel methodology.Furthermore, the exploration of the shift in the prominence of crack initiators from surface defects to internal defects as a result of surface treatment has not been explored in the context of PBF-LB/M/316L yet. Sanaei et al. [118] and Cersullo et al. [121] showed, that with decreasing surface roughness, the detrimental effect of internal defects on fatigue performance increases. However, this was only stated for PBF-LB/M/Ti6Al4V and PBF-LB/M/Inconel718. This study confirmed their results for PBF-LB/M/316L. Hence, the criteria set forth in sub-objective SO5 have been fulfilled.

Publication P6 addressed the practical application of the PBF-LB/M process and the implementation into the construction sector. Galjaard et al [122] conducted initial studies to use the PBF-LB/M process for the construction industry. The final components have been manufactured. They have however never been tested and installed in a larger structure. In Publication P6 not only the mechanical testing including tensile and fatigue testing was conducted. Additionally, a processing route was proposed to implement shape-optimisation and the PBF-LB/M process into the construction design and manufacturing process. Sub-objective SO6 was therefore also achieved.

8 Summary and Outlook

8.1 Summary

The PBF-LB/M process finds its primary application in the production of complex and often shape-optimised metal components. Initially developed for the aerospace and automotive sectors, its potential advantages are also increasingly being explored in the construction industry. Notably, it can be advantageous for producing critical elements such as load-bearing connection nodes and steel hysteretic dampers. However, for the safe and effective utilisation of this process in construction, it is imperative to have a thorough understanding of and control over the origins of the mechanical properties. The PBF-LB/M process has yet to be incorporated into any industry standards specifically for the construction sector. This absence can be attributed to the many aspects of this manufacturing process that have not undergone thorough investigation and assessment. Ensuring the safe and reliable implementation of the PBF-LB/M process in the construction industry requires a comprehensive exploration of these unexplored areas. One crucial aspect of this understanding is connected to the fatigue performance of PBF-LB/M/316L. This performance is greatly influenced by the surface topology, the porosity, and the microstructure of the manufactured components.

The fundamental concept driving the research conducted in this dissertation is mainly, but not wholly, focused on enhancing the comprehension of the impact of process-induced defects in PBF-LB/M/316L on the fatigue performance. It also aims to establish a framework for predicting the fatigue resistance of each specific manufactured component based on its intended application. This framework is not limited to the construction industry, as the aerospace and automotive industries are challenged with the same issues. Future developments in the additive manufacturing sector, particularly in improving optical tomography and overall process monitoring, can facilitate a more accurate prediction of the fatigue resistance for each component.

The exploratory research approach adopted in this dissertation encompasses several key areas, including investigations into cooling rates and their impact on static mechanical properties (Chapter 7.1), the analysis of low-cycle fatigue behaviour (Chapters 7.2 and 7.3), examination of high-cycle fatigue behaviour and the influence of post-processing methods (Chapter 7.4), fatigue life prediction through machine learning algorithms (Chapter 7.5), and practical applications of the PBF-LB/M process (Chapter 7.6). Advancements in the state of the art could be achieved across all of these research fields, as detailed in Chapter 7.7.

From the aforementioned studies, the following main advancements in fatigue research of PBF-LB/M/316L are shown:

- The fine subgrains result from the high cooling rate during the PBF-LB/M process. These subgrains not only increase the yield strength, they also increase the fatigue resistance.
- PBF-LB/M/316L softens during cyclic plastic deformation, whereas hot-rolled 316L hardens.
- The primary factor contributing to the softening phenomenon can likely be ascribed to the elevated dislocation density after the manufacturing process. During plastic deformation, these dislocations may gradually assume a more stable arrangement in relation to each other, thereby reducing the back stress. Consequently, this reduction in back stress leads to a decrease in the applied stress under a given strain amplitude.
- The main reason for the hardening of hot-rolled 316L can be attributed to martensite phase transformation and strain-induced twining.

- The low-cycle fatigue resistance of PBF-LB/M/316L is higher in comparison to hot-rolled 316L.
- The high-cycle fatigue resistance of PBF-LB/M/316L is higher in comparison to hot-rolled 316L.
- Hot isostatic pressing reduces the fatigue resistance of PBF-LB/M/316L.
- The grain size has the highest influence on the fatigue resistance of PBF-LB/M/316L, followed by the surface roughness and the residual stresses on the surface.
- A pore classification machine learning algorithm was successfully developed with an accuracy of 92.4 %. This algorithm serves as a base for future investigations regarding a combined effect of surface defects and internal defects.
- A fatigue life prediction machine learning algorithm has been effectively developed, achieving a Root Mean Square Error (RMSE) of 29,139 cycles. This was achieved by incorporating newly introduced parameters, specifically the depth of the depression from the zero line (a) and the spacing between the zero-crossings as the notch width (2b).
- The primary cause of fatigue crack initiation in polished fatigue specimens is attributed to internal defects. Conversely, in as-built fatigue specimens, crack initiation consistently occurs on the surface.
- The implementation of the PBF-LB/M process, along with shape optimisation, is feasible without requiring significant alterations to the construction design and manufacturing process.

In conclusion, it can be affirmed that the safe utilisation of PBF-LB/M/316L in the construction industry is attainable, provided that specific considerations are taken into account. Notably, PBF-LB/M/316L tends to soften rather than harden during cyclic plastic deformation. Therefore, applying an optimal laser parameter set that has been thoroughly tested before implementing the PBF-LB/M process is imperative.

8.2 Outlook

This dissertation has demonstrated the viability of employing the PBF-LB/M process for manufacturing shape-optimised components that can be confidently applied in the construction industry. Nevertheless, the full potential of the PBF-LB/M process remains untapped. While the utilisation of shape optimisation has already resulted in weight reduction and the establishment of optimal force flow, there is still room for further exploration in terms of integrating tailored component properties into these components. Lattice structures offer the potential to engineer customised stiffness within connection nodes. When applied to an entire structure, this approach can enable the creation of an optimised force distribution with specifically tailored stiffness profiles, much like the branching structure of a tree with varying branch sizes. This not only allows for the adjustment of stiffness but also opens possibilities for tailoring damping characteristics, potentially enhancing the ability of a structure to dampen vibrations during smaller seismic events within larger structures. Therefore, materials with a high strength and a high ductility are necessary. Recently, new materials specifically for the PBF-LB/M process have been developed (Printdur HSA, Bainidur).

Another vital factor which should be investigated in the future is the fatigue life prediction. In this thesis, μCT was used to detect and classify pores and the surface topology. μCT measurements are time-consuming and expensive. Recently, new process-monitoring methods were developed. These include, for example, optical tomography.

The system comprehensively monitors the entire manufacturing environment using an sCMOS industrial camera and captures the heat emissions of the melting process at a high resolution The versatile software provides comprehensive insights into the quality of components within each layer. Optical tomography enables the monitoring of reproducibility, enhances comparability among components, manufacturing projects, and pPBF-LB/M machines, and offers a pathway for cost-effective quality assurance integration into series manufacturing applications. [123] This system could be used to replace μCT to detect defects in the material during

manufacturing. The defects can be directly correlated to the fatigue resistance with the developed machine learning algorithms in this study. The surface topology could be digitised using 3D-scanning techniques as an alternative to μCT.

In addition to these additional research activities concerning custom component properties, it is essential to explore the interface between these components and semi-finished parts. This investigation would help ensure that failures do not occur at the welds connecting the PBF-LB/M components and the semi-finished parts.

Bibliography

[1] Beuth: DIN EN ISO/ASTM 52900:2022-03, Additive Fertigung_- Grundlagen_- Terminologie (ISO/ASTM 52900:2021); Deutsche Fassung EN_ISO/ASTM 52900:2021 / Beuth Verlag GmbH. Berlin, 2022. – Forschungsbericht

[2] Gross, Doug: *Obama's speech highlights rise of 3-D printing | CNN Business — edition.cnn.com.* https://edition.cnn.com/2013/02/13/tech/innovation/obama-3d-printing/index.html, 2013. – [Accessed 04-12-2023]

[3] *SLM NXG 600 — slm-pushing-the-limits.com.* https://www.slm-pushing-the-limits.com/?utm_term=selective%20laser%20melting&utm_campaign=SLM+Verticals+DACH&utm_source=adwords&utm_medium=ppc&hsa_acc=2258688895&hsa_cam=20426750151&hsa_grp=153179978578&hsa_ad=668815014647&hsa_src=g&hsa_tgt=kwd-299879920028&hsa_kw=selective%20laser%20melting&hsa_mt=p&hsa_net=adwords&hsa_ver=3&gad_source=1&gclid=Cj0KCQiA67CrBhC1ARIsACKAa8QWth8H9Qa7_zJnE_fqNjReE-N5_m5hD3kir9QsWb48R66dkZxiuCoaApQFEALw_wcB, 2021. – [Accessed 04-12-2023]

[4] Grünewald, Jonas ; Reinelt, Jonas ; Sedlak, Holger ; Wudy, Katrin: Support-free laser-based powder bed fusion of metals using pulsed exposure strategies. In: *Prog. Addit. Manuf.* (2023), März

[5] sumaart.com: *BLT-S1000 Metal Additive Manufacturing System.* https://www.xa-blt.com/en/product/blt-s1000/?category=8, 2023. – [Accessed 04-12-2023]

[6] Gümpel, Paul ; Blumhofer, Gunter ; Dören, Horst ; Gebel, Wolfgang ; Heimann, Winfried ; Morach, Rudolf ; Schmitz, Karl W. ; Uhlig, Georg: *TAE.* Bd. Band 493: *Rostfreie Stähle: Grundwissen, Konstruktions- und Verarbeitungshinweise.* 5., durchgesehene Auflage. Renningen : expert verlag, 2016. – ISBN 978–3–8169–3148–5

[7] Gottstein, Günter: *Materialwissenschaft und Werkstofftechnik: Physikalische Grundlagen.* 4. Aufl. 2014. Berlin, Heidelberg : Springer Berlin Heidelberg, 2014 (Springer-Lehrbuch). http://nbn-resolving.org/urn:nbn:de:bsz:31-epflicht-1582309. – ISBN 978–3–642–36603–1

[8] Marshall, P: *Austenitic Stainless Steels.* 1984. Dordrecht, Netherlands : Kluwer Academic, 1984

[9] Callister, William D.: *Materials science and engineering: An introduction.* 7. ed. New York, NY : Wiley, 2007 http://www.loc.gov/catdir/enhancements/fy0625/2005054228-d.html. – ISBN 978–0–471–73696–7

[10] Hosson, J Th M. ; Pestman, B P.: Interactions between lattice dislocations and grain boundaries in L12 ordered compounds investigated by in situ transmission electron microscopy and computer modelling experiments. In: *Fundamental Aspects of Dislocation Interactions.* Elsevier, 1993, S. 415–420

[11] *DIN EN 10088-1:2022-01, Nichtrostende Staehle-Teil1: Verzeichnis der nichtrostenden Staehle; Deutsche und Englische Fassung prEN10088-1:2021*

[12] Schaeffler, AL: Welding dissimilar metals with stainless electrodes. In: *Iron Age* 162 (1948), Nr. 7, S. 72–79

[13] Thyssen Krupp Materials: *Stainless Steel 1.4404 Datasheet.* 2022

[14] Diller, Johannes ; Auer, Ulrich ; Radlbeck, Christina ; Mensinger, Martin ; Krafft, Frank: Einfluss der Abkühlrate auf die mechanischen Eigenschaften von additiv gefertigten Zugproben aus 316L. In: *Stahlbau* 89 (2020), Nr. 12, S. 970–980. http://dx.doi.org/10.1002/stab.202000034. – DOI 10.1002/stab.202000034. – ISSN 0038–9145

[15] Braun, Moritz ; Mayer, Eduard ; Kryukov, Igor ; Wolf, Christian ; Böhm, Stefan ; Taghipour, Aliakbar ; Wu, Rachael E. ; Ehlers, Sören ; Sheikhi, Shahram: Fatigue strength of PBF-LB/M and wrought 316L stainless steel: effect of post-treatment and cyclic mean stress. In: *Fatigue Fract. Eng. Mater. Struct.* 44 (2021), November, Nr. 11, S. 3077–3093

[16] Obrtlik, Karel ; Polak, Jaroslav ; Kruml, Tomas: Effect of hardcor surface treatment on fatigue behaviour of 316L austenitic stainless steel. In: *J. Mech. Behav. Mater.* 10 (1999), Dezember, Nr. 5-6, S. 311–324

[17] Mohammad, Khairul A. ; Zainudin, Edi S. ; Sapuan, S M. ; Zahari, Nur I. ; Aidy, Ali: Fatigue life for type 316L stainless steel under cyclic loading. In: *Adv. Mat. Res.* 701 (2013), Mai, S. 77–81

[18] Werner, Tiago ; Madia, Mauro ; Zerbst, Uwe: Comparison of the fatigue behavior of wrought and additively manufactured AISI 316L. In: *Procedia Struct. Integr.* 38 (2022), S. 554–563

[19] Hall, E. O.: The Deformation and Ageing of Mild Steel: III Discussion of Results. In: *Proceedings of the Physical Society. Section B* 64 (1951), Nr. 9, S. 747–753. http://dx.doi.org/10.1088/0370-1301/64/9/303. – DOI 10.1088/0370–1301/64/9/303. – ISSN 0370–1301

[20] Petch, N. J.: The Cleavage Strength of Polycrystals. In: *J. Iron Steel Inst. London* 1953 (1953), Nr. 173, S. 25–28

[21] van Vlack, Lawrence H.: *A textbook of materials technology*. Reading : Addison-Wesley, 1973 (Addison-Wesley series in metallurgy and materials). – ISBN 978–0201080667

[22] Bargel, Hans-Jurgen (Hrsg.): *Werkstoffkunde*. 13. Wiesbaden, Germany : Springer Vieweg, 2022 (Springer-Lehrbuch)

[23] Lodh, Arijit ; Thool, Khushahal ; Samajdar, Indradev: X-ray diffraction for the determination of residual stress of crystalline material: An overview. In: *Trans. Indian Inst. Met.* 75 (2022), April, Nr. 4, S. 983–995

[24] Waseda, Yoshio ; Matsubara, Eiichiro ; Shinoda, Kozo: *X-ray diffraction crystallography*. 2011. Berlin, Germany : Springer, 2011

[25] Harrington, George F. ; Santiso, José: Back-to-Basics tutorial: X-ray diffraction of thin films. In: *J. Electroceram.* (2021), Oktober

[26] Harrington, Peter: *Machine Learning in Action*. Manning Publications, 2012

[27] Tanaka, K ; Suzuki, K ; Akiniwa, Y: X-ray evaluation of residual stress. In: *Yokendo: Tokyo, Japan* (2006)

[28] Hayashi, Makoto: Residual stresses induced by surface working and their improvement by Emery paper polishing. In: *Quantum Beam Sci.* 4 (2020), Mai, Nr. 2, S. 21

[29] MURAKAMI, Y ; IBUCHI, H: PRODUCTION OF– RESIDUAL STRESSES DUE TO THE MILLING OPERATION. In: *J SOC MATER SCI JAP* 16 (1967), Nr. 171

[30] Ferro, P ; Berto, F ; Bonollo, F ; Tang, K: Does metallurgy affect the residual notch stress intensity factor value induced by welding operations? A comprehensive study via a 3D numerical model. In: *Int. J. Fatigue* 149 (2021), August, Nr. 106261, S. 106261

[31] Haibach, Erwin: *Betriebsfestigkeit*. 3. Berlin, Germany : Springer, 2006 (VDI-Buch)

[32] Schubert, Tim: *Efficient microstructure characterization of metals using light microscopy*. https://www.zeiss.com/microscopy/en/resources/insights-hub/materials-sciences/efficient-microstructure-characterization-of-metals-using-light-microscopy.html. Version: Apr 2020

[33] MURAKAMI, Yukitaka: *Metal fatigue: Effects of small defects and nonmetallic inclusions*. Second edition. Amsterdam and London and San Diego, CA : Academic Press an imprint of Elsevier, 2019. – ISBN 9780128138762

[34] Gross, Dietmar ; Seelig, Thomas: *Fracture mechanics*. 3. Cham, Switzerland : Springer International Publishing, 2017 (Mechanical Engineering Series)

[35] MURAKAMI, Yukitaka ; TAKAHASHI, Koji ; YAMASHITA, Teruo: Quantitative Evaluation of the Effect of Surface Roughness on Fatigue Strength. Effect of Depth and Pitch of Roughness. In: *TRANSACTIONS OF THE JAPAN SOCIETY OF MECHANICAL ENGINEERS Series A* 63 (1997), Nr. 612, S. 1612–1619. http://dx.doi.org/10.1299/KIKAIA.63.1612. – DOI 10.1299/KIKAIA.63.1612. – ISSN 0387–5008

[36] Dowling, Norman E.: *Mechanical Behavior of Materials - Engineering Methods for Deformation, Fracture, and Fatigue*. München : Pearson, 2013. – ISBN 978–0–131–39506–0

[37] ITOGA, Hisatake ; TOKAJI, Keiro ; NAKAJIMA, Masaki ; KO, Haeng-Nam: Effects of Notch and Surface Roughness on Long Life Fatigue Behaviour in High Strength Steels. In: *Journal of the Society of Materials Science, Japan* 54 (2005), Nr. 12, S. 1249–1254. http://dx.doi.org/10.2472/JSMS.54.1249. – DOI 10.2472/JSMS.54.1249. – ISSN 0514–5163

[38] François, D: The influence of the microstructure on fatigue. In: *Advances in Fatigue Science and Technology*. Dordrecht : Springer Netherlands, 1989, S. 23–76

[39] Järvenpää, Antti ; Karjalainen, L. P. ; Jaskari, Matias: Effect of grain size on fatigue behavior of Type 301LN stainless steel. In: *International Journal of Fatigue* 65 (2014), August, 93–98. http://dx.doi.org/10.1016/j.ijfatigue.2013.05.012. – DOI 10.1016/j.ijfatigue.2013.05.012

[40] Schino, A. D. ; Kenny, J.M.: Grain size dependence of the fatigue behaviour of a ultrafine-grained AISI 304 stainless steel. In: *Materials Letters* 57 (2003), Juli, Nr. 21, 3182–3185. http://dx.doi.org/10.1016/s0167-577x(03)00021-1. – DOI 10.1016/s0167–577x(03)00021–1

[41] Hamada, A.S. ; Karjalainen, L.P.: High-cycle fatigue behavior of ultrafine-grained austenitic stainless and TWIP steels. In: *Materials Science and Engineering: A* 527 (2010), August, Nr. 21-22, 5715–5722. http://dx.doi.org/10.1016/j.msea.2010.05.035. – DOI 10.1016/j.msea.2010.05.035

[42] Liu, J. ; Deng, X.T. ; Huang, L. ; Wang, Z.D.: High-cycle fatigue behavior of 18Cr-8Ni austenitic stainless steels with grains ranging from nano/ultrafine-size to coarse. In: *Materials Science and Engineering: A* 733 (2018), August, 128–136. http://dx.doi.org/10.1016/j.msea.2018.07.043. – DOI 10.1016/j.msea.2018.07.043

[43] Shin, Jong-Ho ; Kim, Young-Deak ; Lee, Jong-Wook: Effects of Grain Size on the Fatigue Properties in Cold-Expanded Austenitic HNSs. In: *Metals and Materials International* 24 (2018), Mai, Nr. 6, 1412–1421. http://dx.doi.org/10.1007/s12540-018-0127-2. – DOI 10.1007/s12540–018–0127–2

[44] Lucas, J. ; Gerberich, W.: Cyclic strain hardening of polygonal and acicular ferrite/bainite microstructures in microalloyed steels in the temperature range -150°C to 27°C. In: *International Journal of Fatigue* 7 (1985), Nr. 2, S. 117–125

[45] Seeger, Alfred ; Seeger, Alfred (Hrsg.): *Moderne Probleme Der Metallphysik*. Berlin, Germany : Springer, 2013

[46] Haasen, Peter: *Physikalische Metallkunde*. 3. Berlin, Germany : Springer, 2013

[47] Burkov, Andriy: *The hundred-page machine learning book the hundred-page machine learning book*. Andriy Burkov, 2019

[48] Peng, Junjie ; Jury, Elizabeth C. ; Dönnes, Pierre ; Ciurtin, Coziana: Machine learning techniques for personalised medicine approaches in immune-mediated chronic inflammatory diseases: Applications and challenges. In: *Front. Pharmacol.* 12 (2021), September, S. 720694

[49] Guido, Sarah ; Mueller, Andreas C.: *Introduction to machine learning with python*. Sebastopol, CA : O'Reilly Media, 2016

[50] Kelleher, John D. ; Namee, Brian M. ; D'Arcy, Aoife: *Fundamentals of machine learning for predictive data analytics*. London, England : MIT Press, 2015 (The MIT Press)

[51] Meiners, Wilhelm: *Direktes selektives Laser Sintern einkomponentiger metallischer Werkstoffe*, RWTH Aachen, Dissertation, 1999

[52] Antonau, Ihar ; Warnakulasuriya, Suneth ; Bletzinger, Kai-Uwe ; Bluhm, Fabio M. ; Hojjat, Majid ; Wüchner, Roland: Latest developments in node-based shape optimization using Vertex Morphing parameterization. In: *Struct. Multidiscipl. Optim.* 65 (2022), Juli, Nr. 7

[53] Gibson, Ian ; Rosen, David ; Stucker, Brent ; Khorasani, Mahyar: Direct Write Technologies. In: *Additive Manufacturing Technologies*. Cham : Springer International Publishing, 2021, S. 319–345

[54] Yadroitsev, Igor ; Yadroitsava, Ina ; Du Plessis, Anton ; MacDonald, Eric: *Fundamentals of Laser Powder Bed Fusion of metals*. Elsevier, 2021

[55] Dietrich, Kai: *Der Einfluss von Spurengasen und Lagerbedingungen auf der pulverbettbasierte Laser-Strahlschmelzen The influence of residual gases and storage conditions on laser powder bed fusion*. Duisburg, Duisburg University, PhD thesis, February 2021. – Available on request

[56] Sun, Zhongji ; Tan, Xipeng ; Tor, Shu B. ; Yeong, Wai Y.: Selective laser melting of stainless steel 316L with low porosity and high build rates. In: *Mater. Des.* 104 (2016), August, S. 197–204

[57] Krakhmalev, Pavel ; Fredriksson, Gunnel ; Svensson, Krister ; Yadroitsev, Igor ; Yadroitsava, Ina ; Thuvander, Mattias ; Peng, Ru: Microstructure, Solidification Texture, and Thermal Stability of 316 L Stainless Steel Manufactured by Laser Powder Bed Fusion. In: *Metals* 8 (2018), Nr. 8, S. 643. http://dx.doi.org/10.3390/met8080643. – DOI 10.3390/met8080643

[58] Lippold, John C.: *Welding Metallurgy and Weldability*. Nashville, TN : John Wiley & Sons, 2014

[59] Hooper, Paul A.: Melt pool temperature and cooling rates in laser powder bed fusion. In: *Additive Manufacturing* 22 (2018), S. 548–559. http://dx.doi.org/10.1016/j.addma.2018.05.032. – DOI 10.1016/j.addma.2018.05.032. – ISSN 22148604

[60] Yakout, Mostafa ; Elbestawi, M. A. ; Veldhuis, Stephen C.: Density and mechanical properties in selective laser melting of Invar 36 and stainless steel 316L. In: *Journal of Materials Processing Technology* 266 (2019), S. 397–420. http://dx.doi.org/10.1016/j.jmatprotec.2018.11.006. – DOI 10.1016/j.jmatprotec.2018.11.006. – ISSN 09240136

[61] Charmi, A ; Falkenberg, R ; Ávila, L ; Mohr, G ; Sommer, K ; Ulbricht, A ; Sprengel, M ; Saliwan Neumann, R ; Skrotzki, B ; Evans, A: Mechanical anisotropy of additively manufactured stainless steel 316L: An experimental and numerical study. In: *Mater. Sci. Eng. A Struct. Mater.* 799 (2021), Januar, Nr. 140154, S. 140154

[62] DebRoy, T ; Wei, H L. ; Zuback, J S. ; Mukherjee, T ; Elmer, J W. ; Milewski, J O. ; Beese, A M. ; Wilson-Heid, A ; De, A ; Zhang, W: Additive manufacturing of metallic components – Process, structure and properties. In: *Prog. Mater. Sci.* 92 (2018), März, S. 112–224

[63] Godec, Matjaž ; Zaefferer, Stefan ; Podgornik, Bojan ; Šinko, Mario ; Tchernychova, Elena: Quantitative multiscale correlative microstructure analysis of additive manufacturing of stainless steel 316L processed by selective laser melting. In: *Materials Characterization* 160 (2020), S. 110074. http://dx.doi.org/10.1016/j.matchar.2019.110074. – DOI 10.1016/j.matchar.2019.110074. – ISSN 10445803

[64] Nuland, T F W. ; Dommelen, J A W. ; Geers, M G D.: Microstructural modeling of anisotropic plasticity in large scale additively manufactured 316L stainless steel. In: *Mech. Mater.* 153 (2021), Februar, Nr. 103664, S. 103664

[65] Wang, Lu ; Zhang, Yanming ; Chia, Hou Y. ; Yan, Wentao: Mechanism of keyhole pore formation in metal additive manufacturing. In: *Npj Comput. Mater.* 8 (2022), Januar, Nr. 1

[66] Nudelis, Natan ; Mayr, Peter: A novel classification method for pores in laser powder bed fusion. In: *Metals (Basel)* 11 (2021), November, Nr. 12, S. 1912

[67] Tang, Ming ; Pistorius, P C.: Oxides, porosity and fatigue performance of AlSi10Mg parts produced by selective laser melting. In: *Int. J. Fatigue* 94 (2017), Januar, S. 192–201

[68] Solberg, Klas ; Guan, Shuai ; Razavi, Seyed Mohammad J. ; Welo, Torgeir ; Chan, Kang C. ; Berto, Filippo: Fatigue of additively manufactured 316L stainless steel: The influence of porosity and surface roughness. In: *Fatigue and Fracture of Engineering Materials and Structures* 42 (2019), Juli, Nr. 9, 2043–2052. http://dx.doi.org/10.1111/ffe.13077. – DOI 10.1111/ffe.13077

[69] Shrestha, Rakish ; Simsiriwong, Jutima ; Shamsaei, Nima ; Thompson, Scott M. ; Bian, Linkan: Effect of build orientation on the fatigue behavior of stainless steel 316L manufactured via a Laser-Powder Bed Fusion process. (2016)

[70] Fergani, O ; Bratli Wold, A ; Berto, F ; Brotan, V ; Bambach, M: Study of the effect of heat treatment on fatigue crack growth behaviour of 316L stainless steel produced by selective laser melting. In: *Fatigue Fract. Eng. Mater. Struct.* 41 (2018), Mai, Nr. 5, S. 1102–1119

[71] Kleszczynski, Stefan ; Ladewig, Alexander ; Friedberger, Katrin ; Jacobsmühlen, Joschka zur ; Merhof, Dorit ; Witt, Gerd: Position Dependency of Surface Roughness in Parts from Laser Beam Melting Systems. In: *Solid Freeform Fabrication 2015: Proceedings of the 26th Annual International* (2015), S. 360–370

[72] Yu, Cheng-Han ; Leicht, Alexander ; Peng, Ru L. ; Moverare, Johan: Low cycle fatigue of additively manufactured thin-walled stainless steel 316L. In: *Materials Science and Engineering: A* 821 (2021), S. 141598. http://dx.doi.org/10.1016/j.msea.2021.141598. – DOI 10.1016/j.msea.2021.141598. – ISSN 09215093

[73] Beard, William ; Lancaster, Robert ; Adams, Jack ; Buller, Dane: *Fatigue Performance of Additively Manufactured Stainless Steel 316L for Nuclear Applications*

[74] Pelegatti, Marco ; Lanzutti, Alex ; Salvati, Enrico ; Srnec Novak, Jelena ; Bona, Francesco de ; Benasciutti, Denis: Cyclic Plasticity and Low Cycle Fatigue of an AISI 316L Stainless Steel: Experimental Evaluation of Material Parameters for Durability Design. In: *Materials (Basel, Switzerland)* 14 (2021), Nr. 13. http://dx.doi.org/10.3390/ma14133588. – DOI 10.3390/ma14133588. – ISSN 1996–1944

[75] Kluczyński, Janusz ; Śnieżek, Lucjan ; Grzelak, Krzysztof ; Torzewski, Janusz ; Szachogłuchowicz, Ireneusz ; Oziębło, Artur ; Perkowski, Krzysztof ; Wachowski, Marcin ; Małek, Marcin: The Influence of Heat Treatment on Low Cycle Fatigue Properties of Selectively Laser Melted 316L Steel. In: *Materials (Basel, Switzerland)* 13 (2020), Nr. 24. http://dx.doi.org/10.3390/ma13245737. – DOI 10.3390/ma13245737. – ISSN 1996–1944

[76] Liang, Xiaoyu ; Hor, Anis ; Robert, Camille ; Salem, Mehdi ; Morel, Franck: Correlation between microstructure and cyclic behavior of 316L stainless steel obtained by Laser Powder Bed Fusion. In: *Fatigue Fract. Eng. Mater. Struct.* 45 (2022), Mai, Nr. 5, S. 1505–1520

[77] Shrestha, Rakish ; Simsiriwong, Jutima ; Shamsaei, Nima: Fatigue behavior of additive manufactured 316L stainless steel parts: Effects of layer orientation and surface roughness. In: *Addit. Manuf.* 28 (2019), August, S. 23–38

[78] Avanzini, Andrea: Fatigue behavior of additively manufactured stainless steel 316L. In: *Materials (Basel)* 16 (2022), Dezember, Nr. 1, S. 65

[79] Souza Neto, E A. ; Peric, D ; Owen, D R J.: *Computational methods for plasticity*. Hoboken, NJ : Wiley-Blackwell, 2008

[80] Liu, C Y. ; Tong, J D. ; Jiang, M G. ; Chen, Z W. ; Xu, G ; Liao, H B. ; Wang, P ; Wang, X Y. ; Xu, M ; Lao, C S.: Effect of scanning strategy on microstructure and mechanical properties of selective laser melted reduced activation ferritic/martensitic steel. In: *Mater. Sci. Eng. A Struct. Mater.* 766 (2019), Oktober, Nr. 138364, S. 138364

[81] Spierings, A.B. ; Starr, T.L. ; Wegener, K.: Fatigue performance of additive manufactured metallic parts. In: *Rapid Prototyping Journal* 19 (2013), März, Nr. 2, 88–94. http://dx.doi.org/10.1108/13552541311302932. – DOI 10.1108/13552541311302932

[82] Leuders, Stefan ; Lieneke, Tobias ; Lammers, Stefan ; Tröster, Thomas ; Niendorf, Thomas: On the fatigue properties of metals manufactured by selective laser melting – The role of ductility. In: *J. Mater. Res.* 29 (2014), September, Nr. 17, S. 1911–1919

[83] Mower, Todd M. ; Long, Michael J.: Mechanical behavior of additive manufactured, powder-bed laser-fused materials. In: *Mater. Sci. Eng. A Struct. Mater.* 651 (2016), Januar, S. 198–213

[84] Uhlmann, Eckart ; Fleck, Claudia ; Gerlitzky, Georg ; Faltin, Fabian: Dynamical Fatigue Behavior of Additive Manufactured Products For a Fundamental Life cycle Approach. In: *Procedia CIRP* 61 (2017), 588–593. http://dx.doi.org/10.1016/j.procir.2016.11.138. – DOI 10.1016/j.procir.2016.11.138

[85] Zhang, Meng ; Sun, Chen-Nan ; Zhang, Xiang ; Goh, Phoi C. ; Wei, Jun ; Hardacre, David ; Li, Hua: Fatigue and fracture behaviour of laser powder bed fusion stainless steel 316L: Influence of processing parameters. In: *Mater. Sci. Eng. A Struct. Mater.* 703 (2017), August, S. 251–261

[86] Zhang, Meng ; Sun, Chen-Nan ; Zhang, Xiang ; Goh, Phoi C. ; Wei, Jun ; Li, Hua ; Hardacre, David: Elucidating the Relations Between Monotonic and Fatigue Properties of Laser Powder Bed Fusion Stainless Steel 316L. In: *JOM* 70 (2018), Nr. 3, S. 390–395. http://dx.doi.org/10.1007/s11837-017-2640-z. – DOI 10.1007/s11837–017–2640–z. – ISSN 1047–4838

[87] Zhang, Dan: Effect of heat treatment on fatigue crack initiation of laser powder bed fusion stainless steel 316L. In: *MATEC Web Conf.* 179 (2018), S. 00001

[88] Blinn, Bastian ; Klein, Marcus ; Gläßner, Christopher ; Smaga, Marek ; Aurich, Jan ; Beck, Tilmann: An investigation of the microstructure and fatigue behavior of additively manufactured AISI 316L stainless steel with regard to the influence of heat treatment. In: *Metals (Basel)* 8 (2018), März, Nr. 4, S. 220

[89] Blinn, Bastian ; Ley, Maximilian ; Buschhorn, Nils ; Teutsch, Roman ; Beck, Tilmann: Investigation of the anisotropic fatigue behavior of additively manufactured structures made of AISI 316L with short-time procedures PhyBaLLIT and PhyBaLCHT. In: *Int. J. Fatigue* 124 (2019), Juli, S. 389–399

[90] Elangeswaran, Chola ; Cutolo, Antonio ; Muralidharan, Gokula K. ; Formanoir, Charlotte de ; Berto, Filippo ; Vanmeensel, Kim ; Van Hooreweder, Brecht: Effect of post-treatments on the fatigue behaviour of 316L stainless steel manufactured by laser powder bed fusion. In: *Int. J. Fatigue* 123 (2019), Februar, S. 31–39

[91] Shrestha, Rakish ; Simsiriwong, Jutima ; Shamsaei, Nima: Comparison of Rotating-Bending and Axial Fatigue Behaviors of LB-PBF 316L Stainless Steel, 2019, nn

[92] Wood, Paul ; Libura, Tomasz ; Kowalewski, Zbigniew L. ; Williams, Gavin ; Serjouei, Ahmad: Influences of horizontal and vertical build orientations and post-fabrication processes on the fatigue behavior of stainless steel 316L produced by selective laser melting. In: *Materials (Basel)* 12 (2019), Dezember, Nr. 24, S. 4203

[93] Zhang, Meng ; Sun, Chen-Nan ; Zhang, Xiang ; Goh, Phoi C. ; Wei, Jun ; Hardacre, David ; Li, Hua: High cycle fatigue life prediction of laser additive manufactured stainless steel: A machine learning approach. In: *Int. J. Fatigue* 128 (2019), November, Nr. 105194, S. 105194

[94] Blinn, Bastian ; Krebs, Florian ; Ley, Maximilian ; Teutsch, Roman ; Beck, Tilmann: Determination of the influence of a stress-relief heat treatment and additively manufactured surface on the fatigue behavior of selectively laser melted AISI 316L by using efficient short-time procedures. In: *Int. J. Fatigue* 131 (2020), Februar, Nr. 105301, S. 105301

[95] Elangeswaran, Chola ; Cutolo, Antonio ; Muralidharan, Gokula K. ; Vanmeensel, Kim ; Van Hooreweder, Brecht: Microstructural analysis and fatigue crack initiation modelling of additively manufactured 316L after different heat treatments. In: *Mater. Des.* 194 (2020), September, Nr. 108962, S. 108962

[96] Hatami, Sepehr ; Ma, Taoran ; Vuoristo, Taina ; Bertilsson, Jens ; Lyckfeldt, Ola: Fatigue Strength of 316 L Stainless Steel Manufactured by Selective Laser Melting. In: *Journal of Materials Engineering and Performance* 29 (2020), Mai, Nr. 5, 3183–3194. http://dx.doi.org/10.1007/s11665-020-04859-x. – DOI 10.1007/s11665–020–04859–x

[97] Kumar, Punit ; Jayaraj, R. ; Suryawanshi, J. ; Satwik, U. R. ; McKinnell, J. ; Ramamurty, U.: Fatigue strength of additively manufactured 316L austenitic stainless steel. In: *Acta Materialia* 199 (2020), S. 225–239. http://dx.doi.org/10.1016/j.actamat.2020.08.033. – DOI 10.1016/j.actamat.2020.08.033. – ISSN 13596454

[98] Afkhami, Shahriar ; Dabiri, Mohammad ; Piili, Heidi ; Björk, Timo: Effects of manufacturing parameters and mechanical post-processing on stainless steel 316L processed by laser powder bed fusion. In: *Materials Science and Engineering: A* 802 (2021), S. 140660. http://dx.doi.org/10.1016/j.msea.2020.140660. – DOI 10.1016/j.msea.2020.140660. – ISSN 09215093

[99] Gnanasekaran, Balachander ; Song, Jie ; Vasudevan, Vijay ; Fu, Yao: Corrosion fatigue characteristics of 316L stainless steel fabricated by laser powder bed fusion. In: *Metals (Basel)* 11 (2021), Juni, Nr. 7, S. 1046

[100] Kotzem, Daniel ; Kleszczynski, Stefan ; Stern, Felix ; Elspass, Arno ; Tenkamp, Jochen ; Witt, Gerd ; Walther, Frank: Impact of single structural voids on fatigue properties of AISI 316L manufactured by laser powder bed fusion. In: *Int. J. Fatigue* 148 (2021), Juli, Nr. 106207, S. 106207

[101] Lai, Wei-Jen ; Ojha, Avinesh ; Li, Ziang ; Engler-Pinto, Carlos ; Su, Xuming: Effect of residual stress on fatigue strength of 316L stainless steel produced by laser powder bed fusion process. In: *Prog. Addit. Manuf.* 6 (2021), August, Nr. 3, S. 375–383

[102] Wang, Yingyu ; Wang, Wenxuan ; Susmel, Luca: Constant/variable amplitude multiaxial notch fatigue of additively manufactured AISI 316L. In: *Int. J. Fatigue* 152 (2021), November, Nr. 106412, S. 106412

[103] Wang, Yingyu ; Su, Zhenli: Effect of micro-defects on fatigue lifetime of additive manufactured 316L stainless steel under multiaxial loading. In: *Theor. Appl. Fract. Mech.* 111 (2021), Februar, Nr. 102849, S. 102849

[104] Cui, Luqing ; Jiang, Fuqing ; Deng, Dunyong ; Xin, Tongzheng ; Sun, Xiaoyu ; Mousavian, Reza T. ; Peng, Ru L. ; Yang, Zhiqing ; Moverare, Johan: Cyclic response of additive manufactured 316L stainless steel: The role of cell structures. In: *Scr. Mater.* 205 (2021), Dezember, Nr. 114190, S. 114190

[105] Kedziora, Slawomir ; Decker, Thierry ; Museyibov, Elvin ; Morbach, Julian ; Hohmann, Steven ; Huwer, Adrian ; Wahl, Michael: Strength properties of 316L and 17-4 PH stainless steel produced with additive manufacturing. In: *Materials (Basel)* 15 (2022), September, Nr. 18, S. 6278

[106] Rautio, Timo ; Jaskari, Matias ; Gundgire, Tejas ; Iso-Junno, Terho ; Vippola, Minnamari ; Järvenpää, Antti: The effect of severe shot peening on fatigue life of laser powder bed fusion manufactured 316L stainless steel. In: *Materials (Basel)* 15 (2022), Mai, Nr. 10, S. 3517

[107] Zulić, Sanin ; Rostohar, Danijela ; Kaufman, Jan ; Pathak, Sunil ; Kopeček, Jaromir ; Böhm, Marek ; Brajer, Jan ; Mocek, Tomáš: Fatigue life enhancement of additive manufactured 316l stainless steel by LSP using a DPSS laser system. In: *Surf. Eng.* 38 (2022), Februar, Nr. 2, S. 183–190

[108] Riemer, A ; Leuders, S ; Thöne, M ; Richard, H A. ; Tröster, T ; Niendorf, T: On the fatigue crack growth behavior in 316L stainless steel manufactured by selective laser melting. In: *Eng. Fract. Mech.* 120 (2014), April, S. 15–25

[109] Andreau, Olivier ; Pessard, Etienne ; Koutiri, Imade ; Penot, Jean-Daniel ; Dupuy, Corinne ; Saintier, Nicolas ; Peyre, Patrice: A competition between the contour and hatching zones on the high cycle fatigue behaviour of a 316L stainless steel: Analyzed using X-ray computed tomography. In: *Mater. Sci. Eng. A Struct. Mater.* 757 (2019), Mai, S. 146–159

[110] Cao, Yinfeng ; Moumni, Ziad ; Zhu, Jihong ; Zhang, Yahui ; You, Yajun ; Zhang, Weihong: Comparative investigation of the fatigue limit of additive-manufactured and rolled 316 steel based on self-heating approach. In: *Eng. Fract. Mech.* 223 (2020), Januar, Nr. 106746, S. 106746

[111] Andreau, Olivier ; Pessard, Etienne ; Koutiri, Imade ; Peyre, Patrice ; Saintier, Nicolas: Influence of the position and size of various deterministic defects on the high cycle fatigue resistance of a 316L steel manufactured by laser powder bed fusion. In: *Int. J. Fatigue* 143 (2021), Februar, Nr. 105930, S. 105930

[112] Zeng, Fanyu ; Yang, Yongtai ; Qian, Guian: Fatigue properties and S-N curve estimating of 316L stainless steel prepared by SLM. In: *Int. J. Fatigue* 162 (2022), September, Nr. 106946, S. 106946

[113] Voloskov, Boris ; Evlashin, Stanislav ; Dagesyan, Sarkis ; Abaimov, Sergey ; Akhatov, Iskander ; Sergeichev, Ivan: Very high cycle fatigue behavior of additively manufactured 316L stainless steel. In: *Materials (Basel)* 13 (2020), Juli, Nr. 15, S. 3293

[114] Voloskov, Boris ; Mishurova, Tatiana ; Evlashin, Stanislav ; Akhatov, Iskander ; Bruno, Giovanni ; Sergeichev, Ivan: Artificial defects in 316L stainless steel produced by laser powder bed fusion: Printability, microstructure, and effects on the very-high-cycle fatigue behavior. In: *Adv. Eng. Mater.* 25 (2023), Januar, Nr. 1, S. 2200831

[115] Diller, Johannes ; Rier, Lukas ; Siebert, Dorina ; Radlbeck, Christina ; Krafft, Frank ; Mensinger, Martin: Cyclic plastic material behavior of 316L manufactured by laser powder bed fusion (PBF-LB/M). In: *Materials Characterization* 191 (2022), 112153. `http://dx.doi.org/10.1016/j.matchar.2022.112153`. – DOI 10.1016/j.matchar.2022.112153. – ISSN 10445803

[116] Diller, Johannes ; Siebert, Dorina ; Radlbeck, Christina ; Mensinger, Martin: PBF-LB/M/316L vs. hot-rolled 316L – comparison of cyclic plastic material behavior. In: *Procedia Struct. Integr.* 42 (2022), S. 58–65

[117] Diller, Johannes ; Blankenhagen, Jakob ; Siebert, Dorina ; Radlbeck, Christina ; Mensinger, Martin: Combined effect of surface treatment and heat treatment on the fatigue properties of AISI 316L, manufactured by powder bed fusion of metals using a laser (PBF-LB/M). In: *Int. J. Fatigue* 178 (2024), Januar, Nr. 108025, S. 108025

[118] Sanaei, Niloofar ; Fatemi, Ali: Analysis of the effect of surface roughness on fatigue performance of powder bed fusion additive manufactured metals. In: *Theoretical and Applied Fracture Mechanics* 108 (2020), August, 102638. http://dx.doi.org/10.1016/j.tafmec.2020.102638. – DOI 10.1016/j.tafmec.2020.102638

[119] Diller, Johannes ; Radlbeck, Christina ; Siebert, Dorina ; Blankenhagen, Jakob ; Gubetini, Drilon ; Oberhaidinger, Florian ; Mensinger, Martin: Additive manufacturing in construction—implementing powder-bed fusion of metals using a laser (PBF-LB/M) and shape optimization in the construction design process. In: *INALCO 2023*. Basel Switzerland : MDPI, September 2023, S. nn

[120] Li, Jun ; Yang, Zhengmao ; Qian, Guian ; Berto, Filippo: Machine learning based very-high-cycle fatigue life prediction of Ti-6Al-4V alloy fabricated by selective laser melting. In: *Int. J. Fatigue* 158 (2022), Mai, Nr. 106764, S. 106764

[121] Cersullo, Nicola ; Mardaras, Jon ; Emile, Philippe ; Nickel, Katja ; Holzinger, Vitus ; Hühne, Christian: Effect of Internal Defects on the Fatigue Behavior of Additive Manufactured Metal Components: A Comparison between Ti6Al4V and Inconel 718. In: *Materials* 15 (2022), Oktober, Nr. 19, 6882. http://dx.doi.org/10.3390/ma15196882. – DOI 10.3390/ma15196882

[122] Galjaard, S. ; Hofman, S. ; Perry, N. ; Ren, S.: Optimizing Structural Building Elements in Metal by using Additive Manufacturing. In: *Proceedings of the International Association for Shell and Spatial Structures (IASS) Symposium 2015*. Amsterdam, The Netherlands : Futurevisions, August 17-20 2015, S. 1–12

[123] *eos.info*. https://www.eos.info/04_consulting_service_software/software/pdf_software/cs_m_aerospace_mtu_en_web.pdf, 2018. – [Accessed 29-12-2023]

A Appendix

A.1 List of supervised student research projects

During this research, the author of this thesis supervised numerous student research projects in both content and organization at the Chair of Metal Structures of the Technical University of Munich. Insights gained collaboratively have been integrated into this dissertation and the publications discussed in Chapter 7. The author expresses profound gratitude to the students for their valuable contributions, discussions, and the innovative ideas developed through this collaborative effort.

Table A.1: *Supervised theses of the author during the time at the chair of metal structures; BT: Bachelor's thesis, MT: Master's thesis*

Name	Year	Title
Korbinian Hausmann (BT)	2020	Prozessverständnis und mechanische Eigenschaften von AlSi10Mg hergestellt durch pulverbettbasiertes Laserstrahlschmelzen
Johannes Reichlmair (BT)	2020	Einfluss unterschiedlicher T6 Wärmebehandlungsparameter auf die Werkstoffeigenschaften von additiv gefertigten Bauteilen aus AlSi10Mg
Magdalena Fuchs (BT)	2020	Schwingungsbewertung von Verbunddecken am Beispiel eines Schulneubaus
Michael Winkler (BT)	2020	Erstellung eines Thermographiemessstandes zur Messung von Abkühlraten in additiv (LPBF) gefertigtem AlSi10Mg
Julia Suchoverchow (BT)	2020	Untersuchung und Entwicklung von Eigenspannungsmessmethoden für die Anwendung in der additiven Fertigung
Korbinian Hausmann (BT)	2020	Prozessverständnis und mechanische Eigenschaften von AlSi10Mg hergestellt durch pulverbettbasiertes Laserstrahlschmelzen
Andreas Burkart (BT)	2020	Untersuchung von Träger-Stützenanschlüssen Vergleich Komponentenmethode mit Finite Elemente Berechnungen
Oliver von Eitzen Toni (BT)	2022	Kohlenstoffarme Stahlerzeugungstechnologien zur Förderung eines umweltfreundlichen Wandels der Stahlindustrie
Felix Schmiz (BT)	2022	Analyse der Wirtschaftlichkeit und Nachhaltigkeit des pulverbettbasierten Laserstrahlschmelzprozesses PBF-LB/M für das Bauwesen
Kilian Lachner (BT)	2024	Wirtschaftlichkeitsanalyse - Vergleich zwischen Laser-DED und herkömmlichen Schweißverfahren
Lukas Rier (MT)	2021	Dehnungsgesteuerte Versuche zur Bestimmung von Materialparametern von additiv gefertigtem austenitischen Stahl
Ludwig Siebert (MT)	2022	Defektanalyse µ-CT-gescannter additiv gefertigter Ermüdungsproben unter Anwendung von Machine Learning
Jakob Blankenhagen (MT)	2022	Einfluss der Oberflächenrauheit auf die Ermüdungseigenschaften von 316L, hergestellt durch das pulverbettbasierte Laserstrahlschmelzen von Metallen
Nadine Wallner (MT)	2022	Extraterrestrisches Bauen - Von der Planung bis zur Ausführung einer Forschungsstation auf dem Mars mittels additiver Fertigung
Michael Winkler (MT)	2023	Estimation of the Fatigue Limit of Additively Manufactured 316L Stainless Steel (PBF-LBM316L) Based on Surface Defects Extracted from μ-CT Scans
Julia Suchoverchow (MT)	2023	Gitterstrukturen: Numerische Untersuchung der mechanischen Eigenschaften in Bezug auf Dämpfung von Erdbeben
Anton Sauter (MT)	2023	Ermüdungsrisswachstumsverhalten von additiv gefertigtem AISI 316L mit Visualisierung des Dehnungsfeldes an der Rissspitze mittels digitaler Bildkorrelation

A.2 Publications of the author

The publications of the author, which were elaborated in the course of writing this dissertation, are listed below in chronological order.

Publications embedded into this dissertation

- **Diller, J.**; Auer, U.; Radlbeck, C.; Mensinger, M.; Krafft, F.: Einfluss der Abkühlrate auf die mechanischen Eigenschaften von additiv gefertigten Zugproben aus 316L. Stahlbau 89 (2020), H. 12, pp. 970 – 980, https://doi.org/10.1002/stab.202000034 . **Publication P1 of this dissertation.**

- **Diller, J.**; Rier, L.; Siebert, D.; Radlbeck, C.; Krafft, F.; Mensinger, M.:Cyclic plastic material behavior of 316L manufactured by laser powder bed fusion (PBF-LB/M). Materials Characterization 191 (2022), 112153, https://doi.org/10.1016/j .matchar.2022.112153 . **Publication P2 of this dissertation.**

- **Diller, J.**; Siebert, D.; Radlbeck, C.; Mensinger, M.: PBF-LB/M/316L vs. hot-rolled 316L – comparison of cyclic plastic material behavior. Procedia Structural Integrity 42 (2022), pp. 58-65, 10.1016/j .prostr.2022.12.006. **Publication P3 of this dissertation.**

- **Diller, J.**; Blankenhagen, J.; Siebert, D.; Radlbeck, C.; Mensinger, M.: Combined effect of surface treatment and heat treatment on the fatigue properties of AISI 316L, manufactured by powder bed fusion of metals using a laser (PBF-LB/M). International Journal of Fatigue 178 (2024), pp. 108025, https://doi.org/10.1016/j.ijfatigue.2023.108025 **Publication P4 of this dissertation.**

- **Diller, J**; Siebert, L.; Winkler, M.; Siebert, D.; Blankenhagen, J.; Wenzler, D.; Radlbeck, C.; Mensinger, M.; An integrated approach for detecting and classifying pores and surface topology for fatigue assessment in PBF-LB/M-manufactured 316L using μCT and machine learning algorithms. Fatigue and Fracture of Engineering Materials and Structures, 2024;47:3392–3407 https://doi.org/10.1111/ffe.14375 . **Publication P5 of this dissertation.**

- **Diller, J.**; Radlbeck, C.; Siebert, D.; Blankenhagen, J.; Gubetini, D.; Oberhaidinger, F.; Mensinger, M.: Additive Manufacturing in Construction—Implementing Powder-Bed Fusion of Metals Using a Laser (PBF-LB/M) and Shape Optimization in the Construction Design Process. Eng. Proc. 2023, 43, 10. https://doi.org/10.3390/engproc2023043010 . **Publication P6 of this dissertation.**

Other publications

- Dietrich, K.; **Diller, J.**; Dubiez-Le Goff, S.; Bauer, D.: The influence of oxygen on the chemical composition and mechanical properties of Ti-6Al-4V during laser powder bed fusion (L-PBF). Additive Manufacturing 32 (2020), 100980, https://doi.org/10.1016/j .addma.2019.100980 .

- **Diller, J.**; Radlbeck, C.; Mensinger, M.: Einfluss der Abkühlrate auf das Korngefüge von Bauteilen aus austenitischem Edelstahl, hergestellt durch pulverbettbasiertes Laserstrahlschmelzen (LPBF). Conference, DASt-Kolloqium (2020)

- Ghantasala, A.; **Diller, J.**; Geiser, A.; Wenzler, D.; Siebert, D.; Radlbeck, C.; Wuechner, R.; Mensinger, M.; Bletzinger, K.-U.: Node-Based Shape Optimization and Mechanical Test Validation of Complex Metal Components and Support Structures, Manufactured by Laser Powder Bed Fusion. Advances in Manufacturing, Production Management and Process Control (2021), pp. 10 – 17, doi:10.1007/978-3-030-80462-6 _2.

- Siebert, D.; Radlbeck, C.; Mensinger, M. **Diller, J.**: Influence of alloy and weld angle on the fatigue performance of aluminum structures. Conference, LCF9 - Ninth International Conference on Low Cycle Fatigue (2022), pp. 53-58, doi:https://doi.org/10.48447/LCF9-2022-012 .

- Kloft, H.; Dörfler, K.; Bährens, M.; Dielemans, G.; **Diller, J**.; Dörrie, R.; Gantner, S.; Hensel, J.; Keune, A.; Lowke, D.; Mai, I.; Mainka, J.; Pla-czek, G.; Saile, B.; Scharf-Wildenhain, R.; Schwerdtner, P.; Kock, S.; Siebert, D.; Talke, D.; Wenzler, D. (2022) Die Forschungsinfrastruktur des SFB TRR 277 AMC Additive Fertigung im Bauwesen. Bautechnik 99, H. 10, S. 758–773. https://doi.org/10.1002/bate.202200076
- Wenzler, D.L.; Bergmeier, K.; Baehr, S.; **Diller, J.**; Zaeh, M.F.: A Novel Methodology for the Thermographic Cooling Rate Measurement during Powder Bed Fusion of Metals Using a Laser Beam. Integrating Materials and Manufacturing Innovation 12, 41–51 (2023). https://doi.org/10.1007/s40192-023-00291-w
- Panzer, H; **Diller, J.**; Ehrenfels, F.; Brandt, J.; Zaeh, M. F.: Experimental investigation of process parameter variations on the microstructure and failure behavior of IN718 structures in PBF-LB/M. Journal of Laser Applications 36 (2024), 012015. https://doi.org/10.2351/7.0001232
- Goetz, D.; **Diller, J.**; Achatz, K.; Zaeh, M. F.: Shrink line impact on the fatigue resistance of Inconel 718 parts manufactured by powder bed fusion of metals using a laser beam. Journal of Manufacturing Processes 115 (2024), pp. 481-490, https://doi.org/10.1016/j.jmapro.2024.02.030

A.2.1 Publication 1: Einfluss der Abkühlrate auf die mechanischen Eigenschaften von additiv gefertigtem 316L

Reproduced from:

Stahlbau 89 (2020) 12, pp. 970 – 980
Weblink: https://doi.org/10.1002/stab.202000034

with the permission of Wiley and Sons.

Ernst & Sohn
A Wiley Brand

ECCS
CECM
E K S

European Steel Design Awards (ESDA) 2021

Steel Construction – Special Issue

Steel is recognized for its high potential in terms of strength, durability, design flexibility, adaptability, recyclability and reusability. Steel is also the perfect material for reaching a circular economy while leaving the necessary room for creativity in design.

The **European Steel Design Awards** (ESDA) are given by the European Convention for Constructional Steelwork (ECCS) every two years to encourage the creative and outstanding use of steel in architecture and construction. The awards are dedicated to the owner, the general contractor, the architects, the engineers and the steelwork contractors of each project. An ECCS International Jury will select the projects to be awarded in all categories, except for the Public Award, which will be selected by public vote online.

Ernst & Sohn will publish the special issue „**European Steel Design Awards 2021**“ in November 2021. If you are interested in presenting your company in this special issue, feel free to contact us. Additionally have set up a website where you can find all the information about the European Steel Design Award, including the nominees, the jury, the award ceremony and the announcement of the winner in November 2021.

prelim. fig.

November 2021 · 100 pages
English

Order-No.: 5489 0121 **€ 27,10***

Available for pre-order.

CONTACT
Dominique Riedel
+49 (0)30 470 31-252
dominique.riedel@wiley.com
www.ernst-und-sohn.de/esda-2021

* All journal prices are net-prices exclusive of VAT but inclusive postage and handling charges.

DOI: 10.1002/stab.202000034

Johannes Diller, Ulrich Auer, Christina Radlbeck, Martin Mensinger, Frank Krafft

AUFSATZ

Einfluss der Abkühlrate auf die mechanischen Eigenschaften von additiv gefertigten Zugproben aus 316L

Ernst & Sohn Nachwuchspreis bester Vortrag Münchener Stahlbautage 2019

Das pulverbettbasierte Laserstrahlschmelzen (LPBF) ist ein additiver Fertigungsprozess, mit dem steifigkeitsoptimierte Bauteile gewichtsreduziert gefertigt werden können. Die mechanischen Eigenschaften sind vergleichbar mit denen von gegossenen Bauteilen, im Idealfall sogar mit geschmiedeten. In der Luft- und Raumfahrtbranche sowie im Automotive-Bereich und Medizinsektor wird die additive Fertigung bereits eingesetzt. Für sicherheitsrelevante Bauteile wird jedoch die additive Fertigung bisher nur selten verwendet. Dies ist auf die unzuverlässige Reproduzierbarkeit der mechanischen Eigenschaften zurückzuführen. Großer Forschungsbedarf besteht bspw. bei der Verknüpfung von LPBF-Produktionsparametern mit zuverlässigen Produktionsparametern. In diesem Bericht wird der Zusammenhang zwischen Abkühlraten im LPBF-Prozess und den resultierenden mechanischen Eigenschaften von 316L (1.4404) untersucht. Zu diesem Zweck wurden unterschiedliche Probengeometrien additiv gefertigt und die jeweiligen Abkühlraten in situ mittels Thermografie erfasst. Anschließend wurden Zugversuche und metallografische Untersuchungen durchgeführt. Je nach Geometrie der Zugproben konnten verschiedene Abkühlraten nachgewiesen werden, die schlussendlich zu unterschiedlichen Zugfestigkeiten führten.

Stichworte additive Fertigung; pulverbettbasiertes Laserstrahlschmelzen (LPBF); Abkühlrate; 316L (1.4404)

Effect of cooling rate on the mechanical properties of 316L tensile specimen, manufactured by Laser Powder Bed Fusion
Laser-Powder Bed Fusion (LPBF) is an additive manufacturing process, which allows weight savings of components through structural optimization without loss of stiffness. The mechanical properties are comparable with casted and – under ideal conditions – even with forged components. In the aerospace industry, as well as in the automotive and medical sector, LPBF is already applied. However, LPBF has only been used for components which are not safety-related. This is mainly due to the unreliable reproducibility of the mechanical properties of this process. Research has to be executed to find correlations between LPBF-parameters and reliable product properties. This report investigates the relationship between cooling rates in the LPBF process and the resulting mechanical properties of 316L (1.4404). For this purpose, different sample geometries were manufactured. The respective cooling rates were measured by in-situ-thermography. After that, tensile tests and metallurgical investigations were performed. Depending on the geometry, different cooling rates were observed, which finally led to different tensile strength results.

Keywords additive manufacturing; Laser Powder-Bed Fusion (LPBF); cooling rate; 316L (1.4404)

1 Pulverbettbasierter Laserstrahlschmelzprozess und Einflussparameter

Das pulverbettbasierte Laserstrahlschmelzen (LPBF) erfreut sich aufgrund des hohen Grads an Flexibilität und seiner Möglichkeit, strukturoptimierte Komponenten herzustellen, großer Beliebtheit. Im Prozess wird zunächst ein 3D-CAD-Modell in Schichten von 20 µm bis 100 µm aufgeteilt. Für den schichtweisen Aufbau des Bauteils trägt die Maschine eine gleichmäßige Pulverschicht mit definierter Schichtdicke auf eine materialverwandte Bauplattform auf. Anschließend belichtet der Laser die zu verfestigenden Regionen der aktuellen Schicht. Dem folgt ein erneuter Pulverauftrag. Dieser Vorgang wird so lange fortgeführt, bis das Bauteil vollends aufgebaut ist (schematisch in Bild 1) [1].

LPBF ermöglicht es, komplexe Strukturen herzustellen, die mit konventionellen Fertigungsmethoden nur sehr schwer oder mit hohen Kosten zu fertigen wären. Der entscheidende Grund, weshalb aktuell kaum sicherheitsrelevante LPBF-Bauteile gefertigt werden, ist jedoch die unzuverlässige Reproduzierbarkeit [2]. Dies ist hauptsächlich auf die fehlende Korrelation zwischen LPBF-Produktionsparametern und resultierenden Produkteigenschaften zurückzuführen.

Laserparameter werden bisher materialabhängig eingestellt. Die Geometrie des Bauteils wird dabei nicht be-

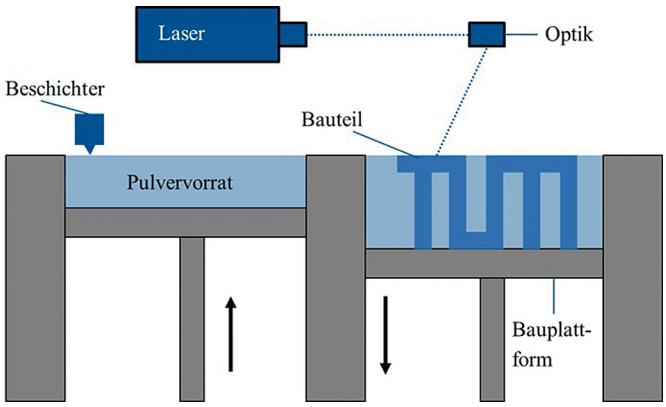

Bild 1 Grundsätzliches Funktionsprinzip des pulverbettbasierten Laserstrahlschmelzens
Basic principle of laser-powder bed fusion

rücksichtigt. Laserparameter haben jedoch einen entscheidenden Einfluss auf die Abkühlrate. Diese beeinflusst die Kristallisationsgeschwindigkeit und somit die Korngröße. Unterschiedliche Korngrößen können wiederum zu veränderten mechanischen Eigenschaften führen [3].

2 Einflussparameter beim LPBF-Prozess

Ziel dieser Untersuchung ist es, die Korrelation zwischen Abkühlrate und mechanischen Eigenschaften bei verschiedenen Geometrien von additiv gefertigten Zugproben zu untersuchen. Es wird dafür der Prozess von der Emission des Lasers bis zur Verfestigung des Materials kurz erläutert.

2.1 Energiedichte

Der Energieeintrag des Lasers in das Pulver ist mit folgender Gl. (1) definiert [4]:

$$E = \frac{P}{h \cdot v_s \cdot t} \left[\frac{\mathrm{J}}{\mathrm{mm}^3} \right] \tag{1}$$

Dabei ist P die Laserleistung in W, h der Spurabstand des Lasers in mm, v_s die Scangeschwindigkeit in mm/s sowie t die Schichtdickte des aufgetragenen Pulvers in mm. Dieser Energieeintrag resultiert in einer Wärmeleitung und führt damit zu den Festigkeitseigenschaften des Materials im Pulverbett.

2.2 Wärmeleitung

Die Wärmeleitung im Pulverbett kann mit folgender Gl. (2) im stationären Zustand beschrieben werden [5]:

$$\rho c \cdot \frac{\partial T}{\partial t} = \nabla \left(k_e \nabla T \right) + g\left(x, y, z\right) \tag{2}$$

Dabei ist ρ die Dichte in g/mm^3, c die spezifische Wärmekapazität eines perfekt dichten Materials in J/K, k_e die thermische Leitfähigkeit des Pulverbetts in W/(m · K), $g(x, y, z)$ die Wärmefunktion der aufgeschmolzenen Fläche im Pulverbett durch den Laser, T die Temperatur in K und t die Zeit in s.

Da die thermische Leitfähigkeit des Pulverbetts aufgrund der Partikeldichte nicht als homogen angenommen werden kann, wird k_e mit folgender Gl. (3) beschrieben [5]:

$$k_e = \frac{\mu k_s}{1 + \Phi \frac{k_s}{k_g}} \tag{3}$$

Dabei ist k_s die Leitfähigkeit des Festmaterials in W/(m · K), k_g die Leitfähigkeit von Luft in W/(m · K), $\mu = \frac{\rho}{\rho_s}$ der Anteil des Festmaterials im Pulverbett sowie Φ ein empirischer Wert, beziffert mit $0{,}02 \cdot 10^{2(0{,}7-\mu)}$. Es ist zu erwähnen, dass der Wärmeleitungskoeffizient an der Grenzfläche zwischen Schmelzbad und Pulver zehnmal kleiner ist. Folglich kann davon ausgegangen werden, dass die Wärmeleitung in das nicht aufzuschmelzende Pulver vernachlässigbar klein ist [1].

2.3 Abkühlrate

Die aus der Wärmeleitung resultierende Abkühlrate wird mit der Exponentialfunktion nach Newton (Gl. (4)) beschrieben und ist allgemeingültig [6].

$$T\left(t\right) = T_s + \left(T_b - T_s\right) \cdot e^{-\mathrm{f} \cdot \mathrm{t}} \tag{4}$$

Dabei ist T_s die Umgebungstemperatur in °C, T_b die Starttemperatur in °C sowie f der Abkühlfaktor und t die Zeit in s. Die Veränderung der Laserparameter verursacht unterschiedliche Temperaturgradienten und damit auch unterschiedliche Abkühlraten [5]. Wenn die aufgeschmolzene Fläche größer ist, erwärmt sich diese langsamer als kleinere Flächen. Da der Laserstrahl jedoch gepulst einzelne Punkte hintereinander aufschmilzt, entsteht nur eine lokale Erwärmung mit gleicher Fläche. Wenn die Wärme durch den Laserstrahl in das aufgeschmolzene Material eingeführt ist, hat diese bei einer größeren Fläche die Möglichkeit, sich schneller auszubreiten. Die Folge ist eine höhere Abkühlrate, da der Wärmestrom höher ist [1]. Die Wärmeleitfähigkeit ist demnach also proportional zur Fläche. Für eine größere aufzuschmelzende Fläche ist auch eine längere Belichtungszeit notwendig. Dies führt zu höheren Temperaturgradienten und könnte in höheren Eigenspannungen resultieren [3].

2.4 Hall-Petch-Beziehung

Je höher die Abkühlrate ist, desto schneller erstarrt das Material, wodurch das Kornwachstum verhindert wird [7]. Somit entstehen sehr kleine Körner im Gefüge. Eine Möglichkeit, das Gefüge mit der Streckgrenze zu verknüpfen, ist die Hall-Petch-Beziehung. Diese beschreibt die quantitative Abhängigkeit der Streckgrenze $R_{p0.2}$ (σ_y) von der Korngröße d_k. Die Gleichung (Gl. (5)) lautet wie folgt [7]:

$$\sigma_y = \sigma_o + \frac{K}{\sqrt{d_k}} \tag{5}$$

Dabei ist σ_y die Streckgrenze in N/mm^2, σ_o die maximale Schubspannung eines Einkristalls, um Versetzungsbewegungen zu erzeugen, in N/mm^2, der Korngrenzwiderstand K eine Materialkonstante in MPa$\sqrt{\mathrm{mm}}$ sowie d_k die mittlere Korngröße in mm.

Mit kleiner werdender Korngröße erhöht sich die Anzahl der Korngrenzen. Durch die vielen Korngrenzen ist eine erhöhte Spannung notwendig, um eine Versetzungsbewegung von Korn zu Korn zu erzeugen.

Bild 2 stellt eine schematische Versetzungsbehinderung an der Korngrenze zweier Körner dar. Sobald die maxi-

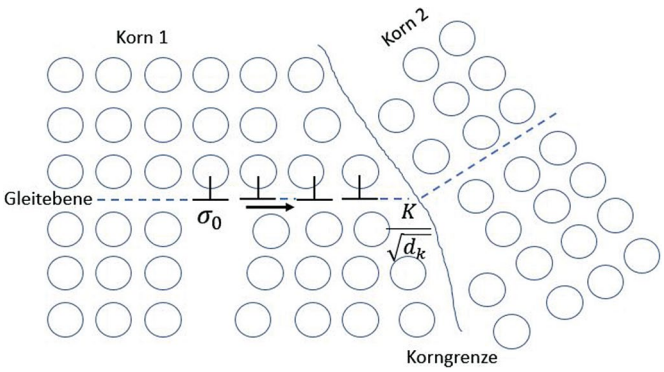

Bild 2 Schematische Darstellung einer Versetzungsbehinderung an Korngrenzen zweier Körner nach [7]
Schematic representation of dislocation impediment at grain boundaries of two grains according to [7]

male Schubspannung σ_0 der Einkristalle überwunden wurde, entsteht im Anschluss eine Aufstauung der in einem Korn bereits versetzten Atome. Die Gleitebenen im Nachbarkorn weisen eine andere Orientierung auf und sind für gewöhnlich nicht parallel zueinander. Die aufgestauten Versetzungen an der Korngrenze üben eine Rückspannung auf nachfolgende Versetzungen aus und die Streckgrenze wird somit erhöht [7].

2.5 Stand der Technik

In [8] wurden Abkühlraten im Schmelzbad aus Hochgeschwindigkeitsaufnahmen des Schmelzbads untersucht. Die Abkühlrate wurde dabei jedoch nicht mit Infrarotkameras ermittelt, sondern nachträglich berechnet. Des Weiteren wurden nur einzelne Schweißbahnen hergestellt.

Ein vielversprechender Ansatz wurde 1984 von [9] untersucht. Dort wurde mittels Laserschweißen und Thermoelementen die Abkühlrate bestimmt und eine Korrelation zwischen Abkühlrate und Korngröße hergestellt. Es wird jedoch auch erwähnt, dass zu dem Zeitpunkt die Messmethoden noch nicht ausreichend waren, um die hohen Abkühlraten zu messen. Die Abkühlrate konnte daher nur mithilfe der Korngröße extrapoliert werden.

In [10] wurde mit einer statistischen Versuchsplanung der Einfluss der Laserparameter untersucht. Dabei wurden Laserleistung, Spurabstand sowie Aufbaurichtung variiert. Es wurde festgestellt, dass die Laserleistung die Bruchdehnung verändert, aber keinen Einfluss auf die Streckgrenze hat. Korngrößen wurden dabei jedoch nicht untersucht.

3 Herstellung von Probekörpern

Für diese Studie wurden additiv gefertigte Bauteile aus austenitischem Stahl 316L (1.4404) [11] hergestellt. Die Korngrößenverteilung liegt zwischen 20 µm und 63 µm. Die chemische Zusammensetzung des Materials ist in Tab. 1 dargestellt.

Die Probekörper (PK) wurden auf einer EOS M270 mit einem 200 W Yb:YAG-Laser hergestellt. Als Inertgas wurde in der Kammer Argon 6.0 verwendet. Das entsprechende CAD-Modell besteht aus insgesamt acht Probekörpern, welche in Bild 3 dargestellt sind. Es wurden drei unterschiedlich große Zugprobengeometrien (PK 1–PK 5) nach [10] sowie zwei Würfel (PK4, PK8) mit $10 \times 10 \times 10$ mm^3 gefertigt.

Tab. 1 Chemische Zusammensetzung in Gewichts-% des Stahlpulvers des 316L laut Hersteller [12]
Chemical composition in wt-% of the steel powder (316L) according to the manufacturer [12]

Fe	Ni	Cr	Mn	Si	Mo	C
Bal.	12,0–14,0	16,0–18,0	max. 0,2	0,5–1,0	2,0–3,0	max. 0,03

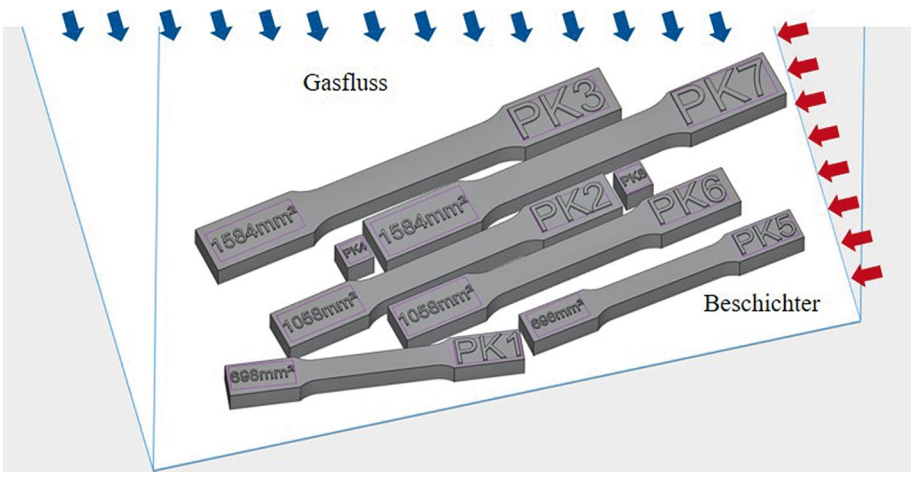

Bild 3 Probekörper und Lage auf der Bauplattform sowie Größe der aufgeschmolzenen Flächen
Specimen and position on the building platform as well as size of the melted areas

Tab. 2 Laserparameter (inner solid) der hergestellten Probekörper
Laser parameters (inner solid) of the manufactured specimens

Probekörper [–]	Laserleistung [W]	Scangeschwindigkeit [mm/s]	Spurabstand [µm]	Energiedichte [J/mm³]	Schichtdicke [µm]
1, 2, 3, 4	175	750	90	129,6	20
5, 6, 7, 8	175	1000	90	97,2	20

Tab. 2 zeigt die Laserparameter der jeweiligen Zugproben mit einer Querschnittsfläche von 12 (PK1,5), 24 (PK2,6) und 50 (PK3,7) mm^2.

Die Aufbaurichtung hat einen hohen Einfluss auf die mechanischen Eigenschaften. Wird eine Probe vertikal aufgebaut, ist eine niedrigere Festigkeit zu erwarten, da die Wärmeabfuhr auf eine kleinere Fläche wirkt, somit langsamer abläuft und so gröbere Körner liefert. Das Materialverhalten ist entlang der Probenachse inhomogen [1]. Für die vorliegende Studie wurden die Proben daher horizontal hergestellt.

Die Proben wurden ohne Wärmebehandlung mittels einer Bandsäge von der Bauplatte getrennt. Eine Wärmebehandlung könnte je nach Temperatur und Haltezeit in einem veränderten Gefüge und damit auch veränderten mechanischen Eigenschaften resultieren [7]. Da diese Studie den Auftakt eines größeren DFG-Forschungsprojekts darstellt, wurde dieser Fertigungsschritt allerdings noch bewusst vernachlässigt. Das Gleiche gilt für die Betrachtung möglicher Eigenspannungen und den Einfluss einer nachträglichen Oberflächenbearbeitung.

3.1 Thermografische Auswertung der Probenherstellung

Die Fertigung der PK wurde mit dem Thermografiesystem VarioCam HR Head überwacht. Der Spektralbereich der Kamera liegt zwischen 7,5 µm und 14 µm, die Bildrate beträgt 50 Hz mit einer maximalen Auflösung von 640 × 480 pix.

Um die absolute Temperatur mit einer Infrarotkamera zu messen, muss der Emissionsgrad bekannt sein. Dieser ist jedoch abhängig vom Material und der Wellenlänge. Somit liefert dieser Beitrag keine Absolutwerte, allerdings untereinander vergleichbare Relativwerte. Aus diesem Grund werden nur normierte Ergebnisse hinsichtlich Abkühlrate sowie der Temperatur angegeben. Es können Abkühlraten von bis zu 40 K/µs entstehen [3].

Bei der Analyse der Thermografiedaten werden die höchsten Abkühlraten jeder Schicht ausgewertet. Der Effekt des Wiederaufschmelzens der vorhergehenden Schicht und eine damit verbundene reduzierte Abkühlrate kann aus physikalischen Gründen nicht berücksichtigt werden, da in dieser Situation nur die Oberflächenmessung erfolgen kann. Bild 4 zeigt die Messpunkte zur Auswertung der Thermografiedaten. Die Aufnahmen starten bei einer Bauteilhöhe von 600 µm und umfassen insgesamt neun Schichten. Zur Auswertung der Daten werden im maßgebenden Bereich der Zugproben je neun Messpunkte definiert. Folglich werden für jeden Probekörper 81 Abkühlraten ausgewertet.

In Bild 5 wird der Schmelzprozess von PK1 innerhalb 1 s dargestellt. Es ist zu erkennen, dass die Abkühlrate in sehr kurzer Zeit (0,7 s) nichtlinear absinkt. Die exakte Abkühlrate kann aufgrund der geringen Bildfrequenz mit der verwendeten Kamera nicht erfasst werden.

Aus der statistischen Auswertung der Abkühlraten ist zu erkennen, dass signifikante Unterschiede in den gemittelten Abkühlraten der jeweiligen Probekörper herrschen

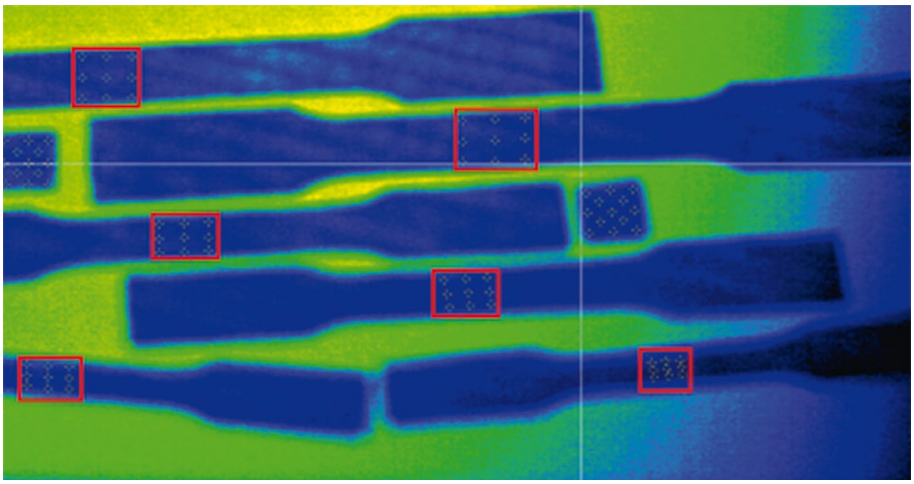

Bild 4 Messbereich (rot markiert) mit Messpunkten zur Auswertung der Thermografiedaten
Measuring sections (marked red) with measuring points for evaluating the thermographic data

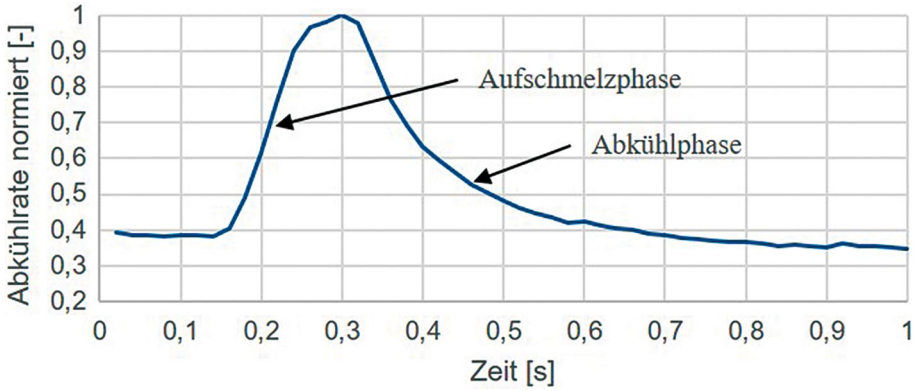

Bild 5 Temperaturverlauf (normiert anhand von PK7) bei Schmelzvorgang und Abkühlung
Temperature curve (standardized on specimen 7) during melting and cooling

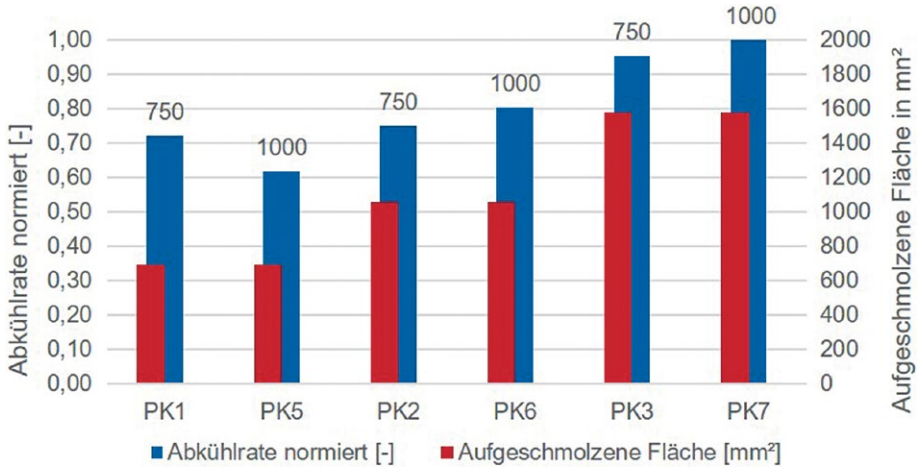

Bild 6 Durchschnittliche Abkühlrate der PK und aufgeschmolzene Fläche der PK, Zahlen über den Balken geben die Scangeschwindigkeit in mm/s an
Average cooling rate of the samples and melted area, numbers above the bars indicate the scanning speed in mm/s

(Bild 6). Die Abkühlrate nimmt in der Gesamtbetrachtung mit größer werdender Probengeometrie zu. Des Weiteren ist ersichtlich, dass die Scangeschwindigkeit, und daraus resultierend die Energiedichte, einen Einfluss auf die Abkühlrate hat. Beispielsweise ist im Vergleich zwischen PK3 und PK7 zu erkennen, dass eine höhere Scangeschwindigkeit (von 750 mm/s auf 1 000 mm/s) zu einer höheren Abkühlrate (von 0,95 auf 1,0) führt.

Lediglich bei PK1 und PK5 ist dies nicht der Fall. Dies ist evtl. auf die Lage auf der Bauplattform und den größeren Abstand von Probe 5 zu den anderen Proben zurückzuführen. In [13] wird gezeigt, dass eine höhere thermische Masse zu einer langsameren Abkühlrate führt. Die Mittelwerte der Abkühlraten der anderen Probekörper verhalten sich proportional zur Probengröße. Somit steigt die Abkühlrate mit zunehmender aufzuschmelzender Fläche, d.h. dem Wärmeabtransport zur Verfügung stehenden Querschnitt, an.

3.2 Mechanische Eigenschaften aus Zugversuchuen

Zur Ermittlung der Festigkeit wurden Zugversuche mit einer Zwick Roell Z100 Zentralspindel-Prüfmaschine durchgeführt. Diese Maschine arbeitet weggesteuert und

Tab. 3 Parameter und Ergebnisse der Zugversuche: Querschnittsfläche S_0; Messfühlerabstand L_0; E-Modul; Streckgrenze $R_{p\,0,2}$; Zugfestigkeit R_m; Bruchdehnung A
Parameters and results of the tensile tests: cross-sectional area S_0; probe distance L_0; Young's modulus, yield strength $R_{p\,0.2}$; tensile strength R_m; elongation at break A

Probekörper	S_0 [mm²]	L_0 [mm]	E [GPa]	$R_{p\,0,2}$ [MPa]	R_m [MPa]	A [%]
1	10,95	20	197,77	575,86	665,06	29,45
5	11,91	20	210,53	572,10	672,99	28,17
2	23,35	30	185,26	582,34	679,05	26,36
6	23,49	30	193,14	590,25	683,61	27,33
3	49,41	40	191,26	599,59	689,64	30,54
7	50,45	40	189,47	601,19	692,32	29,37

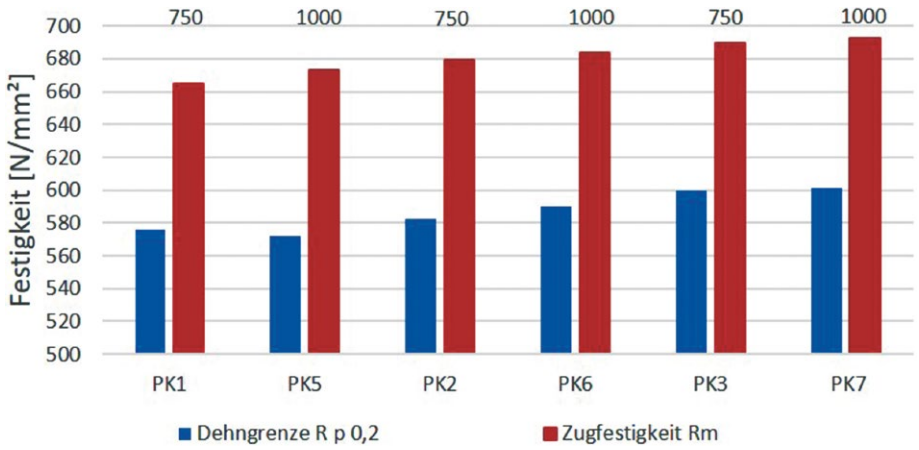

Bild 7 Ergebnisse der Zugversuche, Probengröße von klein (links) nach groß (rechts), Zahlen über den Balken geben Scangeschwindigkeit in mm/s an
Results of tensile tests, sample size from small (left) to large (right), numbers above the bar indicate scanning speed in mm/s

die Ermittlung des E-Moduls erfolgt als Tangente im Bereich von 100 MPa bis 300 MPa. Die Versuche wurden mit einer Vorspannung von 5 MPa gefahren. In Tab. 3 sind die entsprechenden Ergebnisse je Probekörper dargestellt.

In Tab. 3 ist zu erkennen, dass die hier gemessenen 0,2 %-Streckgrenzen weit größere Werte als bspw. gewalztes 316L-Material erreichen ([14], 190–240 MPa). Grundsätzlich steigen die Werte für die Streckgrenze und die Zugfestigkeit mit zunehmender Probengröße an.

Die etwas geringere 0,2 %-Streckgrenze von PK5 im Vergleich zu PK1 ist auf die kleinere normierte Abkühlrate zurückzuführen (Abschn. 3.1). Die Kaltverfestigung im weiteren Verlauf des Zugversuchs kompensiert diese geringere 0,2 %-Streckgrenze durch erhöhte Versetzungsbildung. Die größere Verfestigung geht auch mit einer kleineren Gesamtdehnung einher. Im weiteren Verlauf von PK2 bis hin zu PK7 nimmt die Abkühlrate zu, 0,2 %-Streckgrenze sowie Festigkeit steigen jeweils leicht bei nur geringen Unterschieden in der Bruchdehnung (Bild 7, Tab. 3).

Die Ergebnisse sind mit Materialien vergleichbar, die einer deutlichen Kornfeinung unterzogen werden. Eine Verringerung der Korngröße kann entweder durch hohe Abkühlgeschwindigkeiten oder durch Zugabe von weiteren Legierungselementen erzielt werden [7].

Die erhöhten Festigkeiten könnten auch mit einer Aufnahme von Stickstoff während des Produktionsprozesses erklärt werden. Tatsächlich wurde während des Druckens ein maximaler Anteil von 1 000 ppm Restsauerstoff aus der Luft gemessen. Daraus ergibt sich ein rechnerischer Anteil von 3 728 ppm N_2 in der Baukammer. Der Einfluss von N_2 und O_2 ist damit vernachlässigbar klein [15], wodurch die Aufnahme von Stickstoff auszuschließen ist.

3.3 Bruchflächen der Zugproben

Die Bruchflächen der Probekörper PK5–PK7 wurden unter dem Rasterelektronenmikroskop (REM) untersucht. Es sind weder optisch noch in den Zugversuchen Unterschiede im Bruchverhalten der Proben festzustellen. Bild 8 zeigt die Bruchflächen von den Probekörpern PK5 und PK7. Beide Brüche weisen eine unter nahezu 45° verlaufende Bruchfläche auf.

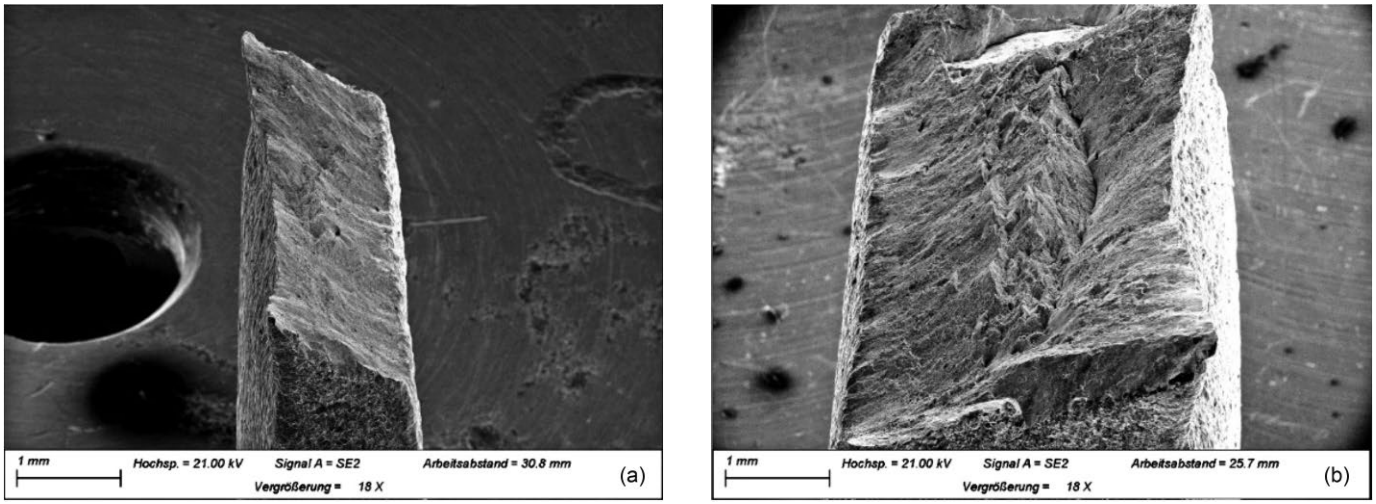

Bild 8 Bruchflächen von PK5 (a) und PK7 (b) unter 18-facher Vergrößerung
Fracture surfaces of sample 5 (a) and 7 (b) with 18 x magnification

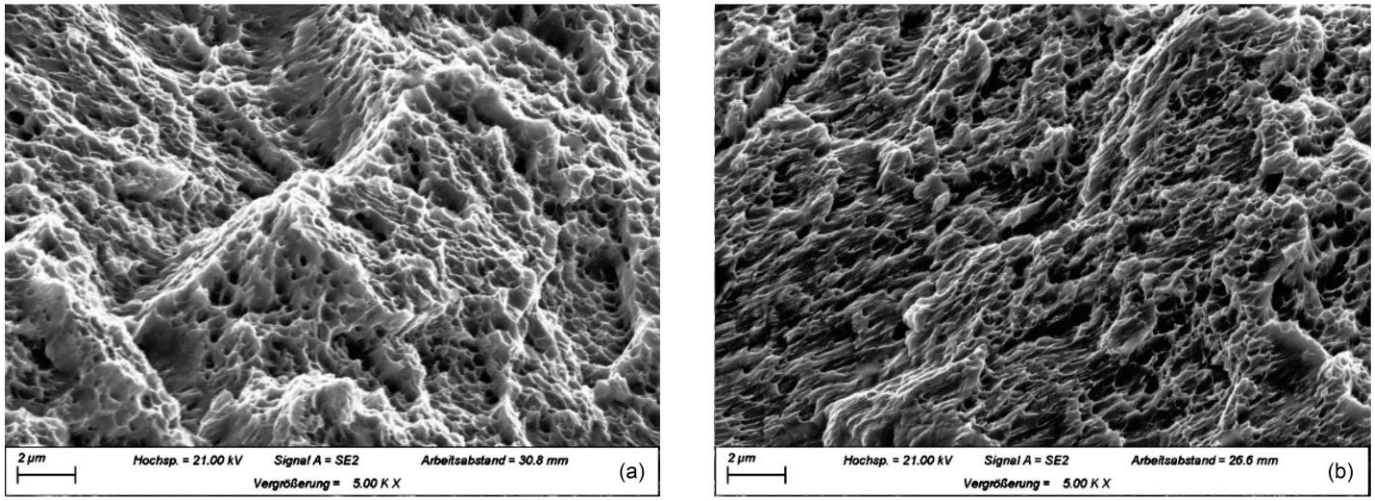

Bild 9 Bruchflächen von PK5 (a) und PK7 (b) unter 5 000-facher Vergrößerung
Fracture surfaces of sample 5 (a) and 7 (b) with 5 000 x magnification

In Bild 9 sind exemplarisch die Bruchflächen der Probekörper PK5 und PK7 unter 5 000-facher Vergrößerung im REM zu sehen. Es sind Scherwaben zu erkennen, die bei PK7 noch etwas deutlicher als bei PK5 ausgeprägt sind (Bild 9). Beide Bruchflächen sind folglich einem Duktilbruch durch Abgleiten als Folge normalkraftinduzierter, mikroskopischer Schubspannungen zuzuordnen [16].

Die Aufnahmen des REM weisen damit deutlich auf ein duktiles Bruchverhalten hin und liefern keinerlei Anhaltspunkte für eine Versprödung des Materials. Die Tendenz der Zugversuche wird damit bestätigt.

3.4 Untersuchung der Porosität

Für die Untersuchung des Gefüges wurden die in Abschn. 3 genannten Probewürfel verwendet. Diese wurden bei 180 °C für 5 min heiß eingebettet und in vier Schritten mit Siliciumcarbid (180), einer Struers MD-Allegro mit Diamantsuspension 6 µm, einer Struers DAC mit Diamantsuspension 3 µm und als Endpolitur einer Struers MD-NAP mit Diamantsuspension 1 µm geschliffen und poliert. Mittels eines Lichtmikroskops wurden Bilder der polierten Oberflächen aufgenommen. Über die Software ImageJ konnte im Nachgang die Bauteildichte über einen Hell-Dunkel-Vergleich errechnet werden. Die Dichte ist mit 99,92 % für Probe 4 sowie mit 99,98 % für Probe 8 beziffert. Mit dem LPBF-Verfahren hergestellten hochlegierten Kaltarbeitswerkzeugen können Bauteildichten von ≥ 99,0 % im industriellen Maßstab erreicht werden [17, 18].

Auch die Zugproben wurden im gleichen Ablauf wie die Würfel präpariert. Mit der Software ImageJ wurde für PK5 eine Dichte von 99,95 %, für PK6 99,96 % sowie für PK7 eine Dichte von 99,91 % ermittelt. Aufgrund der geringen Porosität ist ein Einfluss von zu geringer Dichte auf die mechanischen Eigenschaften auszuschließen.

Die in Bild 10 rot markieren Poren stellen Gasporen dar. Gase dehnen sich bei Erhöhung der Umgebungstemperatur, in diesem Fall durch den Laserpuls, isotrop aus. Sie sind überwiegend sphärolithisch [15]. Die blau markierten Ellipsen stellen Bindefehler dar. Diese können durch verschiedenste Einflüsse entstehen, wie z. B. Verunreinigung des Metallpulvers, Verunreinigung der Laserlinse, Belichtungsstrategie oder Oxidation und Stickstoffaufnahme des Metallpulvers.

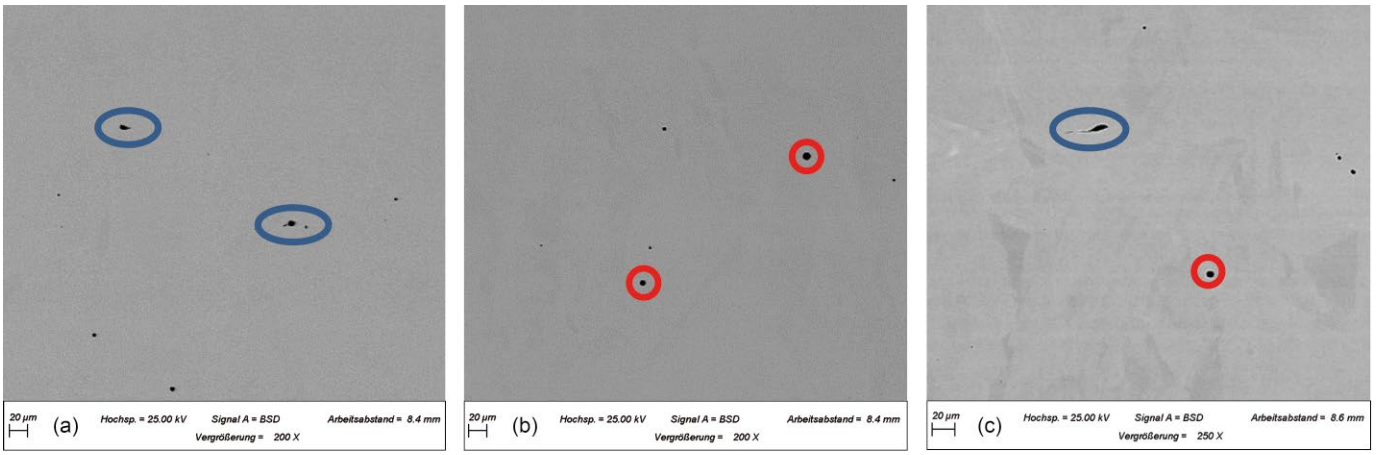

Bild 10 Polierte Proben, PK5 (a) mit 99,95 % Dichte, PK6 (b) mit 99,96 % Dichte und PK7 (c) mit 99,91 % Dichte; rot: Gasporen; blau: Bindefehler
Polished samples, sample 5 (a) 99.95 % density, sample 6 (b) 99.96 % density and sample 7 (c) with 99.91 % density, red: gas pores, blue: lack of fusion pores

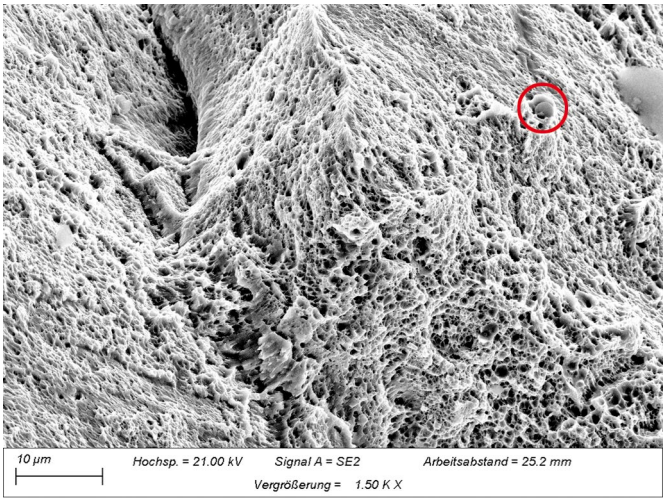

Bild 11 Bruchfläche von PK7, rot: nicht aufgeschmolzenes Metallpartikel, 1 500-fache Vergrößerung
Fracture surface of sample 7, red: unmelted metal particle, 1 500 × magnification

In den meisten Fällen besitzt das Metallpulver bei Verunreinigungen einen erhöhten Schmelzpunkt. Da die Laserparameter auf die Schmelztemperatur des jeweiligen Materials eingestellt sind, kann es zu nicht komplett aufgeschmolzenen Pulverpartikeln kommen [1]. Bild 11 zeigt die Bruchfläche von PK7. Rot markiert ist dort ein nicht aufgeschmolzenes Metallpartikel.

Würfel und Zugproben erreichen mit einer Dichte von mehr als 99,9 % industrielle Standardwerte. Zudem konnte bei Zugversuchen kein Versagen aufgrund von Poren festgestellt werden. Ein Einfluss von Porosität auf die mechanischen Eigenschaften der LPBF-Probekörper ist daher nach aktuellem Stand der Technik in dieser Studie ausgeschlossen.

3.5 Untersuchung des Gefüges

3.5.1 Schweißbahnen

Um das Gefüge sichtbar zu machen, wurden die Probekörper PK4 und PK8 für 30 s in V2A-Beize getaucht. Die Schweißbahnen sind in Bild 12a durch ihre dunklen Schmelzlinien erkennbar. Es sind keine Karbide oder Delta-Ferrit ersichtlich. Dies wurde mit EBSD-Messungen ebenfalls bestätigt. Vereinzelt sind mithilfe von EDX-Messungen in den Bindefehlerporen Oxide und Nitride detektiert worden. Die Einschmelztiefe variiert zwischen 50 und 60 µm, was aufzeigt, dass mehr als nur eine Schicht pro Schmelzvorgang aufgeschmolzen wird, da die Schichtdicke mit 20 µm beziffert ist. Dies bedeutet, dass bereits verfestigte Schichten erneut aufgeschmolzen werden. Es lässt sich somit folgern, dass die reale Abkühlrate etwas geringer ist als an der Oberfläche gemessen. Dies könnte in größeren Korngrößen resultieren.

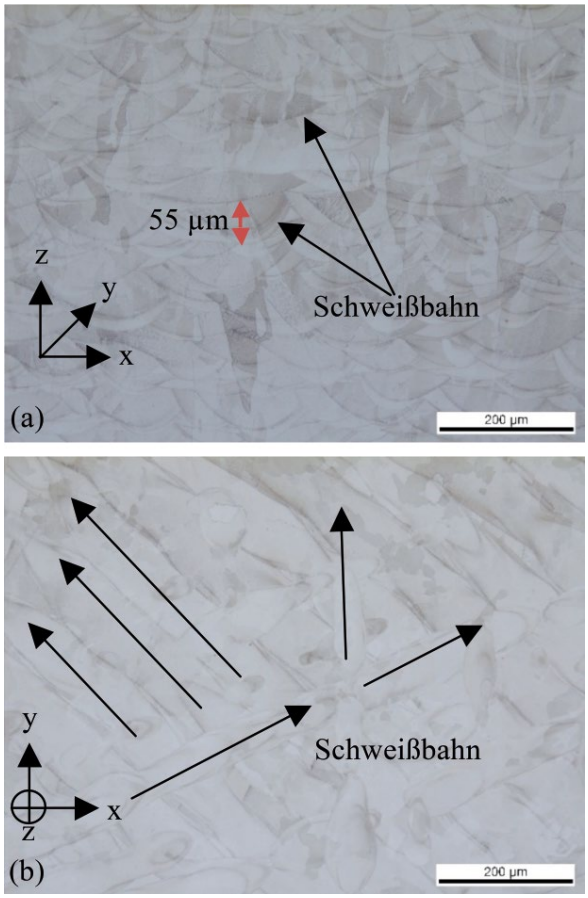

Bild 12 Geätzte Proben mit V2A-Beize, PK4 (a) (Seitenansicht), PK8 (b) (Draufsicht), 20-fache Vergrößerung, z ist Aufbaurichtung
Etched samples with V2A etchant, sample 4 (a) (side view), sample 8 (b) (top view), 20 × magnification, z build direction

3.5.2 Korngrößenermittlung

Bild 13 zeigt exemplarisch ein geätztes Schliffbild von PK5 in 5 000-facher Vergrößerung. Mit den Linienschnittverfahren mit Körnern wurde nach DIN EN ISO 643 [19] die mittlere Kornbreite ermittelt. Bei einer Messlänge von

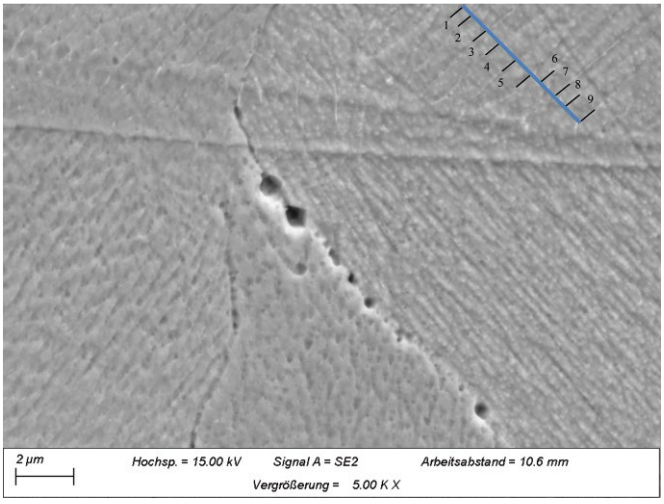

Bild 13 Schliffbild von PK5, Messung der Korngröße mit dem Linienschnittverfahren nach DIN EN ISO 643 [19], Querschliff
Micrograph of sample 5, measurement of grain size with the linear intercept method according to DIN EN ISO 643 [19], cross sectional view

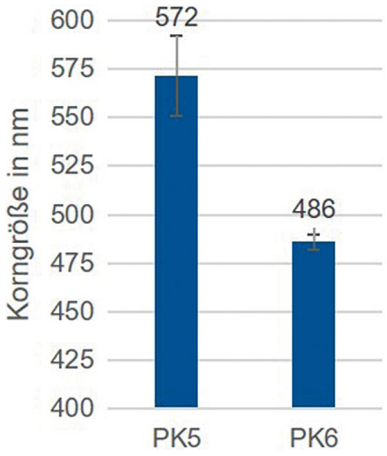

Bild 14 Korngrößen von PK5 und PK6
Grain sizes of sample 5 and sample 6

6 542 nm, verteilt auf neun Körner, ergibt sich eine mittlere Korngröße von 626,9 nm.

Um eine statistische Aussage treffen zu können, wurden für PK5 insgesamt 28 und für PK6 22 Körner gemessen. Diese sind in Bild 14 dargestellt. Es ist zu erkennen, dass PK5 einen größeren mittleren Korndurchmesser hat als PK6. Eine größere Korngröße führt demnach zu einer niedrigeren Streckgrenze, was die Ergebnisse der Zugversuche bestätigt.

Die ermittelten Korngrößen von PK 5 und PK 6 dienen im Folgenden zur Ermittlung der Konstanten der Hall-Petch-Beziehung.

3.5.3 Anwendung der Hall-Petch-Beziehung

Für die grafische Darstellung der Hall-Petch-Beziehung müssen zunächst die Steigung der linearen Kurve K und σ_o (Abschn. 2.4) nach Gl. (6) berechnet werden:

$$K = \frac{\sigma_{y\,PK6} - \sigma_{y\,PK5}}{\frac{1}{\sqrt{d_{k\,PK6}}} - \frac{1}{\sqrt{d_{k\,PK5}}}} = \frac{590{,}25 - 572{,}1}{\frac{1}{\sqrt{\frac{486}{10^6}}} - \frac{1}{\sqrt{\frac{572}{10^6}}}} = 5{,}13\ \text{MPa}\sqrt{\text{mm}}. \quad (6)$$

Die Werte von $\sigma_{y\,PK5,6}$ stammen aus den Ergebnissen der Zugversuche in Abschn. 3.2. Die maximale Schubspannung eines Einkristalls wird nach Umstellung von Gl. (5) folgendermaßen berechnet (Gl. (7)):

$$\sigma_0 = \sigma_{y\,PK5} - \frac{K}{\sqrt{d_k}} = 572{,}1 - \frac{5{,}13}{\sqrt{\frac{572}{10^6}}} = 357{,}6\ \text{N/mm}^2 \quad (7)$$

Als Ergebnis kann die resultierende Streckgrenze in Abhängigkeit von der Korngröße d_k ermittelt werden. In Bild 15 sind die entsprechenden Werte für die Probekörper PK 1, PK 5 und PK 6 dargestellt.

Wie in Bild 6 bereits gezeigt, ist die Abkühlrate von PK5 geringer als die von PK6. Die Korngröße von PK 5 ist jedoch größer und die Streckgrenze geringer, bei PK 6 ist die Korngröße geringer und die Abkühlrate höher. Diese experimentell gefundenen Zusammenhänge werden somit durch die Hall-Petch-Beziehung bestätigt.

Da die Abkühlrate und die experimentell ermittelte Streckgrenze von PK1 höher ist als die von PK5, ist zu folgern, dass das Korngefüge in PK1 kleiner ist. Rechnerisch müsste PK1 somit eine mittlere Korngröße von 552 nm besitzen. Dies ist im Zuge weiterer Untersuchungen des Gefüges von PK1 zu prüfen.

Es ist zu erwähnen, dass die Hall-Petch-Beziehung bei kleiner werdenden Korngrößen Anwendungsgrenzen besitzt. Zudem besagt [20], dass es weder experimentelle noch theoretische Beweise für die 60 Jahre alte Hall-Petch-Gleichung gibt. [21] weist allerdings darauf hin, dass die Hall-Petch-Beziehung eine gültige empirische Beziehung ist. Sie ist somit als solche für die Vorhersage von Materialeigenschaften durch Interpolation und Extrapolation nützlich. Dies ist unabhängig davon, ob sie theoretisch korrekt ist. Diese Aussage wird u. a. auch in [22] bestätigt. Dort wird die Hall-Petch-Beziehung mit Korngrößen von bis zu 16 nm angewendet und als eine valide Methode zur Bestimmung der Korngrößen bezeichnet. Die Korngrößen dieser Studie sind mit d_k im Bereich von 400 nm bis 600 nm weitaus größer.

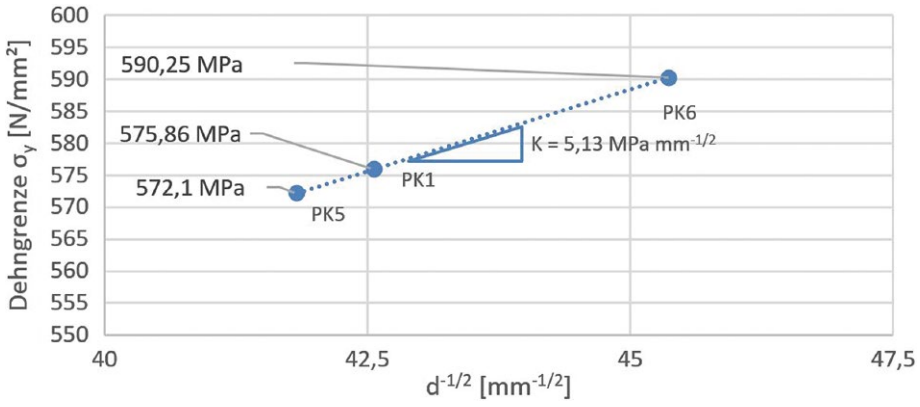

Bild 15 Abhängigkeit der Streckgrenze von der Korngröße von additiv gefertigtem 316L, die Korngröße von PK1 ist rechnerisch ermittelt
Dependency of the yield strength on the grain size of additive manufactured 316L, the grain size of PK1 is calculated

4 Zusammenfassung und Diskussion

Es konnte gezeigt werden, dass die Abkühlrate eines LBPF-Bauteils sowohl von der Geometrie als auch von den Laserparametern des Schmelzprozesses abhängig ist. So führt eine schnellere Scangeschwindigkeit zur Erhöhung der Abkühlgeschwindigkeit. Dies wiederum beeinflusst die resultierenden Festigkeitswerte. Zwischen kleinster und größter Probengeometrie ist ein Unterschied von bis zu 29 MPa in der Streckgrenze erkennbar. Im Vergleich zu herkömmlich hergestelltem 316L liegt die Streckgrenze bei den LPBF-hergestellten um das 2,5-Fache höher.

Die Messungen der Korngrößen und die anschließende Aufstellung der Hall-Petch-Beziehung lassen darauf schließen, dass der Unterschied der Streckgrenze verschiedener Probengeometrien auf unterschiedlich feines Korngefüge zurückzuführen ist.

Grundsätzlich zeigt sich, dass die Bauteilgeometrie einen starken Einfluss auf die mechanischen Eigenschaften hat. So kann bei kleineren Probenabmessungen abkühlungsbedingt nur von einer niedrigeren 0,2 %-Streckgrenze ausgegangen werden. Bei dickwandigeren Bereichen ist diese 0,2 %-Streckgrenze jedoch höher. Die Bruchdehnung hingegen ändert sich nur minimal.

5 Ausblick

Die additive Fertigung hat im vergangenen Jahrzehnt deutliche Fortschritte im Bereich Forschung und Entwicklung erzielt. Ein einheitlicher Stand der Technik fehlt jedoch, da das resultierende Verhalten der für den Druck verwendeten Materialien noch nicht ausreichend erforscht ist. Nur einzelne Unternehmen haben mit hohem Aufwand wenige 3D-Drucker so optimiert, dass sie mit definierten Prozessparametern reproduzierbare Produkte fertigen können. Entsprechende Laserparameter sind bisher allerdings nur material- und maschinenabhängig verfügbar. Die Geometrie des aufzuschmelzenden Bereichs und somit des Bauteils wird bis dato nicht berücksichtigt. Die Ergebnisse der vorliegenden Studie zeigen nun jedoch die Tendenz, dass die Bauteilgeometrie eine deutliche Rolle spielt und in die Prozessparameter Eingang finden sollte. Tatsächlich bedarf es weiterer Versuche mit einer größeren Variation von Probengeometrien und Prozessparametern, um diese ersten Ergebnisse zu bestätigen. Ein entsprechendes Forschungsprojekt ist am Lehrstuhl für Metallbau der TUM bereits angelaufen.

Dabei sollten außerdem zusätzlich der Einfluss von Wärmebehandlung, prozessbedingten Eigenspannungen und der Oberflächenrauigkeit untersucht werden.

Dank

Für die Finanzierung und die Unterstützung gilt der Dank der Verfasser der Förderung durch die Deutsche Forschungsgemeinschaft (DFG) – Projektnummer 414265976 – TRR 277. Der Lehrstuhl für Metallbau dankt dem Institut für Werkzeugmaschinen und Betriebswissenschaften (iwb) der TU München für die Fertigung der Proben auf ihrer EOS M270. Des Weiteren danken die Autoren Herrn Prof. F. Krafft von der Hochschule München für die technische Unterstützung bei der Metallografie.

Literatur

[1] Meiners, W. (1999) *Direktes Selektives Laser-Sintern einkomponentiger metallischer Werkstoffe.* Aachen: Shaker.

[2] Dowling, J. K. L. (2020) *A review of critical repeatability and reproducibility issues in powder bed fusion* in: Materials & Design 186, 15 January, 108346. https://doi.org/10.1016/j.matdes.2019.108346

[3] Hooper, P. A. (2018) *Melt pool temperature and cooling rates in Laser Powder Bed Fusion.* Imperial College London. London: Elsevier.

[4] McMillan, M. (2017) *Computationally efficient finite difference method for metal additive manufacturing: A reduced-order DFAM tool applied to SLM* in: Materials & Design 132, June. https://doi.org/10.1016/j.matdes.2017.06.058

[5] Bugeda, G. (1999) *Numerical prediction of temperatur and density distributions in selective laser melting processes* in: Rapitd Prototyping Journal 5, no. 1, pp. 12–26. https://doi.org/10.1108/13552549910251846

[6] Besson, U. (2010) T*he History of the Cooling Law: When the Search for Simplicity can be an Obstacle* in: Science & Education 21, no. 8, pp. 1–26. https://doi.org/10.1007/s11191-010-9324-1

[7] Gottstein, G. (2014) *Materialwissenschaft und Werkstofftechnik*. Aachen: Springer Vieweg.

[8] Scipioni Bertoli, U. (2017) *In-situ characterization of laser-powder interaction and cooling rates through high-speed imaging of powder bed fusion additive manufacturing* in: Materials & Design 135, pp. 385–396. https://doi.org/10.1016/j.matdes.2017.09.044

[9] Katayama, S.; Matsunawa, A. (1984) *Solidification microstructure of laser welded stainless steels* in: Mazumder, J. [ed.] *Proceedings of the Materials Processing Symposium: ICALEO '84*. Boston, Nov. 12–15, 1984.

[10] Liverani, E. (2016) *Effect of Selective Laser Melting (SLM) process parameters on microstructure and mechanical properties of 316L austenitic stainless steel* in: Journal of Materials Processing Technology 249, pp. 255–263. https://doi.org/10.1016/j.jmatprotec.2017.05.042

[11] DIN EN 10083-2:2006-10 (2006) *Vergütungsstähle – Teil 2.* Berlin: Beuth.

[12] Höganäs (2019) *Sainless Steel 316L* [online]. Höganäs, Sweden. https://www.hoganas.com/en/powder-technologies/products/hot-polymer-filtration-powders/316l [Zugriff am: 8. Okt. 2019]

[13] Fitzgerald, W. E. E. (2016) *The Effect of Location on the Structure and Mechanical Properties of Selective Laser Melted 316L Stainless Steel* in: *Annual International Solid Freeform Fabrication Symposium – An Additive Manufacturing Conference*. SFF2016, Kansas City, Aug. 8–10, 2016.

[14] ThyssenKrupp (2017) *Stainless Steel 316L 14404* [online]. ThyssenKrupp, UK. https://d13qmi8c46i38w.cloudfront.net/

media/UCPthyssenkruppBAMXUK/assets.files/material-data-sheets/stainless-steel/stainless-steel-1.4404-316l.pdf [Zugriff am: 8. Okt. 2019]

[15] Pauzon, C. (2019) *Effect of argon and nitrogen atmospheres on the properties of stainless steel 316 L parts produced by laser-powder bed fusion* in: Materials & Design 179, October, 107873. https://doi.org/10.1016/j.matdes.2019.107873

[16] VDI-Fachbereich Werkstofftechnik (2008) *VDI 3822 Blatt 2 – Schadensanalyse – Schäden durch mechanische Beanspruchungen.* Ausgabe Apr. 2008.

[17] SLM Solutions *Materialdatenblatt Tool Steel 1.2344 / A681 H13 / H13* [online]. SLM Solutions, Lübeck. https://www.slm-solutions.com/fileadmin/user_upload/MDS_FE-Alloy_1.2344_0219.pdf [Zugriff am: 20. März 2020]

[18] H&H Innovations *Materialdatenblatt Werkzeug – Stahl 1.2709/M300-3* [online]. H&H Innovations, Leopoldshöhe. https://www.huh.de/fileadmin/dateien/pdfs/Materialdatenblaetter/huhMaterialdatenblatt_Werkzeug-Stahl.pdf [Zugriff am: 20. März 2020]

[19] DIN EN ISO 643:2013-05 (2013) *Stahl – Mikrophotographische Bestimmung der erkennbaren Korngröße (ISO 643:2012)*; Deutsche Fassung EN ISO 643:2012. Berlin: Beuth. Ausgabe Mai 2013.

[20] Li, Y. et al. (2016) *The Hall–Petch effect as a manifestation of the general size effect* in: Proceedings of the Royal Society 472, 20150890. https://doi.org/10.1098/rspa.2015.0890

[21] Hirt, J. (1972) *The influence of grain boundaries on mechanical properties* in: Metallurgical Transactions 3, no. 12, pp. 3047–3067.

[22] Yin, F. et al. (2018) *Ultrastrong nanocrystalline stainless steel and its Hall-Petch relationship in the nanoscale* in: Scripta Materialia 155, October, pp. 26-31. https://doi.org/10.1016/j.scriptamat.2018.06.014

Autoren

Johannes Diller, M.Sc. (Korrespondenzautor)
Johannes.Diller@tum.de
Technische Universität München
Lehrstuhl für Metallbau
Arcisstr. 21
80333 München

Ulrich Auer, M.Sc.
Ulrich.Auer@tum.de
Technische Universität München
Lehrstuhl für Metallbau
Arcisstr. 21
80333 München

Dr.-Ing. Christina Radlbeck
C.Radlbeck@tum.de
Technische Universität München
Lehrstuhl für Metallbau
Arcisstr. 21
80333 München

Univ.-Prof. Dr.-Ing. Dipl.-Wirt.-Ing. (NDS) Martin Mensinger
Mensinger@tum.de
Technische Universität München
Lehrstuhl für Metallbau
Arcisstr. 21
80333 München

Prof. Dr.-Ing. Frank Krafft
Frank.Krafft@hm.edu
Hochschule München
Labor für angewandte Werkstofftechnik
Lothstr. 64
80335 München

Zitieren Sie diesen Beitrag

Diller, J.; Auer, U.; Radlbeck, C.; Mensinger, M.; Krafft, F. (2020) *Einfluss der Abkühlrate auf die mechanischen Eigenschaften von additiv gefertigten Zugproben aus 316L*. Stahlbau 89, H. 12, S. 970–980. https://doi.org/10.1002/stab.202000034

Dieser Aufsatz wurde in einem Peer-Review-Verfahren begutachtet. Eingereicht: 9. April 2020; angenommen: 1. September 2020.

A.2.2 Publication 2: Cyclic plastic material behaviour of 316L, manufactured by laser powder bed fusion (PBF-LB/M)

Reproduced from:

Materials Characterization 191 (2022), 112153
Weblink: https://doi.org/10.1016/j .matchar.2022.112153

with the permission of Elsevier BV.

Materials Characterization 191 (2022) 112153

Contents lists available at ScienceDirect

Materials Characterization

journal homepage: www.elsevier.com/locate/matchar

Cyclic plastic material behavior of 316L manufactured by laser powder bed fusion (PBF-LB/M)

Johannes Diller [a,*], Lukas Rier [a], Dorina Siebert [a], Christina Radlbeck [a], Frank Krafft [b], Martin Mensinger [a]

[a] Technical University of Munich, Chair of Metal Structures, Germany
[b] Hochschule München, Germany

ARTICLE INFO

Keywords:
Laser powder bed fusion
316L
Low-cycle fatigue
Strain-controlled fatigue testing
Strengthening mechanisms

ABSTRACT

In laser powder bed fusion of metals (PBF-LB/M), the influence of laser parameters on the static mechanical properties is well known. Different laser parameters result in a higher or a lower tensile strength. Only little is known about the influence of the laser parameters on the cyclic plastic behavior at high strain amplitudes. Different laser parameters may result in a significant change in the stress levels during cyclic loading.

In this study, the cyclic plastic material behavior at high strain amplitudes of up to 3.0% of AISI-316L manufactured by PBF-LB/M is investigated. Two different laser parameter sets are applied. One laser parameter set is outside the stable melting zone and the other one is inside the stable melting zone according to [1]. Metallographic analyses and static, as well as strain-controlled fatigue tests with a strain ratio of $R = -1$ were conducted.

The plastic material behavior is dominated by softening, which is reduced with increasing strain amplitude due to mechanical twinning. Indeed, for strain amplitudes >2.5% twin-induced strain hardening is observed. A correlation between the twin-induced strain hardening behavior and the resulting maximum stress curve per endured cycle is observed. The laser parameters influence the generated stress level during cyclic plastic loading. It is shown, that the porosity highly affects the fatigue life in the low-cycle fatigue range. Finally, the strain-life curve is determined and approximated by the Manson-Coffin fatigue parameters.

1. Introduction

Laser powder bed fusion of metals (PBF-LB/M) is a digital process, which is capable of manufacturing lightweight, shape-optimized metal parts. In research, steels, like AISI-316L (1.4404), are often used to elaborate the influencing factors from the manufacturing process of PBF-LB/M [2–4].

316L is a high-alloyed stainless steel. It is widely used in the chemical industry, since a main advantage of the material is its high corrosion resistance. It is also applied in the medical sector and the automotive industry. According to the Schaeffler diagram, 316L consists of mainly γ-austenite with a maximum of 5% retained δ-ferrite, depending on the chemical composition. The face-centered cubic lattice structure has a lattice parameter of 3596 nm [5].

The yield strength of hot-rolled and solution annealed AISI 316L is usually within 200 to 220 MPa [6–9]. PBF-LB/M manufactured 316L however has a yield strength of up to 650 MPa [10–12]. This is due to the high cooling rate of up to 40 K/µs the material is subjected to during the manufacturing process, resulting in grain boundary strengthening. A laser beam with a focal length of 50 to 100 µm melts metal powder with a high energy density. This may result in a melt pool width of up to 200 µm [13]. As the scanning speed is usually in the range of 700–1400 mm/s, the melting time of one spot is very short resulting in rapid melting, followed by rapid cooling due to the high-temperature gradient [1,11,12,14]. This rapid cooling rate between 1 K/µs and 40 K/µs creates a unique, very fine-grained microstructure with cell sizes of 200–300 nm [10,15]. This effect is called grain refinement. These small cell sizes affect the yield strength as there are more grain boundaries that inhibit the dislocation motion of the atoms. This effect is described with the Hall-Petch-relationship [16,17].

However, the cooling rate of the material changes with different laser parameters [18]. In [10], different scanning velocities and surface areas for the manufacturing of tensile samples were applied. This resulted in different cooling rates and hence different static mechanical

* Corresponding author.
E-mail address: johannes.diller@tum.de (J. Diller).

https://doi.org/10.1016/j.matchar.2022.112153
Received 31 May 2022; Received in revised form 19 July 2022; Accepted 20 July 2022
Available online 25 July 2022

properties. The effect of different laser parameters on the cyclic plasticity behavior however has not yet been investigated.

This study focuses on the cyclic plasticity behavior of 316L, manufactured by PBF-LB/M. Two different laser parameters with varying scanning velocity, laser power and therefore energy density are applied. All samples were manufactured vertically and then tensile testing, as well as strain-controlled fatigue testing, was carried out. So far, strain amplitudes of only up to 2% were applied in the literature [19–21]. Hence, strain amplitudes of up to 3% were applied. This is done to investigate the hardening behavior of high strain amplitudes. Additionally, the microstructure is investigated to determine the porosity, orientation and grain size. The goal is to investigate the cyclic plastic fatigue behavior at high strain amplitudes with its resulting cyclic material behavior with respect to the strain amplitude.

2. Experimental method

During this research, 316L stainless steel (1.4404) metal powder by Oerlikon Metco was used on an EOS M280 PBF-LB/M machine equipped with a 400 W Ytterbium continuous wave fiber laser. The particle size distribution is 20 to 63 µm with the respective volume percentile values D10, D50 and D90 of 19, 30 and 46 µm. Argon 5.0 was used as inert gas during the manufacturing with a residual oxygen concentration of <1300 ppm. The build job consisted of 36 fatigue specimens, 6 tensile specimens as well as 2 microstructure specimens with two different laser parameters. These are listed in Table 1. The layer thickness, as well as the hatch distance were kept constant, whereas the scanning velocity and the laser power were varied, resulting in different energy densities.

According to [1] the laser parameter set E1 is outside the stable melting zone, theoretically resulting in balling and lack of fusion porosity. Laser parameter set E2 however is in the stable melting zone, theoretically providing a high density and toughness, continuous beads, and homogeneous melt tracks. Therefore, these two laser parameter sets were used, to investigate the effect of porosity on the low cycle fatigue behavior as well. A hatch-angle of 60° was used.

The resulting 36 strain-controlled fatigue testing specimens, 18 per laser parameter set, were further subdivided based on the applied strain amplitudes into 6 groups of 3 specimens each. The complete experimental design, including the 6 tensile and 2 microstructure specimens, 3 and 1 specimens per laser parameter set respectively, is shown in Table 2. To minimize the effect of specimen geometries, the same geometry was used for the tensile specimens, the fatigue specimens and the microstructure evaluation. To compare the microstructure before and after a dynamically applied strain amplitude, one specimen for each laser parameter set was used to investigate the porosity, the phase composition and the orientation of the microstructure. The specimens with no applied load were compared with the strain-loaded specimens.

The fatigue sample geometry is shown in Fig. 1 and was chosen according to the ASTM E606 [22] standard. A clamping area length of 55 mm was used to ensure sufficient grip. The measurement area has a length of 16 mm with a diameter of 8 mm.

To reduce the influence of the surface roughness on the fatigue behavior, the tensile and fatigue specimens were ground and polished on a lathe. First, sanding papers with a grain size of 320, 500, 800 and 1000 (each for 4 min) were used. Subsequently, two polishing steps with zirconia aluminum abrasive and a polishing paste with 6 µm and 3 µm (each for 5 min) diamond slurry were applied. After the polishing step, the surface roughness was measured with a Keyence VK-X1000 3D laser scanning microscope. A multiline roughness profile with a length of 6 mm was measured, consisting of 65 lines.

Tensile testing was done employing a Zwick 100 hydraulic testing machine. For strain-controlled fatigue testing an Instron model 8032 using the Instron 8500 digital control with a dynamic load capacity of ±100kN was used in combination with a clip-on extensometer (L_0 = 12.5 mm). A strain ratio of $R = -1$ was applied with a strain rate of 0.004 s^{-1}. To investigate the microstructure, the specimens were cut inside the measuring range, hot embedded in epoxy resin, ground, polished and etched for 30 s. The used etchant was Beraha II as well as V2A-etchant. The pictures of the etched samples were taken with a Leica DM4 B light microscope (LM). The porosity was measured with a GE Phoenix Nanotom S µ-computed tomography machine with a voltage of 180 kV. A copper filter with a thickness of 0.5 mm was used to reduce the beam hardening effect. The number of projections was set to 1440 with a change of the angle of 0.25° per image and an exposure time of 1500 ms. With that setup, a resolution of 3.749 µm/voxel was achieved. The µ-CT-measurements were performed for one sample of each parameter set. An area of 4 mm in height and 8 mm in diameter was measured. The fracture surfaces were investigated by scanning electron microscopy (SEM) using a Zeiss Leo 1530vp. The phase composition, as well as the possible formation of twins and the orientation of the material was measured by electron backscatter diffraction (EBSD) with an EDAX EBSD-system and a Hikari EBSD-camera.

Table 1
Applied laser parameters for the fatigue and tensile samples.

Laser parameter set	Energy density [J/mm³]	Scanning velocity [mm/s]	Laser Power [W]	Layer thickness [µm]	Hatch distance [µm]
E1	52.08	1000	250	40	120
E2	65.97	600	190	40	120

3. Results and discussion

3.1. Metallographic analysis

3.1.1. Porosity and surface roughness

In order to draw the conclusions about the material properties of the specimens of both parameter sets correctly, a quantification of the porosity is fundamental. Pores in the additively manufactured material represent a decisive factor in failure behavior [23]. Parameter set E1 resulted in a density of 99,948%. Parameter set E2 however achieved a density of 99.996%. Fig. 2 shows the number of pores and their respective sphericity. It can be seen that parameter set E1 has a higher number of pores with a lower sphericity compared to parameter set E2, which shows a prevalence for more spherical pores. This is consistent with the statement of [1], as energy density E1 is theoretically outside the stable melting zone.

After the polishing, an average surface roughness of Ra = 0.592 µm and Rz = 4.179 µm was measured. Fig. 3 shows the surface roughness profile of the measurement.

Since the grinding and polishing was conducted with the same amount of pressure and time, it is assumed, that the other samples resulted in roughly the same values, diminishing the influence of the surface roughness on the crack initiation during fatigue testing [24–26].

3.1.2. Melt pool geometry

Fig. 4 represents light microscope images for etched samples of parameter set E1 (left) and parameter set E2 (right) each at 50 times magnification. With respect to the melt pool geometry, no decisive differences can be found between the two parameter sets. Both images show continuous melt traces, with hardly any difference in continuity between parameter sets E1 and E2. Also visible is the changing scan direction per layer. The width of the melt traces can be accurately measured from light microscope images at 100 times magnification and is about 120 µm for both parameter sets. Thus, the used hatch distance of 120 µm can be validated.

3.1.3. Cell sizes

Fig. 5 shows a SEM-image of a specimen, manufactured with laser parameter set E1. It is magnified 15,000 times, etched with V2A-etchant which reveals the cells and their grain boundaries. An average cell size

Table 2
Experimental design with type and number of specimens for each conducted type of investigation.

Laser parameter set	Applied strain amplitude						Tensile testing	Microstructure
	0.5%	1.0%	1.5%	2.0%	2.5%	3.0%		
E1	3	3	3	3	3	3	3	1
E2	3	3	3	3	3	3	3	1

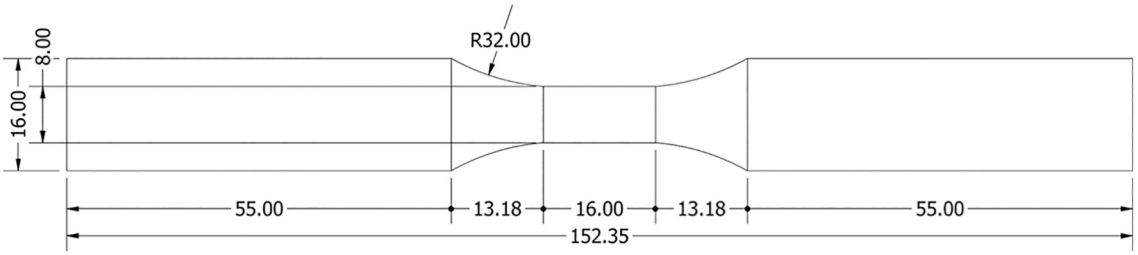

Fig. 1. Fatigue specimen geometry with dimensions in mm according to ASTM E606.

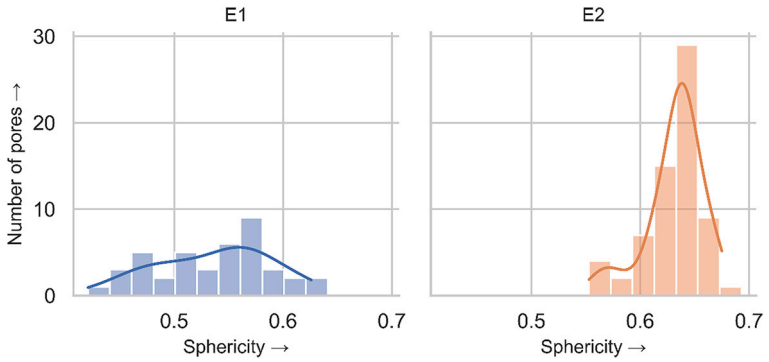

Fig. 2. Number of pores vs. the sphericity of the fatigue specimens of laser parameter set E1 (left) and E2 (right) with a kernel-density estimation (KDE) graph.

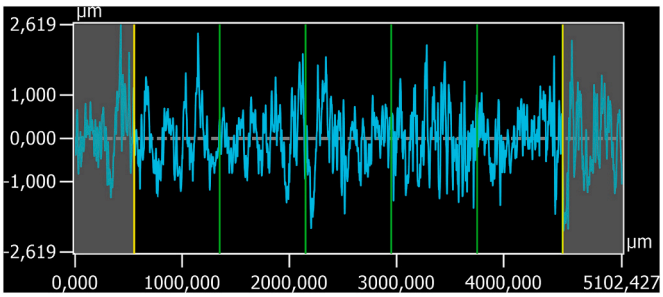

Fig. 3. Surface roughness profile of the multiline surface roughness measurement.

of 656 nm was measured in this picture by applying the line intercept technique according to ASTM E112–13 [27].

However, there are also areas in which the cells show balanced expansions in all directions, but the cell size differs significantly. This can be seen in Fig. 6. It is recognizable, that the cell sizes change depending on the investigated area. There are always areas in which the cells are significantly larger or smaller than in others. This is due to the fact that different orientations occur, since an x-rotation hatch strategy was used for manufacturing. With a separate measurement of the largest and smallest diameter of the cells and a comparison of these, it is possible to roughly infer the angle at which the cells intersect the image plane. Fig. 6 shows light microscope images at 1000× magnification of the microstructure of an etched sample with Beraha II of laser parameter sets E1 and E2. It can be seen, that the cell sizes differ not only from E1 to E2, but within one image section. This confirms the statements from [28], that the cell sizes are dependent on the location and the investigation angle.

For an initial estimation of the cell sizes, an optical microscope can be used as well, as it can represent several cell areas. This seems to be a more suitable method if compared to an exact determination of only a few cells with a large magnification by using a SEM. However, in such heterogeneous microstructures with varying grain and sub-grain areas, images for a global determination of the cell sizes of a whole sample may pretend a false accuracy. This is due to the fact that the orientation of the cell sizes results in the course of the PBF-LB/M process. The orientation establishes due to the complex thermal situation in a conflict between the variable thermal gradient and the variable solidification rate [28]. Fig. 7 shows a schematic of the dendrite growth formation after the melting of metal powder with a laser.

Depending on the location of the cell, different cell diameters are measured. This is due to the inclination in which the dendrites intersect the image plane and how the thermal gradient and the solidification rate are formed in the relevant point of the molten bath. Thus, the orientation of the dendrites mainly follows the direction of the thermal gradient. The preferred crystallographic direction as well as the cell size is determined by the cooling rate. This means, that the thermal gradient is highest at the bottom of the melt pool and the solidification rate is highest at the melt pool boundaries [29,30]. Therefore, the cell size cannot be independent of its point of location.

However, if the cell sizes, or the subgrain sizes, are to be determined quantitatively and precisely, a new method is proposed here, namely a correlation with the dislocation density. The dislocation density can be measured by electron channeling contrast imaging (ECCI), transmission

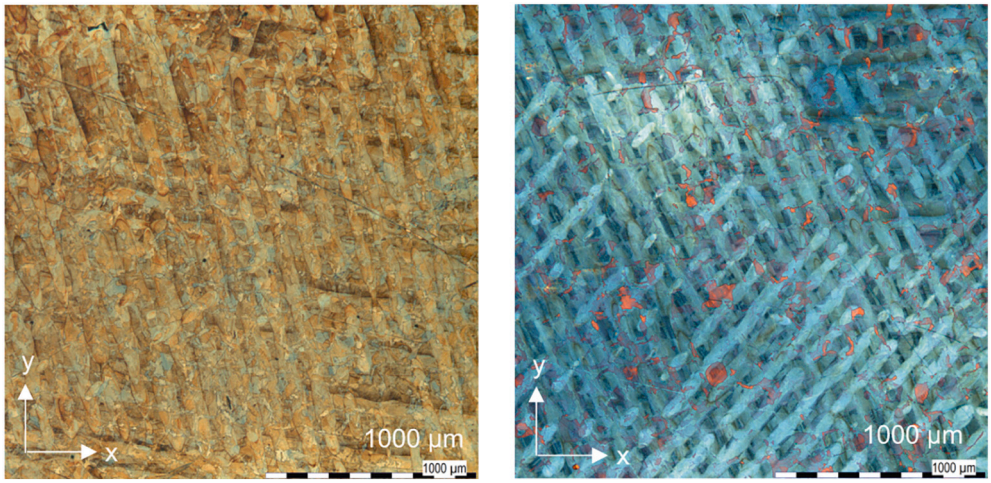

Fig. 4. Light microscope images (50 times magnification, Beraha-II etching) of a sample of parameter set E1 (left) and parameter set E2 (right).

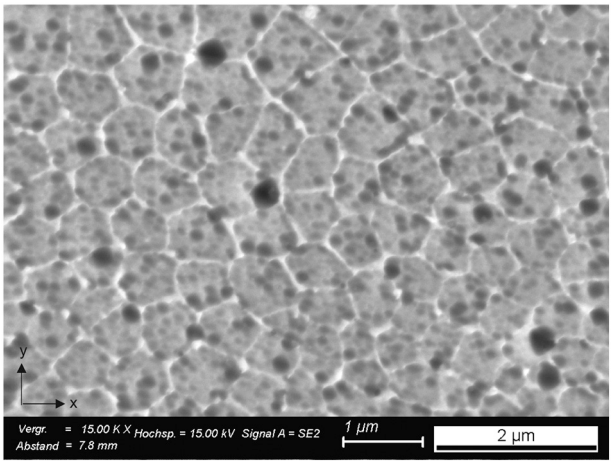

Fig. 5. SEM-image of a sample of laser parameter E1, 15,000× magnification, V2A-etchant, showing the cells and their grain boundaries. The average cell diameter is 656 nm.

electron microscopy (TEM), as well as x-ray diffraction (XRD) [31]. If the cell sizes of a sample tend to be smaller, the dislocation density must increase, since the dislocation-poor areas in the center of the cells become smaller [28,32]. One could also argue that the spacing of the cell walls decreases. In addition, the high dislocation density of PBF-LB/M manufactured samples is due to the high solidification rate, which plays an important role in scaling the subgrain size in terms of the cooling rate. Thus, by comparing the dislocation density of two parameter sets, one could infer the cell sizes and, subsequently, relate to consequences in the material microstructure. However, to compare two specimens with different laser parameter sets, a broad volume should be measured. This is only possible with electron synchrotron methods.

3.2. Mechanical properties

3.2.1. Tensile testing

The results of the tensile tests of the additively manufactured specimens are summarized in Table 3. In Fig. 8, the obtained tensile stress [N/mm^2] - tensile strain [%] curves for each respective specimen of the parameter sets E1 and E2 until the elongation at fracture are shown.

It can be seen that the specimens of parameter set E1 achieved higher tensile strengths than the specimens of parameter set E2. Specimen E1_3 in particular has a high tensile strength of 651 MPa. It is also noticeable that the samples manufactured with parameter set E1 reach a lower

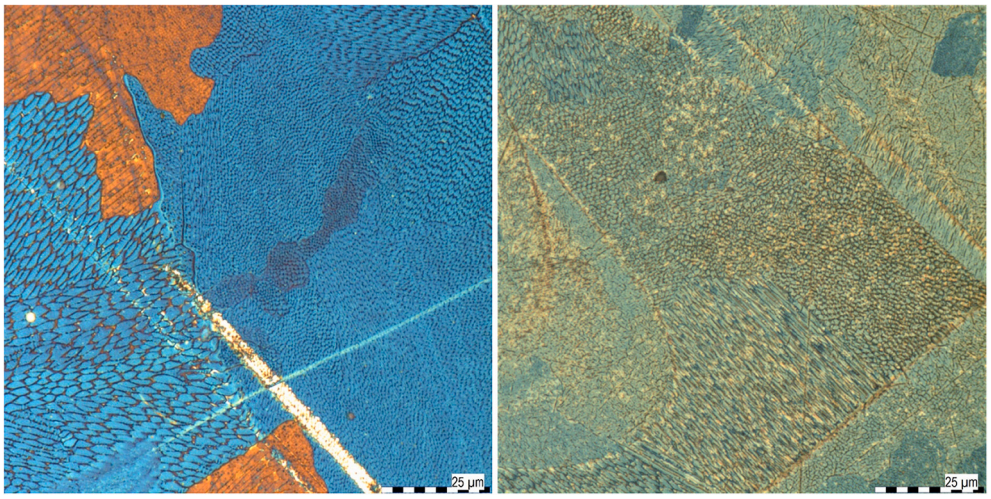

Fig. 6. Light microscope images at 1000 times magnification (Beraha-II etchant) of the microstructure of a sample of parameter set E1 (left) and parameter set E2 (right).

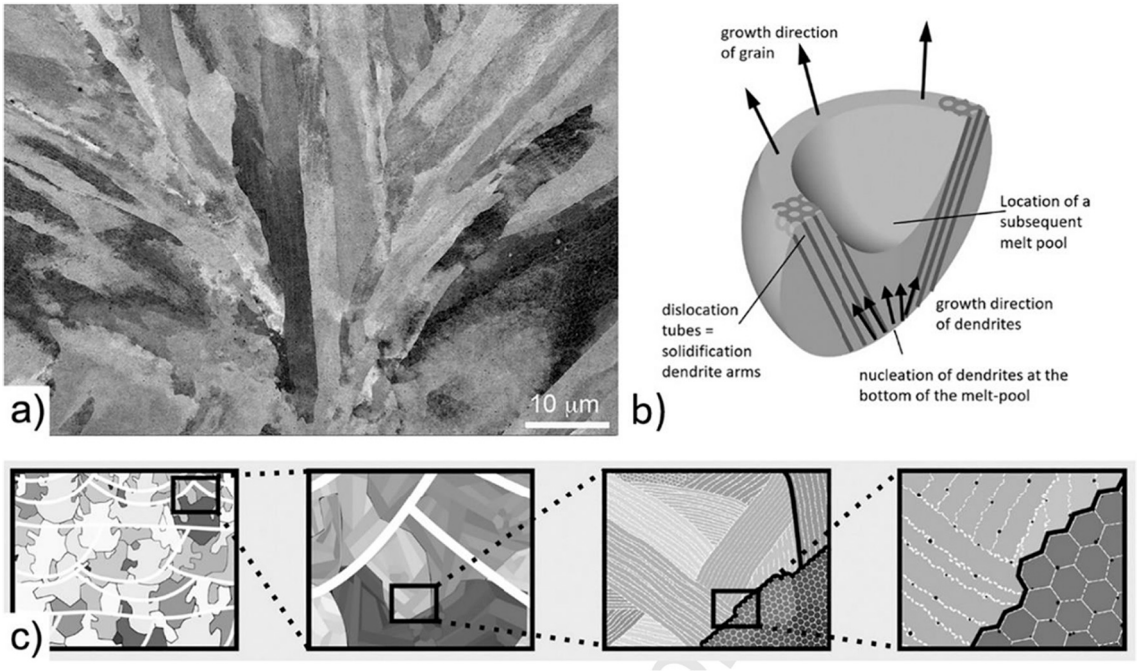

Fig. 7. Growth of dislocation cells from Godec: (a) Energy channeling contrast imaging (ECCI) micrograph of dendrite growth. (b) Schematically shown dendrite formation and growth direction. (c) Sketch of hierarchical PBF-LB/M structure development, extracted from [28].

Table 3
Results of static tensile tests of specimens of parameter sets E1 and E2.

Specimen number	$R_{p\ 0.2}$ [MPa]	R_m [MPa]	A_5 [%]	Standard deviation $R_{p\ 0.2}$ [MPa]	Std. deviation R_m [MPa]	Mean value $R_{p\ 0.2}$ [MPa]	Mean value R_m [MPa]
E1_1	464	634	48.5	12.3	8.0	480.0	639.7
E1_2	482	634	54.1				
E1_3	494	651	44.5				
E2_1	459	612	56.9	4.5	2.5	455.3	611.3
E2_2	449	614	59.1				
E2_3	458	608	53.6				

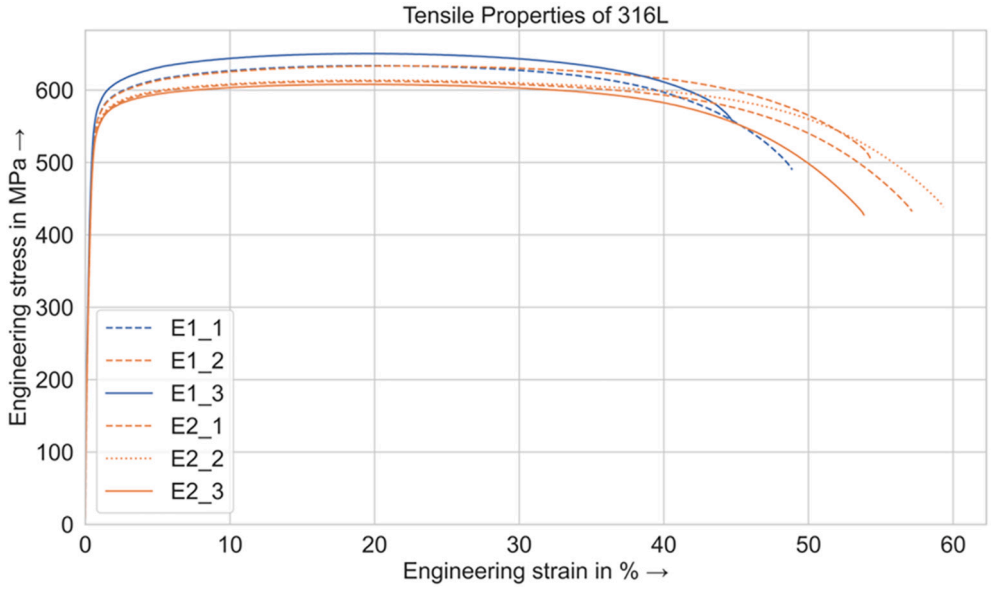

Fig. 8. Stress-strain diagram of quasi-statically tensile loaded specimens of parameter set E1 and parameter set E2.

elongation at fracture, with the sample measuring the highest tensile strength achieving the lowest elongation at fracture.

The quantitative analysis of the tensile tests is described in Table 3, where it can be observed that the largest difference between the achieved tensile strengths (R_m) was 43 MPa between the specimens E2_3 and E1_3. On average, the specimens manufactured with parameter set E1 have a tensile strength of 639.7 MPa with a standard deviation of 8 MPa. The specimens manufactured with parameter set E2 have an average tensile strength of 611.3 MPa with a standard deviation of 2.5 MPa. The average difference between the two build jobs is therefore 28.4 MPa. The same difference in strength can be seen for the yield strength ($R_{p0.2}$). Here, the average difference amounts to 24.7 MPa between parameter set E1 and parameter set E2, and the maximum difference is 45 MPa between specimens E1_3 and E2_2.

The standard deviation of the yield strength $R_{p,0.2}$ of parameter set E1 is 12.3 MPa, with a maximum difference of 30 MPa between E1_1 and E1_3. This deviation can be explained with Fig. 9. Fig. 9(a) shows the fracture surface of specimen E1_1. A large quantity of lack of fusion pores with a diameter of up to 200 µm were observed, magnified in Fig. 9 (c) and (d). This concurs with the results from the porosity measurements. It is assumed, that the larger quantity of lack of fusion pores leads to a reduction of the yield strength. Lack of fusion pores exhibit a low sphericity, which lead to local stress concentrations [33]. Hence, the yield strength is reached faster. This results in a local plastic deformation and therefore an earlier crack initiation.

Also highlighted is the difference between the elongations at fracture, which amount to a maximum difference of 14.6% between sample E1_3 and sample E2_2. As mentioned previously, the samples of parameter set E2 reach higher elongation at fracture values, with an average of 57%, compared to an average of 49% for the samples of parameter set E1, but also show significantly lower tensile strengths.

3.2.2. Summary of tensile testing

In summary, a clear tendency was observed that the specimens manufactured with parameter set E1 achieved higher static strengths than the specimens of parameter set E2. These specimens were produced with a lower energy density of 52.08 J/mm^3, in contrast to 65.97 J/mm^3 of parameter set E2. The product of the thermal gradient and the solidification rate (G*R) controls the expansion of the cells. Hence, a higher solidification rate results in smaller cell diameters. The relationship between the cell expansion and the higher tensile strength and tensile stress at the yield strength can be described with the Hall-Petch relationship. It explains the increase in strength due to grain refinement [16,17]. According to recent studies [28,34,35], this relationship can also be applied to the reduction of the cell diameter in additively manufactured specimens. This is conclusive, since cell walls consist of a dense dislocation network, which, similar to grain boundaries, can inhibit the movement of dislocations. This results in a buildup of dislocations, which in turn contributes to the increase of stress generated in the material. In the following, the Hall-Petch relationship formula is applied, using the parameters evaluated in [35]. These are $\sigma_0 = 188\ MPa$ as the starting stress for dislocation movement as well as $k_y = \sqrt{275}\ MPa{\cdot}\mu m$ for the strengthening coefficient. For the resulting yield stress, the average yield stresses obtained for the respective parameter sets E1 and E2 are used. Solving the Hall-Petch formula for the grain size diameter d, parameter set E1 equates to a cell diameter 180 nm smaller than compared to the parameter set E2. However, this calculation should be considered merely as a theoretical estimate. Since due to the complex thermal situation during solidification of the melt baths mentioned above, the cell size for an entire sample cannot be exactly

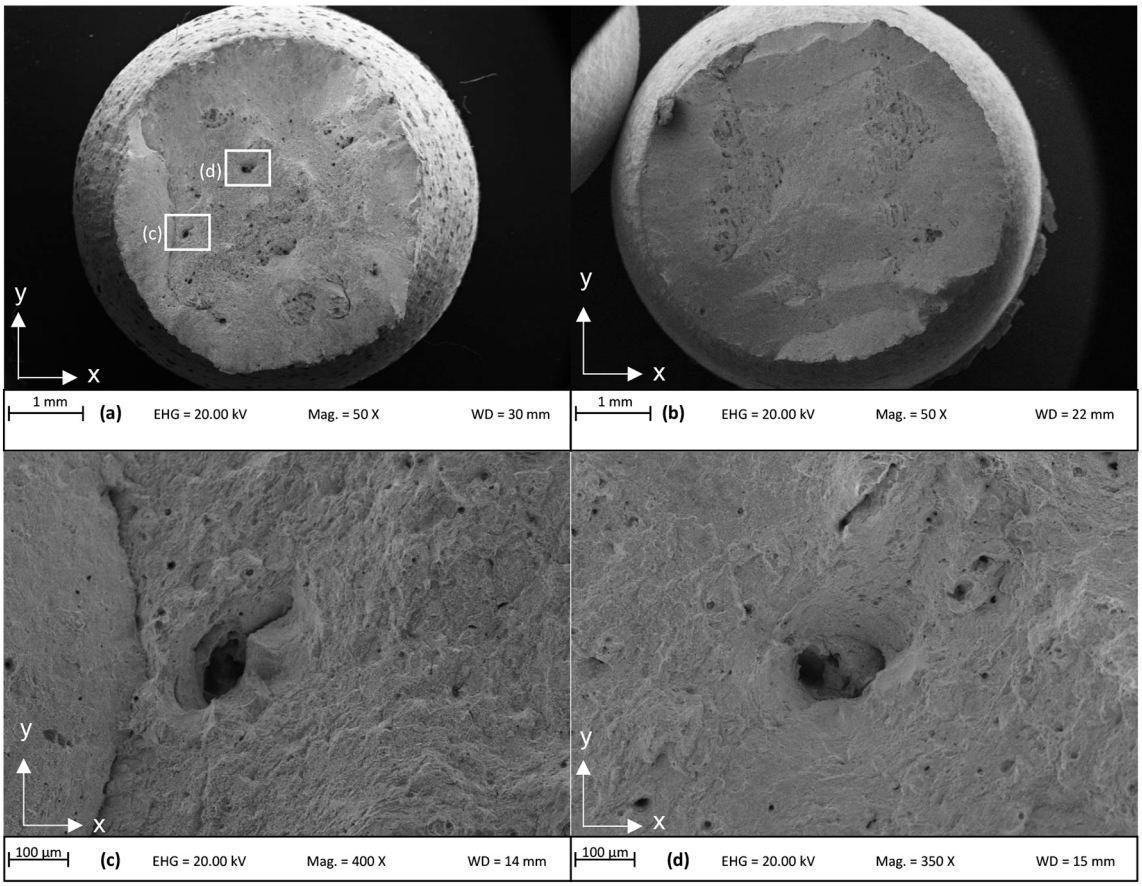

Fig. 9. SEM fracture surfaces of specimen E1_1 (a) and E1_3 (b), (a) showing a large quantity of lack of fusion pores (see (c) and (d)), (b) showing lower quantity of pores overall and pores assumed to be gas pores.

determined yet. If the average cell diameter of a sample can be determined in the future using new methods (possible correlation via dislocation density), the difference in cell diameter calculated here will provide a comparison.

The elongation values of all investigated specimens are above 44.5%, with the average value being 52.8%. Following the example of the investigation by [36], the investigated specimens are incorporated in Fig. 10. Hence, all the specimens are within the green range (target range), which indicates a good quality of the two parameter sets E1 and E2. The results from the investigation according to [36] can also be confirmed, which reinforce the fact that vertically produced specimens exhibit a higher elongation at fracture than horizontally produced specimens as can be seen in Fig. 10.

Also noticeable in Fig. 10 is the fact that all specimens of the same parameter set are in clearly separated groups. Thus, the affiliation of the individual specimens to the respective parameter set is already evident merely from the distribution of the diagram points, since both the results of the specimens of parameter set E1 and those of parameter set E2 are close to each other. This fact should also emphasize that different process parameters, represented here by the scanning speed and the laser power, have an influence on the material properties of samples produced by means of a PBF-LB/M process. Thus, in this work, it can be argued that in PBF-LB/M, by choosing different laser parameters, it is possible to selectively control the material properties depending on the required purpose (strength, elongation at fracture).

The lower standard deviation of the results of the parameter set E2 is also worth mentioning. From this, a conclusion can be drawn concerning the assessment of the harmfulness of the defects. In the literature, the prevailing opinion is that existing defects are the main contributors to the early failure of the specimens in relation to the maximum number of cycles endured or the elongation at fracture achieved [37]. Thus, based on the higher elongation at fracture of the specimens of parameter set E2, it can be concluded that there are fewer harmful defects and pores around which stress concentrations could form, a circumstance which could explain the lower standard deviation of the results of parameter set E2. This can also be seen in Fig. 9 and agrees with the porosity measurements.

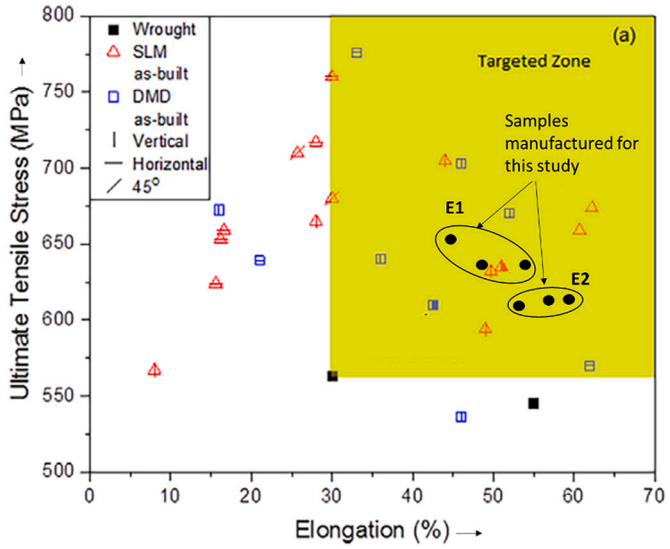

Fig. 10. Incorporated results of the static tensile tests of the specimens of the parameter sets E1 and E2 into the diagram according to [36], which sets the tensile strength achieved in relation to the elongation at fracture. Also shown are many results of other PBF-LB/M specimens from the literature (SLM in the legend) for which the direction of manufacturing is marked with vertical, horizontal or diagonal lines. The area marked in green indicates a good quality of the resulting part. (For interpretation of the references to colour in this figure legend, the reader is referred to the web version of this article.)

3.3. Strain-controlled fatigue testing

A plot of the maximum stresses in the tensile and compressive range versus the cycles endured on a semi-logarithmic scale is particularly well suited for depicting the hardening and softening behavior of specimens produced by PBF-LB/M. These plots provide a good overview of the fatigue behavior of materials, since a wide range of applied strain amplitudes are summarized. Fig. 11 and Fig. 12 show a respective plot for the specimens manufactured with parameter set E1 and parameter set E2. They display the curves resulting from the alternating application ($R = -1$) of different strain amplitudes in the range of 0.5 to 3.0% with a strain rate of 0.004 1/s separately for the tensile and compression ranges.

The curves of both parameter sets clearly show, that the material behavior differs only slightly between the strain amplitudes. Over almost the entire cycle range, the material softens with an increase in cycles. It is also evident that the softening decreases more with an increase in strain amplitude. Table 4 and Table 5 present a quantitative analysis of the softening achieved for the applied strain amplitudes.

It is shown, that the absolute values of the stresses at tension and compression are not symmetric. The tension-compression stresses change with increasing strain amplitude with a maximum difference of 211 MPa for parameter set E1 and 135 MPa for parameter set E2 respectively. Lam, Wu et al. [38] mainly attribute the asymmetry behavior to the dislocation density and the phase transformation of the material during cyclic plastic deformation. The influence of the porosity was stated as a secondary effect.

The focus in this study however lays on the stresses in the tensile range, since this corresponds to the common evaluation method in literature [20,39]. Moreover, the critical material behavior due to the formation of cracks is more likely to be expected in the tensile range. The aim of these tables is to clarify the relationships between the curve progressions in Fig. 11 and Fig. 12. For this purpose, a new characteristic value is introduced, which is called $Cycles_{\Delta\sigma,80\%}$. This denotes the number of cycles at which 80% of the total tensile stress difference relieved in the course of softening is reached. Furthermore, this value is related to the maximum number of cycles before the begin of failure of the respective test (here denoted by $Cycles_{tot}$). Note that this value does not correspond to the total number of cycles in terms of fatigue life (number of cycles until crack initiation), since this is usually associated with a 10% decrease in stress with respect to that in the stabilized region. The change of maximum tensile stress from the beginning to the $Cycles_{\Delta\sigma,80\%}$ is called $\Delta\sigma_{softening}$ in Table 4 and Table 5. However, only the softening behavior before the beginning of the failure was considered in this paper. This means that the area, which shows a clear increase of the softening rate and initiates the subsequent failure, is disregarded.

The characteristic values in Table 4 and Table 5 as well as Fig. 11 and Fig. 12 indicate, that the shape of the curves is almost identical when compared with each other, regardless of the applied strain amplitude. Summarizing this in numerical terms, 80% of the total tensile stress difference during softening is always relieved within the first 25% of the total cycle range. Most of the softening of the specimens loaded with a strain amplitude of 0.5% to 2.0% occurs in the first quarter of the total cycle range. Also noticeable is the fact that as the strain amplitude increases, the softening decreases, from 158 MPa at an applied strain amplitude of 0.5% to 55 MPa at $\varepsilon_a = 2.0\%$ in case of parameter set E1. The tendency that with higher strain amplitudes the ratio $cycles_{\Delta\sigma 0\%}$ / $cycles_{tot}$ slightly decreases can be attributed to the fact that in the stable region of the maximum stress curve the softening rate also slightly decreases.

However, the previously mentioned descriptions of the softening behavior of the specimens become less definite with higher applied strain amplitudes. This circumstance begins to unfold from a strain amplitude of 2.0%. Here, the strengthening behavior is evident, which shows that a secondary hardening phenomenon may occur. Even if softening is present over the entire cycle range, the relieve of stresses

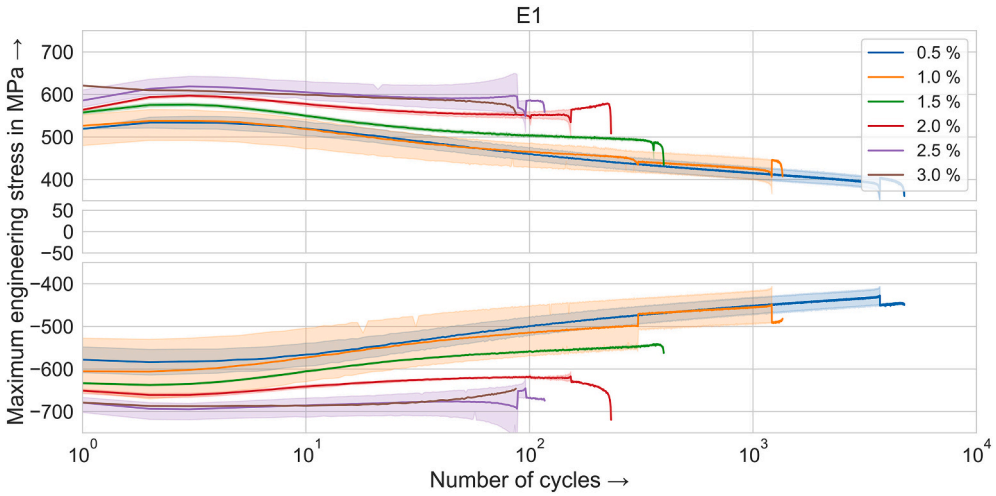

Fig. 11. Plot of the maximum stresses per cycle in tension and compression over the endured cycles for the specimens of parameter set E1 for different strain amplitudes including the standard deviation at each cycle (colored surfaces).

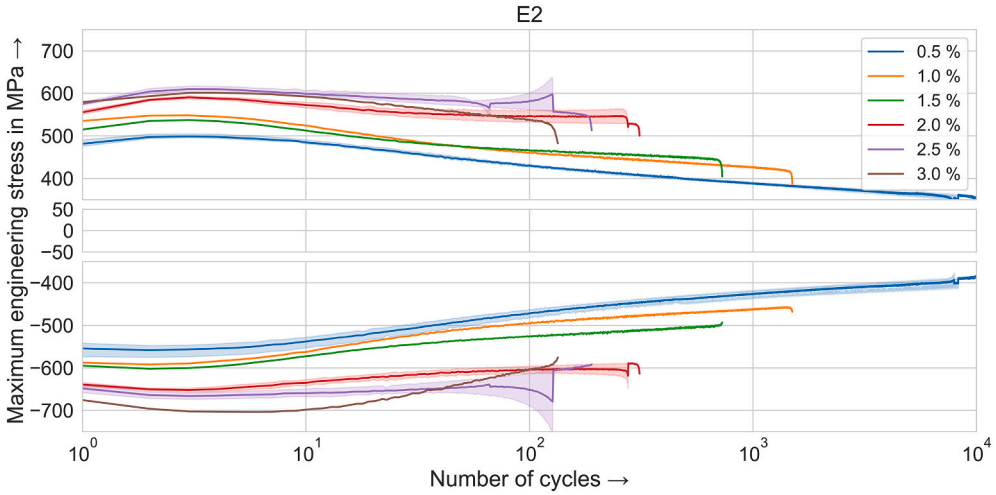

Fig. 12. Plot of the maximum stresses per cycle in tension and compression over the endured cycles for the specimens of parameter set E2 for different strain amplitudes including the standard deviation at each cycle (colored surfaces).

Table 4
Quantitative analysis of the maximum stress curves of the parameter set E1.

Strain amplitude [%]	$\Delta\sigma_{softening}$ [N/mm^2]	$Cycles_{tot}$ [−]	$Cycles_{\Delta\sigma 80\%}$ [−]	$\frac{Cycles_{\Delta\sigma_{80\%}}}{Cycles_{tot}}$ [%]
$\varepsilon_a = 0.5$	158	4400	1100	25
$\varepsilon_a = 1.0$	125	1320	300	23
$\varepsilon_a = 1.5$	85	380	75	20
$\varepsilon_a = 2.0$	55	145	30	21

Table 5
Quantitative analysis of the maximum stress curves of the parameter set E2.

Strain amplitude [%]	$\Delta\sigma_{,softening}$ [N/mm^2]	$Cycles_{tot}$ [−]	$Cycles_{\Delta\sigma_{80\%}}$ [−]	$\frac{Cycles_{\Delta\sigma_{80\%}}}{Cycles_{tot}}$ [%]
$\varepsilon_a = 0.5$	147	9000	2100	23
$\varepsilon_a = 1.0$	133	1460	350	24
$\varepsilon_a = 1.5$	95	700	140	20
$\varepsilon_a = 2.0$	61	300	47	16

occur in a different way than previously described at strain amplitudes from higher than 2.0%. The stresses are relieved more uniformly and the softening phase in the first few cycles for both sets of parameters is less distinct. It shows that it takes significantly more cycles to relieve 80% of the total softening. Even though the specimens exhibit persistent softening behavior. For example, in the case of the specimens of parameter set E1 loaded with a strain amplitude of 3.0%, 80% of the total softening occurs after 82% of the total cycles endured. It is assumed, that there is a hardening process that counteracts the softening present in all specimens in the first few cycles. At lower strain amplitudes, the softening phase is dominant and no secondary hardening phenomenon is observed. However, at higher strain amplitudes of 2.5% and above, a secondary hardening phenomenon is visible. One phenomenon that could be considered as the hardening process sought for this steel grade is mechanical twinning, which is already known in the literature for additively manufactured specimens [14,32,40]. The reason for the higher probability of occurrence of this behavior in AISI-316L steel is, on the one hand, its low stacking fault energy, which leads to the formation of extended and, due to the more difficult necking possibility, to stable planar stacking faults. On the other hand, the face-centered cubic crystal structures with a large number of possible slip systems allows these stacking faults to come close to each other and eventually form twin

boundaries. Moreover, these microtwins tend to form only at higher strain ranges [41]. This could explain the fact that at smaller strain amplitudes of up to 2.0%, the softening phase remains unaffected.

This is supported by the fact that the probability of mechanical twinning occurrence increases mainly at higher strains in the range of 20% to 50%. Effectively, for both sets of parameters at smaller strain amplitudes (up to 2.0%), the softening phase seems to remain unaffected in the initial region of the first quarter of the lifetime, leading to an earlier onset of the softening tendency as the strain amplitude increases. As shown by Wang et al. [14], the mechanically formed twins first penetrate the cell walls in the form of microtwins, decreasing the expansion of the cells and further lowering the mobility of the dislocations by subdividing the cells, which could explain the decrease in strain softening rate, or the hardening phenomena. The fact that there is not always a dominant strain hardening could be due to the mechanically formed twins, which in turn contribute to plastic strain by their lenticular shape. The hypothesis of micro-twinning is further supported by Shamsujjoha et al. [32], who discovered that vertically manufactured specimens, as those produced in this work, possess a higher tendency to twinning than horizontally manufactured ones. Thus, mechanical twinning could be considered a hardening process counteracting the initial softening present in all specimens. At first, this process leads to a decreasing softening rate in the stable region of the maximum stress curve at smaller strain amplitudes and, at higher strain amplitudes, it eventually affects the softening phase at the beginning of the service life and can lead to hardening phenomena.

To support this thesis experimentally, microstructural examinations of a specimen were carried out after cyclic testing using a light microscope. The specimen had previously been loaded cyclically until failure with a strain amplitude of 3.0%. A changed structure was evident, which can be explained as mechanically formed twins and is depicted in Fig. 13. Those changes were not detected in the microstructural examinations of unloaded specimens and thus appear to occur in the course of plastic deformation. The microstructures are illustrated in Fig. 13, which show the transverse section in the gauge length of the specimen geometry of the previously mentioned specimen at 500 times and 1000 times magnification, respectively. The areas colored in red show microstructural crack-like structures, which are similar in shape and size to a mechanical twinning in an additively manufactured AISI-316L steel [32]. As different colour regions show different crystal orientations, the grain region depicted in red is interspersed by lens-like structures with different orientation, as may occur in a mechanical twinning.

The starting point for the following explanation is the background for the formation of the present microstructure. The PBF-LB/M-process, by using a high-energy laser in combination with a fast movement, causes a melting with subsequent solidification. The melting takes place in the range of microseconds. This results in crystallization, which, due to the high solidification rate, is not flat but tends to be cell-like and dendritic [29]. The formed dendrites split again into finer dendrites due to the complex thermal gradient. Additionally rotational changes due to thermal stresses attract dislocations in order to compensate for these small differences in orientation [28]. Subsequently, the material solidifies so rapidly, that diffusion and recovery processes barely pose an influence, which may result in an energetic imbalance in the dislocation network. It is assumed that the material does not have sufficient time to approach an energy minimum [42,43]. If a cyclic load in the plastic range is applied to the material, a large accumulated plastic strain is induced, especially in the alternating range of $R = -1$. This allows the dislocations to move and approach an optimal energy minimum. During the process, the opposing dislocations annihilate each other. The equidirectional dislocations increase their distance from each other. The stacked dislocations may reach a more stable position relative to each other. Expressed in terms of back stress, the intragranular and intergranular back stress components can thus decrease. These aforementioned phenomena could explain the softening phase at the beginning of the fatigue tests. This thesis could be supported by an evaluation of the internal stresses throughout the complete stress-strain hystereses over all endured cycles using the Handfield-Dickson method [44]. Thereby, it is possible to trace the evolution of the intra- and intergranular internal stress components over the cycle range. Another possibility would be measuring and then comparing the dislocation density at the start of the fatigue tests and at the end of the softening phase. If the dislocation density decreases or increases significantly less, as is usual for conventional steel, this can be seen as a confirmation of this thesis.

A phenomenon that still requires an explanation is the changing softening behavior at higher strain amplitudes. The material softens with a significantly higher softening rate at smaller strain amplitudes within the first quarter of the entire cycle range. However, this behavior changes from an applied strain amplitude of 2.5% and the softening in the initial range of the fatigue test is less pronounced. One assumption for the changing behavior at higher strain amplitudes could be that more mechanically formed twins form earlier. Additionally, the latter could provide a strengthening due to the subdivision of the cell structures and the associated shortening of dislocation movements, and on the other hand, they may partly contribute to the plastic strain. If microtwins form primarily under higher strains, they could also form earlier during

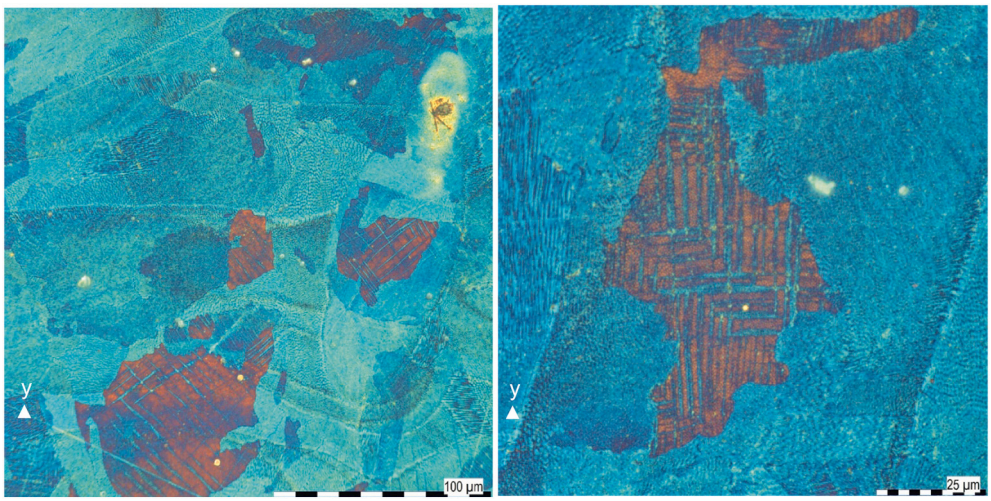

Fig. 13. Light microscope image at 500 times (left) and 1000 times magnification (right, Beraha-II etchant) of the microstructure of a specimen loaded to failure (ε_a = 3.0%). The red areas in this view could show grains interspersed by mechanical twinning. (For interpretation of the references to colour in this figure legend, the reader is referred to the web version of this article.)

fatigue testing at higher strain amplitudes. Added to this could be the fact that with a higher number of microtwins forming, the strengthening effect of micro-twin formation increases as the dislocation movement is increasingly inhibited. Therefore, EBSD measurements were carried out at strain amplitudes $\Delta\varepsilon$ of 0.0%, 1.0%, 2.5% and 3.0%. To measure mechanical twinning, the intergranular misorientations are shown for a range between 58° and 62°. This was shown in [45,46], regarding AISI-316L, that the misorientation at around 60° can be traced back to mechanical twinning. The results are shown in Fig. 14, where the intergranular misorientations as well as the image quality are presented. The applied plastic strain to a specimen degrades the image quality [47]. If a high magnitude of darker areas is present, the deformation of the specimen is also high. In Fig. 14 (a), a light pattern is revealed. Fig. 14 (c) and (d) show a dark pattern, substantiating the statements made in [47].

At a strain amplitude of $\Delta\varepsilon = 0.0\%$, i. e. an unloaded specimen, only a negligible amount of twinning formation is achieved. With increasing strain amplitude, the magnitude of twinning formation increases. However, the mechanical twin fraction at a strain amplitude of $\Delta\varepsilon = 2.5\%$ shows a higher magnitude, compared to a strain amplitude of $\Delta\varepsilon = 3.0\%$. This can be explained using Fig. 11. The specimen loaded with a strain amplitude of $\Delta\varepsilon = 3.0\%$ did not experience a secondary hardening phenomenon. The specimen loaded with a strain amplitude of $\Delta\varepsilon = 2.5\%$ in contrary did experience a secondary hardening phenomenon. Hence, it can be assumed, that with the increasing mechanical twin formation, the hardening increases as well. Additionally, no phase transformation was detected via EBSD. Therefore, the strain hardening effect can be mainly attributed to twinning.

It should also be emphasized that all the previously described effects occur for parameter set E1 and E2 respectively, which means that a higher energy density does not pose any significant consequence in this respect. In addition, the almost congruent occurrence of the transient processes described for both parameter sets can be seen as confirmation of the same for the general fatigue behavior of additively manufactured

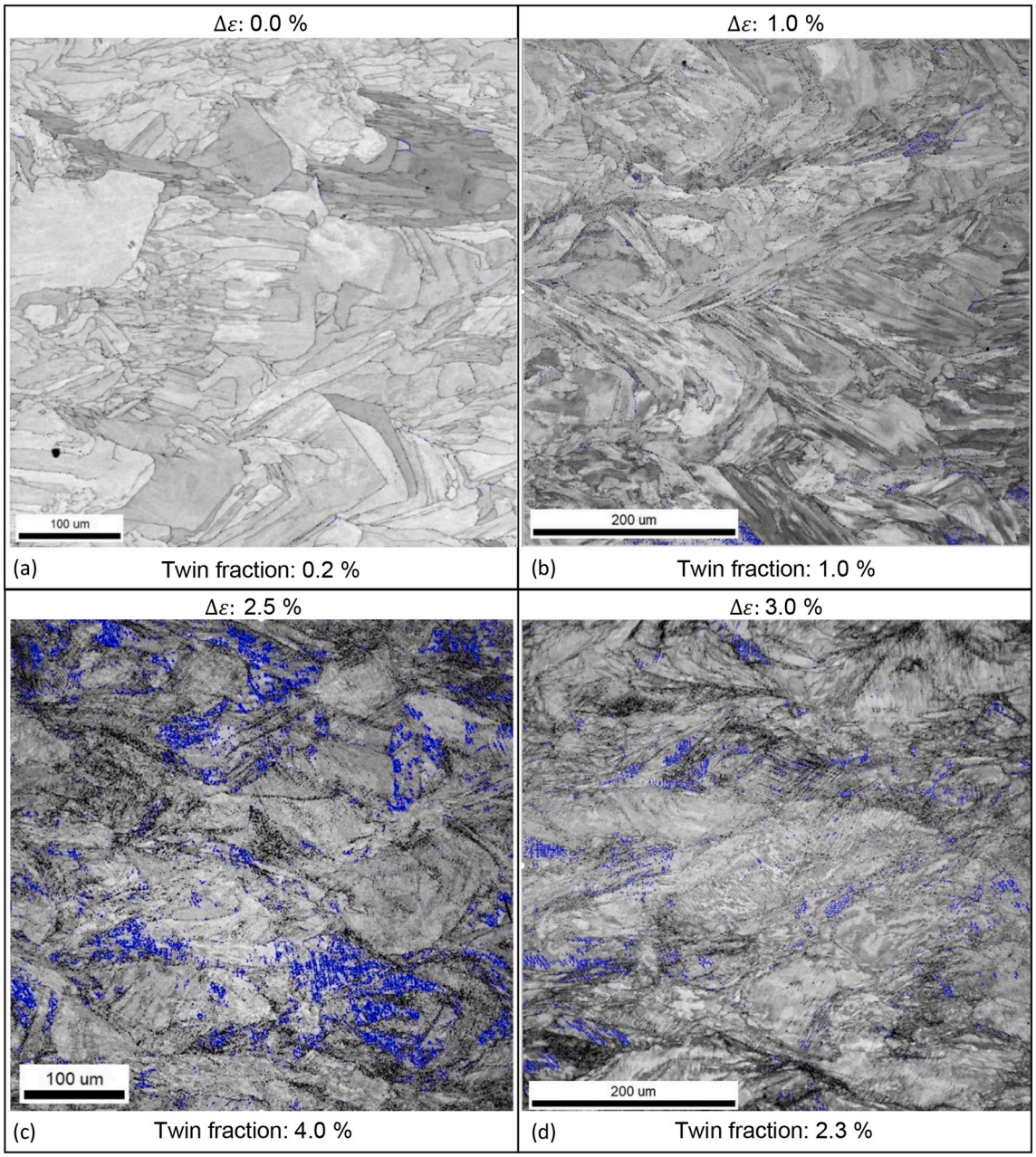

Fig. 14. Mechanical twin formation and image quality at different strain amplitudes, quantified by EBSD.

PBF-LB/M specimens in the low-cycle range.

To ease the comparison of the evaluation of the fatigue tests between the two parameter sets E1 and E2, Fig. 15 is introduced. This shows and compares the maximum stresses in the tensile range per cycle for parameter set E1 and parameter set E2. This figure is intended to give a general comparative overview. Therefore, aspects such as the stresses generated over the cycles and the lifetimes achieved are specifically brought up in separate figures and associated text sections and compared between the two parameter sets. However, it is already clear using this figure that different energy densities have a clear influence on the cyclic material behavior. Thus, the specimens of parameter set E1 show significantly higher maximum tensile stresses generated via the cycle numbers and, on the other hand, lower service lives. These aspects will now be examined in detail and taken up again in the associated sections.

The fact that different laser parameters, represented by a variance in scanning speed and laser power in this paper, have an influence on the static mechanical behavior of this material has already been proven in [10]. However, even if the transient processes remain approximately the same in both parameter sets, this does not apply to all mechanical aspects measurable in the course of a cyclic test. One of them concerns the achievable stresses. When comparing the visualization of the maximum and minimum stress curves over the endured cycles in Fig. 11, Fig. 12 and Fig. 15, it is noticeable that the specimens of parameter set E1 reach higher stresses than those of parameter set E2. However, since a detailed comparison of the stresses achieved between the two parameter sets using this figure proves to be difficult and only characteristic curves are included, Fig. 16 is introduced. It compares the stresses over the normalized number of cycles generated during the strain-controlled fatigue tests for all specimens investigated of each parameter set. For each applied strain amplitude, the mean stress and the calculated standard deviation confidence interval for all respective specimens are shown.

This diagram shows that the specimens of parameter set E1 generated higher stresses over the endured cycles than the specimens of parameter set E2. At a strain amplitude of 0.5% the difference was consistently at around 30 MPa, and at a strain amplitude of 1.5% the difference was as high as 50 MPa in some cases. Thus, the higher stress generation of the static tensile tests continues in the fatigue tests. This reinforces the fact that a variation in the laser parameter set influences the resulting mechanical behavior. This can also be attributed to the low-cycle fatigue range, whereby a lower energy density (parameter set E1) developed larger stresses. Additionally, the stresses of parameter set E1 remain higher than those of parameter set E2 at all characteristic points of the lifetime for all strain amplitudes. The stresses do not equalize over the endured cycles. This indicates a high stability of the cells, since the smaller cell diameter of the microstructure of parameter set E1 does not seem to increase over the entire cycle range compared to parameter set E2.

3.4. Determination of strain-based S-N-curve

Fundamental for the investigation of fatigue behavior is the number of cycles to crack initiation (N_f), the definition of which is not entirely clear. In [22], for example, a distinction is made between four criteria. These are the separation of the sample, the change of the Young's modulus, the stress drop and the microcracking. In this work, however, the number of cycles until crack initiation is characterized according to [48], to which cracking is assumed to occur at a stress drop of 10% compared to the stabilized upper stress. In the case of hardening behavior up to fracture, the maximum stress is chosen as the reference stress.

The Manson-Coffin equation is intended to describe the fatigue life of the material in the elastic and the plastic region. This means that this equation is becoming increasingly important in the low-cycle fatigue range, where fatigue tests are carried out at higher strain amplitudes than in the high-cycle range. Therefore, only the plastic part of this equation is particularly relevant to the results in this paper.

The plastic Manson-Coffin equation is described as the following:

$$\varepsilon_{a,p} = \varepsilon_f^{'}(2N_f)^c \tag{1}$$

The fatigue parameters that can be determined herewith are thus the cyclic ductility coefficient $\varepsilon_f^{'}$ and the cyclic ductility exponent c. The data required are the applied plastic strain amplitude $\varepsilon_{a,p}$ and the endured cycles to crack initiation N_f. There are several ways to determine the fatigue parameters, the most common being the linear regression method, which has been applied in this study [49].

Fig. 17 shows the estimation of the fatigue parameters $\varepsilon_f^{'}$ and c for the investigated specimens of the parameter sets E1 and E2 by means of linear regression. The applied strain amplitudes and the number of cycles until crack initiation are logarithmically plotted and the original experimental data can be approximated by a straight line.

After a linear approximation, for the parameter set E1 a cyclic ductility coefficient of $\varepsilon_f^{'} = 0.210$ and a cyclic ductility exponent of $c = -0.406$ result. The determination coefficient is $R^2 = 0.897$. In the case of

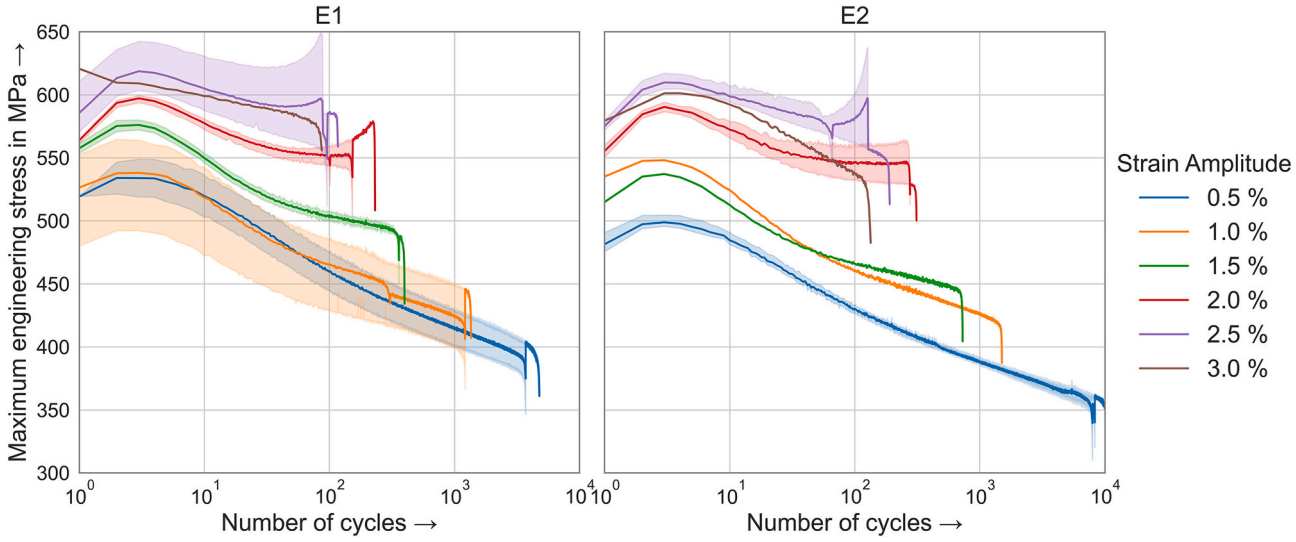

Fig. 15. Comparison of the maximum stress curves over the endured cycles between the parameter set E1 and the parameter set E2 including the standard deviation at each cycle (colored surfaces).

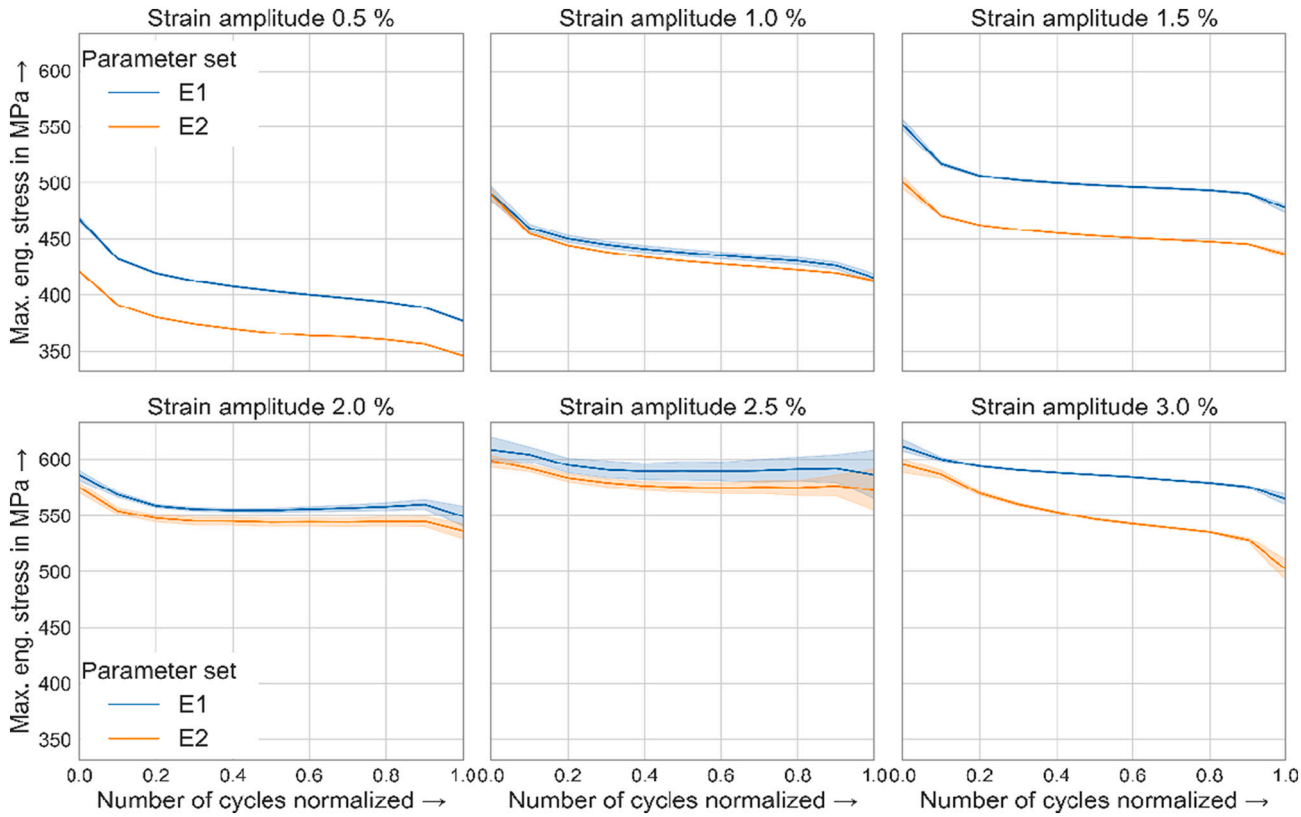

Fig. 16. Comparison of the average maximum tensile stress curves of parameter set E1 and E2 differentiated on the basis of the tested strain amplitudes and using a normalized representation of the elapsed number of cycles.

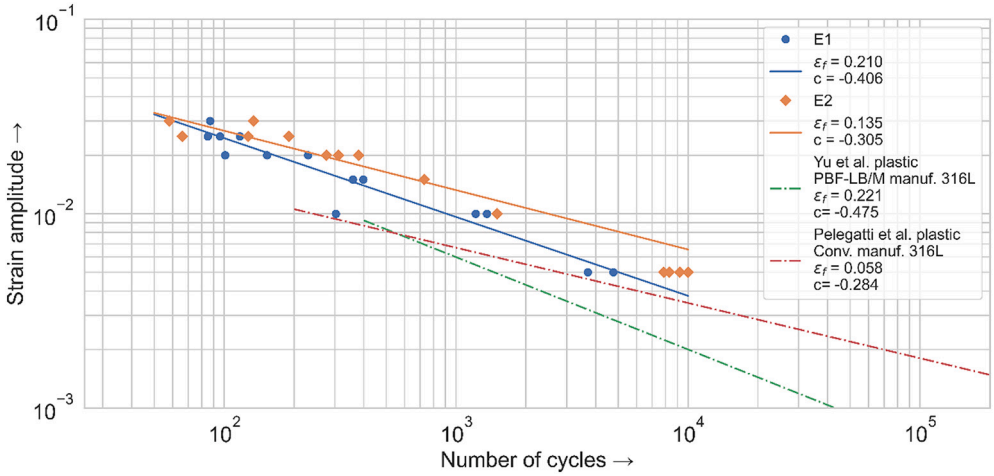

Fig. 17. Linear regression approximation of the plastic strain-based S-N-curve for the parameter set E1 (blue) and the parameter set E2 (orange) with indication of the determined fatigue parameters. These values are compared to the results of Yu et al. [20] and Pelegatti et al. [50]. (For interpretation of the references to colour in this figure legend, the reader is referred to the web version of this article.)

parameter set E2, a cyclic ductility coefficient of $\varepsilon_f^{'}$= 0.135 and a cyclic ductility exponent of $c = -0.305$ can be determined. The coefficient of determination is $R^2 = 0.921$. The values for the curve fit were calculated using Scipy [51].

By comparing the strain-dependent S-N-curves generated for the parameter sets E1 and E2 in a double-logarithmic scale (see Fig. 17), it becomes clear that, based on the specimens of parameter set E2, a strain-dependent S-N-curve with a lower inclination and therefore also a better fatigue life is obtained. While the differences are limited at higher loads, they are quite clear at the smaller strain amplitudes. The S-N-curves are also compared to the results from Yu et al. [20]. For comparison, the Manson-Coffin equation of Yu et al. is split up in the elastic and plastic approximation curve. Their tests show a similar behavior in the plastic range. This study is also compared to conventionally manufactured 316L of Pelegatti et al. [50]. Both parameter sets E1 and E2 show a higher fatigue life but have a steeper slope. The latter could be due to a lack of data at higher strain amplitudes for Pelegatti et al. [50] and a lack of data at lower strain amplitudes for this study.

When establishing a correlation with the static material properties, the thesis mentioned in the literature [52] is confirmed that in the case

of PBF-LB/M manufactured 316L steel, the fatigue strength is less related to the tensile strength or yield strength, as expressed in several estimation formulas for fatigue parameters for conventional steels, but seems to correlate with the elongation at fracture. In the static tensile tests of the specimens of parameter set E1 and parameter set E2, the result was that although the specimens of parameter set E1 had higher yield strengths and tensile strengths, the elongations at fracture were smaller than was the case for the specimens of parameter set E2. Consequently, the specimens of parameter set E1 tend to exhibit a poorer fatigue life.

In literature, the defects (e.g. lack of fusion porosity) resulting from the PBF-LB/M process in the material are also mainly blamed for the fatigue failure [35]. This agrees with the porosity measurement and the fatigue results of this study. The effect of defects on the fatigue life becomes more visible with a lower strain amplitude or a higher number of endured cycles. Thus, also on the basis of the results in the case of fatigue life, the thesis that different printing parameters, here represented by the scanning velocity and laser power, have a clear influence on the material behavior, both in static and dynamic terms, is strengthened.

4. Conclusions

From this study, the following conclusions can be drawn:

- A higher porosity leads to a lower number of cycles until failure due to stress concentrations of the pores, resulting in an early failure of the specimens.
- At every strain amplitude a primary softening behavior after the third cycle is observed.
- Most of the softening of the specimens loaded with a strain amplitude of 0.5% - 2.0% always occurs in the first quarter of the total cycle range.
- From a strain amplitude of 2.0% and above, the primary softening rate decreases, as most of the softening can take up to 82% of the whole lifetime.
- From a strain amplitude of 2.0% and above, a secondary hardening behavior is partly observed regardless of the laser parameters.
- The secondary hardening behavior can be traced back to strain induced mechanical twinning.
- It is assumed that the twinning induced hardening, resulting from a higher strain, leads to a slower softening rate of the material.
- It is assumed, that the dislocation density is higher for energy density E1 in comparison to energy density E2, resulting in higher generated stresses.
- The latter has to be confirmed with in-situ x-ray measurements during strain-controlled fatigue testing with an electron synchrotron particle accelerator.

Therefore, it can be stated, that the energy density affects the static tensile properties and the low cycle fatigue behavior. This finding also has practical relevance, because the material properties can be controlled as required by a suitable choice of printing parameters.

Declaration of Competing Interest

Johannes Diller reports financial support was provided by German Research Foundation.

Data availability

Data will be made available on request.

Acknowledgements

This study was funded by the Deutsche Forschungsgemeinschaft (DFG, German Research Foundation) – Project number 414265976 – TRR 277.

References

[1] M. Yakout, M.A. Elbestawi, S.C. Veldhuis, Density and mechanical properties in selective laser melting of invar 36 and stainless steel 316L, J. Mater. Process. Technol. 266 (2019) 397–420, https://doi.org/10.1016/j.jmatprotec.2018.11.006.
[2] M. Gor, H. Soni, V. Wankhede, P. Sahlot, K. Grzelak, I. Szachgluchowicz, J. Kluczyński, A critical review on effect of process parameters on mechanical and microstructural properties of powder-bed fusion additive manufacturing of SS316L, Materials (Basel) 14 (2021), https://doi.org/10.3390/ma14216527.
[3] J. Yu, D. Kim, K. Ha, J.B. Jeon, D.J. Kim, W. Lee, Size effect due to contour laser scanning in 316L stainless steel produced by laser powder bed fusion, J. Mater. Res. Technol. 15 (2021) 5554–5568, https://doi.org/10.1016/j.jmrt.2021.11.034.
[4] S. Afkhami, M. Dabiri, H. Piili, T. Björk, Effects of manufacturing parameters and mechanical post-processing on stainless steel 316L processed by laser powder bed fusion, Mater. Sci. Eng. A 802 (2021), 140660, https://doi.org/10.1016/j.msea.2020.140660.
[5] S. Afkhami, M. Dabiri, S.H. Alavi, T. Björk, A. Salminen, Fatigue characteristics of steels manufactured by selective laser melting, Int. J. Fatigue 122 (2019) 72–83, https://doi.org/10.1016/j.ijfatigue.2018.12.029.
[6] B. Ravi Kumar, Influence of crystallographic textures on tensile properties of 316L austenitic stainless steel, J. Mater. Sci. 45 (2010) 2598–2605, https://doi.org/10.1007/s10853-010-4233-x.
[7] Thyssen Krupp Materials, Stainless Steel 1.4404 Datasheet, 2022.
[8] D.E.W. Stahl, Acidur 4404 Materialdatenblatt, 2022.
[9] Arcelor Mittal, U.R. Industeel, 316L Material Data Sheet, 2022.
[10] J. Diller, U. Auer, C. Radlbeck, M. Mensinger, F. Krafft, Einfluss der Abkühlrate auf die mechanischen Eigenschaften von additiv gefertigten Zugproben aus 316L, Stahlbau 89 (2020) 970–980, https://doi.org/10.1002/stab.202000034.
[11] J. Liu, Y. Song, C. Chen, X. Wang, H. Li, C. Zhou, J. Wang, K. Guo, J. Sun, Effect of scanning speed on the microstructure and mechanical behavior of 316L stainless steel fabricated by selective laser melting, Mater. Des. 186 (2020), 108355, https://doi.org/10.1016/j.matdes.2019.108355.
[12] E. Liverani, S. Toschi, L. Ceschini, A. Fortunato, Effect of selective laser melting (SLM) process parameters on microstructure and mechanical properties of 316L austenitic stainless steel, J. Mater. Process. Technol. 249 (2017) 255–263, https://doi.org/10.1016/j.jmatprotec.2017.05.042.
[13] Q. Guo, C. Zhao, M. Qu, L. Xiong, L.I. Escano, S.M.H. Hojjatzadeh, N.D. Parab, K. Fezzaa, W. Everhart, T. Sun, L. Chen, In-situ characterization and quantification of melt pool variation under constant input energy density in laser powder bed fusion additive manufacturing process, Additive Manuf. 28 (2019) 600–609, https://doi.org/10.1016/j.addma.2019.04.021.
[14] Y.M. Wang, T. Voisin, J.T. McKeown, J. Ye, N.P. Calta, Z. Li, Z. Zeng, Y. Zhang, W. Chen, T.T. Roehling, R.T. Ott, M.K. Santala, P.J. Depond, M.J. Matthews, A. V. Hamza, T. Zhu, Additively manufactured hierarchical stainless steels with high strength and ductility, Nat. Mater. 17 (2018) 63–71, https://doi.org/10.1038/nmat5021.
[15] P.A. Hooper, Melt pool temperature and cooling rates in laser powder bed fusion, Additive Manuf. 22 (2018) 548–559, https://doi.org/10.1016/j.addma.2018.05.032.
[16] N.J. Petch, The cleavage strength of polycrystals, J. Iron Steel Inst. London 1953 (1953) 25–28.
[17] E.O. Hall, The deformation and ageing of mild steel: III discussion of results, Proc. Phys. Soc. B 64 (1951) 747–753, https://doi.org/10.1088/0370-1301/64/9/303.
[18] J.A. Cherry, H.M. Davies, S. Mehmood, N.P. Lavery, S.G.R. Brown, J. Sienz, Investigation into the effect of process parameters on microstructural and physical properties of 316L stainless steel parts by selective laser melting, Int. J. Adv. Manuf. Technol. 76 (2015) 869–879, https://doi.org/10.1007/s00170-014-6297-2.
[19] J. Kluczyński, L. Śnieżek, K. Grzelak, J. Torzewski, I. Szachogłuchowicz, A. Oziębło, K. Perkowski, M. Wachowski, M. Małek, The influence of heat treatment on low cycle fatigue properties of selectively laser melted 316L steel, Materials (Basel) 13 (2020), https://doi.org/10.3390/ma13245737.
[20] C.-H. Yu, A. Leicht, R.L. Peng, J. Moverare, Low cycle fatigue of additively manufactured thin-walled stainless steel 316L, Mater. Sci. Eng. A 821 (2021), 141598, https://doi.org/10.1016/j.msea.2021.141598.
[21] W. Beard, R. Lancaster, J. Adams, D. Buller, Fatigue Performance of Additively Manufactured Stainless Steel 316L for Nuclear Applications, University of Texas at Austin, 2019.
[22] E08 Committee, Test Method for Strain-Controlled Fatigue Testing, ASTM International, West Conshohocken, PA, 2021.
[23] T. Ronneberg, C.M. Davies, P.A. Hooper, Revealing relationships between porosity, microstructure and mechanical properties of laser powder bed fusion 316L stainless steel through heat treatment, Mater. Des. 189 (2020), 108481, https://doi.org/10.1016/j.matdes.2020.108481.
[24] Y. Murakami, K. Takahashi, T. Yamashita, Quantitative evaluation of the effect of surface roughness on fatigue strength. Effect of depth and pitch of roughness, Trans. JSME Ser. A 63 (1997) 1612–1619, https://doi.org/10.1299/KIKAIA.63.1612.
[25] H. Itoga, K. Tokaji, M. Nakajima, H.-N. Ko, Effects of notch and surface roughness on long life fatigue behaviour in high strength steels, J. Soc. Mat. Sci., Japan 54 (2005) 1249–1254, https://doi.org/10.2472/JSMS.54.1249.

[26] S. As, B. Skallerud, B. Tveiten, Surface roughness characterization for fatigue life predictions using finite element analysis, Int. J. Fatigue 30 (2008) 2200–2209, https://doi.org/10.1016/j.ijfatigue.2008.05.020.
[27] E04 Committee, Test Methods for Determining Average Grain Size, ASTM International, West Conshohocken, PA, 2021.
[28] M. Godec, S. Zaefferer, B. Podgornik, M. Šinko, E. Tchernychova, Quantitative multiscale correlative microstructure analysis of additive manufacturing of stainless steel 316L processed by selective laser melting, Mater. Charact. 160 (2020), 110074, https://doi.org/10.1016/j.matchar.2019.110074.
[29] P. Krakhmalev, G. Fredriksson, K. Svensson, I. Yadroitsev, I. Yadroitsava, M. Thuvander, R. Peng, Microstructure, solidification texture, and thermal stability of 316 L stainless steel manufactured by laser powder bed fusion, Metals 8 (2018) 643, https://doi.org/10.3390/met8080643.
[30] C. Di Wang, Y. Song, Y. Yang, Bai, investigation of crystal growth mechanism during selective laser melting and mechanical property characterization of 316L stainless steel parts, Mater. Des. 100 (2016) 291–299, https://doi.org/10.1016/j.matdes.2016.03.111.
[31] I. Gutierrez-Urrutia, D. Raabe, Dislocation density measurement by electron channeling contrast imaging in a scanning electron microscope, Scr. Mater. 66 (2012) 343–346, https://doi.org/10.1016/j.scriptamat.2011.11.027.
[32] M. Shamsujjoha, S.R. Agnew, J.M. Fitz-Gerald, W.R. Moore, T.A. Newman, High strength and ductility of additively manufactured 316L stainless steel explained, Metall and Mat Trans A 49 (2018) 3011–3027, https://doi.org/10.1007/s11661-018-4607-2.
[33] M. Wächter, C. Müller, A. Esderts, Angewandter Festigkeitsnachweis nach FKM-Richtlinie: Kurz und bündig, Springer Vieweg, Wiesbaden, Germany, 2017.
[34] T. Kurzynowski, K. Gruber, W. Stopyra, B. Kuźnicka, E. Chlebus, Correlation between process parameters, microstructure and properties of 316 L stainless steel processed by selective laser melting, Mater. Sci. Eng. A 718 (2018) 64–73, https://doi.org/10.1016/j.msea.2018.01.103.
[35] P. Kumar, R. Jayaraj, J. Suryawanshi, U.R. Satwik, J. McKinnell, U. Ramamurty, Fatigue strength of additively manufactured 316L austenitic stainless steel, Acta Mater. 199 (2020) 225–239, https://doi.org/10.1016/j.actamat.2020.08.033.
[36] D. Zhang, S. Sun, D. Qiu, M.A. Gibson, M.S. Dargusch, M. Brandt, M. Qian, M. Easton, Metal alloys for fusion-based additive manufacturing, Adv. Eng. Mater. 20 (2018) 1700952, https://doi.org/10.1002/adem.201700952.
[37] K. Solberg, S. Guan, S.M.J. Razavi, T. Welo, K.C. Chan, F. Berto, Fatigue of additively manufactured 316L stainless steel: the influence of porosity and surface roughness, Fatigue Fract. Eng. Mater. Struct. 42 (2019) 2043–2052, https://doi.org/10.1111/ffe.13077.
[38] T.-N. Lam, Y.-H. Wu, C.-J. Liu, H. Chae, S.-Y. Lee, J. Jain, K. An, E.-W. Huang, Transient phase-driven cyclic deformation in additively manufactured 15-5 PH steel, Materials (Basel) 15 (2022), https://doi.org/10.3390/ma15030777.
[39] M. Okayasu, H. Fukui, H. Ohfuji, T. Shiraishi, Strain-induced martensite formation in austenitic stainless steel, J. Mater. Sci. 48 (2013) 6157–6166, https://doi.org/10.1007/s10853-013-7412-8.
[40] M.S. Pham, B. Dovgyy, P.A. Hooper, Twinning induced plasticity in austenitic stainless steel 316L made by additive manufacturing, Mater. Sci. Eng. A 704 (2017) 102–111, https://doi.org/10.1016/j.msea.2017.07.082.
[41] G. Gershteyn, N. Shevchenko, M. Diekamp, A. Brosius, M. Schaper, F.-W. Bach, Features of austenitic steels' microstructure following plastic deformation, Mat.-wiss. u. Werkstofftech. 43 (2012) 262–267, https://doi.org/10.1002/mawe.201200853.
[42] W. Shifeng, L. Shuai, W. Qingsong, C. Yan, Z. Sheng, S. Yusheng, Effect of molten pool boundaries on the mechanical properties of selective laser melting parts, J. Mater. Process. Technol. 214 (2014) 2660–2667, https://doi.org/10.1016/j.jmatprotec.2014.06.002.
[43] H. Sohrabpoor, V. Salarvand, R. Lupoi, Q. Chu, W. Li, B. Aldwell, W. Stanley, S. O'Halloran, R. Raghavendra, C.-H. Choi, D. Brabazon, Microstructural and mechanical evaluation of post-processed SS 316L manufactured by laser-based powder bed fusion, J. Mater. Res. Technol. 12 (2021) 210–220, https://doi.org/10.1016/j.jmrt.2021.02.090.
[44] J.I. Dickson, J. Boutin, L. Handfield, A comparison of two simple methods for measuring cyclic internal and effective stresses, Mater. Sci. Eng. 64 (1984) L7–L11, https://doi.org/10.1016/0025-5416(84)90083-1.
[45] A.F. Brust, S.R. Niezgoda, V.A. Yardley, E.J. Payton, Analysis of misorientation relationships between austenite parents and twins, Metall and Mat Trans A 50 (2019) 837–855, https://doi.org/10.1007/s11661-018-4977-5.
[46] N. Guo, C. Sun, M. Fu, M. Han, Misorientation-dependent twinning induced hardening and texture evolution of TWIP steel sheet in plastic deformation process, Metals 7 (2017) 348, https://doi.org/10.3390/met7090348.
[47] S.I. Wright, M.M. Nowell, D.P. Field, A review of strain analysis using electron backscatter diffraction, Microsc. Microanal. 17 (2011) 316–329, https://doi.org/10.1017/S1431927611000055.
[48] VdEh Stahlinstitut, Stahl-Eisen-Prüfblatt (SEP) 1240: testing and documentation guideline for the experimental SEP 1240: 2006-07: testing and documentation guideline for the experimental determination of mechanical properties of steel sheets for CAE-calculations, Beuth. Duesseldorf, 2006, pp. 6–48.
[49] M. Wächter, A. Esderts, R. Masendorf, Methoden zur Abschätzung zyklischer Werkstoffkennwerte (2015), https://doi.org/10.21268/20160726-132801.
[50] M. Pelegatti, A. Lanzutti, E. Salvati, J. Srnec Novak, F. de Bona, D. Benasciutti, Cyclic plasticity and low cycle fatigue of an AISI 316L stainless steel: experimental evaluation of material parameters for durability design, Materials (Basel) 14 (2021), https://doi.org/10.3390/ma14133588.
[51] P. Virtanen, R. Gommers, T.E. Oliphant, M. Haberland, T. Reddy, D. Cournapeau, E. Burovski, P. Peterson, W. Weckesser, J. Bright, S.J. van der Walt, M. Brett, J. Wilson, K.J. Millman, N. Mayorov, A.R.J. Nelson, E. Jones, R. Kern, E. Larson, C. J. Carey, İ. Polat, Y. Feng, E.W. Moore, J. VanderPlas, D. Laxalde, J. Perktold, R. Cimrman, I. Henriksen, E.A. Quintero, C.R. Harris, A.M. Archibald, A.H. Ribeiro, F. Pedregosa, P. van Mulbregt, SciPy 1.0: fundamental algorithms for scientific computing in Python, Nat. Methods 17 (2020) 261–272, https://doi.org/10.1038/s41592-019-0686-2.
[52] M. Zhang, C.-N. Sun, X. Zhang, P.C. Goh, J. Wei, H. Li, D. Hardacre, Elucidating the relations between monotonic and fatigue properties of laser powder bed fusion stainless steel 316L, JOM 70 (2018) 390–395, https://doi.org/10.1007/s11837-017-2640-z.

A.2.3 Publication 3: PBF-LB/M/316L vs. hot-rolled 316l – comparison of cyclic plastic material behaviour

Reproduced from:

Procedia Structural Integrity 42 (2022), 58-65
Weblink: https://doi.org/10.1016/j .prostr.2022.12.006

with the permission of Elsevier BV.

Available online at www.sciencedirect.com

ScienceDirect

Procedia Structural Integrity 42 (2022) 58–65

Structural Integrity Procedia

www.elsevier.com/locate/procedia

23 European Conference on Fracture - ECF23

PBF-LB/M/316L vs. hot-rolled 316L – comparison of cyclic plastic material behavior

Johannes Diller[a]*, Dorina Siebert[a], Christina Radlbeck[a], Martin Mensinger[a]

a) Chair of Metal Structures, Technical University of Munich, Arcisstr. 21, 80333 Munich, Bavaria, Germany

Abstract

Powder-Bed Fusion of AISI 316L (1.4404) using a laser (PBF-LB/M) is known for its very high cooling rate of up to 40 K/µs (Hooper 2018). This high cooling rate results in a fine needle-like microstructure. In comparison, hot-rolled, annealed AISI 316L consists of coarser grain structures. The quasi-static tensile properties, therefore, differ significantly. This may result in a completely different cyclic plastic material behavior due to the grain boundary strengthening during the PBF-LB/M manufacturing process.
This study compares the cyclic plastic material behavior of PBF-LB/M-manufactured 316L with that of hot-rolled, annealed AISI 316L. Strain-controlled fatigue testing of both, PBF-LB/M and hot rolled, annealed AISI 316L, was conducted. The strain amplitudes vary from 0.5 % to 3.0 % in steps of 0.5 %. A microstructural investigation of selected specimens was conducted before and after testing. It consists of surface etching, electron backscatter diffraction (EBSD) as well as spark spectrometry. The orientation, phase transformation, twinning formation as well as the general microstructure is compared.
It is found, that the PBF-LB/M-manufactured specimens mainly showed a softening behavior. Only from 2.5 % applied strain amplitude, a secondary hardening phenomenon is observed. The hot-rolled and annealed specimens on the other hand mainly show a continuous hardening behavior.

Peer-review under responsibility of the scientific committee of the 23 European Conference on Fracture – ECF23

Keywords: Low-cycle fatigue, Additive Manufacturing, AISI 316L, Hot-rolling, Strain hardening, Cyclic plastic material behavior

* Corresponding author. Tel.: +49 89 289 22528; fax: +49 89 289 22522
E-mail address: johannes.diller@tum.de

Peer-review under responsibility of the scientific committee of the 23 European Conference on Fracture – ECF23
10.1016/j.prostr.2022.12.006

1. Introduction

Laser powder bed fusion of metals (PBF-LB/M) enables the production of highly complex parts which can, in many situations, not be manufactured by conventional manufacturing methods like casting or forging. However, the mechanical properties of PBF-LB/M manufactured parts are not yet fully understood or characterized. Often, the austenitic stainless steel AISI 316L is used to gain more knowledge about the PBF-LB/M manufacturing process (Gor et al. 2021). 316L is mainly used for chemical, medical and automotive applications (Afkhami et al. 2021). It could however also be used in the construction industry as a structural steel for special applications like steel hysteretic dampers due to its high ductility. For conventional manufacturing methods like forging, the yield strength usually lies in between 200 – 220 MPa (Ravi Kumar 2010). The yield strength of PBF-LB/M manufactured 316L however can rise up to 650 MPa, depending on the orientation of the part and the applied laser parameters (Diller et al. 2020). The high yield strength results from a grain boundary strengthening, which is caused by the high cooling rate (Liu et al. 2020). During the PBF-LB/M manufacturing, cooling rates of up to 40 K/µs can occur (Hooper 2018). This creates fine lamellar subgrains with a diameter of 200 – 300 nm. Hence, the higher yield strength of PBF-LB/M manufactured 316L can be attributed to the inhibition of dislocation motion at each grain boundary. With a smaller subgrain size, more grain boundaries occur, developing a high yield strength. (Diller et al. 2022). This study compares the cyclic plastic material behavior of PBF-LB/M-manufactured and hot-rolled AISI 316L. The cyclic plastic material behavior of additively manufactured 316L was investigated in detail in a different study and was compared to a different laser parameter set which was outside the stable melting zone (Diller et al. 2022). For each manufacturing process, strain-controlled fatigue testing was conducted with strain amplitudes of up to 3.0 % with steps of 0.5 %. Tensile testing, as well as a microstructural investigation before and after testing was conducted.

2. Experimental procedure

An EOS M280 PBF-LB/M machine with a 400 W Ytterbium continuous wave fiber laser was used to manufacture the PBF-LB/M specimens for this study. AISI 316L stainless steel metal powder by Oerlikon Metco with a particle size distribution of 20 – 63 µm was used. The respective volume percentile values D10, D50 and D90 were numerated with 19, 30 and 40 µm respectively. The used inert gas was Argon 5.0. During the build job, a residual oxygen concentration of < 1300 ppm was kept. The laser parameters used in this study are shown in Table 1. According to (Yakout et al. 2019) the used laser parameters are inside the stable melting zone. The application of these laser parameters should therefore result in a high density and toughness with continuous weld beads and homogeneous melt tracks. The x-hatch angle was kept at 60° after each layer.

Table 1: Applied laser parameters of the PBF-LB/M manufactured for the fatigue and tensile specimens

Energy Density [J/mm³]	Scanning Velocity [mm/s]	Laser Power [W]	Layer Thickness [µm]	Hatch Distance [µm]
65.97	600	190	40	120

Strain-controlled fatigue testing was conducted with a strain ratio of R = -1 and a strain rate of 0.004 s^{-1}. Additionally, tensile tests were conducted with the same specimen geometry according to ASTM E606, shown in Fig. 1, to reduce any geometrical effect. The experimental design can be seen in Table 2.

Table 2: Experimental design with type and number of specimens for each conducted type of investigation and process

Manufacturing Process	Applied Strain Amplitude						Tensile Testing	Microstructure
	0.5 %	1.0 %	1.5 %	2.0 %	2.5 %	3.0 %		
PBF-LB/M	3	3	3	3	3	3	3	1
Hot-rolled	3	3	3	3	3	3	3	1

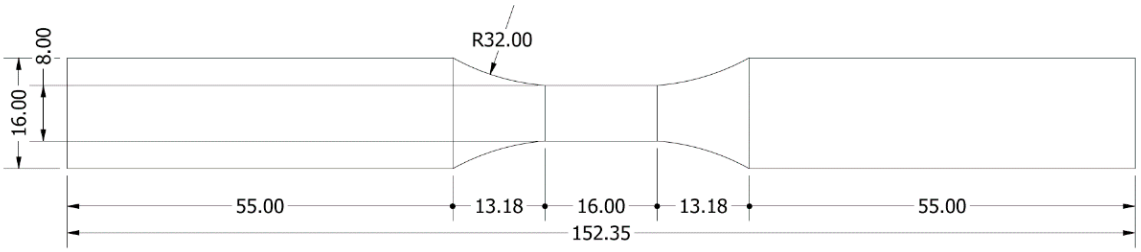

Fig. 1. Fatigue and tensile specimen geometry (round) with dimensions in mm according to ASTM E606

The unique surface roughness of PBF-LB/M manufactured AISI 316L may affect the low-cycle fatigue behavior (AS et al. 2008; Solberg et al. 2019; ITOGA et al. 2005). To diminish the effect of surface roughness on the low-cycle fatigue behavior, both PBF-LB/M and hot-rolled AISI 316L specimens were ground and polished on a lathe. Sanding papers with a grain size of 320, 500, 800 and 1000 µm were used for 4 minutes each, followed by two polishing steps. For this, zirconia aluminum abrasive and a polishing paste with 6 µm and 3 µm diamond slurry was applied. The polishing steps were applied for 5 minutes each. Subsequently, the surface roughness was measured with a Keyence VK-X1000 3D laser scanning microscope resulting in an Ra = 0.562 µm and Rz = 4.326 µm. The microstructure was investigated before and after testing by cutting the specimens longitudinally inside the measuring range. The specimens were hot embedded in resin, ground, polished and etched for 30s. The used etchant was Beraha II as well as V2A-etchant at 60 °C. The ferrite content was measured before and after testing with a Fischer Feritscope FMP30. The Feritscope was calibrated using a calibration block with a ferrite content of 0.3 % and 10 %. Electron backscatter diffraction (EBSD) measurements were conducted to investigate the phase composition, as well as the possible formation of twins and the orientation of the material. Therefore, an EDAX EBSD-system and a Hikari EBSD-camera was used. The overall chemical composition was investigated using an OBFL QSG 750-II spark spectrometer.

3. Experimental results

3.1. Chemical composition

The chemical composition of the AISI 316L of both manufacturing processes is shown in Table 3. It can be seen, that the Ni-content is at the lower spectrum for hot-rolled AISI 316L. The Ni-content of the PBF-LB/M manufactured AISI 316L however is at the upper end of the defined range (Wegst 2001).

Table 3: Chemical composition of 316L, manufactured by PBF-LB/M and hot-rolling in % including the range AISI 316L is defined (Wegst 2001).

Chemical Element	C	Si	Mn	Cr	Ni	Nb	Ti	Mo
PBF-LB/M	0.015	0.582	1.349	17.85	12.0	0.011	<0.001	2.277
Hot-rolled	0.035	0.41	1.52	17.01	10.02	0.019	<0.001	2.021
Range	<0.03	<1.0	<2.0	16.5-18.5	10.0-13.0			2.0-2.5

3.2. Tensile properties

Fig. 2 shows the tensile testing results of both PBF-LB/M manufactured and hot-rolled AISI 316L. The PBF-LB/M manufactured AISI 316L showed a higher yield strength of 455 MPa in comparison to the hot-rolled AISI 316L with a yield strength of 245 MPa respectively. The ultimate tensile strength revealed closer results with 611 MPa for the PBF-LB/M manufactured AISI 316L and 585 MPa for the hot-rolled AISI 316L respectively. It can also be seen, that

both manufacturing processes resulted in different strengthening mechanisms. The PBF-LB/M manufactured AISI 316L showed a plateau in the plastic range whereas the hot-rolled AISI 316L hardened during plastic deformation

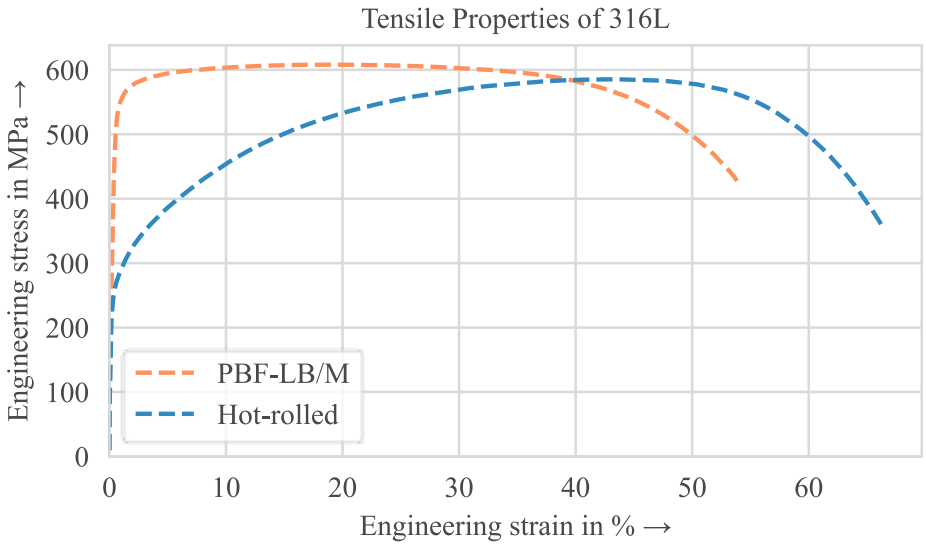

Fig. 2: Tensile properties of AISI 316L, manufactured by PBF-LB/M and hot-rolling

3.3. Microstructure before testing

The microstructure of the PBF-LB/M manufactured and hot-rolled AISI 316L is shown in Fig. 3. The weld beads revealed the x-scan strategy of 60 ° in picture (1). It also revealed the subgrain size. Columnar grains with a diameter of 400-600 nm were visible. The subgrains were oriented differently to each other, depending on the scan angle. In picture (2) the microstructure of the hot-rolled AISI 316L revealed larger grains with a diameter of up to 192 µm. Initial twinning was visible. A ferrite content of 0.0 % was measured for the PBF-LB/M manufacturing process and 0.3 % for the hot-rolling process respectively.

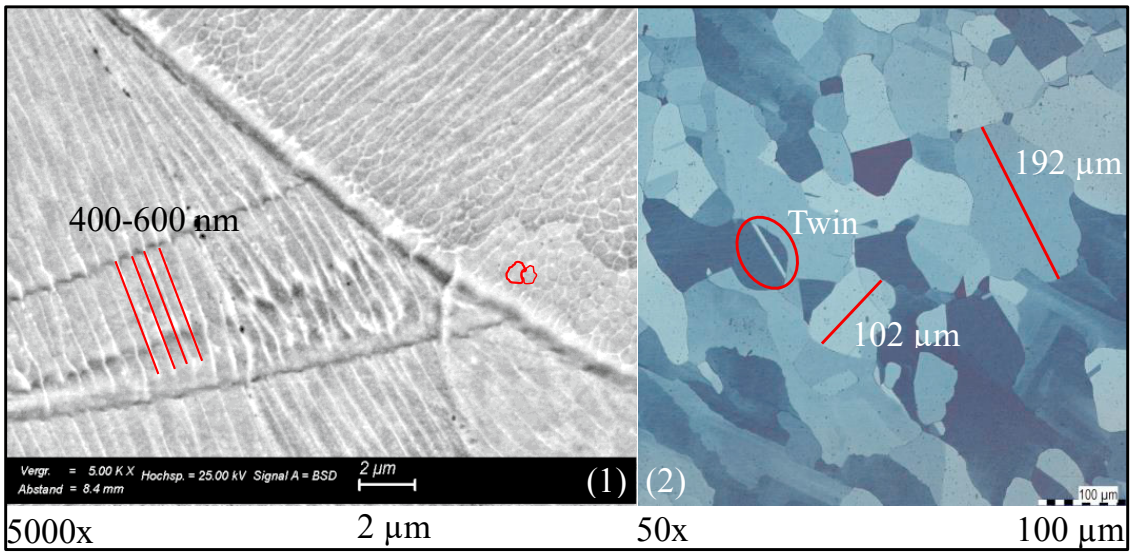

Fig. 3: Microstructure of both PBF-LB/M (1) manufactured and hot-rolled (2) AISI 316L, (1) showing columnar grains with a diameter of 400 – 600 nm and (2) showing twins and grains with a diameter of up to 192 µm.

3.4. Strain-controlled fatigue testing

Fig. 4 shows the results of the strain-controlled fatigue testing of the specimens of both the PBF-LB/M and the hot-rolling processes. A comparison of the maximum stresses in the tensile range is conducted. The PBF-LB/M manufacturing process results showed high initial stresses during cyclic plastic deformation. An initial hardening effect in the first 10 cycles was observed, followed by secondary softening during the whole fatigue life. Only from a strain amplitude of 2.5 % upwards, a hardening effect occurred close to the end of the fatigue life of the specimen.

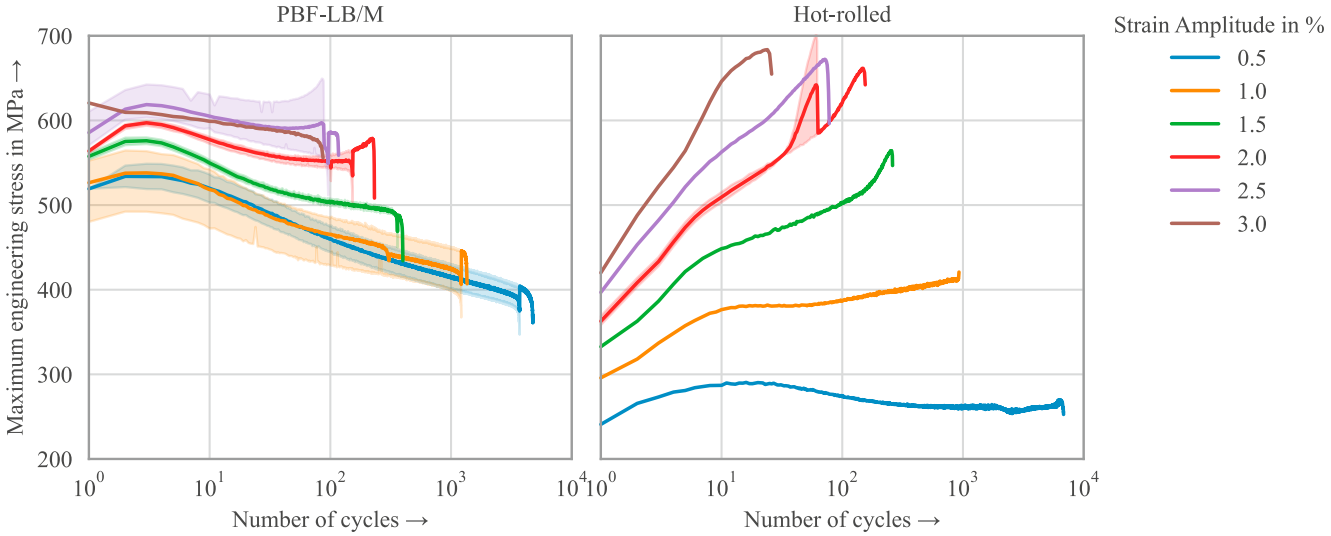

Fig. 4: Comparison of the maximum stress curves over the endured cycles between the PBF-LB/M manufacturing process and the hot-rolling process of AISI 316L including the standard deviation at each cycle (colored surfaces).

The specimens of hot-rolled AISI 316L showed low initial stresses, followed by an initial hardening behavior during cyclic plastic deformation. This hardening behavior continues through to the end of the fatigue life. Stresses of up to 700 MPa were generated. The strain-based S-N-curve for both the PBF-LB/M manufacturing process and the

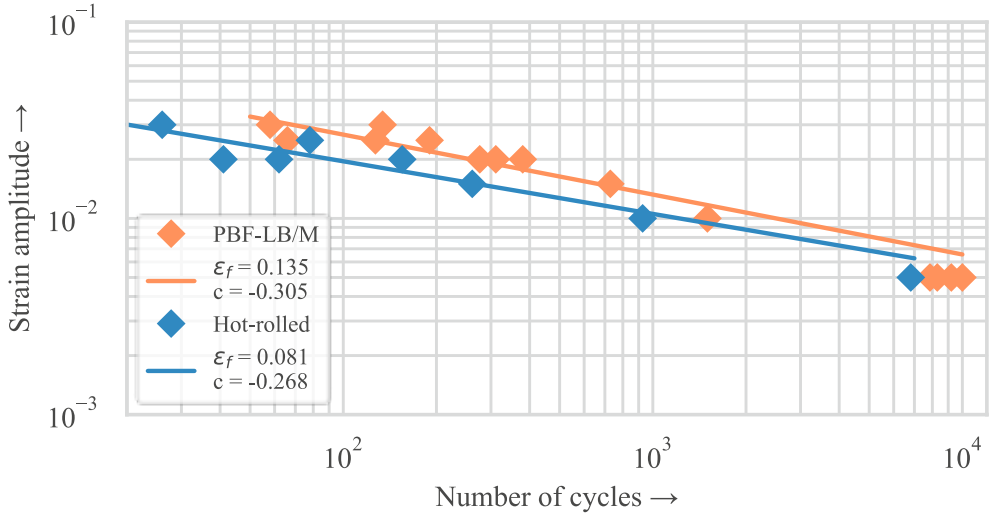

Fig. 5: Linear regression approximation of the plastic strain-based S-N-curve for the PBF-LB/M manufacturing process and the hot-rolling process of AISI 316L.

hot-rolling process are described with the plastic part of the Manson-Coffin equation in Fig. 5. The PBF-LB/M manufactured AISI 316L has a higher fatigue life compared to the hot-rolled AISI 316L.

3.5. Microstructure after fatigue testing with 2.5 % strain amplitude

The microstructure was investigated after the application of 2.5 % strain amplitude for both manufacturing processes. The twin formation was measured by EBSD. The orientation between 58° and 62° is shown in Fig. 6 (1) and (2) as this is the usual angle where twinning occurs (Brust et al. 2019; Guo et al. 2017). A twin fraction of 2.2 % was measured for the PBF-LB/M manufactured AISI 316L after applying 2.5 % strain amplitude, see Fig. 6 (1). The twin fraction of the hot-rolled AISI 316L after fatigue testing with 2.5 % strain amplitude however shows a substantially higher twin fraction of 10.2 %. Additionally, the phase fraction was measured by EBSD. For the PBF-LB/M manufactured AISI 316L no martensite was measured before and after an applied strain amplitude of 2.5 %. The hot-rolled AISI 316L however shows a martensite fraction of 11.5 % which can be seen in Fig. 6 (3). The ferrite content was also measured after an applied strain amplitude of 2.5 %. The PBF-LB/M manufactured AISI 316L revealed a ferrite or martensite content of 0.31% whereas for the hot-rolled AISI 316L a ferrite content of 11.5 % was measured.

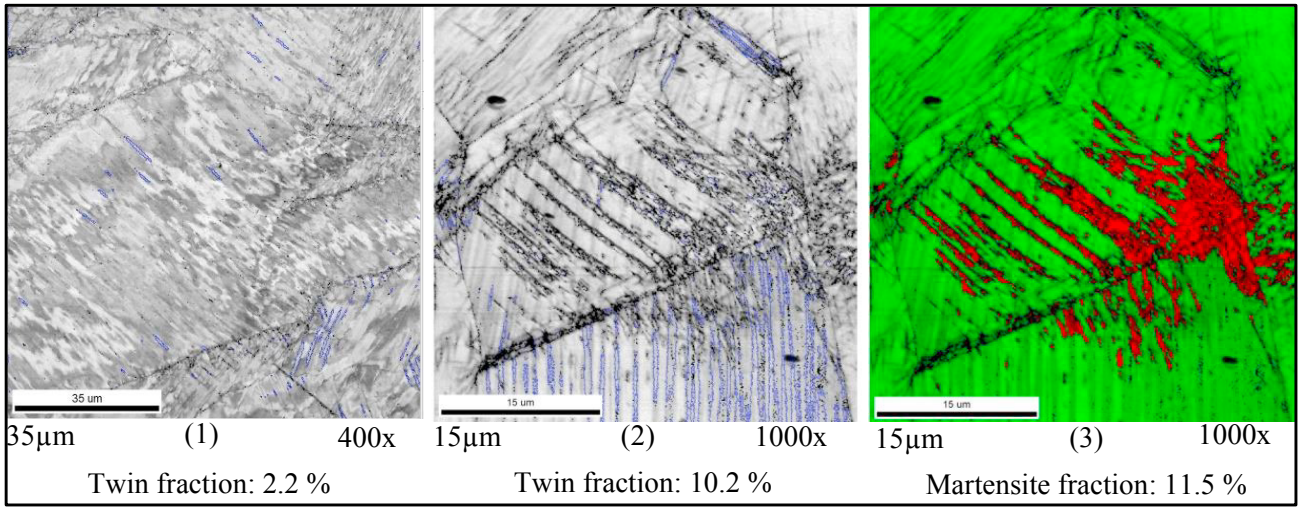

Fig. 6: Microstructure after fatigue testing with 2.5 % strain amplitude, (1) showing the mechanical twin formation and image quality of the PBF-LB/M manufactured AISI 316L, (2) showing the mechanical twin formation and image quality of the hot-rolled AISI 316L, (3) showing the phase composition of the hot-rolled AISI 316L with a martensite fraction of 11.5 %.

4. Discussion

The two different manufacturing processes reveal a completely different strengthening behavior. To investigate this behavior, Fig. 7 is introduced. The normalized number of cycles is compared to the change of the maximum tensile stress for each strain amplitude and both manufacturing processes. It can be seen, that at strain amplitudes from 0.5 % to 1 %, the PBF-LB/M manufactured AISI 316L constantly shows higher stresses. From 1.5 % strain amplitude onwards, a clear hardening effect of the hot-rolled AISI 316L is observed, exceeding the resulting stresses of the PBF-LB/M manufactured AISI 316L.

While the cyclic plastic behavior of the PBF-LB/M manufactured AISI 316L is mainly dominated by softening, the hot-rolled manufactured AISI 316L is mainly dominated by hardening. This may be due to multiple reasons. The chemical composition shows a lower Ni-content for the hot-rolled AISI 316L. This may lead to a higher transformation affinity from austenite to martensite, as the Ni-equivalent of the Schaeffler-diagram is lower (Schoß 2000). The grain size of the material also may have a significant influence on the strain induced martensite transformation. With increasing grain size, the transformation rate from austenite to martensite increases as well (Celada-Casero et al. 2019).

As martensite can only grow inside a grain due to their specific orientation relation with the austenite, it is very likely that the magnitude of the martensite transformation of the hot-rolled AISI 316L is higher in comparison to the PBF-LB/M manufactured AISI 316L. Additionally the strain induced twin formation is significantly higher at the hot-rolled AISI 316L in comparison to the PBF-LB/M manufactured AISI 316L.

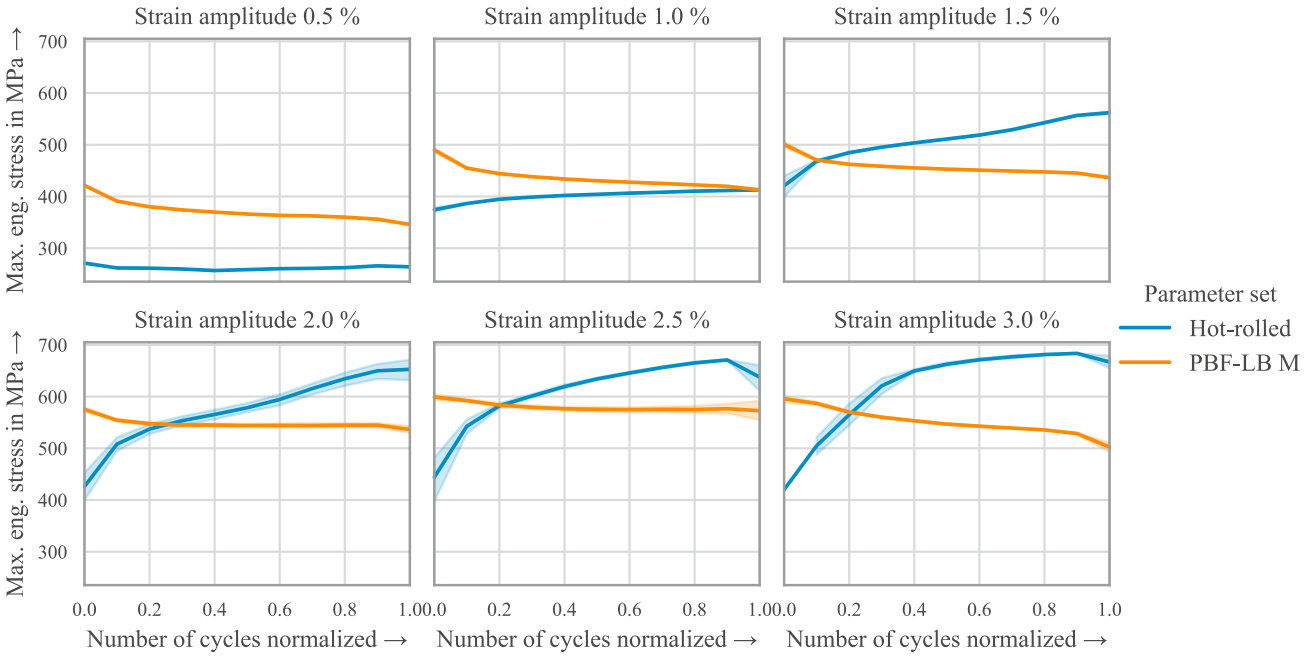

Fig. 7: Comparison of the maximum stress curves over the endured cycles between the PBF-LB/M manufacturing process and the hot-rolling process. The tested strain amplitudes are shown in separate plots with a normalized representation of the elapsed number of cycles.

5. Conclusion

From this study, the following conclusions can be drawn about the cyclic plastic material behavior of both PBF-LB/M manufactured and hot-rolled AISI 316L:

- The PBF-LB/M manufactured AISI 316L reveals higher initial maximum stresses, followed by a softening behavior.
- The hot-rolled AISI 316L has lower initial maximum stresses, followed by a hardening behavior.
- The PBF-LB/M manufactured AISI 316L has a higher fatigue life in comparison to hot-rolled AISI 316L.
- During cyclic plastic deformation of the PBF-LB/M manufactured AISI 316L, no to little martensite transformation occurs due to the small crystallite size.
- The martensite transformation during cyclic plastic deformation of the hot-rolled AISI 316L occurs due to the large grain size.
- The lower Ni-content of the hot-rolled AISI 316L leads to a higher transformation affinity from austenite to martensite.
- The hardening behavior of the hot-rolled AISI 316L can therefore be reasoned with both martensite transformation and strain induced twinning.

6. Acknowledgements

This study was funded by the Deutsche Forschungsgemeinschaft (DFG, German Research Foundation) – Project number 414265976 – TRR 277.

Literaturverzeichnis

Afkhami, Shahriar; Dabiri, Mohammad; Piili, Heidi; Björk, Timo (2021): Effects of manufacturing parameters and mechanical post-processing on stainless steel 316L processed by laser powder bed fusion. In: *Materials Science and Engineering: A* 802, S. 140660. DOI: 10.1016/j.msea.2020.140660.

AS, S.; SKALLERUD, B.; TVEITEN, B. (2008): Surface roughness characterization for fatigue life predictions using finite element analysis. In: *International Journal of Fatigue* 30 (12), S. 2200–2209. DOI: 10.1016/j.ijfatigue.2008.05.020.

Brust, A. F.; Niezgoda, S. R.; Yardley, V. A.; Payton, E. J. (2019): Analysis of Misorientation Relationships Between Austenite Parents and Twins. In: *Metall and Mat Trans A* 50 (2), S. 837–855. DOI: 10.1007/s11661-018-4977-5.

Celada-Casero, Carola; Sietsma, Jilt; Santofimia, Maria Jesus (2019): The role of the austenite grain size in the martensitic transformation in low carbon steels. In: *Materials & Design* 167, S. 107625. DOI: 10.1016/j.matdes.2019.107625.

Diller, Johannes; Auer, Ulrich; Radlbeck, Christina; Mensinger, Martin; Krafft, Frank (2020): Einfluss der Abkühlrate auf die mechanischen Eigenschaften von additiv gefertigten Zugproben aus 316L. In: *Stahlbau* 89 (12), S. 970–980. DOI: 10.1002/stab.202000034.

Diller, Johannes; Rier, Lukas; Siebert, Dorina; Radlbeck, Christina; Krafft, Frank; Mensinger, Martin (2022): Cyclic plastic material behavior of 316L manufactured by laser powder bed fusion (PBF-LB/M). In: *Materials Characterization* 191, S. 112153. DOI: 10.1016/j.matchar.2022.112153.

Gor, Meet; Soni, Harsh; Wankhede, Vishal; Sahlot, Pankaj; Grzelak, Krzysztof; Szachgluchowicz, Ireneusz; Kluczyński, Janusz (2021): A Critical Review on Effect of Process Parameters on Mechanical and Microstructural Properties of Powder-Bed Fusion Additive Manufacturing of SS316L. In: *Materials (Basel, Switzerland)* 14 (21). DOI: 10.3390/ma14216527.

Guo, Ning; Sun, Chaoyang; Fu, Mingwang; Han, Mingchuan (2017): Misorientation-Dependent Twinning Induced Hardening and Texture Evolution of TWIP Steel Sheet in Plastic Deformation Process. In: *Metals* 7 (9), S. 348. DOI: 10.3390/met7090348.

Hooper, Paul A. (2018): Melt pool temperature and cooling rates in laser powder bed fusion. In: *Additive Manufacturing* 22, S. 548–559. DOI: 10.1016/j.addma.2018.05.032.

ITOGA, Hisatake; TOKAJI, Keiro; NAKAJIMA, Masaki; KO, Haeng-Nam (2005): Effects of Notch and Surface Roughness on Long Life Fatigue Behaviour in High Strength Steels. In: *J. Soc. Mat. Sci., Japan* 54 (12), S. 1249–1254. DOI: 10.2472/JSMS.54.1249.

Liu, Jiangwei; Song, Yanan; Chen, Chaoyue; Wang, Xiebin; Li, Hu; Zhou, Chang'an et al. (2020): Effect of scanning speed on the microstructure and mechanical behavior of 316L stainless steel fabricated by selective laser melting. In: *Materials & Design* 186, S. 108355. DOI: 10.1016/j.matdes.2019.108355.

Ravi Kumar, B. (2010): Influence of crystallographic textures on tensile properties of 316L austenitic stainless steel. In: *J Mater Sci* 45 (10), S. 2598–2605. DOI: 10.1007/s10853-010-4233-x.

Schoß, Volker (2000): Martensische Umwandlung und Ermüdung austenitischer Edelstähle, Gefügeveränderungen und Möglichkeiten der Früherkennung von Ermüdungsschädigungen. Online verfügbar unter http://slubdd.de/katalog?TN_libero_mab2)500063900.

Solberg, Klas; Guan, Shuai; Razavi, Seyed Mohammad Javad; Welo, Torgeir; Chan, Kang Cheung; Berto, Filippo (2019): Fatigue of additively manufactured 316L stainless steel: The influence of porosity and surface roughness. In: *Fatigue Fract Eng Mater Struct* 42 (9), S. 2043–2052. DOI: 10.1111/ffe.13077.

Wegst, C. W. (2001): Stahlschlüssel. 2001. 19. vollständig neu bearbeitete und erweiterte Auflage 2001. Marbach: Verl. Stahlschlüssel Wegst GMBH.

Yakout, Mostafa; Elbestawi, M. A.; Veldhuis, Stephen C. (2019): Density and mechanical properties in selective laser melting of Invar 36 and stainless steel 316L. In: *Journal of Materials Processing Technology* 266, S. 397–420. DOI: 10.1016/j.jmatprotec.2018.11.006.

A.2.4 Publication 4: Combined effect of surface treatment and heat treatment on the fatigue properties of AISI 316L, manufactured by powder bed fusion of metals using a laser (PBF-LB/M)

Reproduced from:

International Journal of Fatigue 178 (2024), 108025
Weblink: https://doi.org/10.1016/j .ijfatigue.2023.108025

International Journal of Fatigue 178 (2024) 108025

Contents lists available at ScienceDirect

International Journal of Fatigue

journal homepage: www.elsevier.com/locate/ijfatigue

Combined effect of surface treatment and heat treatment on the fatigue properties of AISI 316L, manufactured by powder bed fusion of metals using a laser (PBF-LB/M)

Johannes Diller *, Jakob Blankenhagen, Dorina Siebert, Christina Radlbeck, Martin Mensinger

Technical University of Munich, TUM School of Engineering and Design, Chair of Metal Structures, Arcisstr 21, Munich, 80333, Germany

ARTICLE INFO

Keywords:
Additive manufacturing
Fatigue behavior
Surface roughness
Surface residual stresses
Heat treatment

ABSTRACT

This work deals with the combined influence of surface treatment and heat treatment of 316L manufactured by powder bed fusion of metals using a laser (PBF-LB/M/316L) on the fatigue behavior. Two surface treatment methods (manual polishing, vibratory grinding) were investigated. Fatigue testing of six different surface and heat treatment parameter setups was conducted. Metallurgical investigations such as etching patterns, density measurements, surface roughness measurements, fracture surface analysis with a scanning electron microscope (SEM), X-ray diffraction (XRD) and electron backscatter diffraction (EBSD) were performed. The mechanical properties were examined by tensile tests and fatigue tests. The influence of grain size on fatigue life was found to be the primary factor, followed by the surface roughness and subsequently the residual stresses on the surface ultimately contributing to the overall effect.

1. Introduction

Additive manufacturing of metals has become increasingly popular in recent years. Among other processes, powder bed fusion of metals using a laser beam (PBF-LB/M) is used. Due to the increased use, the development of a design concept for a later standardization is a goal to be striven for. In the case of this comparatively new production method, many questions are still unresolved and are increasingly the subject of research. In order to have a basis for a safe and reliable application, it is necessary to understand and assess the processes involved. The fatigue behavior of PBF-LB/M manufactured parts is still one of the biggest issues to achieve the goal of safe and reliable use of structural components. This is mainly due to the influence of geometrical defects (porosity, surface roughness) and the unique microstructure of the manufacturing process [1–3]. There have been many studies investigating optimal laser parameters to achieve a high density [4–6]. However, porosity as well as a high surface roughness are inevitable regardless of the laser parameters [7,8]. The surface roughness affects the fatigue behavior of PBF-LB/M manufactured 316L due to the high stress intensity at surface defects [9–14]. Fig. 1 compares the aforementioned studies with each other. The stress ranges corresponding to failure were obtained from the S–N curves and a regression curve without extrapolation was created. In summary, it can be stated that investigations on the influence of surface roughness on the fatigue behavior of 316L produced through PBF-LB/M lead to various conclusions. However, a discernible trend is emerging, indicating that the surface roughness of PBF-LB/M-manufactured 316L does have an influence on the fatigue properties of 316L. It is evident that higher stresses are sustained at lower roughness values. However, the values exhibit significant variation, attributed to the diverse manufacturing parameters employed by different authors.

It is noteworthy to mention that the correlation between surface roughness parameters, such as Ra and Rz, is a subject of contentious debate within the literature on materials manufactured using the PBF-LB/M process. Furthermore, the application of optical methods to assess surface topography may not offer precise identification of local minima capable of initiating fatigue cracks. This limitation stems from the potential presence of deep or sharp valleys that may remain hidden from microscopic observation due to the presence of unmelted powder residue on the surface. This observation is supported by research by Lee et al. in 2021 and Gockel et al. in 2019 [15,16]. Additionally, Javadi et al. argue in their work [17] that alternative surface roughness parameters such as Mr2 and Rp exhibit stronger correlations with fatigue resistance. However, it is essential to note that their study focused exclusively on machined parts. An alternative study conducted by Lee et al. in 2020, [18], suggests that, among other factors, standard surface roughness parameters such as Ra, Rt, and Rz can indeed be employed

* Corresponding author.
E-mail address: johannes.diller@tum.de (J. Diller).
URL: https://www.cee.ed.tum.de/en/metallbau/ (J. Diller).

https://doi.org/10.1016/j.ijfatigue.2023.108025
Received 4 August 2023; Received in revised form 7 October 2023; Accepted 25 October 2023
Available online 29 October 2023

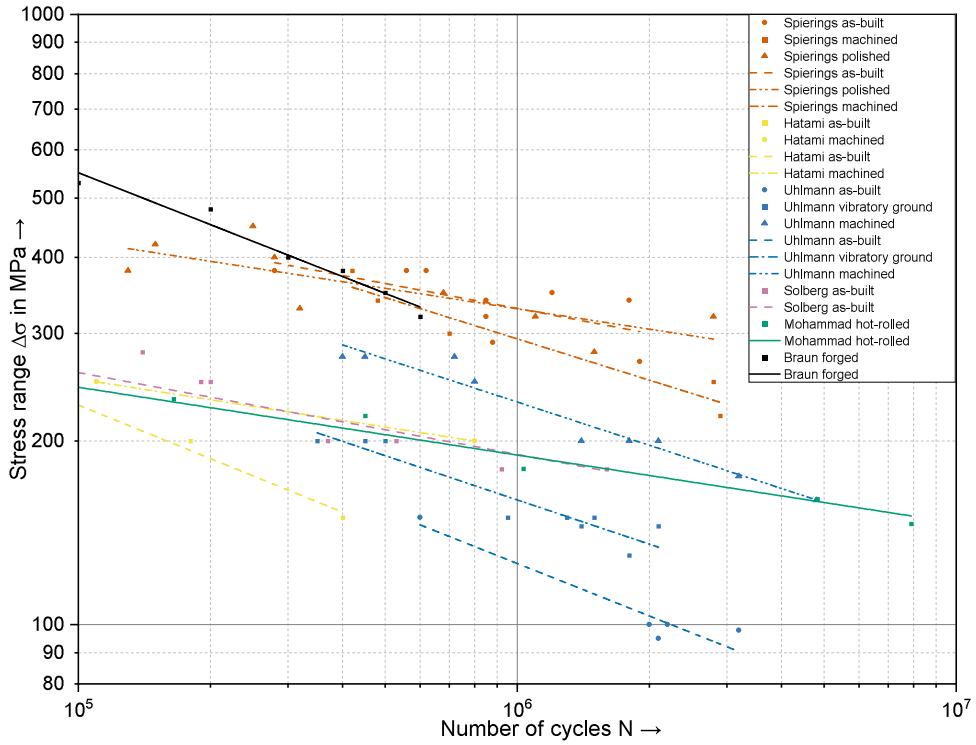

Fig. 1. Comparison of high-cycle fatigue tests from [9–14], Mohammad et al. had failures below 10^5 cycles.

for estimating fatigue life. Additionally, most studies could not exclude other failure causes, such as defects or lack of fusion. This occurs for example due to a high porosity of the specimens. Furthermore, the mentioned studies did not employ hot isostatic pressing (HIP) on the specimens. Since specimens in the as-built state exhibit higher porosity and tend to have a poorer residual stress state, it can be assumed that these studies did not exclusively investigate the pure influence of surface roughness on fatigue behavior but also considered the influence of porosity [19,20]. With regard to varying surface roughness conditions, the impact of grain size on the fatigue characteristics of PBF-LB/M/316L, resulting from recrystallization during heat treatment, remains unexplored. According to the findings of Murakami, presented in [21], fatigue cracks predominantly initiate at free surfaces. Therefore, four primary factors should be considered when evaluating fatigue strength. The first factor is the surface roughness itself, which acts as a stress concentration. The second factor is the presence of residual stresses within a surface layer, induced by machining or various post-processing methods. The third factor is the occurrence of cold work hardening or softening in the surface layer due to plastic deformation. The last factor is the alteration or transformation of the microstructure resulting from plastic deformation.

The cold work hardening and softening behavior of the material has been investigated in [22,23]. The results indicate that cyclic plastic loading leads to softening in fine-grained 316L, while larger grain structures exhibit a hardening behavior. No phase transformation was observed for both grain sizes due to the high austenite stability. Thus, the effects of surface roughness and residual stresses remain as influential factors concerning fatigue on this particular material. It should be mentioned that the aforementioned studies investigated the low-cycle fatigue behavior using strain-controlled fatigue testing methods.

This study aims to investigate the combined influence of surface treatments and hot isostatic pressing on the fatigue behavior. Standardized specimens were manufactured. Three parameter sets were hot isostatically pressed, three parameter sets were left in the as-built state, meaning that no heat treatment was applied. The surface roughness was changed using different post processing methods for all specimens of each parameter set. The fatigue properties were experimentally determined. The effects of the grain size, the kernel averaged misorientation, as well as the surface residual stresses were considered additionally. Finally, the fatigue testing results are compared with each other and a correlation between the microstructural investigations and the fatigue resistance is made.

2. Experimental methods

This chapter elucidates the procedure used to assess the combined impact of surface treatments and hot isostatic pressing on the fatigue resistance. The explanation encompasses the PBF-LB/M manufacturing process, the optical measurement techniques, the post-processing methods, as well as the microstructural investigations. The experimental plan is shown in Table 1.

2.1. Manufacturing of the specimens

In this research, 316L stainless steel (1.4404) metal powder provided by Oerlikon Metco was utilized. The EOS M280 PBF-LB/M machine was used for the study, which features a 400 W Ytterbium continuous wave fiber laser. The metal powder used had a particle size distribution ranging from 20–63 µm, with respective volume percentile values of D10, D50, and D90 measuring 19 µm, 30 µm, and 46 µm. Argon 5.0 gas was used during the manufacturing process, and a residual oxygen concentration below 1300 ppm within the build chamber was maintained. The build platform heating temperature was set to 80 °C. A x-rotation scan strategy with a changing angle of 60° after every layer was applied.

78 fatigue specimens according to ASTM E466 [24] and 6 tensile specimen according to [25] were manufactured by the PBF-LB/M process. All specimens were fabricated in a vertical orientation relative to the build platform. For the tensile test, specimen type no. 3 with a gauge length of four times the diameter according to ASTM E8 was used [25]. The experimental plan is shown in Table 1. The specimen geometry of the fatigue specimens is shown in Fig. 2.

Table 1
Experimental plan, the parameters for HIP are presented in Table 3, the parameters for the surface treatment are shown in Table 4 as well as in Section 2.3.

Specimen	Type of testing	Surface treatment	Heat treatment	Number of specimens
F_{0AB}	Fatigue	None	As-built	13
F_{1AB}	Fatigue	Manually polished	As-built	13
F_{2AB}	Fatigue	Vibratory ground	As-built	13
F_{0H}	Fatigue	None	HIP	13
F_{1H}	Fatigue	Manually polished	HIP	13
F_{2H}	Fatigue	Vibratory ground	HIP	13
T_{0AB}	Tensile	None	As-built	3
T_{0H}	Tensile	None	HIP	3

Table 2
Applied laser parameters for the manufacturing of the specimens.

Parameter	Value
Energy density E [J/mm^3]	65.00
Laser power P [W]	192
Scan velocity v [mm/s]	750
Hatch distance h [mm]	0.1
Layer thickness t [mm]	0.04

Table 3
Applied parameters for the hot isostatic pressing.

Parameter	Value
Heating rate [°C/h]	800
Temperature [°C]	1160
Pressure [bar]	1800
Duration [h]	3
Cooling rate [°C/s]	4
Cooling medium [–]	Air
Pressurization medium [–]	Argon

Table 4
Applied parameters for the vibratory grinding.

Parameter	Grinding	Polishing
Abrasive product	RCP S	RCP S
Filling weight [kg]	100	100
Liquid	RSP 506 S	ZF 113G
Duration [h]	5	1

The used laser parameters are listed in Table 2. According to Yakout et al. the laser parameter set is inside the stable melting zone [26]. This results in a low porosity and a homogeneous melt pool geometry. Since this study is focused on the effect of the surface defects, the porosity needed to be set as low as possible. After the manufacturing, all specimens were cut from the build plate.

2.2. Hot isostatic pressing

Hot isostatic pressing (HIP) was applied to investigate the effects of grain size and twin formation on fatigue properties, as well as to mitigate the internal porosity of the 316L material manufactured through the PBF-LB/M process. The specific parameters utilized in the HIP process are presented in Table 3.

2.3. Surface treatment

Three distinct surface states, denoted as F_0 (no surface treatment), F_1 (manually polished), and F_2 (vibratory ground), were generated. The F_0 state represents the as-built condition without any surface treatment. In the case of F_1, manual polishing was performed in the axial direction of the specimens using a fan grinder on a lathe. The process involved three successive steps: initial grinding with 80 SiC-paper, followed by grinding with 240 SiC-paper, and finally polishing using a zirconium fan grinder. The specimens of F_2 were vibratory ground using a Roesler R125 vibratory grinding machine. The applied grinding and polishing steps are shown in Table 4.

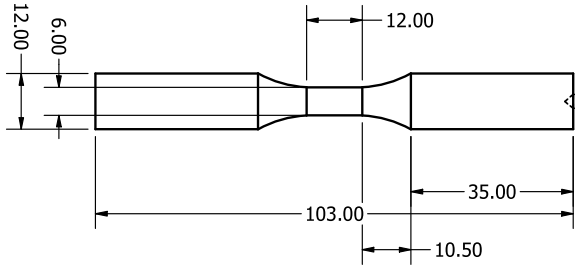

Fig. 2. Fatigue specimen geometry in mm according to ASTM E466 [24].

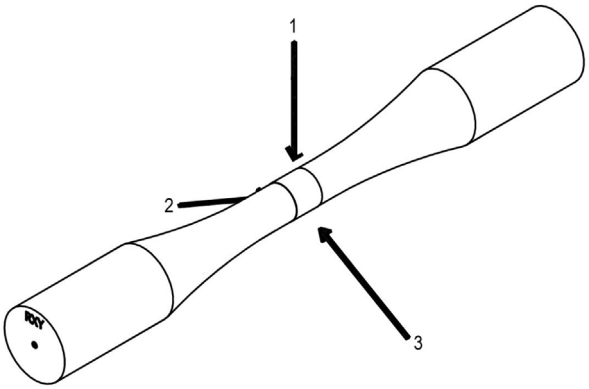

Fig. 3. Positions of the surface measurements.

2.4. Surface topology measurement

For the measurement of the surface roughness, line roughness and surface topology, a *Keyence VK-1000* (Keyence Corporation, Japan) laser confocal microscope was used. In the past ten years, optical methods have been put to use for measuring surface roughness, showing promising outcomes [27]. For the measurement of the line roughness, a cutoff wavelength λ_c of 0.25 mm and an evaluation length λ_s of 25 µm was applied. For the surface roughness measurement, a low-pass filter (S-filter) wavelength of 0.25 µm and a high-pass filter (L-filter) wavelength of 25 µm was applied. Fig. 3 shows the positions of the measurement areas. The measurements were carried out in three areas in the measuring zone. To enhance measurement traceability and ensure consistent test locations during or after fatigue experiments, a plastic template was fabricated to facilitate the marking of measurement points. The marking process was performed using a permanent marker, ensuring that the surface remained unaltered and undamaged.

A total area of 3.04 mm^2 was used for the measurement of the surface roughness. For the line roughness, 183 lines with a length of 5.1 mm and a distance of 6 pixel at each line were measured. A subset of specimens was selected to assess the surface roughness before and after fatigue testing in order to examine the alterations of the surface topology caused by fatigue loading. For selected specimens in test series F_{1H} (manually polished, HIP) and F_{2H} (vibratory ground, HIP), the surface roughness was additionally measured after 500, 5000, 50,000, 100,000 cycles and after failure. The applied stress range of the selected specimens in the experiment was 350 MPa.

2.5. Microstructural investigation

To determine the relative density, the specimens underwent grinding using abrasive papers with grit sizes of 180 SiC, 500 SiC, 800 SiC, and 1200 SiC, each for a duration of 240 s. The grinding plate operated at a speed of 300 revolutions per minute (rpm), while the revolver rotated at 120 rpm. The polishing of the specimens was performed using a *Struers* Dac polishing plate, utilizing diamond suspensions of 6 µm and 3 µm sequentially. Subsequently, a *Struers* Nap polishing plate with a 1 µm diamond suspension was employed, followed by a *Struers* Chem polishing plate with a 0.04 µm diamond suspension. During the polishing process, the grinding plate operated at a rotational speed of 150 revolutions per minute (rpm), while the revolver rotated at 120 rpm for each step, with each step lasting 180 s. The contact pressure was kept at 20 N. The relative density was measured using a gray-scale calibration with a light microscope. This means that the pore density based on image analysis was carried out. The relative density was measured in the longitudinal and transversal direction. For each direction, 5 layers were measured. For imaging, a Keyence VK-1000 laser confocal microscope was used. The open-source software ImageJ was used to evaluate the relative density [28]. To validate the origin of crack initiation, scanning electron microscopy (SEM) was used to detect whether the crack initiated at the surface or inside the specimen due to an internal defect. For that, a *Zeiss Leo 1530 VP* (Zeiss, Germany) scanning electron microscope was used. Additionally, electron backscatter diffraction (EBSD) measurements were carried out to investigate the formation of twins before and after the hot isostatic pressing procedure. Here, a Hikari EBSD-camera (*Ametek, USA*) was used.

2.6. Residual stress measurement on the surface

To measure the surface residual stresses at the surface treatment states mentioned in Section 2.3, x-ray diffraction (XRD) was applied using a Stresstech Xstress G2R XRD machine. The Chromium X-ray tube with a $K\beta$-radiation operated at a voltage of 30.0 kV and a current of 8 mA. The exposure time was set to 30 s. A collimator with a diameter of 3 mm was used. Two detectors were used which were set up in the 2θ-angle of 148.9 to evaluate the bragg peaks, which correlates to the (311) plane. To calculate the residual stresses, the d-$\sin^2\Psi$-method was used [29]. A lattice constant of 0.3596 nm was chosen for the calculations [30]. Rotating angles of 0°, −20.7°, −30.0°, −37.8°, −45.0°, 20.7°, 30.0°, 37.8°, and 45° were chosen, resulting in 18 measurements per specimen.

To obtain quantitative results of the residual stresses on the surface, it is necessary to have surfaces that are both smooth and clean. Nevertheless, in order to prevent any modification of the residual stresses within the specimens resulting from cutting, embedding, and polishing procedures, the measurements were conducted on the surface of the specimen without any alteration. As a result, the findings possess a purely qualitative nature, allowing for a comparison of the distinct surface conditions amongst themselves. For the evaluation of the resulting residual stresses, the software *XTronic* version 1.9.3 by the company *Stresstech* (Germany) was used. A Young's modulus OF 196 GP and a Poisson ratio OF 0.28 were used.

2.7. Mechanical testing

For tensile testing, a *Zwick & Roell Z100 TN* (Zwick & Roell, Germany) tensile testing machine with a load cell of 100 kN was used.

Fatigue testing was performed utilizing an *Instron 8800* test frame integrated with an *Instron 8500 digital control* (Instron mechanical testing systems, USA) system, possessing a dynamic load capacity of ±100 kN. A stress ratio of R = 0.1 and a frequency of 18 Hz was applied. For comparison of all test series, stress ranges of 200 MPa, 250 MPa, 300 MPa and 350 MPa were applied. For F_{1AB} (manually polished, no heat treatment) additionally 450 MPa was applied. The fatigue tests were stopped at 7 million cycles and considered as fatigue tests without failure.

3. Results and discussion

3.1. Microstructure

Fig. 4 reveals the microstructure in the as-built state in (a) (b) and (e) and the hot isostatically pressed state in (d). Fig. 4(a) and (b) show the typical weld lines in the transversal and longitudinal direction. Fig. 4(d) reveals large grains of around 100 µm in diameter with a homogeneous distribution in both directions. Fig. 4(e) shows very fine subgrains with a width of 300–400 nm. Fig. 4(c) and (f) show the results of the kernel averaged misorientation (KAM) in the as-built state (c) and the hot isostatically pressed state (f). It can be seen, that the KAM is significantly higher in the as-built state. The hot isostatic pressing process therefore not only increases the grain size but also decreases the misorientation and therefore also possibly the dislocation density. A high dislocation density leads to a high impediment of atoms at a grain boundary and therefore results in an increased yield strength. The atoms try to move or migrate through a material, particularly at a grain boundary due to a high dislocation density. These dislocations can obstruct the movement of atoms, especially when they try to move across grain boundaries [31,32].

3.2. Density

The 316L manufactured using PBF-LB/M exhibited a relative density of 99.98% in its as-built state, whereas the hot isostatically pressed (HIP) state displayed a relative density of 99.96%. The reduction in relative density following hot isostatic pressing can be attributed to two factors. Firstly, it is possible that Argon gas was trapped within the pores. Since Argon cannot diffuse through the metal, it becomes compressed during the HIP process. Subsequently, after the HIP treatment, the pores expand again, resulting in a decrease in relative density. Secondly, the slight difference of 0.02% in relative density can be attributed to a standard error of the measurement. Hence, it can be stated that no significant change was observed. This finding corroborates the conclusions reported in [33], which suggest that when the density surpasses 99.9%, only the nanoporosity experiences a reduction, while no significant visible change is observed.

3.3. Residual stresses on the surface

Table 5 shows the results of the residual stress measurements on the surface of the different heat treatment states and the surface topology states. The condition F_{0AB} (no surface treatment and no heat treatment) results in elevated tensile residual surface stresses attributed to the high cooling rate, which induces substantial local deformations and consequently increases the residual tensile stresses [34,35]. In contrast to the comparatively lower residual stresses observed in F_{2AB} (vibratory ground, no heat treatment), the residual stresses of F_{1AB} (manually polished, no heat treatment) exhibit a higher magnitude when subjected to the intense pressure applied during manual polishing. This discrepancy may be attributed to the reduced pressure input involved in

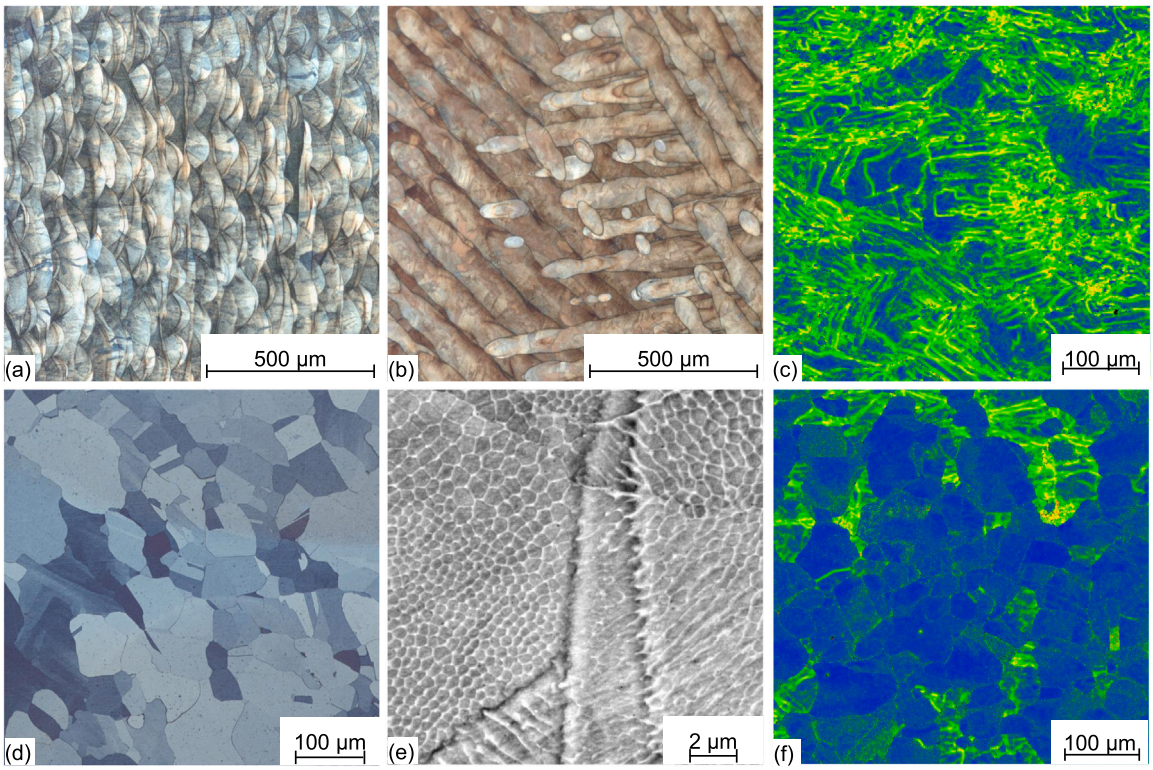

Fig. 4. Microstructure analysis of specimens before (a), (b) and after hot isostatic pressing (d). (c) shows the kernel averaged misorientation (KAM) in the transversal view of the as-built specimens whereas (f) shows the KAM in the hot isostatically pressed state in the transversal view, (a) presents the longitudinal view of the as-built specimens, (b) displays the transversal view of the as-built specimens, (d) showcases the grain structure of the hot isostatically pressed specimens, and (e) reveals the presence of fine subgrains measured with a SEM.

Table 5
Residual stresses on the surface. Index 0: no surface treatment, index 1: manually polished, index 2: vibratory ground, H: hot isostatically pressed, AB: no heat treatment.

Specimen	Residual stress [MPa]
F_{0AB}	144
F_{1AB}	−51
F_{2AB}	−11
F_{0H}	32.9
F_{1H}	−302.2
F_{2H}	−414.5

the vibratory grinding process. The hot isostatically pressed specimens (F_{0H} (no surface treatment), F_{1H} (manually polished), F_{2H}) (vibratory ground) generally show reduced residual surface stresses due to the recrystallization and reduction of tensile residual stresses during the heat treatment process. It is also apparent, that the surface treatment procedures (F_{1H}, F_{2H}) result in high compressive residual stresses on the surface.

The findings from the untreated surface state, denoted as F_{0AB} and F_{0H}, are consistent with the outcomes reported by Shin et al. in their 2021 study [36]. In the aforementioned study, the application of hot isostatic pressing resulted in a noticeable reduction of residual stresses. In the untreated condition, residual stresses resulted in 110 MPa, while the specimens subjected to hot isostatic pressing exhibited substantially lower values, measuring at 25 MPa.

3.4. Surface topology

For the purpose of enhancing the result comparability, the results of the surface roughness measurements were averaged based on the aforementioned three individual measurement areas per specimen. Consequently, each specimen is represented by an averaged roughness value. These values are shown in Fig. 5. For comparison with the aforementioned studies in Fig. 1, the line roughness and surface roughness values Ra, Rz, Sa and Sz are shown. Measurements were conducted on both hot isostatically pressed specimens and specimens in their as-built state. However, no significant difference was observed between the two conditions. Consequently, the results are categorized and presented as F_0 (no surface treatment), F_1 (manually polished), and F_2 (vibratory ground). The data clearly indicates that the roughness level is most pronounced for F_0, as evidenced by the highest overall roughness value. Furthermore, F_0 (no surface treatment) also exhibits the highest standard deviation among the tested parameters. The line roughness measurements demonstrate comparable results for F_1 (manually polished) and F_2 (vibratory ground), albeit with a slightly higher standard deviation observed for F_1. In contrast, the surface roughness (Sa and Sz) analysis reveals that F_2 exhibits a higher surface roughness compared to F_1, while maintaining a slightly lower standard deviation. The comparison of surface conditions F_1 (manually polished) and F_2 (vibratory ground) reveals that there is not a significant difference in line roughness values, such as Ra and Rz. However, a noticeable distinction is observed in the surface roughness value Sz, between surface condition F_1 (manually polished) and F_2 (vibratory ground).

Fig. 6 illustrates the surface topology of various specimens in the hot isostatically pressed state, both before and after fatigue testing, along with specimens in the polished and vibratory ground states. Table 6 denotes the respective values of the change of the arithmetical mean height (Sa), the maximum height (Sz) as well as the arithmetic mean peak curvature (Spc). The latter is shown because it corresponds to the average principal curvature of the surface peaks. A smaller value of Spc indicates that the contact points with other objects possess rounded shapes, while a larger value suggests pointed shapes at the contact points. Observing F_{1H} (manually polished, HIP) at stress ranges of 200 MPa and 300 MPa, it is evident that there is no significant alteration

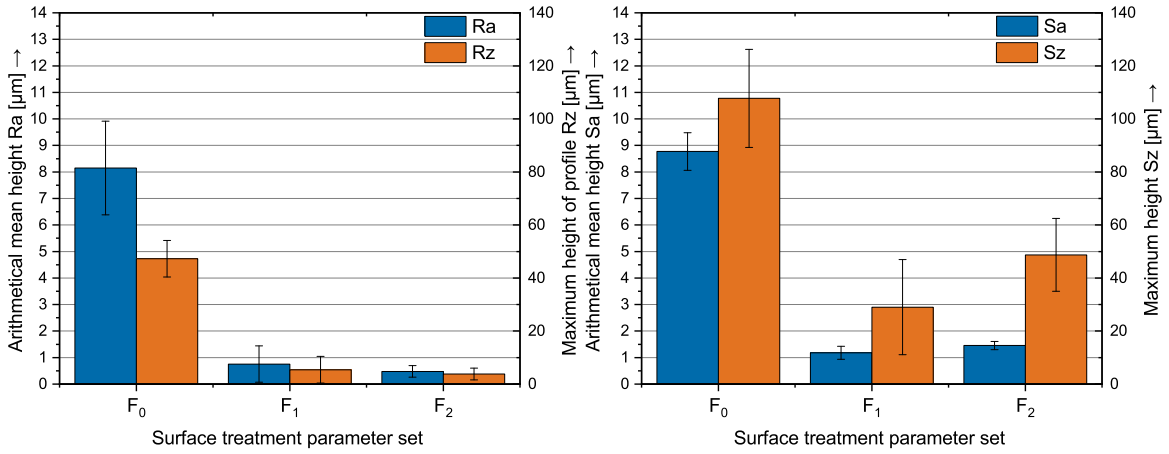

Fig. 5. Results of the line roughness measurements Ra and Rz (left graph) as well as the surface roughness measurements Sa and Sz (right graph) before testing. F_0 (no surface treatment), F_1 (manually polished) as well as F_2 (vibratory ground) represent the different surface roughness states explained in Table 1.

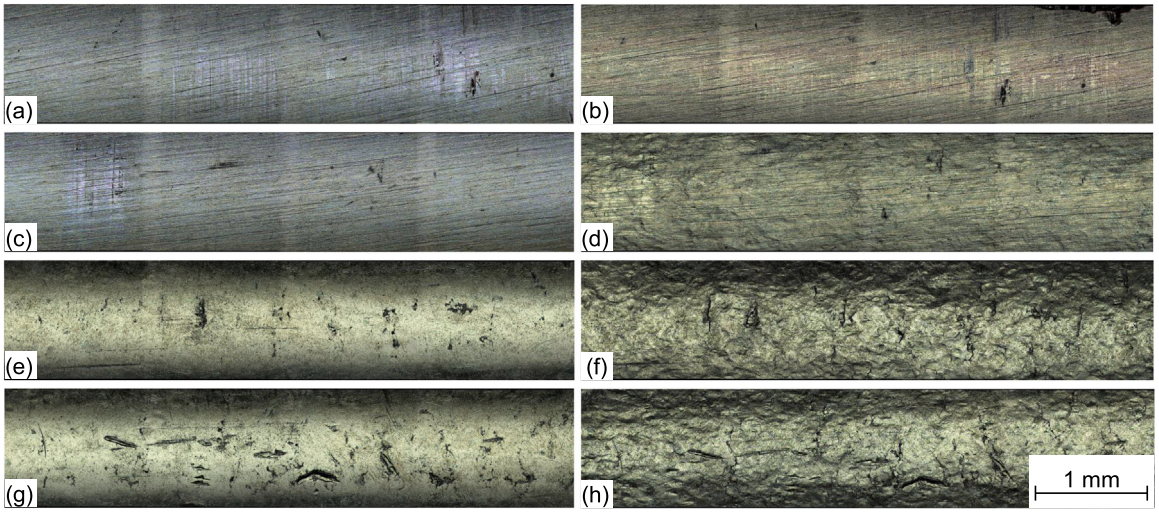

Fig. 6. Surface topology before fatigue testing and after fatigue failure; F_1 (manually polished) at 200 MPa stress range before (a) and after (b) fatigue testing, F_1 (manually polished) at 300 MPa stress range before (c) and after (d) testing, F_2 (vibratory ground) at 200 MPa stress range before (e) and after (f) testing, F_2 (vibratory ground) at 300 MPa stress range before (g) and after (h) testing.

Table 6
Change in surface roughness before and after fatigue testing of manually polished (F_1) and vibratory ground (F_2) fatigue specimens in the hot isostatically pressed state (H) and without heat treatment (AB); ΔSa represents the change in the arithmetical mean height, ΔSz denotes the maximum height, and ΔSpc refers to the arithmetic mean peak curvature. The initial values of Spc are shown in Fig. 12.

Specimen	Stress range [MPa]	ΔSa [µm]	ΔSa [%]	ΔSz [µm]	ΔSz [%]	ΔSpc [1/mm]	ΔSpc [%]
F_{1AB}	200	−0.41	−64.3	−4.58	−30.0	−11.91	−70.2
F_{1AB}	300	−0.46	−72.1	−9.74	−63.8	−12.70	−74.8
F_{2AB}	200	+0.80	+65.1	+9.99	+18.03	+7.0	+106.5
F_{2AB}	300	+3.69	+302.5	−16.58	+29.93	+38.4	+582.1
F_{1H}	200	+0.01	+1.1	−2.33	−24.97	−1.0	−6.9
F_{1H}	300	+0.65	+161.6	+4.25	+45.65	+6.2	+42.6
F_{2H}	200	+0.92	+249.0	+14.53	+107.27	+15.0	+139.5
F_{2H}	300	+1.09	+295.3	+6.11	+45.10	+18.0	+160.2

observed in terms of Sa, Sz, and particularly Spc. Conversely, notable changes are apparent in Sz and Spc for F_{2H} (vibratory ground, HIP). The Spc values exhibit a doubling effect, indicating that the surface displays a more acute topology. The observed alteration in the parameter Spc is notably more pronounced in the case of F_{2AB} (vibratory ground, no heat treatment).

The alteration of surface roughness after the fatigue test can be attributed to several effects. An increase can be explained by the formation of twins and grain displacements perpendicular to the surface. Conversely, a decrease can be caused by changes in surface topography due to grain displacements perpendicular to the surface and microplastic deformations, as they elongate the surface. According to Wang et al. [27], an increase in surface roughness in hot-rolled 316L is primarily caused by the formation of twins during the first 200 fatigue cycles. Subsequently, the surface roughness increases due to the displacement of individual grains perpendicular to the surface.

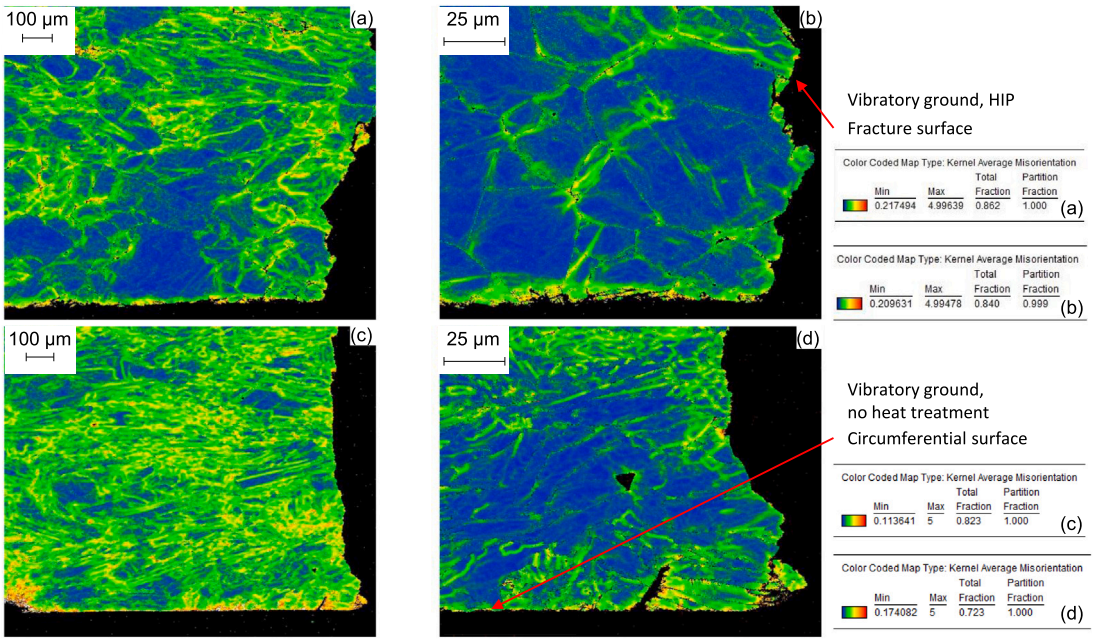

Fig. 7. Kernel Averaged Misorientation (KAM) analysis of fatigue tested specimens. Images (a) and (b) depict specimens subjected to fatigue testing with a stress range of 350 MPa under the influence of F_{2H} conditions (vibratory ground, HIP). Images (c) and (d) illustrate a specimen tested under the same stress range of 350 MPa but subjected to F_{2AB} conditions (vibratory ground, no heat treatment). Notably, the circumferential surface in the lower region of the images exhibits a pronounced high KAM. Images (b) and (d) provide closer views of the lower right areas within images (a) and (c), respectively.

This displacement is induced by varying stress concentrations in different grains. Similarly, Hoffmann et al. [37] describe an increase in surface roughness due to twinning in the austenitic TWIP (twinning induced plasticity) steel Fe22Mn0.6C. It can be assumed that the surface roughness of samples altered by hot isostatic pressing undergoes more significant changes compared to the as-built specimens due to the presence of formed twins, which continue to grow under loading conditions. It is assumed that the reason for the decrease in measured surface roughness is the occurrence of grain boundary sliding, which is perpendicular to the surface. The formation of these sliding movements can completely alter the roughness profile. As the sliding occurs uniformly across the entire surface, the valleys of the old roughness profile rise, resulting in a potential reduction in roughness. In the case of test specimens subjected to fatigue loading, the reduction in roughness can be attributed to the elongation introduced during the fatigue test. However, since the loading level of the test specimens remains below the yield strength, only elastic and microplastic deformations occur. It is believed that the presence of microplastic deformations is sufficient to decrease the roughness. To confirm this, measurements of strain fields with a digital image correlation setup during the fatigue test are necessary. Alternatively, post-fatigue testing EBSD measurements can be conducted to assess the kernel averaged misorientation on the surface. Fig. 7 depicts the kernel averaged misorientation (KAM) for two specimens after fatigue testing.

A longitudinal cut was performed, revealing the fracture surface on the right side and the circumferential surface at the bottom of the images. Both specimens were exposed to a stress range of 350 MPa, but in distinct states: F_{2H} (vibratory ground, HIP) and F_{2AB} (vibratory ground, no heat treatment). The circumferential surface reveals notably elevated KAM values, potentially signaling grain boundary sliding [38]. An intriguing observation to note involves the contrast in surface characteristics when examining the states of F_{2H} (vibratory ground, HIP) and F_{2AB} (vibratory ground, no heat treatment), as illustrated in Fig. 7. In the F_{2H} state (vibratory ground, HIP) depicted in (a) and (b), there is a notable disparity in the circumferential surface, which appears noticeably irregular in comparison to the F_{2AB} state (vibratory ground, no heat treatment) shown in (c) and (d). This is crucial to emphasize that the initial surface topology was identical for both states before undergoing testing.

The significant alteration in surface roughness and topology, as illustrated in Fig. 6(e) and (f), as well as (g) and (h), is observed to transpire after only 500 cycles of testing and does not change significantly until failure. This is also shown in Fig. 8. This indicates that plastic deformation of the surface occurs shortly after the initiation of the testing process. Considering the relatively low number of cycles at that point, it can be assumed that the initial surface roughness of F_{2H} may not accurately show a good correlation to the fatigue behavior. Instead, the surface roughness after a few number of cycles should be considered for a more reliable assessment.

3.5. Tensile testing

The results of the tensile tests are shown in Fig. 9.

Specimens in the as-built state exhibit a high yield strength of up to 471 MPa. Moreover, the ultimate tensile strength reaches values as high as 577 MPa. These results align with the published data of Roettger et al. [39], Liverani et al. [4] as well as Puichaud et al. [33].

In contrast, specimens that underwent hot isostatic pressing (HIP) display a noticeable reduction in yield strength, reaching a maximum value of 264 MPa. On one hand, this reduction of the yield strength can be explained with the Hall–Petch relationship. With finer grain size, the dislocation impediment increases. A high dislocation impediment results in a high yield strength [40]. The PBF-LB/M manufactured 316L in the as-built state shows very fine subgrains with a width of around 300–400 nm, as can be seen in Fig. 4(d). This statement aligns with the findings of [33]. On the other hand it can be explained with the dislocation density. Shin et al. [36] as well as Puichaud et al. [33] showed that hot isostatic pressing decreases the dislocation density and slightly increases the grain size, which resulted in a reduction of the yield strength. Puichaud et al. stated in [33] that the strong intragranular misorientation can be roughly correlated to the dislocation density. Fig. 4(c) and (f) show a significant reduction in the intragranular misorientation. Nonetheless, the ultimate tensile strength of the hot isostatically pressed specimens remains relatively high, with

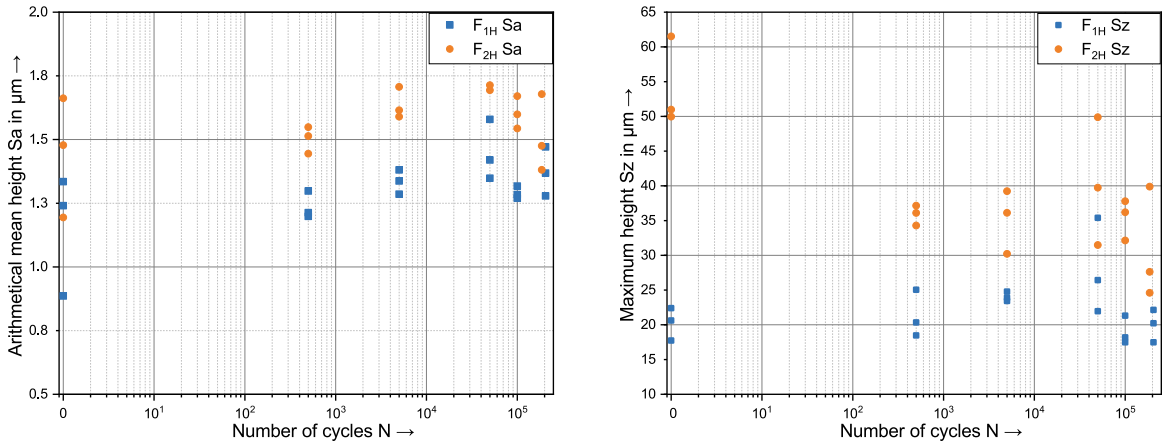

Fig. 8. Surface roughness analysis of specimens F_{1H} and F_{2H} before testing and at various fatigue stages (500 cycles, 5000 cycles, 50,000 cycles, 100,000 cycles, and after failure).

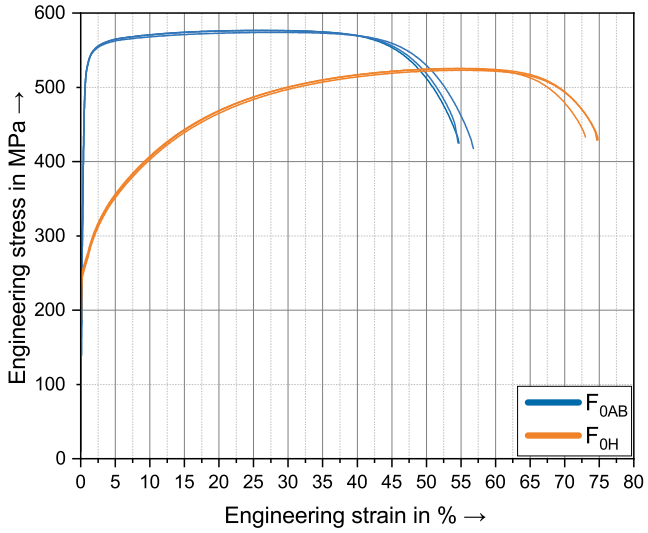

Fig. 9. Results of the tensile tests in the as-built state (F_{0AB}) and the hot isostatically pressed state (F_{0H}) without any surface treatment.

values of up to 525 MPa. Another noteworthy observation is the change in elongation at fracture between the two states. The as-built specimens exhibit an elongation at fracture of 54%, indicating their ability to undergo substantial deformation before fracturing. However, the HIPed specimens demonstrate an improved elongation at fracture, reaching 74%. These findings align with the assertion made by Qin et al. [41] that a larger grain size can potentially yield increased ductility.

3.6. Fracture surface

The image clearly illustrates that the crack initiated at the surface, particularly in the bottom region, as indicated by the red arrow. This observation is consistent with the findings from subsequent measurements conducted on multiple specimens, which consistently indicate surface-initiated crack propagation for each tested specimen. Additionally, a half-moon shaped surface was observed on the opposite side of the crack initiation area. This distinct surface morphology indicates the rupture of the last cycles leading to failure. Notably, this half-moon shaped elevated surface tends to appear on the side opposite to the crack initiation site [42]. Fig. 10 depicts a representative fracture surface of a fractured fatigue specimen after fatigue testing. The observed data indicates the presence of multiple surface irregularities. It is hypothesized that these are not attributable to near-surface porosity but rather to insufficient material removal during vibratory grinding processes. Consequently, the valleys were not effectively eliminated. It is worth noting that the effect observed, where the surface appears uneven, could also be attributed to the possible opening of pores near the surface during vibratory grinding. This could create a similar appearance to uneven valleys that may not have been adequately removed.

3.7. Fatigue testing

Fig. 11 shows the results of the high cycle fatigue tests. R^2 depicts the coefficient of determination, whereas m represents the slope of the fitted regression curve. Run outs were not considered for the creation of the regression curve. In general, the fatigue resistance of the hot isostatically pressed specimens is noticeably inferior when compared to the specimens in their as-built state. F_{1AB} (manually polished, no heat treatment) exhibits the highest overall resistance against cyclic loading. In terms of fatigue life, there is minimal disparity between F_{0AB} (no surface treatment, no heat treatment) and F_{2AB} (vibratory ground, no heat treatment); they show almost identical performance. Among the hot isostatically pressed specimens, the surface condition F_{1AB} (manually polished, no heat treatment) consistently delivers the most favorable outcomes concerning fatigue life across varying stress ranges. Conversely, F_{2H} (vibratory ground, HIP) exhibits the lowest resistance to fatigue. F_{0H} (no surface treatment, HIP) displays superior fatigue resistance when compared to F_{2H} (vibratory ground, HIP). However, since all values from the hot isostatically pressed specimens are closely clustered, no definitive statement can be made regarding the superiority of one treatment state over another.

The lower fatigue resistance of the hot isostatically pressed specimens compared to the specimens in the as-built state can be attributed to differences in grain size. With finer grain size, the fatigue resistance increases. The main reason for this improvement is the retardation of fatigue crack initiation. This improvement can be attributed to the homogeneous deformation occurring on the surface of the fine grains as a result of the high cooling rate during the PBF-LB/M manufacturing process. As a result, no slip deformation is formed. Consequently, cracks tend to occur at the grain boundaries [43–49].

The presence of residual compression stresses at the surface has been observed to result in an increase in fatigue life, as demonstrated by the case of F_{1AB} (manually polished, no heat treatment) (see Table 5). This is also the case for F_{1H} (manually polished, HIP), as it shows the best fatigue resistance of all hot isostatically pressed specimens. However, counterintuitively, F_{2H} (vibratory ground, HIP) reveals higher residual compression stresses but shows the lowest fatigue life. This

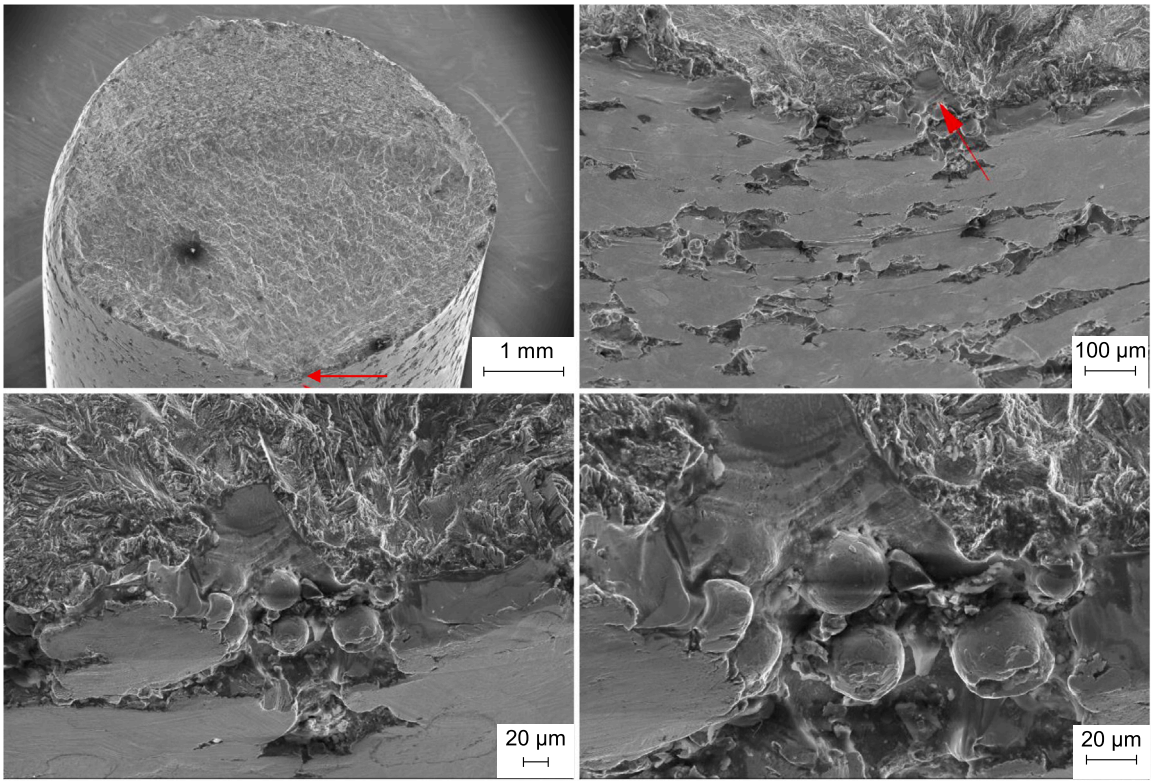

Fig. 10. Fracture surface of a broken specimen of F_{2H} (vibratory ground, HIP) after failure due to fatigue. The magnification of the crack initiation increases from the top left to the bottom right. The circumferential surface exhibits inadequate material removal due to vibratory grinding, resulting in the retention of valleys within the material.

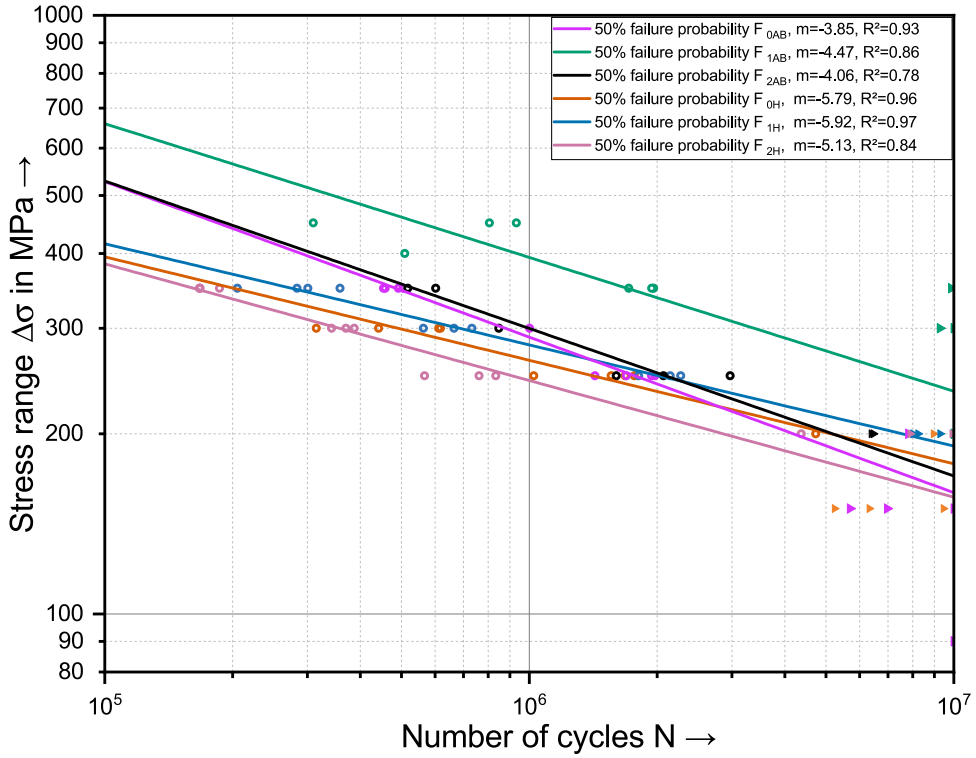

Fig. 11. Results of fatigue tests with different heat treatment states and different surface treatment states. A stress ratio of $R = 0.1$ was applied. m represents the slope of the different regression lines, R^2 represents the coefficient of determination. The triangles indicate the run outs.

may be due to the inadequately removed surface topology or due to opened pores after vibratory grinding. The studies conducted by Vayssette et al. [50,51] demonstrated that valleys, in comparison to particles that undergo partial melting onto the surface, experience higher levels of stress. This observation may provide an explanation for the similarity in fatigue life between F_{0AB} (no surface treatment, no

heat treatment) and F_{0H} (no surface treatment, HIP) when compared to F_{2AB} (vibratory ground, no heat treatment) and F_{2H} (vibratory ground, HIP) respectively.

The fatigue life is influenced by various factors, including the presence of high residual compressive stresses at the surface, which tends to increase it. However, the existence of defects near the surface can subsequently decrease the fatigue life as was shown by Murakami et al. in [21,52,53]. Defects near the surface of metallic structures act as stress concentrators, providing locations where stresses can accumulate during cyclic loading. This can lead to the initiation and propagation of micro-cracks, accelerating the fatigue process of the material. Over time, these micro-cracks can coalesce and grow, reducing the structural integrity of the material and leading to failure under continued cyclic stress. Additionally, it is important to consider that the measured surface residual stresses may not have the same value at the opened pore regions. Residual stresses typically strive to achieve equilibrium, which means that compressive residual stresses on the surface may result in the development of tensile residual stresses at a short distance beneath the surface [54]. A considerable factor which correlates well to the fatigue is the arithmetic mean peak curvature after fatigue testing. A significant change of ΔSpc for F_{2AB} (vibratory ground, no heat treatment) and F_{2H} (vibratory ground, HIP) can be observed between before and after testing.

When comparing the data depicted in Fig. 1, it can be observed that the S–N curves from the study conducted by Spierings et al. [10] exhibit resemblances to both F_{0AB} (no surface treatment, no heat treatment) and F_{2AB} (vibratory ground, no heat treatment). It is crucial to emphasize that none of the referenced sources in Fig. 1 utilized any heat treatment or hot isostatic pressing procedures. Specifically, Uhlmann et al. [11], Hatami et al. [12], and Solberg et al. [9] demonstrated subpar fatigue performance when compared to all the investigated surface conditions and heat treatment variations in this study. Only the machined specimens examined by Uhlmann et al. [11] exhibited fatigue results that were comparable to those of F_{2H} (vibratory ground, HIP). It is worth noting that Solberg et al. [9] intentionally employed specific laser parameters that resulted in a deliberately high level of porosity in their test specimens. The conventionally manufactured 316L material, as investigated by Mohammad et al. [13], exhibited lower fatigue performance when compared to all the surface conditions and heat treatment variations examined in this study. Conversely, the forged 316L material analyzed by Braun et al. [14] displayed results that were comparable to those of F_{0AB} (no surface treatment, no heat treatment).

4. Summary

In the high cycle fatigue tests shown in Fig. 11, the hot isostatically pressed specimens exhibited lower fatigue resistance compared to the as-built specimens. Among the specimens in the as-built state, F_{1AB} demonstrated the highest resistance to cyclic loading, while F_{0AB} (no surface treatment, no heat treatment) and F_{2AB} (vibratory ground, no heat treatment) had similar fatigue performance. In terms of hot isostatically pressed specimens, F_{1H} consistently exhibited the best fatigue life, while F_{2H} (vibratory ground, HIP) had the lowest resistance to fatigue. Nevertheless, no distinct statement can be made about the superiority as all treatment states are very close together. The inferior fatigue resistance of hot isostatically pressed specimens can be attributed to differences in grain size, with finer grains resulting in improved fatigue resistance due to the prevention of slip deformation and crack initiation. Additionally, the presence of residual compression stresses at the surface generally increased fatigue life, although the existence of opened pores or inadequately removed surface topology after vibratory grinding may have contributed to reduced fatigue life as has been shown by Vaysette et al. [50,51]. The measured surface residual stresses may not be uniform in the opened pore regions, as residual stresses tend to seek equilibrium, leading to the development of tensile stresses beneath the surface. The surface topology of hot isostatically pressed and vibratory ground specimens undergoes rapid changes even after a small number of cycles. Consequently, when establishing a correlation between surface roughness and fatigue, it is advisable to consider the surface roughness after a few hundred cycles rather than the initial state. This approach takes into account the evolving surface conditions and provides a more accurate representation of the surface roughness relevant to fatigue performance. Additionally, the arithmetic mean peak curvature (AMPC) can provide crucial insights about the surface profile of a metallic structure. These stress concentrations are potential initiation sites for micro-cracks under cyclic loading, leading to accelerated fatigue. Thus, monitoring and controlling AMPC can be an effective strategy in fatigue life prediction and enhancement, helping guide processes like surface finishing or treatments to reduce fatigue failures.

5. Conclusion

From this study, the following conclusions can be drawn:

- The hierarchy of the impact on fatigue resistance may be established as follows: Grain size holds the greatest magnitude of influence, followed by surface roughness, and subsequently residual surface stresses.
- A small grain size increases the fatigue resistance.
- Locally opened pores and insufficient material removal due to vibratory grinding may reduce the fatigue resistance.
- Manual polishing closes pores near the surface and increases the compressive residual stresses, resulting in a higher fatigue resistance.
- Residual stresses on the surface may have a small influence on the fatigue resistance if opened pores near the surface are present.
- Surface topology of hot isostatically pressed and vibratory ground specimens changes rapidly after a few cycles in contrast to as-built PBF-LB/M/316L with the same surface treatment. To correlate surface roughness with fatigue, it is recommended to consider roughness after a few hundred cycles, accounting for evolving surface conditions and ensuring accurate representation for fatigue performance.
- The line roughness parameters, specifically Ra and Rz, do not exhibit a strong correlation between roughness and fatigue resistance. On the other hand, the surface roughness parameter Sz demonstrates a more favorable correlation in this regard. In addition to surface roughness parameters, other factors such as grain size, grain boundary sliding, twinning affinity, and residual stresses present on the surface exert a significant influence on fatigue resistance.

6. Outlook

Given the constraints associated with manual polishing of complex structures, and the potential for vibratory grinding to either expose near-surface pores or inadequately remove material resulting in valleys, it becomes imperative to investigate alternative surface treatment methodologies. This would involve investigating and evaluating different methods to achieve desired surface properties while mitigating the drawbacks associated with the existing processes. Overpotential electrochemical polishing could be a promising approach for improving fatigue life and addressing the presence of opened pores near the surface by smoothing out sharp edges which has been shown by Chang et al. in [55]. Additionally, to accurately assess residual stresses, neutron diffraction measurements should be conducted to investigate stress distribution across the cross section. This will enable the characterization of the transition of residual stresses from compression to tension and provide a comprehensive understanding of their changes.

CRediT authorship contribution statement

Johannes Diller: Conceptualization, Methodology, Validation, Formal analysis, Investigation, Resources, Data curation, Writing – original draft, Writing – review & editing, Visualization, Project administration, Funding acquisition. **Jakob Blankenhagen:** Conceptualization, Methodology, Software, Validation, Formal analysis, Investigation, Data curation, Visualization. **Dorina Siebert:** Conceptualization, Writing – review & editing, Funding acquisition. **Christina Radlbeck:** Resources, Writing – review & editing, Supervision, Project administration, Funding acquisition. **Martin Mensinger:** Resources, Writing – review & editing, Supervision.

Declaration of competing interest

The authors declare the following financial interests/personal relationships which may be considered as potential competing interests: Johannes Diller reports financial support was provided by German Research Foundation.

Data availability

Data will be made available on request.

Acknowledgments

This study was funded by the Deutsche Forschungsgemeinschaft (DFG, German Research Foundation) – Project number 414265976 – TRR 277. We would like to express our gratitude to the DFG for their funding support, which significantly contributed to the completion of this paper. Additionally, we would like to express our gratitude to the anonymous reviewers for their insightful comments and constructive suggestions, which significantly contributed to enhancing the quality of the manuscript.

Appendix

See Fig. 12.

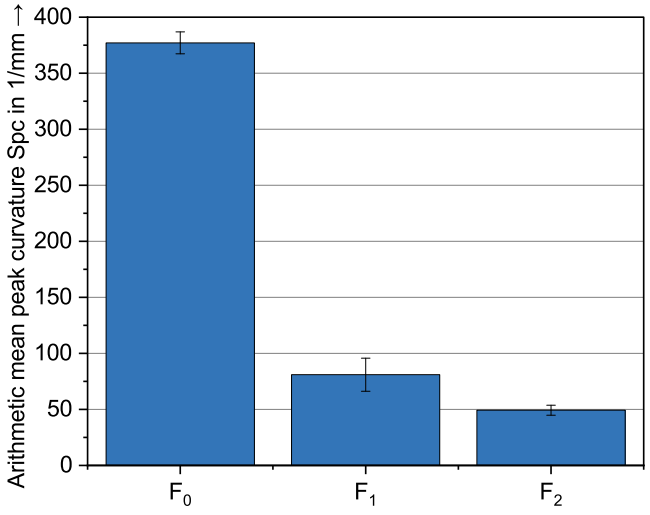

Fig. 12. Results of the arithmetic mean peak curvature Spc before testing. F_0 (no surface treatment), F_1 (manually polished) as well as F_2 (vibratory ground) represent the different surface roughness states explained in Table 1.

References

[1] Al-Maharma Ahmad Y, Patil Sandeep P, Markert Bernd. Effects of porosity on the mechanical properties of additively manufactured components: a critical review. Mater Res Express 2020;7(12):122001. http://dx.doi.org/10.1088/2053-1591/abcc5d.

[2] Kan Wen Hao, Chiu Louis Ngai Sam, Lim Chao Voon Samuel, Zhu Yuman, Tian Yang, Jiang Derui, Huang Aijun. A critical review on the effects of process-induced porosity on the mechanical properties of alloys fabricated by laser powder bed fusion. J Mater Sci 2022;57(21):9818–65. http://dx.doi.org/10.1007/s10853-022-06990-7.

[3] Jaskari Matias, Mäkikangas Jarmo, Järvenpää Antti, Mäntyjärvi Kari, Karjalainen Pentti. Effect of high porosity on bending fatigue properties of 3D printed AISI 316L steel. Procedia Manuf 2019;36:33–41. http://dx.doi.org/10.1016/j.promfg.2019.08.006.

[4] Liverani E, Toschi S, Ceschini L, Fortunato A. Effect of selective laser melting (SLM) process parameters on microstructure and mechanical properties of 316L austenitic stainless steel. J Mater Process Technol 2017;249:255–63. http://dx.doi.org/10.1016/j.jmatprotec.2017.05.042.

[5] Casati R, Lemke J, Vedani M. Microstructure and fracture behavior of 316L austenitic stainless steel produced by selective laser melting. J Mater Sci Technol 2016;32(8):738–44. http://dx.doi.org/10.1016/j.jmst.2016.06.016.

[6] Zhang Baicheng, Dembinski Lucas, Coddet Christian. The study of the laser parameters and environment variables effect on mechanical properties of high compact parts elaborated by selective laser melting 316L powder. Mater Sci Eng A 2013;584:21–31. http://dx.doi.org/10.1016/j.msea.2013.06.055.

[7] Chahal Vedant, Taylor Robert M. A review of geometric sensitivities in laser metal 3D printing. Virtual Phys Prototyp 2020;15(2):227–41. http://dx.doi.org/10.1080/17452759.2019.1709255.

[8] Hosseini E, Popovich VA. A review of mechanical properties of additively manufactured Inconel 718. Addit Manuf 2019;30:100877. http://dx.doi.org/10.1016/j.addma.2019.100877.

[9] Solberg Klas, Guan Shuai, Razavi Seyed Mohammad Javad, Welo Torgeir, Chan Kang Cheung, Berto Filippo. Fatigue of additively manufactured 316L stainless steel: The influence of porosity and surface roughness. Fatigue Fract Eng Mater Struct 2019;42(9):2043–52. http://dx.doi.org/10.1111/ffe.13077.

[10] Spierings AB, Starr TL, Wegener K. Fatigue performance of additive manufactured metallic parts. Rapid Prototyp J 2013;19(2):88–94. http://dx.doi.org/10.1108/13552541311302932.

[11] Uhlmann Eckart, Fleck Claudia, Gerlitzky Georg, Faltin Fabian. Dynamical fatigue behavior of additive manufactured products for a fundamental life cycle approach. Procedia CIRP 2017;61:588–93. http://dx.doi.org/10.1016/j.procir.2016.11.138.

[12] Hatami Sepehr, Ma Taoran, Vuoristo Taina, Bertilsson Jens, Lyckfeldt Ola. Fatigue strength of 316 L stainless steel manufactured by selective laser melting. J Mater Eng Perform 2020;29(5):3183–94. http://dx.doi.org/10.1007/s11665-020-04859-x.

[13] Mohammad Khairul Azhar, Zainudin Edi Syam, Sapuan SM, Zahari Nur Ismarrubie, Aidy Ali. Fatigue life for type 316l stainless steel under cyclic loading. Adv Mater Res 2013;701:77–81. http://dx.doi.org/10.4028/www.scientific.net/amr.701.77.

[14] Braun Moritz, Mayer Eduard, Kryukov Igor, Wolf Christian, Böhm Stefan, Taghipour Aliakbar, Wu Rachael Elizabeth, Ehlers Sören, Sheikhi Shahram. Fatigue strength of PBF-LB/M and wrought 316L stainless steel: effect of post-treatment and cyclic mean stress. Fatigue Fract Eng Mater Struct 2021;44(11):3077–93. http://dx.doi.org/10.1111/ffe.13552.

[15] Lee Seungjong, Rasoolian Behnam, Silva Daniel F, Pegues Jonathan W, Shamsaei Nima. Surface roughness parameter and modeling for fatigue behavior of additive manufactured parts: A non-destructive data-driven approach. Addit Manuf 2021;46:102094. http://dx.doi.org/10.1016/j.addma.2021.102094.

[16] Gockel Joy, Sheridan Luke, Koerper Brittanie, Whip Bo. The influence of additive manufacturing processing parameters on surface roughness and fatigue life. Int J Fatigue 2019;124:380–8. http://dx.doi.org/10.1016/j.ijfatigue.2019.03.025.

[17] Javadi Hamid, Jomaa Walid, Texier Damien, Brochu Myriam, Bocher Philippe. Surface roughness effects on the fatigue behavior of as-machined Inconel718. Solid State Phenom 2016;258:306–9. http://dx.doi.org/10.4028/www.scientific.net/ssp.258.306.

[18] Lee Seungjong, Pegues Jonathan W, Shamsaei Nima. Fatigue behavior and modeling for additive manufactured 304L stainless steel: The effect of surface roughness. Int J Fatigue 2020;141:105856. http://dx.doi.org/10.1016/j.ijfatigue.2020.105856.

[19] Röttger Arne, Geenen Karina, Windmann Matthias, Binner Florian, Theisen Werner. Comparison of microstructure and mechanical properties of 316 L austenitic steel processed by selective laser melting with hot-isostatic pressed and cast material. Mater Sci Eng A 2016;678:365–76. http://dx.doi.org/10.1016/j.msea.2016.10.012.

[20] Lavery NP, Cherry J, Mehmood S, Davies H, Girling B, Sackett E, Brown SGR, Sienz J. Effects of hot isostatic pressing on the elastic modulus and tensile properties of 316L parts made by powder bed laser fusion. Mater Sci Eng A 2017;693:186–213. http://dx.doi.org/10.1016/j.msea.2017.03.100.

[21] Murakami Y. Metal fatigue. Elsevier; 2019, http://dx.doi.org/10.1016/c2016-0-05272-5.

[22] Diller Johannes, Siebert Dorina, Radlbeck Christina, Mensinger Martin. PBF-LB/M/316L vs. hot-rolled 316L – comparison of cyclic plastic material behavior. Procedia Struct Integr 2022;42:58–65. http://dx.doi.org/10.1016/j.prostr.2022.12.006.

[23] Diller Johannes, Rier Lukas, Siebert Dorina, Radlbeck Christina, Krafft Frank, Mensinger Martin. Cyclic plastic material behavior of 316L manufactured by laser powder bed fusion (PBF-LB/M). Mater Charact 2022;191:112153. http://dx.doi.org/10.1016/j.matchar.2022.112153.

[24] Practice for conducting force controlled constant amplitude axial fatigue tests of metallic materials. ASTM International, http://dx.doi.org/10.1520/e0466-21.

[25] Test methods for tension testing of metallic materials. ASTM International, http://dx.doi.org/10.1520/e0008-04.

[26] Yakout Mostafa, Elbestawi MA, Veldhuis Stephen C. Density and mechanical properties in selective laser melting of invar 36 and stainless steel 316L. J Mater Process Technol 2019;266:397–420. http://dx.doi.org/10.1016/j.jmatprotec.2018.11.006.

[27] Wang Y, Meletis EI, Huang H. Quantitative study of surface roughness evolution during low-cycle fatigue of 316L stainless steel using Scanning Whitelight Interferometric (SWLI) Microscopy. Int J Fatigue 2013;48:280–8. http://dx.doi.org/10.1016/j.ijfatigue.2012.11.009.

[28] Schneider Caroline A, Rasband Wayne S, Eliceiri Kevin W. NIH Image to ImageJ: 25 years of image analysis. Nature Methods 2012;9(7):671–5. http://dx.doi.org/10.1038/nmeth.2089.

[29] Waseda Yoshio, Matsubara Eiichiro, Shinoda Kozo. X-ray diffraction crystallography. Springer Berlin Heidelberg; 2011, http://dx.doi.org/10.1007/978-3-642-16635-8.

[30] Woo W, Jeong JS, Kim D-K, Lee CM, Choi S-H, Suh J-Y, Lee SY, Harjo S, Kawasaki T. Stacking fault energy analyses of additively manufactured stainless steel 316L and CrCoNi medium entropy alloy using in situ neutron diffraction. Sci Rep 2020;10(1). http://dx.doi.org/10.1038/s41598-020-58273-3.

[31] Singh Dharmendra, Nageswararao Palukuri, Jayaganthan R. Microstructural studies of al 5083 alloy deformed through cryorolling. Adv Mater Res 2012;585:376–80. http://dx.doi.org/10.4028/www.scientific.net/amr.585.376.

[32] Piao Yinguang, Le Khanh Chau. Dislocation impediment by the grain boundaries in polycrystals. Acta Mech 2021;232(8):3193–213. http://dx.doi.org/10.1007/s00707-021-03007-3.

[33] Puichaud Anne-Helene, Flament Camille, Chniouel Aziz, Lomello Fernando, Rouesne Elodie, Giroux Pierre-François, Maskrot Hicham, Schuster Frederic, Béchade Jean-Luc. Microstructure and mechanical properties relationship of additively manufactured 316L stainless steel by selective laser melting. EPJ Nucl Sci Technol 2019;5:23. http://dx.doi.org/10.1051/epjn/2019051.

[34] Bayerlein F, Bodensteiner F, Zeller C, Hofmann M, Zaeh MF. Transient development of residual stresses in laser beam melting – A neutron diffraction study. Addit Manuf 2018;24:587–94. http://dx.doi.org/10.1016/j.addma.2018.10.024.

[35] Xiao Zhongxu, Chen Changpeng, Zhu Haihong, Hu Zhiheng, Nagarajan Balasubramanian, Guo Lianbo, Zeng Xiaoyan. Study of residual stress in selective laser melting of Ti6Al4V. Mater Des 2020;193:108846. http://dx.doi.org/10.1016/j.matdes.2020.108846.

[36] Shin Won-Sang, Son Bongkuk, Song Wansu, Sohn Hyonkee, Jang Ho, Kim Yoon-Jun, Park Changkyoo. Heat treatment effect on the microstructure, mechanical properties, and wear behaviors of stainless steel 316L prepared via selective laser melting. Mater Sci Eng A 2021;806:140805. http://dx.doi.org/10.1016/j.msea.2021.140805.

[37] Hoffmann Sascha, Bleck Wolfgang. Experimental investigations on topological surface changes during tensile deformation of steels. Steel Res Int 2010;82(1):32–8. http://dx.doi.org/10.1002/srin.201000220.

[38] Kamaya Masayuki. Assessment of local deformation using EBSD: Quantification of local damage at grain boundaries. Mater Charact 2012;66:56–67. http://dx.doi.org/10.1016/j.matchar.2012.02.001.

[39] Röttger A, Boes J, Theisen W, Thiele M, Esen C, Edelmann A, Hellmann R. Microstructure and mechanical properties of 316L austenitic stainless steel processed by different SLM devices. Int J Adv Manuf Technol 2020;108(3):769–83. http://dx.doi.org/10.1007/s00170-020-05371-1.

[40] Petch NJ. The cleavage strength of polycrystals. J Iron Steel Inst 1953;174:25–8.

[41] Qin Wenbo, Li Jiansheng, Liu Yaoyao, Kang Jiajie, Zhu Lina, Shu Dengfeng, Peng Peng, She Dingshun, Meng Dezhong, Li Yusheng. Effects of grain size on tensile property and fracture morphology of 316L stainless steel. Mater Lett 2019;254:116–9. http://dx.doi.org/10.1016/j.matlet.2019.07.058.

[42] Zorc Borut, Nagode Aleš, Kosec Borut, Kosec Ladislav. Elevator chain wheel shaft break analysis. Case Stud Eng Fail Anal 2013;1(2):115–9. http://dx.doi.org/10.1016/j.csefa.2013.05.004.

[43] Wenzler David L, Bergmeier Katharina, Baehr Siegfried, Diller Johannes, Zaeh Michael F. A novel methodology for the thermographic cooling rate measurement during powder bed fusion of metals using a laser beam. Integr Mater Manuf Innov 2023;12(1):41–51. http://dx.doi.org/10.1007/s40192-023-00291-w.

[44] Diller Johannes, Auer Ulrich, Radlbeck Christina, Mensinger Martin, Krafft Frank. Einfluss der Abkühlrate auf die mechanischen Eigenschaften von additiv gefertigten Zugproben aus 316L. Stahlbau 2020;89(12):970–80. http://dx.doi.org/10.1002/stab.202000034.

[45] Järvenpää Antti, Karjalainen L Pentti, Jaskari Matias. Effect of grain size on fatigue behavior of Type 301LN stainless steel. Int J Fatigue 2014;65:93–8. http://dx.doi.org/10.1016/j.ijfatigue.2013.05.012.

[46] Schino A Di, Kenny JM. Grain size dependence of the fatigue behaviour of a ultrafine-grained AISI 304 stainless steel. Mater Lett 2003;57(21):3182–5. http://dx.doi.org/10.1016/s0167-577x(03)00021-1.

[47] Hamada AS, Karjalainen LP. High-cycle fatigue behavior of ultrafine-grained austenitic stainless and TWIP steels. Mater Sci Eng A 2010;527(21–22):5715–22. http://dx.doi.org/10.1016/j.msea.2010.05.035.

[48] Liu J, Deng XT, Huang L, Wang ZD. High-cycle fatigue behavior of 18Cr-8Ni austenitic stainless steels with grains ranging from nano/ultrafine-size to coarse. Mater Sci Eng A 2018;733:128–36. http://dx.doi.org/10.1016/j.msea.2018.07.043.

[49] Shin Jong-Ho, Kim Young-Deak, Lee Jong-Wook. Effects of grain size on the fatigue properties in cold-expanded austenitic HNSs. Met Mater Int 2018;24(6):1412–21. http://dx.doi.org/10.1007/s12540-018-0127-2.

[50] Vayssette Bastien, Saintier Nicolas, Brugger Charles, May Mohamed El, Pessard Etienne. Numerical modelling of surface roughness effect on the fatigue behavior of Ti-6Al-4V obtained by additive manufacturing. Int J Fatigue 2019;123:180–95. http://dx.doi.org/10.1016/j.ijfatigue.2019.02.014.

[51] Vayssette Bastien, Saintier Nicolas, Brugger Charles, Elmay Mohamed, Pessard Etienne. Surface roughness of Ti-6Al-4V parts obtained by SLM and EBM: Effect on the high cycle fatigue life. Procedia Eng 2018;213:89–97. http://dx.doi.org/10.1016/j.proeng.2018.02.010.

[52] Murakami Yukitaka, Keer LM. Stress intensity factors handbook, Vol. 3. 1993.

[53] Murakami Yukitaka. Metal fatigue: Effects of small defects and nonmetallic inclusions. 2nd ed.. San Diego, CA: Academic Press; 2019.

[54] Torres M. An evaluation of shot peening, residual stress and stress relaxation on the fatigue life of AISI 4340 steel. Int J Fatigue 2002;24(8):877–86. http://dx.doi.org/10.1016/s0142-1123(01)00205-5.

[55] Chang Shuai, Liu Aihong, Ong Chun Yee Aaron, Zhang Lei, Huang Xiaolei, Tan Yong Hao, Zhao Liping, Li Liqun, Ding Jun. Highly effective smoothening of 3D-printed metal structures via overpotential electrochemical polishing. Mater Res Lett 2019;7(7):282–9. http://dx.doi.org/10.1080/21663831.2019.1601645.

A.2.5 Publication 5: An integrated approach for detecting and classifying pores and surface topology in PBF-LB/M-manufactured 316L using µCT and machine learning algorithms for fatigue assessment

Reproduced from:

Fatigue and Fracture of Engineering Materials and Structures 2024;47(9):3392-3407
Weblink: https://doi.org/10.1111/ffe.14375

with the permission of Wiley and Sons.

Received: 16 March 2024 | Revised: 31 May 2024 | Accepted: 12 June 2024

DOI: 10.1111/ffe.14375

ORIGINAL ARTICLE

FFEMS Fatigue & Fracture of Engineering Materials & Structures WILEY

An integrated approach for detecting and classifying pores and surface topology for fatigue assessment 316L manufactured by powder bed fusion of metals using a laser beam using μCT and machine learning algorithms

Johannes Diller[1] | **Ludwig Siebert**[2] | **Michael Winkler**[3] | **Dorina Siebert**[1] | **Jakob Blankenhagen**[1] | **David Wenzler**[2] | **Christina Radlbeck**[1] | **Martin Mensinger**[1]

[1]TUM School of Engineering and Design, Chair of Metal Structures, Technical University of Munich, Bavaria, Germany

[2]TUM School of Engineering and Design, Institute for Machine Tools and Industrial Management (IWB), Technical University of Munich, Bavaria, Germany

[3]Department 9 Component Safety, Bundesanstalt für Materialforschung- und prüfung, Berlin, Germany

Correspondence
Johannes Diller, TUM School of Engineering and Design, Chair of Metal Structures, Technical University of Munich, Bavaria, Germany.
Email: johannes.diller@tum.de

Present address
Arcisstraße 21, 80333 Munich, Germany

Funding information
Deutsche Forschungsgemeinschaft, Grant/Award Number: 414265976

Abstract

This research aims to detect and analyze critical internal and surface defects in metal components manufactured by powder bed fusion of metals using a laser beam (PBF-LB/M). The aim is to assess their impact on the fatigue behavior. Therefore, a combination of methods, including image processing of micro-computed tomography (μCT) scans, fatigue testing, and machine learning, was applied. A workflow was established to contribute to the nondestructive assessment of component quality and mechanical properties. Additionally, this study illustrates the application of machine learning to address a classification problem, specifically the categorization of pores into gas pores and lack of fusion pores. Although it was shown that internal defects exhibited a reduced impact on fatigue behavior compared with surface defects, it was noted that surface defects exert a higher influence on fatigue behavior. A machine learning algorithm was developed to predict the fatigue life using surface defect features as input parameters.

KEYWORDS

fatigue, machine learning, micro-computed tomography, powder bed fusion of metals using a laser beam, quality assurance

Highlights

- Established workflow for extracting surface and internal features.
- Developed pore classification ML algorithm with 92.4% accuracy.
- Effectively developed ML algorithm for predicting fatigue life.

1 | INTRODUCTION

Additive manufacturing of metals has become increasingly popular in recent years. One of the key manufacturing processes in use is powder bed fusion of metals using a laser beam (PBF-LB/M). Given the increasing adoption of this method, there is a growing need to develop a conceptual framework for future

standardization efforts.[1] In the case of this relatively novel production technique, numerous questions regarding the quality assurance remain unresolved and are increasingly becoming the focus of ongoing research. In order to establish a foundation for the safe and reliable application of PBF-LB/M manufactured components, a comprehensive understanding and evaluation of the underlying processes are imperative.

One of the foremost challenges in realizing the objective of safe and reliable usage of structural components produced by PBF-LB/M is assessing their fatigue behavior. While numerous studies have investigated the optimization of laser parameters to attain high material density,[2–4] it is worth noting that porosity and elevated surface roughness are inherent characteristics, irrespective of the laser parameters employed.[5,6] Quality management for complex, shape-optimized thin-walled parts is impossible with the current methods. Micro-computed tomography (μCT) can be used to detect and visualize pores inside metal parts and on the surface and has been increasingly used in the past years.[7,8] In addition, the surface structure of components produced using PBF-LB/M exhibits imperfections caused by partially melted metal particles, resulting in pronounced valleys and an irregular surface. Optical microscopy measurements face challenges in accurately gauging the depths of these valleys on PBF-LB/M fabricated components. Figure 1 illustrates a μCT scan showcasing its ability to discern surface topology, even in the presence of hidden or shadowed areas.

μCT could be the key to correlate the influence of internal defects and surface roughness to the fatigue life and, therefore, determine the number of cycles until failure with the present defects in a component. First, studies have shown that the stress intensity with different models, like the Murakami method[9] or the FKM-Guideline,[10] can be used to predict the fatigue life. Solberg et. al correlated the stress intensity with the number of cycles.[8,11–13] Finding the exact location of the crack initiation is challenging, as it is subjected to multiple influencing factors.[8] For instance, internal defects encompass various aspects such as the morphology of pores, the distance to neighboring pores, the formation of pore clusters, their distance from the surface, and the orientation of these pores within the component. It is important to note that surface defects can significantly impact fatigue performance as well.[14] The question arises as follows: Which one of the aforementioned parameters or which combination of those leads to a reliable prediction of the crack initiation and fatigue life. With the help of machine learning, conclusions can be drawn on the types of pores present in the component. Based on this, it could be possible to determine the respective effects and the degree of influence on the component and the material properties and to carry out a fitting postprocessing method for the repair of the weak points. By applying machine learning, it may be possible to detect and use correlations between individual defect features to ensure a more reliable prediction. Zhang et al. classify the most frequently occurring defects into porosity, lack of fusion (LOF) defects, and cracks.[15] However, the restriction and limitation to conventional defect descriptors such as sphericity and volume can lead to a loss of potential correlation. Machine learning could enable to integrate an individual weighting of the individual factors and to consider several aspects at the same time. Features that might otherwise have been dismissed as unimportant are taken into account. The μCT scans generate a high amount of data, which is a great potential for machine learning. Multiple studies have shown that for brittle materials (e.g., Ti6Al4V), the fatigue life can be predicted with a good prediction accuracy using deep neural networks.[16,17] These specimens of the aforementioned studies have been machined to the dimensions, meaning that the effect of the surface roughness on the fatigue behavior was not considered. Murakami[9] stated that cracks predominantly initiate at free surfaces. The PBF-LB/M process is especially advantageous when manufacturing components with a complex geometry. Attaining a machined surface via the PBF-LB/M process is unfeasible. Consequently, it is imperative to consider the surface topology of PBF-LB/M manufactured components when investigating their fatigue life.

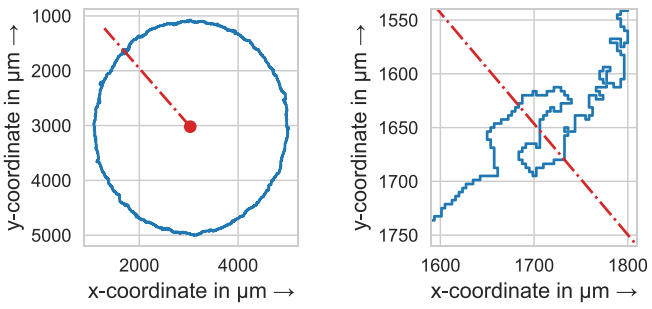

FIGURE 1 Left: Cross-sectional overview of μ computed tomography (CT) scan. Right: close-up of surface with hidden or shadowed area. [Colour figure can be viewed at wileyonlinelibrary.com]

In this work, a methodology is developed to detect, classify, and analyze internal defects and surface defects with regard to the fatigue life by using μCT data, evaluated with the open-source image processing package Fiji[18] and machine learning using the Python scikit-learn library.[19] In order to determine whether surface topology or porosity exerts a greater influence on fatigue life, 13 fatigue tests on specimens with a polished surface and 30 fatigue tests on specimens with an as-built surface

were conducted. Laser parameters were purposely used which resulted in a low material density. Initially, a k-nearest-neighbor machine learning algorithm is developed to categorize critical pores into two distinct groups: gas pores and LOF pores. This classification is achieved by analyzing a dataset consisting of 1000 pores. By focusing solely on the relevant internal defects, this approach optimizes computational efficiency. Following the initial classification, an examination of the relationship between the internal defects, the surface defects, and the fatigue life is conducted. Subsequently, a dedicated machine learning algorithm (Poisson regressor) is developed to predict the fatigue life with regard to the surface topology.

2 | EXPERIMENTAL METHODS

2.1 | Manufacturing of the specimens

During this research, 316L stainless steel (1.4404) metal powder by Oerlikon Metco was used. The machine used for this study is an EOS M280 PBF-LB/M machine. It is equipped with a 400 W Ytterbium continuous wave fiber laser. The metal powder has a particle size distribution of 20-63 μm. The respective volume percentile values D10, D50 ad D90 are 19, 30, and 46 μm. During the manufacturing, Argon 5.0 was used. The residual oxygen concentration was kept below 1300 ppm in the build chamber. Forty-eight fatigue specimens acc. to ASTM E466 - 2021 were manufactured with the PBF-LB/M process. The applied laser parameters are listed in Table 1.

The specimen geometry is shown in Figure 2. To investigate the effect of surface roughness, 13 specimens were manually polished. The surface of the remaining 30 specimens was not altered. According to Yakout et al,[20] the laser parameter set is outside the stable melting zone. This deliberate approach resulted in a significant occurrence of LOF pores, as it was intended to increase porosity levels in order to acquire a larger dataset for defect analysis.

TABLE 1 Applied laser parameters for the fatigue specimens.

Parameter	Value
Energy density E in J/mm^3	41.67
Laser power P in W	250
Scan velocity ν in mm/s	1500
Hatch distance h in mm	0.1
Layer thickness t in mm	0.04

2.2 | Micro-CT

The μCT scans were generated with a *GE Phoenix Nanotom S* (General Electric, New York, USA). The used parameters are shown in Table 2. A voxel-size of 3.75 μm/pixel was achieved with this setup. The specimens were assessed within a measurement region characterized by a vertical extent of 8 mm.

2.3 | Postprocessing

The surface roughness does exert a significant influence on fatigue resistance.[21] To mitigate the influence of surface roughness, 13 specimens underwent a grinding

TABLE 2 Used parameters for the μCT scans.

Parameter	Value
Tube voltage in kV	140
Electric current in A	40
Number of projections	1440
Change of angle per image in °	0.25
Resulting size of voxel in μm	3.75
Exposure time in ms	1500
Magnification in –	13.33
Pixel size of detector in μm	50
Dimension of detector in pixel	2300
Focus-to-object-distance (FOD) in mm	15
Used filter	Copper
Thickness of filter in mm	0.5

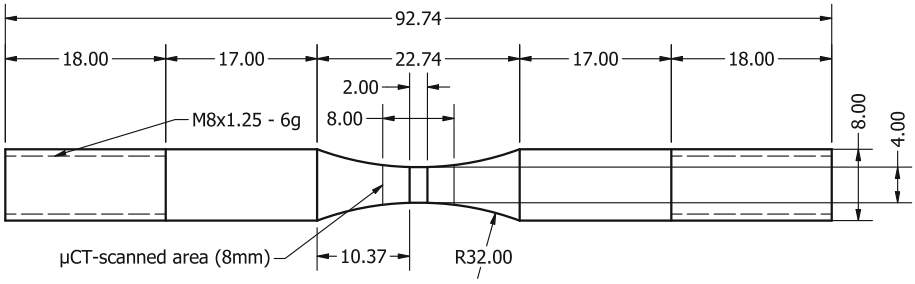

FIGURE 2 Fatigue specimen geometry with dimensions in mm according to ASTM E466 - 2021.

and polishing process on a lathe. This procedure involved the sequential use of sanding papers with grain sizes of 320, 500, 800, and 1000, for 120, 90, 90, and 45 s, respectively. Subsequently, two polishing stages were implemented using zirconium abrasive and diamond slurry with particle sizes of 6 and 3 μm, respectively, both for a duration of 5 min. The evaluation of the surface roughness was conducted with a *Keyence VK-X1000* (Keyence Corporation, Osaka, Japan) 3D laser scanning microscope, which measured a multiline roughness profile spanning 6 mm in length. In total, 65 such profiles were recorded. Three distinct regions within the measurement area were assessed to detect a substantial surface area for analysis. The mean values along with their respective standard deviations for the roughness parameters Ra, Rz, Sa, and Sz were computed and recorded.

2.4 | Mechanical testing

Fatigue testing was conducted using the *Instron 8800 digital control* (Illinois Tool Works, Glenview, IL, USA) with a dynamic load capacity of $\pm$100 kN. A stress ratio of $R = 0.1$ was applied. Thirteen polished specimens were tested at a stress range of 450 MPa. The other 30 specimens with an as-built surface were tested at different stress ranges varying from 200 to 375 MPa. These tests not only served the purpose to generate fatigue life data for the machine learning algorithms. They also served the purpose of investigating whether surface defects or internal defects have a greater influence on the fatigue resistance. Sanaei et al[22] reported that the impact of surface roughness is primary in determining fatigue performance, even when relatively large internal defects and an inhomogeneous microstructure are present. To confirm this statement, the aforementioned fatigue tests were carried out. After the testing, the input features for the fatigue life prediction machine learning algorithm were chosen.

2.5 | Data processing

The raw μCT-data were processed with the open source software Fiji.[18] A total of 8 mm in the measuring range (see Figure 2) was scanned by μCT. This resulted in 2300 slices. Six hundred slices within the area with the smallest diameter were used for the data acquisition. For the extraction of the surface and the internal defects, different filters during the binarization of the original greyscale image stacks were applied. These are explained in the following two sections.

2.5.1 | Internal defects

To properly expose the internal defects, a series of filtering operations were performed. A copper filter has been applied to reduce the beam hardening (see Figure 6A). A voxel size of 3.75 μm was achieved. Compared with similar studies, the voxel size is sufficiently small to reveal all the pores relevant to fatigue analysis.[23–25] To reduce imaging noise in the stacked images of the μCT, a 3D median-filter was applied. The 3D median filter examines each pixel in an image and replaces it based on the median of the neighboring pixels. While the 3D median filter has reduced imaging noise, it cannot completely eliminate it. Therefore, internal defects with a volume of $< 100 \mu m^3$ have been removed in accordance with the approach described by Bao et al.[23] The different brightness in the images would lead to insufficient quality of the pores in the binarized visualization. Hence, a band-pass filter with a shading correction was applied to filter large and small pores and to increase the contrast between the material and the pores. Since the goal was to detect pores, which, expected to have a lower density than the fully dense material, a threshold filter by Ridler and Calvard[26] was applied. This filter results in binarized images (see Figure 6). Subsequently, the resulting images were compared with polished micrograph sections which can be seen in Figure 6. After the calibration of the μCT parameters, the feature extraction was conducted. In Table 3, the extracted features are listed.

TABLE 3 Feature extraction of defects.

Category	Feature
Size	Defect volume
	Defect surface
	Projected maximum surface area per layer
	Feret diameter of maximum surface area
	Extension in z-direction
Morphology	Sphericity
	3D ellipsoid
	Fraction of defect volume to ellipsoid
	3D moment invariants
	Feret diameter aspect ratio
	Aspect ratio of ellipse principal axes
	Flatness related to x-y plane
Location	3D ellipsoid orientation
	Distance of defect from specimen edge
	Distance to other defects
Distribution	Overall porosity
	Number of defects

The Feret diameter is a measure of the size of an object along a specified direction, and it is generally defined as the distance between two parallel planes that constrain the object perpendicular to that specified direction. Figure 3 displays the Feret diameter of merged pores. Closely spaced pores can lead to increased stress intensity factors due to an interaction. An interaction of the pores was assumed if the maximum feret diameter of the maximum projected effective area of a pore is larger than the respective euclidean distance between the pores. The pores are then considered as one merged pore, which can be seen in Figure 3. This effect has been well-documented and validated in various studies within the literature, as evidenced by multiple references including Qian et al. (2024), Peng et al. (2022), and Bale et al. (2013).[27–29]

Additionally, imaging noise can never be fully removed The effect of the effective surface area of multiple pores becomes even more vital, when dealing with high temperatures. The morphology of a defect provides information about the irregularity and elongation of the defect. It can be described via the sphericity calculated by Equation (1)[30,31]

$$\psi = \frac{\pi^{1/3} \cdot (6 \cdot V)^{2/3}}{S} \tag{1}$$

where V is the volume of the pore in mm^3 and S is the surface in mm^2. Another possibility to describe the morphology of a defect is the 3D-ellipsoid described by Equations (2)–(4)[32]

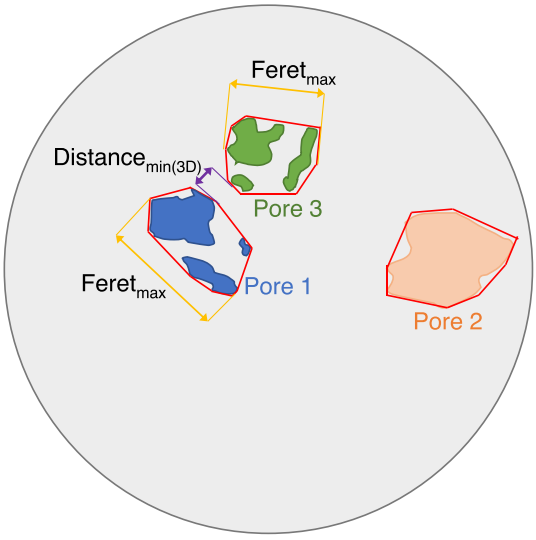

FIGURE 3 Schematic description of effective surface area of three pores with convex hull, showing the principle of the feret diameter. [Colour figure can be viewed at wileyonlinelibrary.com]

$$Elongation_{3D} = \frac{R_1}{R_2} \tag{2}$$

$$Flatness_{3D} = \frac{R_2}{R_3} \tag{3}$$

$$Ratio_{3D} = \frac{\frac{4}{3} \cdot R_1 \cdot R_2 \cdot R_3}{V} \tag{4}$$

where R_1, R_2, and R_3 are the radii of the main axes in mm. In contrast to the 3D-representation, the morphology can also be reduced to a 2D-representation. This can be done via the feret diameter.[33] Here, the maximum projected surface area is considered for each pore. The 2D-representation reduces the complexity of the pore shape. Furthermore, information about the properties of the cross section of the pore perpendicular to the loading direction is generated. The advantage of using the feret diameter is that the maximum and minimum dimensions are used. By means of an approximated ellipse on the other hand, a certain inaccuracy is integrated by the apprximation. To describe the aspect ratio α, the maximum and minimum feret diameters are set in relation to each other which is shown in Equations (5) and (6).

$$\alpha_{Feret} = \frac{Feret_{max}}{Feret_{min}} \tag{5}$$

$$\alpha_{2D} = \frac{Mainaxis_{max}}{Mainaxis_{min}} \tag{6}$$

Due to the two-dimensional description by means of the maximum projected area, no statement can be made about the shape of the pore in the direction of the load. For this reason, the flatness is introduced in Equation (7). It corresponds to the ratio of the minimum feret diameter $Feret_{min}$ with the maximum expansion along the z-direction Z_{max}.

$$Flatness_{2D} = \frac{Feret_{min}}{Z_{max}} \tag{7}$$

The location of an internal defect plays a vital role with regard to fatigue resistance.[9] Hence, the 3D ellipsoid orientation, the distance of a defect from the specimen edge and the distance to other defects were chosen as important features. The severity of the 3D ellipsoid orientation (Equation (4)) with regard to fatigue resistance may vary depending on the loading direction of a component. If the morphology of the defect is elongated and the loading direction is parallel to the defect, the severity is lower comparison to a perpendicular loading direction.

Moreover, if the defect is located closer to the surface, the likelihood of crack initiation intensifies. Similarly, the distance of defects to each other increases the stress intensity.[9]

2.5.2 | Surface defects

In this section, the extraction of surface roughness parameters from the μCT scans is explained. Surface roughness affects the fatigue resistance.[9] In the further course of this work, the surface roughness parameters are called surface defects. The initial raw data underwent a filtering process that involved applying a bandpass filter to identify and subsequently remove excessively large structures (referred to as the background) and excessively small structures (referred to as noise). After that, the data were converted into a binary format. Subsequently, a median filter with a radius of two was applied to further remove noise. It is noteworthy that this median filter operation was carried out after the data had been binarized to ensure the preservation of sharp surface features, as median filters smooth out such details. Surface profiles were assessed along both the circumferential and axial directions. Given that the specimens were subjected to loading along the axial direction, this study focuses exclusively on surface profiles along the axial direction, denoted as the z-direction. The extraction of surface profiles in the z-direction was carried out using the Fiji reslice command. This process entailed the drawing of a slicing plane line originating from the central point and extending outward to intersect the surface, which is illustrated in Figure 4. Subsequently, the reslice command was employed to generate a new image representing a longitudinal view of the plane, effectively extracted from the image stack that had undergone binarization.

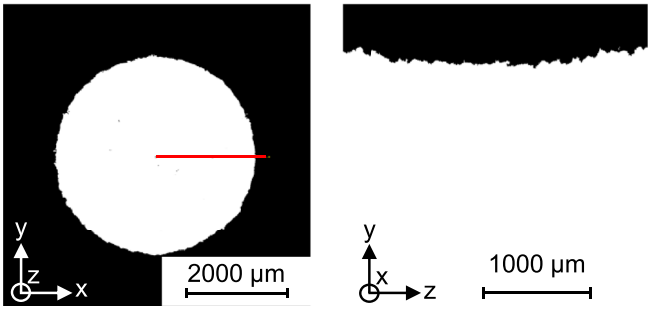

FIGURE 4 Left: Cross-section of μ computed tomography (CT) measurement, red line indicated the reslice plane. Right: Reslice along z-direction. [Colour figure can be viewed at wileyonlinelibrary.com]

Following this step, the coordinates delineating the edge surrounding the white area, indicative of the material, were extracted to a text file. To capture a comprehensive set of surface profiles, the slicing plane line underwent a rotational adjustment of 0.5° in a clockwise direction, followed by the execution of the reslice operation. In summary, this process resulted in a total of 720 surface profiles along the z-direction for each specimen. The profile underwent interpolation, utilizing an evenly spaced and strictly increasing x-coordinate. Following this interpolation step, all necessary prerequisites were met for filtering the surface profile in accordance with the DIN EN ISO 16610-21:2013-06 standard using a Gaussian waviness filter with cut-off values of $\lambda_s = 25$ μm and $\lambda_c = 250$ μm. Figure 5 describes the process from the extracted profile to the final roughness profile according to DIN EN ISO 25178-2:2021. The stress intensity was determined using the method developed by Murakami[9] tailored for the micro-scale.

2.6 | μCT validation

To validate the measurements obtained through μCT for internal defects, a single specimen was selected and subjected to a process involving cutting and subsequent embedding in epoxy resin and analyzed using cross-sectional cuts. Subsequently, it underwent grinding and polishing. To capture images, a Keyence VK-X1000 3D laser scanning microscope was employed.

To assess the accuracy of the μCT images in representing the real specimen, a microscopic image of the specimen was generated and then compared with the binarized μCT images. This comparison is illustrated in Figure 6. When superimposing the polished specimen onto the μCT scanned specimen, it becomes evident that to account for all pores present in the polished specimen due to the orientation of the cutting plane, several layers of the μCT scan must be considered. Layers 1136 and 1152 are shown as the original image, the binary image, and the micrograph visualized with a light microscope in Figure 6.

Figure 6A presents a comparative analysis of various imaging modalities for pore characterization. The upper section displays the original μCT scan images, the middle segment exhibits the binarized μCT scans, and the lower portion showcases micrographs obtained via light microscopy. A specific pore highlighted by a red circle in Figure 6A serves as an illustrative example for comparison across these modalities, as depicted in Figure 6B, where the micrograph, binarized μCT image, and the raw μCT image are shown. Subsequently, Figure 6C provides a three-dimensional representation of this pore. It is

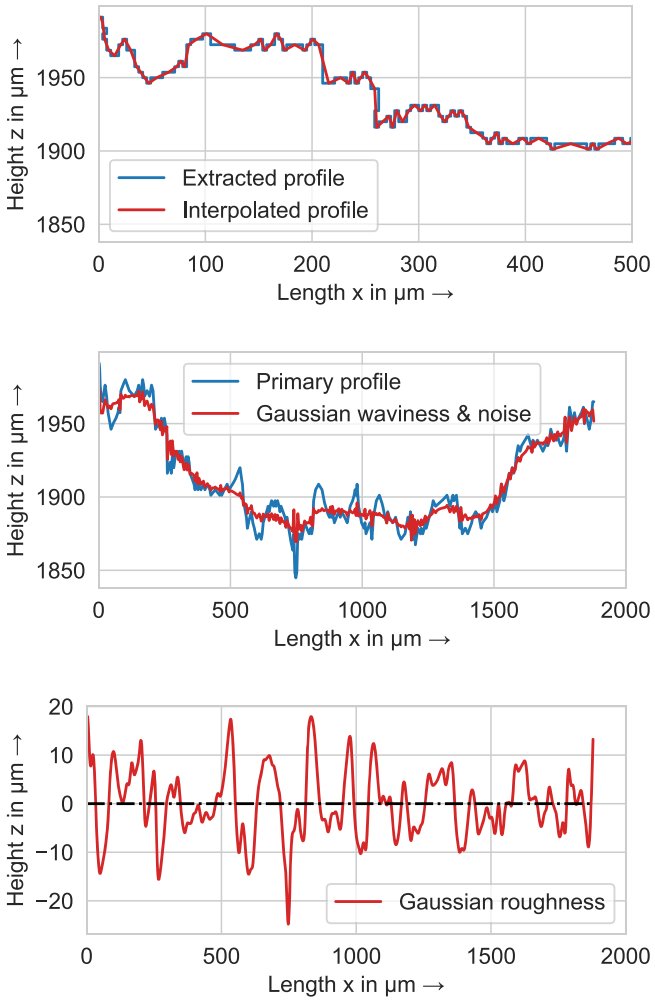

FIGURE 5 Top: Interpolated primary profile along z-direction; Middle: Added waviness and noise profiles and primary profile; Bottom: Final roughness profile. [Colour figure can be viewed at wileyonlinelibrary.com]

evident from the analysis that the μCT images closely correspond to the micrographs, thus substantiating the utility of μCT scans for the representation of internal defects.

2.7 | Feature extraction

The feature extraction is followed by the further processing of the extracted data. With the aid of the characteristic values determined, it is possible to calculate quantities such as the stress intensity factor. Furthermore, a defect analysis provides information about the defects and special features in a specimen. To calculate the stress intensity, the $\sqrt{area}$ -method by Murakami et al[9] has been applied.[8,12] The calculation of the stress intensity is divided into internal defects and surface defects.

2.7.1 | Internal defects

The $\sqrt{area}$-method describes the square root of the projected area of the defect perpendicular to the direction of loading.[9] The stress intensity factor of internal cracks is defined with the following equation by[9,34]:

$$K_{Imax,internalcrack} = 0.5 \cdot \sigma_O \cdot \sqrt{\pi \sqrt{area}} \tag{8}$$

The expression $\sqrt{area}$ denotes the square root of the area, which represents the effective surface area of an irregular crack. This effective surface area is subjected to an applied normal stress denoted as σ_O.

In the case of stress intensity factors for cracks near the surface, the factor is changed from 0.5 to 0.65 since the severity of those is higher.[9,34]

$$K_{Imax,surfacecrack} = 0.65 \cdot \sigma_O \cdot \sqrt{\pi \sqrt{area}} \tag{9}$$

2.7.2 | Surface defects

In general, Equation (9) is used for the calculation of the stress intensity of surface cracks. For wider surface cracks, also representing the surface roughness, the equivalent $\sqrt{area_R}$ is estimated through the following[9]:

$$\frac{\sqrt{\text{area}_R}}{2b} \approx \begin{cases} 2.97 \cdot \frac{a}{2b} - 3.51 \cdot \left(\frac{a}{2b}\right)^2 - 39.74 \cdot \left(\frac{a}{2b}\right)^3 \\ 0.38 \end{cases} \tag{10}$$

where $2b$ is the pitch and a is the depth. This method assigns an equivalent crack to the surface roughness notch. The first case is for $2ab < 0.195$, and the second case is for $2ab > 0.195$. Murakami[9] and Itoga[35] proposed utilizing the average distance between two prominent peaks, encompassing a significant valley, for $2b$, and either the arithmetic mean height Ra or the total height Rt for a. It is important to note that choosing Rt tends to lead to an overestimation of depth and consequently an overestimation of the stress intensity. Using Ra provides qualitatively accurate predictions but may overlook the presence of highly profound surface irregularities, as noted by Itoga.[35] This method is depicted in Figure 7.

The research conducted by Vayssette and colleagues[36,37] has revealed that valleys, as opposed to particles experiencing partial melting and adhering to the surface, show higher levels of mechanical stress. Hence, a different approach for the determination of $2b$ and a is proposed. The novel approach presented here deviates

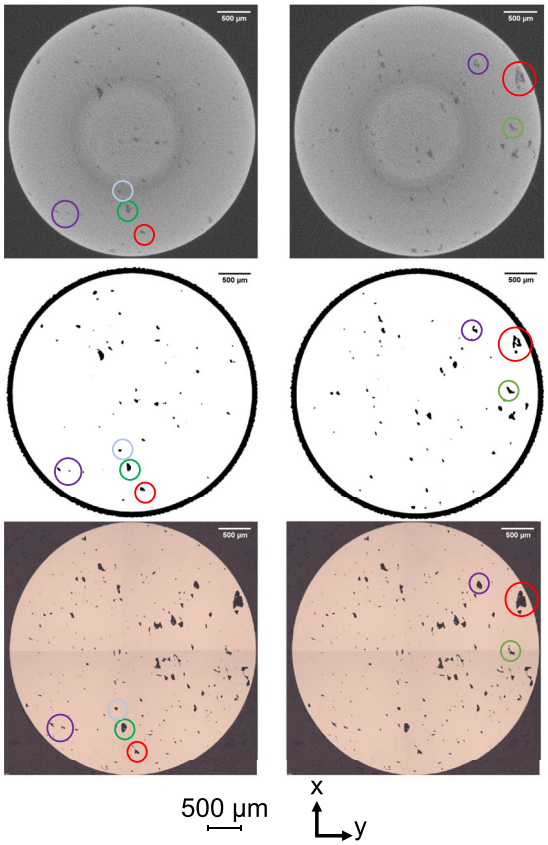

(A) Comparison of existing pores in a cut specimen: Left: layer 1136; Right: layer 1152; Top images: Original image, visualized by µCT; Middle images: Binary image, filtered by Fiji; Bottom images: micrograph, visualized by light microscopy.

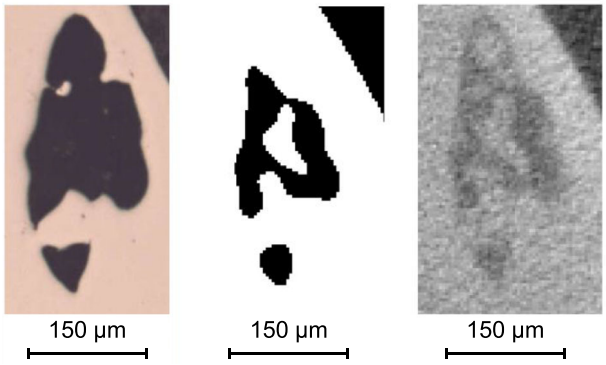

(B) Comparison of a pore: Micrograph (left), µCT scan binary image (middle) and µCT scan original image (right).

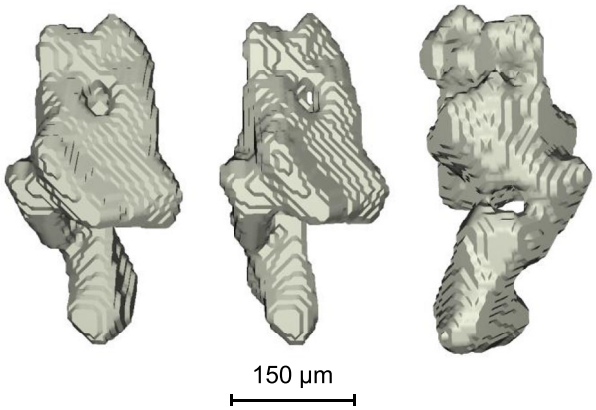

(C) 3D visualization of the examined pore in Figure 6 from different angles.

FIGURE 6 Process of μCT validation using micrographs and 3-dimensional representation of a pore. [Colour figure can be viewed at wileyonlinelibrary.com]

from considering surface peaks. Instead, the depth of the depression is used, denoted as a, and the spacing between the zero-crossings as the pitch parameter, denoted as $2b$. A graphical representation of this methodology is provided in Figure 7.

2.8 | Machine learning

Figure 8 provides a summary of the training sets, test sets, and evaluation sets for the machine learning algorithm to classify pores into gas pores and LOF pores. Evaluating the stress intensity of internal defects requires significant computational time when using numerical methods due to the presence of multi-axial stress conditions. Nevertheless, it is noteworthy that gas pores exhibit a comparatively lower significance in relation to fatigue life compared with LOF pores.[9] The stress intensity of round pores is significantly lower than pores that have very low sphericity (e.g., LOF defects).[34]

2.8.1 | Pore classification

In an effort to mitigate the computational time, a machine learning algorithm is employed to categorize these defects into distinct classes, specifically gas pores and LOF pores. In this case, a k-nearest neighbors classification algorithm is applied. The k -nearest neighbor classification machine learning method is a nonparametric algorithm that is used for classification tasks. It finds the k-nearest instances in the training set to a given test instance. The majority class of those k instances is subsequently assigned to the test instance. The value of k can be chosen through cross-validation. The classification of new data points is determined by looking at the closest

existing data points in the data set and assigning them to a class (either LOF defect or gas pore). The classification is based on the classes of the nearest neighbors. The extracted data from the image processing are used to perform a classification of the existing pores with the help of machine learning. The feasibility of a task is tested with the help of machine learning and exemplified with a selection of the available data. Based on an extension of the data, further optimization of the models is possible. Each pore used has been labeled as either a "gas pore" or a "LOF pore". The used hyperparameters in the python-module scikit-learn were "kneighborsclassifier n-neighbors: 7" and "kneighborsclassifier-weights: uniform"

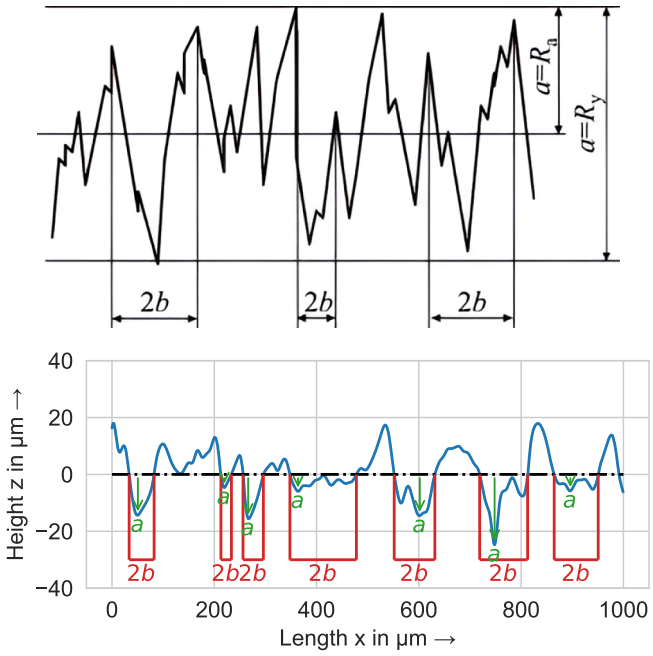

FIGURE 7 Top: Definition of depth a and pitch 2b in surface roughness, adapted from Itoga et al.[35]; Bottom: Proposed definition of depth a and pitch 2b in surface roughness. Ry stands for the maximum distance of the highest peak and the lowest valley inside a sampling length. [Colour figure can be viewed at wileyonlinelibrary.com]

2.8.2 | Fatigue life prediction

In the fatigue life prediction study, a total of 28 fatigue specimens that remained in their as-built condition were utilized for the training process. The input parameters encompassed the stress range, notch depth, and notch width, while the desired output parameters consisted of the number of cycles until failure. In the initial phase, a comprehensive assessment of various machine learning models available within the scikit-learn framework[38] was executed. This evaluation employed the lazypredict library training, testing, and comparing the non-optimized performance of different machine learning models in conjunction with the k-fold cross-validation technique. The k-fold cross-validation method involves the division of the dataset into k discrete subsets or folds, where the model is trained on k-1 folds and subsequently

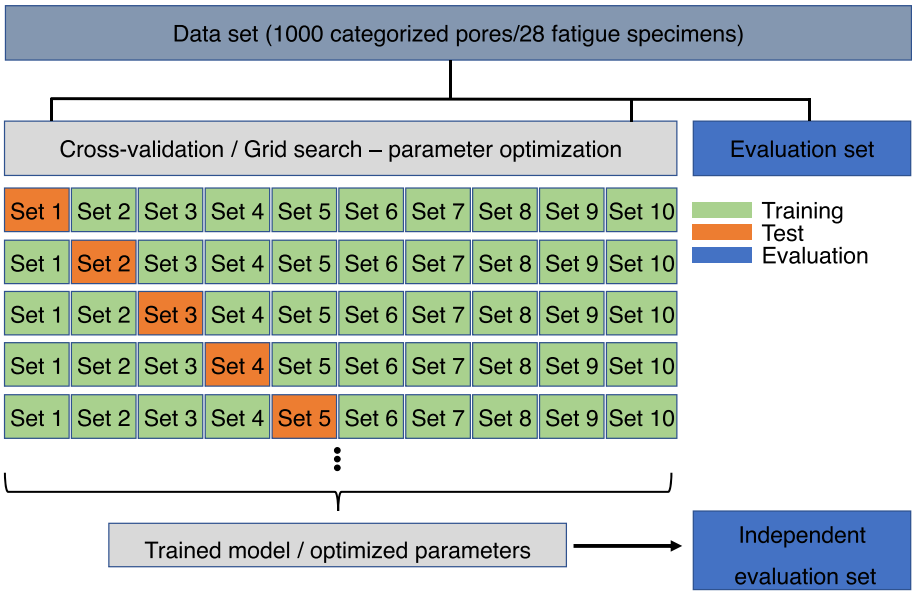

FIGURE 8 Schematic Overview of the training sets, test sets and evaluation sets for the pore classification machine learning algorithm and the fatigue life prediction algorithm. For the fatigue life prediction algorithm the number of folds was set to $k = 5$ [Colour figure can be viewed at wileyonlinelibrary.com]

evaluated on the remaining fold. This process is repeated k times, encompassing all possible combinations of folds, and the average model performance serves as the resultant metric. A graphical representation of this procedure is presented in Figure 8. In this case, 90% of the data were used for the cross-validation and grid search, and 10% was used for the evaluation set. To allocate 10% of the available data for the evaluation set, a choice was made to set $k = 5$ as the number of folds. Subsequent to this initial assessment, the chosen Poisson regressor machine learning model underwent further training, accompanied by the optimization of its hyperparameters (random state) employing the fivefold cross-validation method combined with a grid search. Prior to the hyperparameter optimization, an evaluation set of 10% was randomly selected and isolated to ensure an unbiased final evaluation.

3 | RESULTS AND DISCUSSION

3.1 | Internal defects

Figure 9 shows an exemplary plot of the sphericity and the volume of each internal defect measured by μCT.

Evidently, the material exhibits a notably low density. Additionally, there are pores with a large volume and a very low sphericity inside the specimen. The density of the measured area of the specimen is 99.84%.

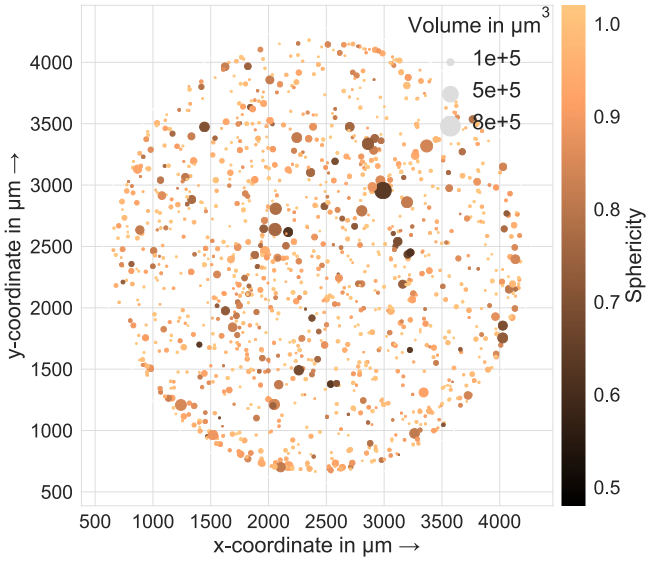

FIGURE 9 Scatterplot of the internal defects, displaying both their volume and respective sphericity. To simplify the visualization, the defects were superimposed along the z-axis. [Colour figure can be viewed at wileyonlinelibrary.com]

3.2 | Surface roughness

Through postprocessing (grinding and polishing), the original diameter of the samples is reduced from 4 mm to an average value of 3.67 mm. The surface condition was examined after polishing. The surface roughness was measured at three locations evenly distributed around the circumference of the component. Both linear and area measurements were conducted. The arithmetic mean height Ra of the polished specimens is noticeably lower compared with that of the as-built surface. The maximum height of profile *Rz* differs greatly between the measurements of the laser confocal microscope and the μCT measurements. This observation may be attributed to the possibility that the measurements were not conducted on precisely the same areas, and the μCT analysis covered a larger surface area. Both the maximum profile valley *Rv* and the total height of the profile *Rt* exhibit similar outcomes, albeit with consistently higher standard deviations in all cases. Table 4 shows the results of the surface roughness at different surface treatment states.

TABLE 4 Comparison between surface roughness measurements of as-built specimens obtained through μ computed tomography (CT) and laser confocal microscopy (LCM) and surface roughness measurements of polished specimens using LCM.

Surface roughness	Mean (μm)	Std. dev. (μm)
Ra		
As-built (LCM)	6.71	0.57
As-built (μCT)	5.85	0.90
Polished (LCM)	0.77	0.32
Rz		
As-built (LCM)	40.50	3.58
As-built (μCT)	27.37	4.23
Polished (LCM)	5.52	2.37
Rv		
As-built (LCM)	17.28	1.69
As-built (μCT)	13.37	2.53
Polished (LCM)	7.90	4.04
Rt		
As-built (LCM)	51.92	6.38
As-built (μCT)	46.67	11.42
Polished (LCM)	2.58	1.08
Rsm		
As-built (LCM)	181.74	27.64
As-built (μCT)	112.42	15.75
Polished (LCM)	109.27	23.68

3.3 | S-N curves

The fatigue test results, as depicted in Figure 10, indicate variations based on different surface treatments.

Specimens with a polished surface exhibited superior fatigue resistance compared with those that were not polished. However, the variability in their results was very high. Specimens that were left in the as-built state displayed less variance in the LCF range. However, in the HCF range, the variability is heightened. This observation aligns with the findings of Sanaei et al.[22] The fatigue strength is noticeably influenced by surface roughness, especially in materials with minimal internal defects and a more pronounced lamellar texture. Lower stresses further emphasize this effect due to decreased localized plastic deformation. Notably, the number of internal defects in the cases of lower stresses is considerably high compared with findings from other studies by Spierings et al,[39] Voloskov et al[40] and Mohammad et al.[41] Sanaei and Fatemi[22] demonstrated that surface roughness has a significant and primary impact on fatigue performance, even when there are substantial internal defects across different microstructures. Their findings also revealed that as surface roughness decreased, the fatigue limit increased, regardless of the microstructure. However, there was notable variance in the results, potentially due to the combined effects of internal defects and microstructural variations.

In a related context, Andreau et al[42] emphasized the pivotal role of defect positioning in determining the fatigue resistance. Pores near the surface are notably more detrimental than internal pores. For instance, surface pores with critical square root areas ($\sqrt{area}$) around 20 μm have a greater negative impact than internal pores with a size of about 200 μm. This aligns with prior research, suggesting that sizable internal LOF defects are less detrimental than surface defects that are 4–10 times smaller in size.[43]

3.4 | Fracture surfaces

SEM images were captured for both the polished and as-built specimens. It was consistently observed that crack initiation in the polished specimens occurred at internal defects, while in the as-built specimens, crack initiation consistently originated from surface defects. Figure 11 illustrates an exemplary fracture surface of a specimen in the as-built state, which failed after 2,519,896 cycles at a stress range of 300 MPa. The crack initiated at the surface due to a large surface defect. The crack initiation and crack growth are indicated by the red arrows.

Figure 12 shows an exemplary fracture surface of a polished specimen that failed after 1,223,362 cycles.

It can clearly be seen that the crack was initiated at a large pore inside the specimen. This substantiates the statements from other studies. With decreasing surface roughness, the detrimental effect of internal defects on fatigue performance increases.[22,43] Furthermore, the influence of compressive residual stresses on the surface, generated as a result of the polishing process, leads to a shift in the predominance from surface defects to internal defects.[14] The results of this study and the results of Andreau et al[42] and Cersullo et al[43] show that the influence of the surface topology is higher in comparison with internal defects. Consequently, it is imperative to develop

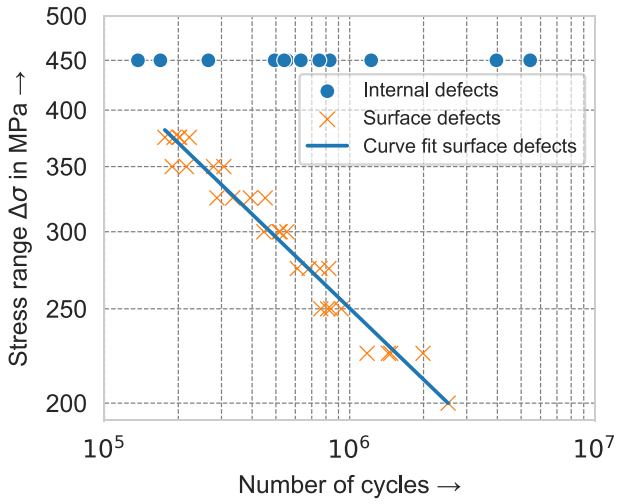

FIGURE 10 S-N curves of the specimens for internal defects (polished) and surface defects (as-built) [Colour figure can be viewed at wileyonlinelibrary.com]

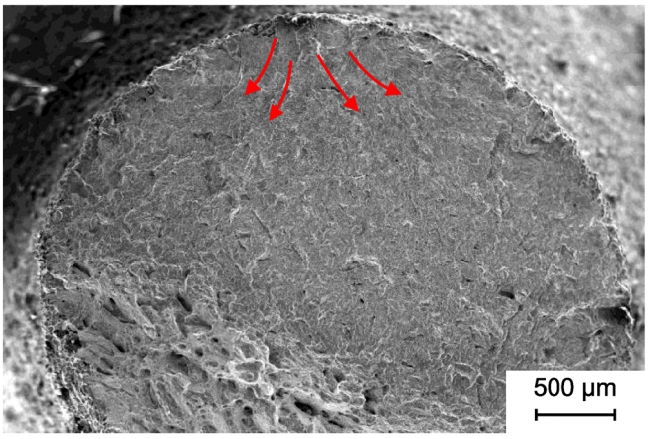

FIGURE 11 Fracture surface of a specimen in the as-built state, showing a surface defect which caused the crack initiation. Red arrows indicate the crack growth direction from the crack initiation location. [Colour figure can be viewed at wileyonlinelibrary.com]

a machine learning algorithm for predicting the fatigue life that prioritizes considering surface defects as the primary contributing factor.

3.5 | Pore classification

Initially, the machine learning algorithm for pore classification was trained using a dataset of 250 labeled internal defects. The labels denoted either gas pores or LOF pores. The chosen input features included volume, 3D expansion, 3D flatness, and surface area, resulting in an accuracy of 71.4%. Expanding the dataset from 250 defects to 1000 defects increased the accuracy to 82.8%. Subsequently, by modifying and augmenting the set of input features to incorporate projected area, feret diameter, 3D expansion, 3D flatness, and surface area, an accuracy of 92.4% was achieved. It is worth noting that hyperparameter optimization did not yield a higher accuracy. Table 5 shows the results of the machine learning algorithm for the pore classification.

This tool helps to identify critical defects including their shape and location inside the material. Additionally, pore classification data can be used to develop predictive models that simulate how pores affect the behavior of PBF-LB/M manufactured components under various loads and conditions. This machine learning algorithm serves as a foundation for integrating the influence of surface defects and internal defects on the fatigue resistance.

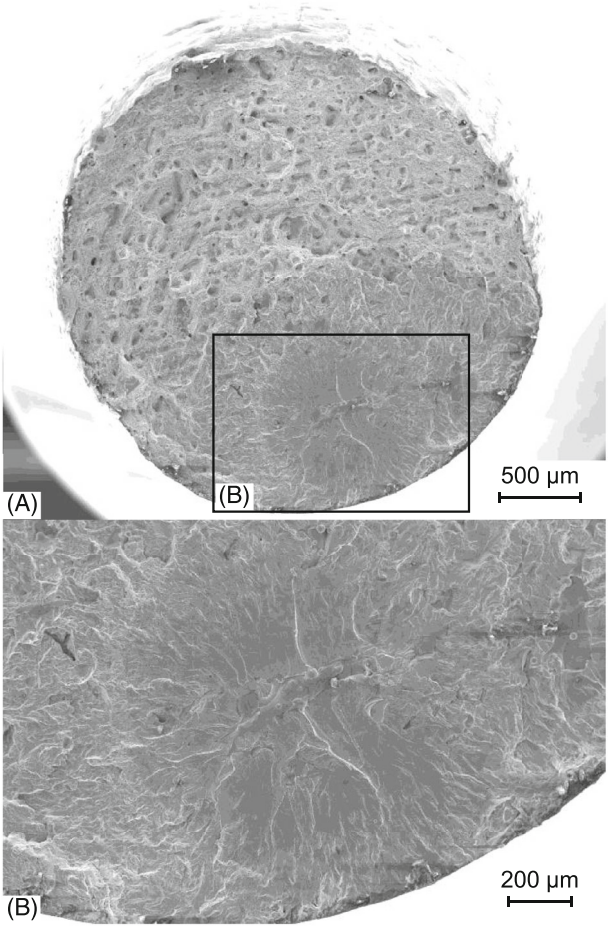

FIGURE 12 Fracture surface of polished specimen, showing a large pore inside the specimen, which caused the crack initiation. Panel (A) provides a comprehensive view of the fracture surface, while panel (B) offers a close-up magnification of the pore.

3.6 | Fatigue life prediction

Figure 13 shows the results of the fatigue life prediction machine learning algorithm.

A root mean-squared error (RMSE) of 29,139 cycles was achieved with this setup. This indicates that the prediction remains accurate even when using a minimal amount of data. However, it is worth noting that overfitting could potentially occur due to the limited dataset size. To enhance the robustness of this machine learning algorithm, an increase in the amount of data is imperative. This entails not only conducting additional fatigue tests under the same configuration but also incorporating a broader range of surface roughness variations into the dataset.

In order to discern the primary input feature impacting the machine learning algorithm, a SHAP[44] evaluation was employed to elucidate the contribution of each feature to the prediction. The SHAP values represent the difference between the expected value, which denotes the average output of the machine learning model across a dataset, and the specific prediction made by the machine

TABLE 5 Results of machine learning algorithm for pore classification with different datasets and features.

	Dataset	Features	Accuracy
Basic model	250 defects	Volume, 3D expansion, 3D flatness, surface area	71.4%
Expansion of dataset	1000 defects	Volume, 3D expansion, 3D flatness, surface area	82.8%
Variation of features	1000 defects	Projected area, feret diameter, 3D expansion, 3D flatness, surface area	92.4%
Hyperparameter optimization	1000 defects	Projected area, feret diameter, 3D expansion, 3D flatness, surface area	92.4%

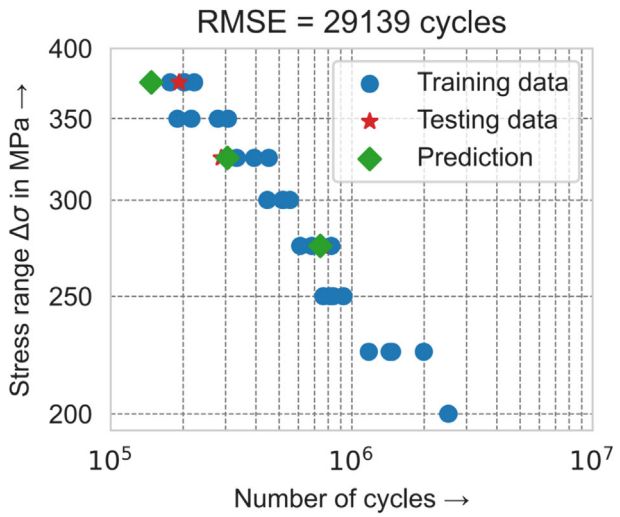

FIGURE 13 Results of the machine learning algorithm for the fatigue life prediction. [Colour figure can be viewed at wileyonlinelibrary.com]

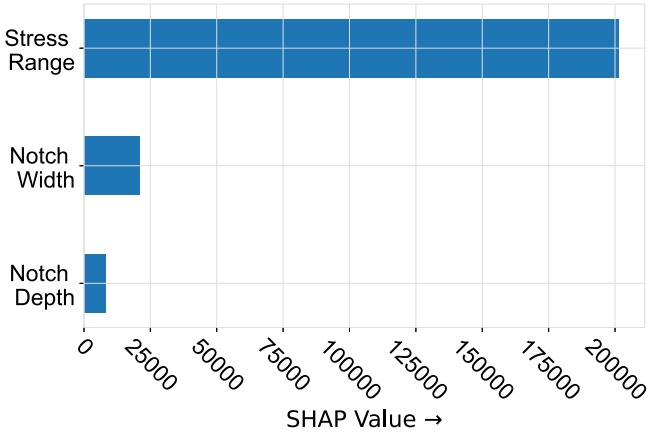

FIGURE 14 Average impact of input features on the fatigue resistance. [Colour figure can be viewed at wileyonlinelibrary.com]

learning model. These SHAP values can be understood as the impact of each individual feature on the prediction for a single observation. Figure 14 illustrates the outcomes of the average SHAP values and their influence on the fatigue resistance concerning the input features. As expected, the stress range exerts the most substantial impact on the machine learning algorithm, which aligns with the findings reported by Peng et al. and Braun et al.[28,45] In contrast, the notch width and notch the depth exhibit a comparatively lesser influence on fatigue life.

To conduct a more comprehensive assessment of the influence of notch depth and notch width, additional data is required. This entails not only incorporating a wider range of surface roughness variations, as previously mentioned, but also conducting more tests at the same stress range. With a substantial dataset featuring a high number of data points at a specific stress range, it may become possible to exclude stress range as an input feature. This adjustment would result in greater emphasis on the notch depth and notch width, ultimately enhancing the overall robustness of the machine learning algorithm.

4 | CONCLUSIONS

This study provides a basis for further investigations to predict the fatigue life with respect to individual defects of PBF-LB/M manufactured 316L. From this study, the following conclusions can be drawn:

- Polished fatigue specimens have a higher fatigue resistance in comparison to as-built fatigue specimens.
- The primary cause of fatigue crack initiation in polished fatigue specimens is attributed to internal defects. Conversely, in as-built fatigue specimens, crack initiation consistently occurs on the surface.
- The scattering of the number of cycles for polished fatigue specimens is notably greater in comparison to as-built fatigue specimens.
- The limited correlation observed in the polished specimens concerning fatigue resistance can be rationalized in accordance with the findings by Sanaei et al.[22] Their research demonstrated that the surface roughness effect is detrimental and primary on the fatigue performance even in the presence of relatively large internal defects and for various microstructures.
- Additionally, Sanaei et al[22] revealed that the fatigue limit increases as surface roughness decreases, irrespective of the microstructure. Nevertheless, some degree of variability was noted, which might be attributed to the secondary influences of internal defects and microstructure. This findings of this study align with and affirm the aforementioned observations.
- A workflow for extracting surface features and internal features was successfully established.
- A pore classification machine learning algorithm was successfully developed with an accuracy of 92.4%. This algorithm serves as a base for future investigations regarding a combined effect of surface defects and internal defects.
- A fatigue life prediction machine learning algorithm has been effectively developed, achieving a RMSE of 29,139 cycles. This was achieved by incorporating newly introduced parameters, specifically the depth of the depression from the zero line (a) and the spacing between the zero-crossings as the notch width ($2b$). To

improve the robustness of the machine learning algorithm, more variety of surface topology and data is necessary.

5 | OUTLOOK

- Enhancing the resolution of μCT images has the potential to enhance the accuracy of measurements related to parameters a and $2b$ consequently leading to a more accurate prediction of fatigue life.
- However, μCT analysis is both time-consuming and costly. In the future, optical tomography measurements could potentially replace the need for μCT in obtaining features related to internal defects during the manufacturing process. Hence, it is imperative to conduct a study that compares μCT measurements with optical tomography measurements.
- For the accurate calculation of stress intensity based on Murakami[9] and Itoga's[35] criteria, overhanging structures had to be omitted. Further research into the stress intensity concerning these overhanging structures should be pursued.
- To investigate the impact of internal defects in conjunction with high ductility on fatigue behavior, it is advisable to employ in-situ μCT imaging during tensile or fatigue tests. This approach can provide insights into how the material surrounding internal defects experiences plastic deformation.

AUTHOR CONTRIBUTIONS

Johannes Diller: Conceptualization; methodology; validation; formal analysis; investigation; writing—original draft; visualization; project administration; funding acquisition. **Ludwig Siebert:** Investigation; formal analysis; validation; writing—review and editing. **Michael Winkler:** Investigation; formal analysis; validation; writing—review and editing. **Dorina Siebert:** Writing—review and editing. **Jakob Blankenhagen:** Writing—review and editing. **David Wenzler:** Writing—review and editing. **Christina Radlbeck:** Supervision; project administration; funding acquisition; writing—review and editing. **Martin Mensinger:** Supervision; project administration; funding acquisition; writing—review and editing.

ACKNOWLEDGMENTS

This study was funded by the Deutsche Forschungsgemeinschaft (DFG, German Research Foundation) - Project number 414265976 - TRR 277. We would like to express our gratitude to the DFG for their funding support, which significantly contributed to the completion of this paper.

CONFLICT OF INTEREST STATEMENT

The authors declare no potential conflict of interests.

DATA AVAILABILITY STATEMENT

Data can be made available by the corresponding author upon reasonable request.

ORCID

Johannes Diller https://orcid.org/0000-0002-0059-0544
Michael Winkler https://orcid.org/0000-0003-3719-4817
Dorina Siebert https://orcid.org/0000-0003-4211-7103
Martin Mensinger https://orcid.org/0000-0001-5210-5400

REFERENCES

1. Associates W. *Wohlers Report 2022: 3D Printing and Additive Manufacturing Global State of the Industry*: Wohlers Associates.; 2022. https://books.google.de/books?id=CyUGzwEACAAJ
2. Casati R, Lemke J, Vedani M. Microstructure and fracture behavior of 316l austenitic stainless steel produced by selective laser melting. *J Mater Sci Technol*. 2016;32(8):738-744. https://doi.org/10.1016/j.jmst.2016.06.016
3. Liverani E, Toschi S, Ceschini L, Fortunato A. Effect of selective laser melting (SLM) process parameters on microstructure and mechanical properties of 316l austenitic stainless steel. *J Mater Process Technol*. 2017;249:255-263. https://doi.org/10.1016/j.jmatprotec.2017.05.042
4. Zhang B, Dembinski L, Coddet C. The study of the laser parameters and environment variables effect on mechanical properties of high compact parts elaborated by selective laser melting 316l powder. *Mater Sci Eng: A*. 2013;584:21-31. https://doi.org/10.1016/j.msea.2013.06.055
5. Chahal V, Taylor RM. A review of geometric sensitivities in laser metal 3D printing. *Virtual Phys Prototyp*. 2020;15(2):227-241. https://doi.org/10.1080/17452759.2019.1709255
6. Hosseini E, Popovich VA. A review of mechanical properties of additively manufactured INCONEL 718. *Addit Manuf*. 2019;30:100877. https://doi.org/10.1016/j.addma.2019.100877
7. Du Plessis A, Yadroitsev I, Yadroitsava I, Le Roux SG. X-ray microcomputed tomography in additive manufacturing: a review of the current technology and applications. *3D Print Addit Manuf*. 2018;5(3):227-247.
8. Solberg K, Guan S, Razavi SMJ, Welo T, Chan KC, Berto F. Fatigue of additively manufactured 316l stainless steel: the influence of porosity and surface roughness. *Fatigue Fract Eng Mater Struct*. 2019;42(9):2043-2052. https://doi.org/10.1111/ffe.13077
9. Murakami Y. *Metal Fatigue: Effects of Small Defects and Nonmetallic Inclusions*. 2nd ed. San Diego, CA: Academic Press; 2019.
10. Berger C, Blauel JG, Hodulak L, Pyttel B. *Fracture Mechanics Proof of Strength for Engineering Components*. Frankfurt am Main, Germany: VDMA; 2009.
11. Solberg K, Berto F. A diagram for capturing and predicting failure locations in notch geometries produced by additive manufacturing. *Int J Fatigue*. 2020;134:105428. https://doi.org/10.1016/j.ijfatigue.2019.105428

12. Solberg K, Berto F. The effect of defects and notches in quasi-static and fatigue loading of INCONEL 718 specimens produced by selective laser melting. *Int J Fatigue*. 2020;137:105637. https://doi.org/10.1016/j.ijfatigue.2020.105637
13. Solberg K, Wan D, Berto F. Fatigue assessment of as-built and heat-treated INCONEL 718 specimens produced by additive manufacturing including notch effects. *Fatigue Fract Eng Mater Struct*. 2020;43(10):2326-2336. https://doi.org/10.1111/ffe.13300
14. Diller J, Blankenhagen J, Siebert D, Radlbeck C, Mensinger M. Combined effect of surface treatment and heat treatment on the fatigue properties of AISI 316l, manufactured by powder bed fusion of metals using a laser (PBF-LB/M). *Int J Fatigue*. 2024;178(108025):108025.
15. Zhang B, Li Y, Bai Q. Defect formation mechanisms in selective laser melting: a review. *Chinese J Mech Eng*. 2017;30(3):515-527. https://doi.org/10.1007/s10033-017-0121-5
16. Li J, Yang Z, Qian G, Berto F. Machine learning based very-high-cycle fatigue life prediction of Ti-6Al-4V alloy fabricated by selective laser melting. *Int J Fatigue*. 2022;158:106764.
17. Zhan Z, Li H. A novel approach based on the elastoplastic fatigue damage and machine learning models for life prediction of aerospace alloy parts fabricated by additive manufacturing. *Int J Fatigue*. 2021;145:106089.
18. Schindelin J, Arganda-Carreras I, Frise E, et al. Fiji: an open-source platform for biological-image analysis. *Nature Methods*. 2012;9(7):676-682. https://doi.org/10.1038/nmeth.2019
19. Pedregosa F, Varoquaux G, Gramfort A, et al. Scikit-learn: machine learning in python. https://api.semanticscholar.org/CorpusID:10659969; 2011.
20. Yakout M, Elbestawi MA, Veldhuis SC. Density and mechanical properties in selective laser melting of INVAR 36 and stainless steel 316l. *J Mater Process Technol*. 2019;266:397-420. https://doi.org/10.1016/j.jmatprotec.2018.11.006
21. Pegues J, Roach M, Williamson RS, Shamsaei N. Surface roughness effects on the fatigue strength of additively manufactured Ti-6Al-4V. *Int J Fatigue*. 2018;116:543-552. https://doi.org/10.1016/j.ijfatigue.2018.07.013
22. Sanaei N, Fatemi A. Analysis of the effect of surface roughness on fatigue performance of powder bed fusion additive manufactured metals. *Theor Appl Fract Mech*. 2020;108:102638. https://doi.org/10.1016/j.tafmec.2020.102638
23. Bao H, Wu S, Wu Z, Kang G, Peng X, Withers PJ. A machine-learning fatigue life prediction approach of additively manufactured metals. *Eng Fract Mech*. 2021;242(107508):107508.
24. Gong H, Nadimpalli VK, Rafi K, Starr T, Stucker B. Micro-CT evaluation of defects in Ti-6Al-4V parts fabricated by metal additive manufacturing. *Technologies (Basel)*. 2019;7(2):44 en.
25. Han S, Dinh TD, De Baere I, Boone M, Josipovic I, Van Paepegem W. Study of the effect of defects on fatigue life prediction of additive manufactured Ti-6Al-4V by combined use of micro-computed tomography and fracture-mechanics-based simulation. *Int J Fatigue*. 2024;180(108110):108110.
26. Ridler T.W., Calvard S.. Picture thresholding using an iterative selection method. *IEEE Trans Syst, Man, Cybern*. 1978;8(8):630-632. https://doi.org/10.1109/TSMC.1978.4310039
27. Bale HA, Haboub A, MacDowell AA, Nasiatka JR, Parkinson DY, Cox BN, Marshall DB, Ritchie RO. Real-time quantitative imaging of failure events in materials under load at temperatures above 1,600 ° C. *Nat Mater*. 2013;12(1):40-46.
28. Peng X, Wu S, Qian W, Bao J, Hu Y, Zhan Z, Guo G, Withers PJ. The potency of defects on fatigue of additively manufactured metals. *Int J Mech Sci*. 2022;221(107185):107185.
29. Qian W, Wu S, Lei L, Hu Q, Liu C. Time lapse in situ X-ray imaging of failure in structural materials under cyclic loads and extreme environments. *J Mater Sci Technol*. 2024;175:80-103.
30. Cruz-Matías I, Ayala D, Hiller D, Gutsch S, Zacharias M, Estradé S, Peiró F. Sphericity and roundness computation for particles using the extreme vertices model. *J Comput Sci*. 2019;30:28-40. https://doi.org/10.1016/j.jocs.2018.11.005
31. Lindblad J. Surface area estimation of digitized 3D objects using weighted local configurations. *Image Vision Comput*. 2005;23(2):111-122. https://doi.org/10.1016/j.imavis.2004.06.012
32. Gul-Mohammed J, Arganda-Carreras I, Andrey P, Galy V, Boudier T. A generic classification-based method for segmentation of nuclei in 3D images of early embryos. *BMC Bioinformatics*. 2014;15(1). https://doi.org/10.1186/1471-2105-15-9
33. Walton WH. Feret's statistical diameter as a measure of particle size. *Nature*. 1948;162(4113):329-330. https://doi.org/10.1038/162329b0
34. Murakami Y, Keer LM. *Stress Intensity Factors Handbook*, Vol. 3: Elsevier; 1993.
35. Itoga H. Effect of surface roughness on step-wise s–n characteristics in high strength steel. *Int J Fatigue*. 2003;25(5):379-385. https://doi.org/10.1016/s0142-1123(02)00166-4
36. Vayssette B, Saintier N, Brugger C, Elmay M, Pessard E. Surface roughness of Ti-6Al-4V parts obtained by SLM and EBM: effect on the high cycle fatigue life. *Procedia Eng*. 2018;213:89-97. https://doi.org/10.1016/j.proeng.2018.02.010
37. Vayssette B, Saintier N, Brugger C, May ME, Pessard E. Numerical modelling of surface roughness effect on the fatigue behavior of Ti-6Al-4V obtained by additive manufacturing. *Int J Fatigue*. 2019;123:180-195. https://doi.org/10.1016/j.ijfatigue.2019.02.014
38. Pedregosa F, Varoquaux G, Gramfort A, et al. Scikit-learn: machine learning in Python. *J Mach Learn Res*. 2011;12:2825-2830.
39. Spierings AB, Starr TL, Wegener K. Fatigue performance of additive manufactured metallic parts. *Rapid Prototyp J*. 2013;19(2):88-94. https://doi.org/10.1108/13552541311302932
40. Voloskov B, Evlashin S, Dagesyan S, Abaimov S, Akhatov I, Sergeichev I. Very high cycle fatigue behavior of additively manufactured 316l stainless steel. *Materials*. 2020;13(15):3293. https://doi.org/10.3390/ma13153293
41. Mohammad KA, Zainudin ES, Sapuan SM, Zahari NI, Aidy A. Fatigue life for type 316l stainless steel under cyclic loading. *Adv Mater Res*. 2013;701:77-81. https://doi.org/10.4028/www.scientific.net/amr.701.77
42. Andreau O, Pessard E, Koutiri I, Peyre P, Saintier N. Influence of the position and size of various deterministic defects on the high cycle fatigue resistance of a 316l steel manufactured by laser powder bed fusion. *Int J Fatigue*. 2021;143:105930. https://doi.org/10.1016/j.ijfatigue.2020.105930

43. Cersullo N, Mardaras J, Emile P, Nickel K, Holzinger V, Hühne C. Effect of internal defects on the fatigue behavior of additive manufactured metal components: a comparison between Ti-6Al-4V and INCONEL 718. *Materials*. 2022;15(19): 6882. https://doi.org/10.3390/ma15196882
44. Shapley LS. *Additive and Non-additive Set Functions*: Princeton University; 1953.
45. Braun M, Kellner L, Schreiber S, Ehlers S. Prediction of fatigue failure in small-scale butt-welded joints with explainable machine learning. *Procedia Struct Integr*. 2022;38: 182-191.

How to cite this article: Diller J, Siebert L, Winkler M, et al. An integrated approach for detecting and classifying pores and surface topology for fatigue assessment 316L manufactured by powder bed fusion of metals using a laser beam using μCT and machine learning algorithms. *Fatigue Fract Eng Mater Struct*. 2024;47(9): 3392-3407. doi:10.1111/ffe.14375

A.2.6 Publication 6: Additive Manufacturing in Construction—Implementing Powder-Bed Fusion of Metals Using a Laser (PBF-LB/M) and Shape Optimization in the Construction Design Process

Reproduced from:

Engineering proceedings 43 (2023), 10
Weblink: https://doi.org/10.3390/engproc2023043010

with the permission of MDPI.

engineering proceedings

MDPI

Proceeding Paper

Additive Manufacturing in Construction—Implementing Powder-Bed Fusion of Metals Using a Laser (PBF-LB/M) and Shape Optimization in the Construction Design Process †

Johannes Diller *, Christina Radlbeck, Dorina Siebert, Jakob Blankenhagen, Drilon Gubetini, Florian Oberhaidinger and Martin Mensinger

Chair of Metal Structures, School of Engineering and Design, Technical University of Munich, 80333 Munich, Germany; c.radlbeck@tum.de (C.R.); dorina.siebert@tum.de (D.S.); jakob.blankenhagen@tum.de (J.B.); d.gubetini@tum.de (D.G.); f.oberhaidinger@tum.de (F.O.); mensinger@tum.de (M.M.)

* Correspondence: johannes.diller@tum.de

† Presented at the 15th International Aluminium Conference, Québec, QC, Canada, 11–13 October 2023.

Abstract: In this study, the implementation of the PBF-LB/M process into the construction design and building process was investigated. To this purpose, a tensegrity-tower was designed, planned, and built. The nodes between the compression rods and the tension cables were manufactured by PBF-LB/M/AlSi10Mg. Four different nodes were designed and shape-optimized by vertex-morphing. In order to qualify the tensegrity nodes according to the German regulations, mechanical as well as microstructural evaluations were conducted. Tensile tests of a manufactured tensegrity node in a fully hinged setup were carried out. Additionally, fatigue testing was conducted. The tensegrity nodes were heat-treated (T6) and subsequently vibratory ground to reduce the surface roughness. The results indicate that it is feasible to integrate the PBF-LB/M process into the design and construction process. The tower is now a permanent and tangible exhibit in the Deutsches Museum in Munich.

Keywords: powder bed fusion of metals using a laser; additive manufacturing; tensegrity tower; additive manufacturing in construction; AlSi10Mg; tensile testing; fatigue

Citation: Diller, J.; Radlbeck, C.; Siebert, D.; Blankenhagen, J.; Gubetini, D.; Oberhaidinger, F.; Mensinger, M. Additive Manufacturing in Construction—Implementing Powder-Bed Fusion of Metals Using a Laser (PBF-LB/M) and Shape Optimization in the Construction Design Process. *Eng. Proc.* **2023**, *43*, 10. https://doi.org/10.3390/engproc2023043010

Academic Editor: Houshang Alamdari

Published: 12 September 2023

1. Introduction

The powder bed fusion of metals using a laser (PBF-LB/M/AlSi10Mg) allows for the creation of complex geometries and intricate designs that would be difficult or impossible to achieve using traditional manufacturing methods. It is already widely used in the aerospace, automotive, and medical sectors. The application of the PBF-LB/M process in the construction sector, however, is a relatively new field. Yet, it has the potential to revolutionize the construction sector with its ability to create complex structures with implemented features like lightweight design by shape optimization. Now, the issue arises regarding the specific applications that require complex but easily adjustable structures. For instance, the roof of the exhibition halls in Milan exemplifies a remarkably intricate structure comprising 16,500 nodes. It is important to note that these nodes do not possess identical geometries, as illustrated in Figure 1. Similar instances can be observed in architectural masterpieces such as the roof of the Jewel Changi airport in Singapore or Waterloo Station in London just to name a few.

Typically, the design engineer is expected to exert significant effort in order to minimize the utilization of diverse node geometries. The capability of the PBF-LB/M process to facilitate the seamless production of complex structures grants designers the freedom to utilize node geometries as needed. This reduces the work of the design. Nonetheless, the PBF-LB/M process remains significantly time-consuming and incurs substantial costs in

comparison to conventional manufacturing methods. Consequently, it is imperative for the application of this manufacturing technique to be economically feasible.

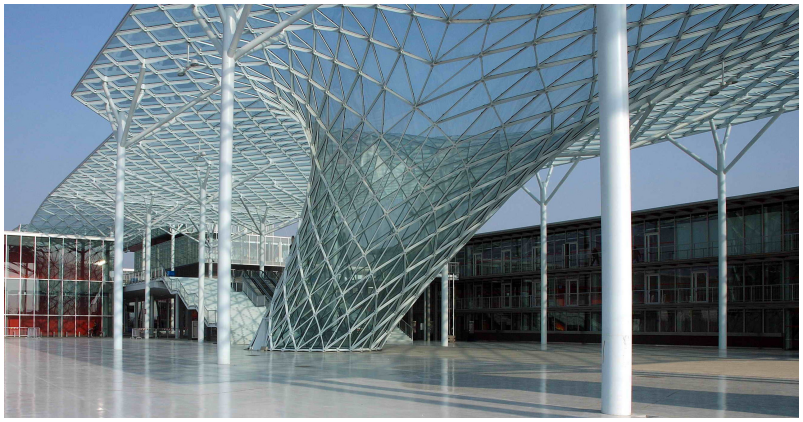

Figure 1. Example of possible application for additive manufacturing [1].

The potential of additive manufacturing compared to conventional processes is based on two fundamental principles, which are depicted in Figure 2. The first principle is the design freedom offered by additive manufacturing. Unlike conventional methods, PBF-LB/M provides a greater opportunity to manufacture complex components without incurring additional costs. The second principle is the quantity dependency. Conventional processes often require a high number of components to generate low component costs. However, additive manufacturing processes such as PBF-LB/M exhibit only a small-scale effect. Since the pre-process is performed only once, a slight decrease in price can be observed even with a high number of components (refer to Figure 2). Therefore, it is possible to achieve low component costs even with a small number of components [2]. It must be mentioned that this graph does not include the cost of redesign. This would result in no decrease in cost per part vs. number of parts in Figure 2.

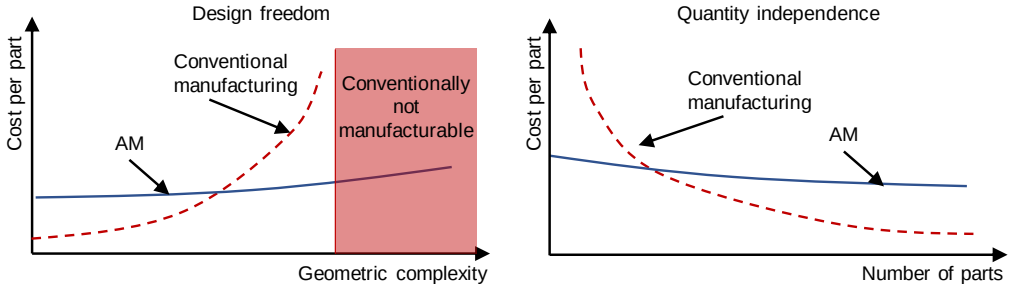

Figure 2. Potential of additive manufacturing (AM) vs. conventional manufacturing methods (e.g., CNC-machining, casting) in accordance to [2].

This is due to a significant dependency on fixed costs in conventional processes. Fixed costs primarily arise from the production of component-specific tooling (e.g., molds for casting). To make conventional manufacturing economically viable, the manufacturer must produce a large number of components to cover these fixed costs. In the case of a smaller quantity of components, additive manufacturing is usually more advantageous since it can be carried out without the need for tooling.

In this work, the implementation of the PBF-LB/M process, including the incorporation of shape optimization into the construction design, is investigated and evaluated. A tensegrity tower with a height of 5 m, consisting of 9 compression rods and 18 connecting nodes with four different initial geometries, was built, which can be seen in Figure 3. First, the global design of the tensegrity tower was carried out, followed by the local design of the connecting nodes between the cables and the compression rods. The four different initial geometries of the connection nodes were developed and shape-optimized using the

vertex-morphing technique [3]. The connecting nodes were subsequently manufactured by the PBF-LB/M process. After manufacturing, post-processing methods like T6-heat treatment, as well as vibratory grinding and polishing, were conducted. These methods will be further explained in the following chapter.

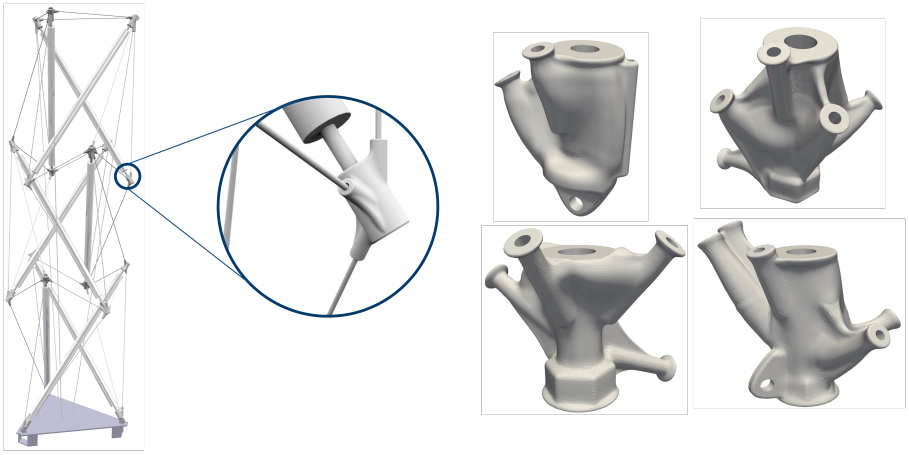

Figure 3. (**Left**): 3D-model of the tensegrity tower with close up of a connecting node (initial design); (**Right**): shape-optimized designs of the four different connecting nodes.

2. Materials and Methods

2.1. Design

Figure 4 provides an overview of the general methodology employed to integrate the PBF-LB/M process and its subsequent integration into the construction design.

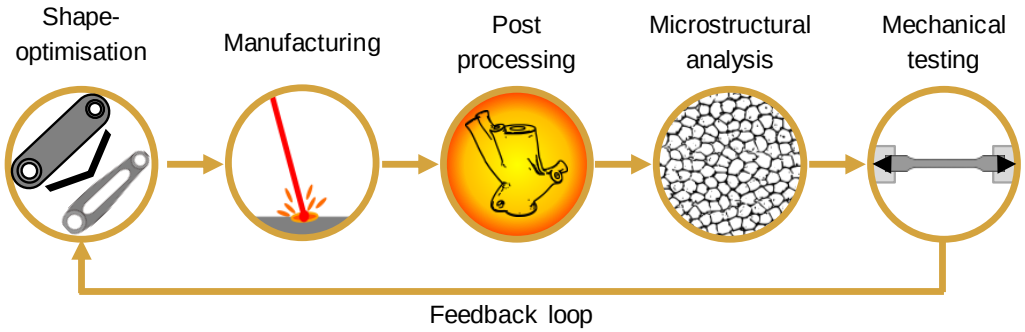

Figure 4. Workflow for the implementation of the PBF-LB/M process into the construction sector.

The overall design of the tensegrity tower was determined through the utilization of form finding techniques. Form finding in engineering is the process of determining the optimal shape and configuration of structural systems. It involves achieving equilibrium between internal forces and external loads while considering factors such as aesthetics, material properties, and construction feasibility. Methods include physical modeling, computational simulations, and optimization techniques. Form finding enables the creation of efficient and visually appealing structures that meet design criteria [4]. The software Rhinoceros 3D (Robert McNeel & Associates, Barcelona, Spain) with the Grasshopper plugin was employed for this purpose. The comprehensive structural analysis was performed utilizing the finite-element software SOFiSTiK (SOFiSTiK AG, Nuernberg, Germany). Subsequently, the obtained loads and loading directions of the cables at each connection node of the global structure were taken out and used for the local design process of the respective connection nodes, see Figure 3. The initial designs of each four nodes can be observed in Figure 3. The compression rods were connected to the nodes by using threaded rods. The attachment of the cables to the nodes was achieved using internal threads within the connection node. These internal threads were machined post-manufacturing, as the

likelihood of higher porosity in threads manufactured through PBF-LB/M is significant. Porosity can give rise to cracks under cyclic loading conditions [5].

Following the initial design, the connection nodes were shape optimized utilizing the vertex-morphing technique. For a comprehensive understanding of the vertex-morphing technique, refer to [6,7].

2.2. Manufacturing and Post-Processing

The applied material for the connection nodes was AlSi10Mg by TLS-Technik GmbH & Co. KG (Hartenstein, Germany). The chemical composition is presented in Table 1. A particle size of 20–63 µm was used. For the manufacturing process, a Realizer SLM 250 machine, outfitted with a 400 W pulsed laser, was used. The laser parameters employed during the manufacturing process of the connection nodes can be found in Table 2. The build platform temperature was set to 165 °C.

Table 1. Chemical composition of AlSi10Mg according to the manufacturer.

Element	Al	Si	Mg	Fe	Ti	Zn	Mn	Cu	Cr
wt.-%	Bal.	9–11	0.20–0.45	≤0.55	≤0.15	≤0.10	≤0.45	≤0.05	≤0.05

Table 2. Applied laser parameters for the manufacturing of the connection nodes.

Laser Parameter	Energy Density	Laser Power	Laser Speed	Hatch Distance	Layer Thickness
Value	80 J/mm^3	400 W	1000 mm/s	0.1 mm	0.05 mm

To investigate the mechanical properties, two additional build jobs were carried out. In each build job, five tensile specimens were manufactured for each building direction (0°, 45°, 90°). Additionally, three cubic specimens measuring 10 mm × 10 mm × 10 mm were produced for microstructural analysis. One of the build jobs was T6 heat-treated T6 as described below, while the other one remained in the as-built state.

After manufacturing, the connection nodes were heat-treated. A T6-heat treatment was applied using the parameters of [8]. The heating rate was set to 10 °C/min. Afterwards, a solution heat treatment was performed at 525 °C for a duration of 6 h. Following the solution heat treatment, the material was quenched. Finally, precipitation hardening was carried out at 165 °C for a period of 7 h. This not only supposedly improves the ductility, it also reduces the possible occuring residual stresses of the PBF-LB/M-manufactured parts [9].

After the completion of the heat treatment process, the nodes were cut from the build plate with a band saw, and the support structure was manually removed. To mitigate surface roughness, a three-step approach of vibratory grinding was employed. Initially, a coarse ceramic grinding material was employed for a duration of 24 h, succeeded by a finer ceramic grinding material for 4 h. The final step encompassed the utilization of fine polishing material for a period of two hours.

2.3. Mechanical Testing and Microstructural Investigation

To investigate the mechanical properties such as yield strength, ultimate tensile strength, and elongation at fracture, uniaxial tensile testing was carried out before and after the T6 heat treatment. Tensile testing was conducted using a Zwick and Roell Z100 tensile testing machine with a 100 kN load cell. To investigate the porosity and the microstructure, the aforementioned cubical specimens with a dimension of 10 mm × 10 mm × 10 mm were hot-embedded in epoxy resin, ground, and polished using a Struers CitoPress and a Struers LaboPol. The grinding parameters are shown in Table 3. The specimens were etched using hydrochloric acid (HCl) and nitric acid (HNO_3), known as aqua regia. The porosity was measured using a grey-scale comparison of the binarized and polished cubicals.

Table 3. Grinding parameters for surface treatment of the connection nodes.

Step	**1**	**2**	**3**	**4**
Grinding disk	MD Molto 220	MD Largo	MD Dac	MD Nap
Duration	4 min	4 min	4 min	3 min
Rev./min	150	150	150	150
Pressure	30 N	30 N	30 N	30 N
Lubricant	Water	6 µm	3 µm	1 µm

As the tensegrity tower is intended to serve as a permanent and tangible exhibit at the Deutsches Museum in Munich, the connection nodes are subjected to both static and cyclic loading. Thus, comprehensive static and cyclic tests were performed to evaluate the structural performance. The internal thread within the connection nodes emerged as the most critical region in terms of fatigue. Therefore, the threaded regions were cut from the tensegrity nodes so that a uni-axial fatigue test of the internal thread was able to be carried out. Two M12 threaded rods were connected to the specimen. The rods were subsequently clamped in the fatigue testing machine. The high cycle fatigue testing was conducted under ultimate limit state (ULS) loading conditions to assess its durability. The region of the internal threads was cut from the node and mounted into a uniaxial fatigue testing machine. An Instron 8032 fatigue testing machine with an Instron 8800 controller was used. The fatigue load was applied in a sinusoidal manner. The fatigue test was stopped at 1×10^7 cycles. The static testing of one complete node with real loading conditions is explained and assessed in [6].

3. Results

3.1. Static Mechanical Properties

Figure 5 displays the results of tensile tests conducted on specimens with various building directions (0°, 45°, and 90°) in both the as-built (AB) and T6 heat-treated states.

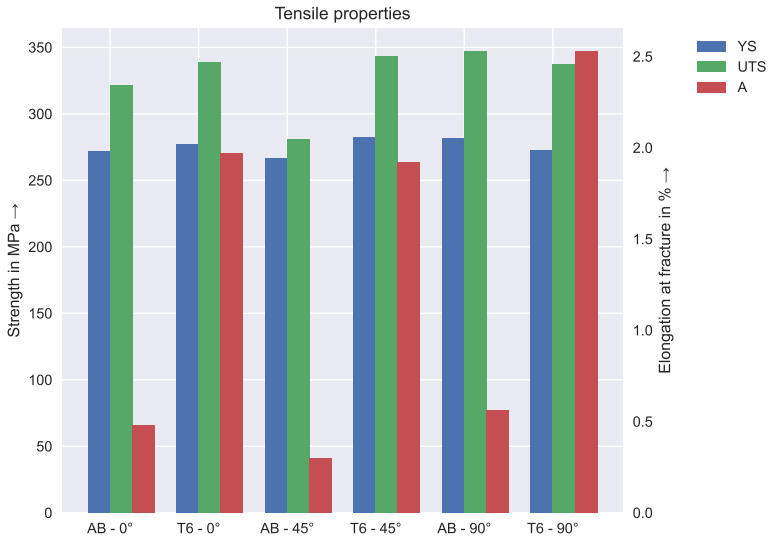

Figure 5. Results of tensile test in the as-built (AB) configuration and after T6 heat treatment (T6), with orientations of 0°, 45°, and 90°. YS: yield strength; UTS: ultimate tensile strength; and A: elongation at fracture.

Applying T6 heat treatment results in an observable increase in the elongation at fracture, whereas the yield strength and ultimate tensile strength show only marginal improvements. For safety considerations, the shape optimization and design of the connection nodes were based on the lowest recorded values of the T6 heat-treated specimens with

regard to the yield strength, the ultimate tensile strength, and the elongation at fracture. Here, the T6-0° condition was used.

3.2. Microstructure

Figure 6 shows the microstructure before and after the T6 heat treatment, with different magnifications.

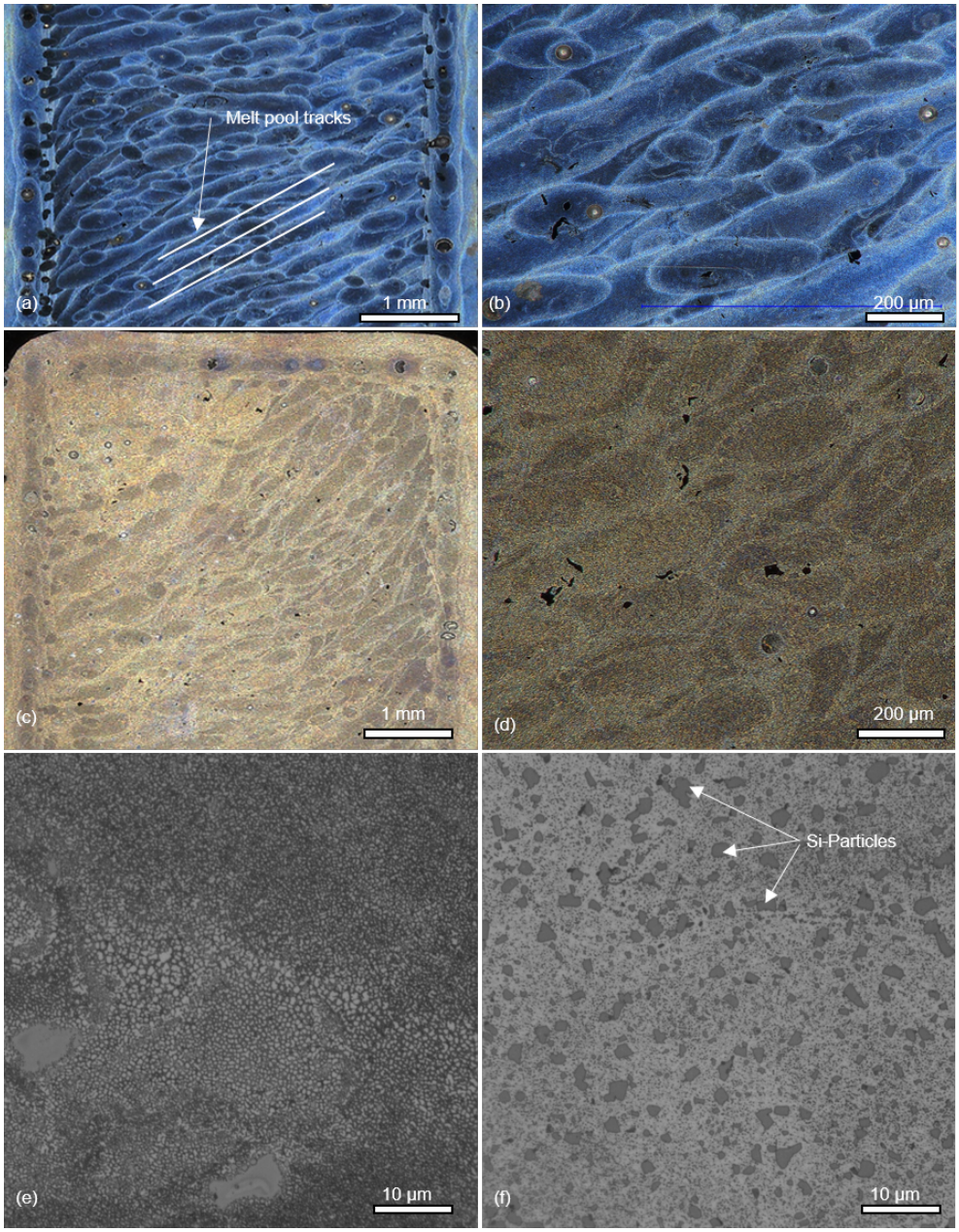

Figure 6. Microstructure of PBF-LB/M/AlSi10Mg before and after T6 heat treatment; (**a**,**b**) as-built microstructure, cross-sectional polish; (**c**,**d**) T6 heat-treated microstructure, cross-sectional polish; (**e**) as-built microstructure cross-sectional polish; and (**f**) T6 heat-treated microstructure showing Si-particles.

During T6 heat treatment of the AlSi10Mg alloy, Ostwald ripening occurs as smaller precipitates dissolve and redeposit onto larger ones, resulting in an increase in their size and a shift in the size distribution. This phenomenon enhances the strength and mechanical properties of the material by creating larger precipitates that act as barriers to dislocation movement. Moreover, the high-temperature aging process promotes the coalescence of Si

particulates in the alloy, facilitated by Ostwald ripening, where smaller Si particles dissolve and merge with larger ones, leading to the formation of larger Si agglomerates with improved mechanical properties [10]. The formation of the Si-particles can be seen in Figure 6, and the respective mechanical properties can be seen in Figure 5. The PBF-LB/M-manufactured parts exhibited a density of 99.94 %. This density is within the upper range of multiple other investigations [11–13].

3.3. Fatigue

The results of the fatigue testing with various loading scenarios are presented in Table 4. The presented data display the loads rather than the stresses; this is attributed to the heterogeneous cross-sectional profiles of the cut off specimens containing internal threads. It is evident that all the applied fatigue loads resulted in run-outs, meaning that no fractures occurred.

Table 4. Results of fatigue tests on four different specimens subjected to ultimate limit state (ULS) loads.

Specimen	Δ*F* (kN)	Min. F (kN)	Max. F (kN)	Stress Ratio	No. of Cycles
1	1.5	6	7.5	0.8	1×10^7
2	1.5	15	16.5	0.9	1×10^7
3	3.0	15	18	0.83	1×10^7
4	3.0	15	18	0.83	1×10^7

4. Discussion

The tensegrity tower was erected in the Deutsches Museum in Munich in June 2022. Since then, the tower has been a successful, educational exhibit. In summary, while the implementation of the PBF-LB/M process in construction design and assembly proves to be feasible (as can be seen in Figure 7), it requires careful attention to laser parameters, post-processing techniques, quality assurance, and addressing fatigue concerns, particularly in high porosity materials like AlSi10Mg. In addition to the previously stated considerations, the unique nature of each stage of PBF-LB/M manufacturing poses economic challenges when it comes to assessing and certifying each geometry. Conducting individual assessments for each unique part would be economically unfeasible. Porosity remains a significant issue, particularly in relation to fatigue problems, making it crucial to adopt a different strategy. To ensure quality assurance, two key areas can be targeted. Firstly, the process itself needs to be qualified, meaning that the PBF-LB/M machine must be certified for manufacturing parts for the construction industry. This qualification ensures that the company producing PBF-LB/M parts is capable of doing so in a reliable and controlled manner. Secondly, design restrictions should be implemented during the geometry optimization phase. By considering design restrictions, such as minimizing overhanging structures like holes, the potential for increased porosity at these critical areas can be reduced. For instance, topology optimization techniques often introduce holes into the parts, while shape optimization techniques do not. By focusing on process qualification and incorporating design restrictions during geometry optimization, the overall quality of PBF-LB/M parts can be effectively controlled. This approach addresses the economic challenges of certifying every unique part while also targeting the issue of porosity, particularly in relation to fatigue problems.

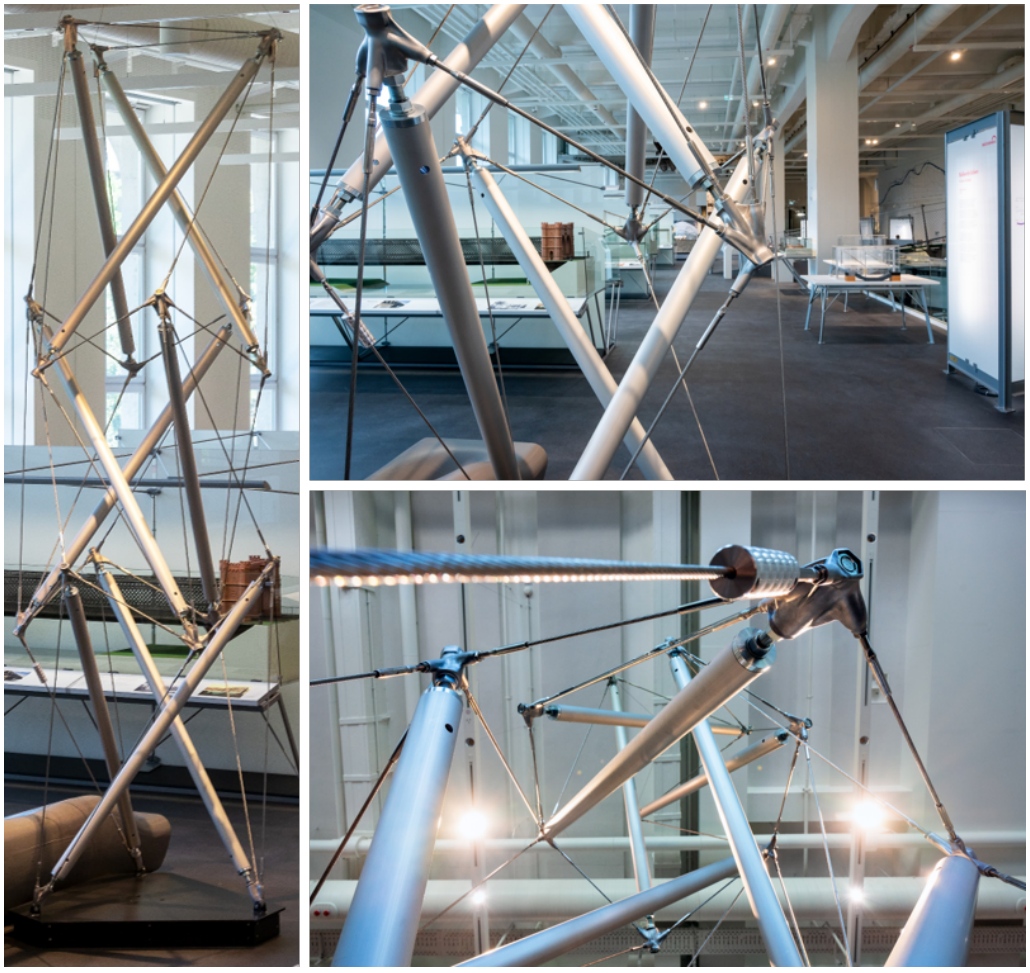

Figure 7. Assembled tensegrity tower with PBF-LB/M-manufactured connection nodes between the cables and the compression rods.

5. Conclusions and Outlook

From this study, the following conclusions can be drawn:

- The PBF-LB/M process was successfully integrated into the construction design process.
- A design and manufacturing route was proposed to safely implement the PBF-LB/M process into the construction design and manufacturing process.
- Shape optimization can be used to optimize the force flow in the part and reduce mass for faster production.
- A qualification method for PBF-LB/M machines for the construction sector is necessary, which is comparable to qualification methods of welding processes.
- Design restrictions should be implemented into the shape optimization process to reduce the danger of internal defects occurring.

Author Contributions: Conceptualization, J.D. and D.S.; methodology, J.D.; software, F.O.; validation, J.D. and J.B.; formal analysis, C.R.; investigation, J.D.; resources, M.M.; data curation, J.D. and D.G.; writing—original draft preparation, J.D.; writing—review and editing, D.S. and C.R.; visualization, J.D.; supervision, M.M.; project administration, C.R.; and funding acquisition, C.R. and J.D. All authors have read and agreed to the published version of the manuscript.

Funding: This study was funded by the Deutsche Forschungsgemeinschaft (DFG, German Research Foundation)—project number 414265976 – TRR 277. We would like to extend our sincere appreciation to the DFG for their invaluable funding and support towards the successful completion of this project.

Informed Consent Statement: Not applicable.

Data Availability Statement: Data available on request.

Acknowledgments: The authors would like to express their gratitude to Roesler Oberflachentechnik GmbH and Hausmann GmbH & Co. Stahlbau KG for their valuable collaboration in this study.

Conflicts of Interest: The authors declare no conflict of interest.

References

1. Schober, H.; Kürschner, K.; Jungjohann, H. Neue Messe Mailand– Netzstruktur und Tragverhalten einer Freiformfläche. *Stahlbau* **2004**, *73*, 541–551. [CrossRef]
2. Klahn, C.; Meboldt, M.; Fontana, F.F.; Leutenecker-Twelsiek, B.; Jansen, J. *Entwicklung und Konstruktion für die Additive Fertigung: Grundlagen und Methoden für den Einsatz in Industriellen Endkundenprodukten*; Vogel Business Media: Wuerzburg, Germany, 2021.
3. Hojjat, M.; Stavropoulou, E.; Bletzinger, K.U. The Vertex Morphing method for node-based shape optimization. *Comput. Methods Appl. Mech. Eng.* **2014**, *268*, 494–513. [CrossRef]
4. Yu, Z.; Dai, H.; Shi, Z. Structural form-finding of bending components in buildings by using parametric tools and principal stress lines. *Front. Archit. Res.* **2022**, *11*, 561–573. [CrossRef]
5. Diller, J.; Rier, L.; Siebert, D.; Radlbeck, C.; Krafft, F.; Mensinger, M. Cyclic plastic material behavior of 316L manufactured by laser powder bed fusion (PBF-LB/M). *Mater. Charact.* **2022**, *191*, 112153. [CrossRef]
6. Ghantasala, A.; Diller, J.; Geiser, A.; Wenzler, D.; Siebert, D.; Radlbeck, C.; Wüchner, R.; Mensinger, M.; Bletzinger, K.U. Node-based shape optimization and mechanical test validation of complex metal components and support structures, manufactured by laser powder bed fusion. In *Advances in Manufacturing, Production Management and Process Control*; Lecture Notes in Networks and Systems; Springer International Publishing: Cham, Switzerland, 2021; pp. 10–17.
7. Asl, R.N.; Shayegan, S.; Geiser, A.; Hojjat, M.; Bletzinger, K.U. A consistent formulation for imposing packaging constraints in shape optimization using Vertex Morphing parametrization. *Struct. Multidiscip. Optim.* **2017**, *56*, 1507–1519. [CrossRef]
8. Ingenieure, V.D. *Additive Manufacturing Processes-Powder Bed Fusion of Metal with Laser Beam (PBF-LB/M)-Material Data Sheet Aluminium Alloy AlSi10Mg*, 2nd ed.; Verband Deutscher Ingenieure: Bonn, Germany, 2020. Available online: https://www.beuth.de/en/technical-rule/vdi-3405-blatt-2-1/326385793 (accessed on 15 May 2023).
9. Padovano, E.; Badini, C.; Pantarelli, A.; Gili, F.; D'Aiuto, F. A comparative study of the effects of thermal treatments on AlSi10Mg produced by laser powder bed fusion. *J. Alloys Compd.* **2020**, *831*, 154822. [CrossRef]
10. Li, Z.; Cheng, C.C.; Dhillon, J.S.; Kwon, S.Y.; Hudon, P.; Brochu, M. Precipitation behavior of an Al7SiMg alloy processed by laser powder bed fusion during non-isothermal and isothermal heat treatments. *Materialia* **2023**, *28*, 101751. [CrossRef]
11. Schneider, M.; Bettge, D.; Binder, M.; Dollmeier, K.; Dreyer, M.; Hilgenberg, K.; Klöden, B.; Schlingmann, T.; Schmidt, J. Reproducibility and Scattering in Additive Manufacturing: Results from a Round Robin on PBF-LB/M AlSi10Mg Alloy. *Pract. Metallogr.* **2022**, *59*, 580–614. [CrossRef]
12. Kan, W.H.; Nadot, Y.; Foley, M.; Ridosz, L.; Proust, G.; Cairney, J.M. Factors that affect the properties of additively-manufactured AlSi10Mg: Porosity versus microstructure. *Addit. Manuf.* **2019**, *29*, 100805. [CrossRef]
13. Aboulkhair, N.T.; Everitt, N.M.; Ashcroft, I.; Tuck, C. Reducing porosity in AlSi10Mg parts processed by selective laser melting. *Addit. Manuf.* **2014**, *1–4*, 77–86. [CrossRef]